Pacific Northwest National Laboratory
Operated by Battelle for the
U.S. Department of Energy

Nuclear Energy Research Initiative Project No. 02-103

Innovative Low-Cost Approaches to Automating QA/QC of Fuel Particle Production Using On-Line Nondestructive Methods for Higher Reliability

February 2006

Final Project Report

S. Ahmed
C. R. Batishko
M. Flake
M.S. Good
R. Mathews
M. Morra
Pacific Northwest National Laboratory

P. D. Panetta
A. F. Pardini
G. A. Sandness
B. J. Tucker
D. R. Weier

R. L. Hockey
Applied Research Associates

J. N. Gray
CNDE, Iowa State University

J. J. Saurwein
General Atomics

L. J. Bond
Idaho National Laboratory

R. A. Lowden
J. H. Miller
Oak Ridge National Laboratory

Nuclear Energy Research Initiative Project No. 02-103

Innovative Low-Cost Approaches to Automating QA/QC of Fuel Particle Production Using On-Line Nondestructive Methods for Higher Reliability

February 2006

Final Project Report

S. Ahmed
C. R. Batishko
M. Flake
M. S. Good
R. Mathews
M. Morra
Pacific Northwest National Laboratory

P. D. Panetta
A. F. Pardini
G. A. Sandness
B. J. Tucker
D. R. Weier

R. L. Hockey
Applied Research Associates

J. N. Gray
CNDE, Iowa State University

J. J. Saurwein
General Atomics

L. J. Bond
Idaho National Laboratory

R. A. Lowden
J. H. Miller
Oak Ridge National Laboratory

EXECUTIVE SUMMARY

Sub-millimeter size, coated fuel particles are the basic component of the fuel elements used in several current and proposed gas-cooled reactor designs. The coated particles consist of a ceramic microsphere of nuclear material (e.g., uranium oxide, uranium oxycarbide, plutonium oxide, thorium oxide, etc.) that is encapsulated in succession by a low-density carbon layer (buffer layer), a high-density isotropic pyrocarbon layer (IPyC), a silicon carbide layer (SiC), and a second high-density isotropic pyrocarbon layer (OPyC). This multi-layered system, known as the Tri-isotopic (TRISO) fuel particle, has been engineered to serve as a mini-pressure vessel that contains the fission products generated in the microspheres of nuclear material during irradiation.

Coated particle fuel has been manufactured on a large scale in the U.S. and in Germany for large gas-cooled reactors, and on a smaller scale in Japan and China for small gas-cooled reactors. To meet the stringent performance requirements imposed on the fuel, the TRISO coated particles must be fabricated in accordance with stringent process specifications and must be inspected to show conformance to a relatively large number of product specifications. Because of the very large number of TRISO fuel particles in a reactor core (around 15 billion in the proposed 600-MW(t) Gas Turbine - Modular Helium Reactor), acceptance testing of fuel particles has historically been done on a sampling basis using a suite of quality control (QC) methods that is, for the most part, common to all coated particle fuel manufacturers. However, most of these QC methods are based on 1970's and 1980's technology and tend to be slow and labor intensive. Furthermore, many of these methods are destructive and thus can be employed only on a sampling basis.

In general, the QC methods currently available for coated-particle fuel manufacturing are inadequate to support economical commercial production of fuel for the anticipated future generation of gas-cooled reactors. It is essential that fully automated nondestructive QC methods be developed for high throughput inspection of coated particles in near real time to provide rapid and accurate feedback to the coated-particle fuel fabrication processes. The ultimate goal in developing new QC methods would be to enable inspection rates on the order of 200 particles/sec (although use of multiple inspection systems operating in parallel would reduce the need for such a high rate) for 100% inspection and sorting of fuel particles for critical defects such as a missing buffer layer or a defective SiC. Although 100% inspection of coated particles is not essential to commercial deployment of gas-cooled reactors, it is desirable in that the resultant improvement in the as-manufactured quality of the fuel achieved by identifying and sorting out defective particles (assuming the fuel fabrication processes produce them) might allow some reduction in the credit taken in gas-cooled reactor design and licensing for other barriers to the release of fission products to the environment (e.g., the fuel element matrix, the graphite blocks in prismatic block cores, the primary circuit boundary, and the reactor building).

In consideration of this need for improved QC methods to support future commercial fabrication of coated particle fuel, Pacific Northwest National Laboratory (PNNL), General Atomics (GA), Iowa State University (ISU), and Oak Ridge National Laboratory) ORNL collaborated to define and perform this Nuclear Energy Research Initiative) NERI quality assurance (QA)/QC project to explore the potential applicability of a number of nondestructive evaluation (NDE) technologies with which PNNL has particular expertise and has had success in deploying in similar applications. The NDE techniques selected for evaluation included:

Inspection Methods and Their Intended Application		
High-Speed in-line Inspection	**Off-line Batch Sampling**	**On-Process**
Electromagnetic (EM) impedance (e.g., induction and capacitance sensors)	Resonant Ultrasound Spectroscopy (RUS)	Ultrasonic Scattering and Through Transmission Of An Entire Batch
Optical Surface Inspection	Acoustic Microscopy	

A number of additional tasks such as a literature review, numerical modeling, particle fabrication (at ORNL) and X-ray characterization (at ISU) of coated particle standards were also defined and conducted to support the NDE method evaluations.

The plan, as defined in the NERI project proposal, was to investigate each of these technologies in the first and second years of the project, then down-select and further develop the most promising methods, which would be demonstrated on a laboratory scale in the third (final) year of the project. The original objective of the project was to develop and demonstrate NDE techniques that could be used to accept or reject both individual particles and batches of coated particles in terms of a quality index. The laboratory-scale demonstrations were deleted from the work scope as a result of a significant reduction in third year funding, and the task to develop a quality index based on the NDE methods was terminated when it became apparent that the NDE methods under investigation did not have the potential to characterize the particles with respect to all of the key properties important to the irradiation performance of the particles. Furthermore, TRISO particles having the key defects that potentially degrade the irradiation performance of the particles were generally unavailable to the project.

In the first year of the project (FY2003), the acoustic microscopy work was suspended after it became apparent that current capability could not resolve defects smaller than about 50 μm in coated TRISO particles, and that it would be necessary to work at the extreme high end of the frequency range for ultrasonics (i.e., above 250 MHz and perhaps as a high as 1 GHz), which would require additional funding to upgrade existing instrumentation. Also, a decision was made at the end of the first year to defer further work on the RUS method until a more suitable transducer could be procured. Consequently, the focus of the project in the second year (FY2004) was development and evaluation of electromagnetic methods and the optical methods. ORNL and ISU performed extensive coated particle fabrication activities and X-radiographic characterization of coated particle dimensional properties, respectively, in support of the EM methods task. Work under the on-process measurement task also continued in the second year, but ran into difficulties when the results from measurement of particle diameters in a model coater using transmission ultrasound at frequencies near 50 kHz were found to fall into a frequency and size domain where published theories on particles in a fluidized bed could not explain the observed behavior. This task was subsequently reduced in scope to resolving the inconsistencies between existing theories and the experimental results.

In the final year of the project (FY2005), the primary effort was in performing the EM measurements on surrogate and uranium coated particles and in attempting to correlate the results of these measurements with physical properties of the coated particles as measured by ORNL and/or by ISU. Also, a prototype high throughput particle inspection system was developed and fabricated, and the RUS task resumed at a relatively low level of effort after a suitable transducer was obtained. The on-process measurement task continued but was curtailed to a few fundamental experiments to determine the maximum resolution of this method, and it was eventually determined that the air-coupled ultrasonic technique under

investigation does not have the required sensitivity to changes in coating thickness within the frequency range and particle sizes of interest.

Of the methods evaluated, the EM methods, RUS, and the optical methods were all shown to be potentially applicable for commercial fuel production quality control. The evaluation of the results of the EM methods presented in Section 5.1 of this report indicate that inductive and capacitive impedance measurements could provide a means of sorting the particles with respect to particle volume and pyrocarbon mass (or volume), respectively, and that these techniques, when used together, should provide an effective means of sorting out particles that are dimensionally atypical, including particles with missing or excessively thin coating layers. Furthermore, PNNL designed and built a prototype automated EM method inspection system and demonstrated the system (in a video provided to DOE) at inspection rates of approximately 500-1000 particles/min, and substantially higher inspection rates would be possible using more sophisticated equipment. The authors consider these to be important results because they indicate that the EM methods could provide enhanced capability to detect and sort out particles that are defective by virtue of having missing or thin coating layers (that are unobservable by visual inspection) relative to other methods that are capable of sorting particles only on the basis of particle diameter (e.g., screening, roller micrometer, particle size analyzer, etc.).

There is also some indication that the inductive impedance method could be used to characterize the IPyC layer (in buffer and IPyC coated particles) and the OPyC layer with respect to density, but it is doubtful that the inductive impedance measurement would detect small density differences in the presence of the expected particle-to-particle variations in PyC layer thickness. However, if the measurement is used as an in-line go/no-go check of the acceptability of batch average PyC density, the capability to detect small differences in density should not be necessary.

Although theory indicates that the inductive impedance measurements might be influenced by differences in PyC microstructure, the project did not develop any empirical evidence supporting this, and it is again doubtful that differences in microstructure could be detected in the presence of the expected variations in PyC layer volume. It is probably correct to conclude that the EM methods, as implemented in this study, do not have the capability to detect microstructural defects in the PyC or the SiC coating layers. However, it should be emphasized that the scope of the EM measurement task did not permit the method to be fully optimized. Modeling of the induction method indicated, for example, that the use of multiple frequencies might provide additional information about the individual carbon volumes. Also, substantially improved spatial resolution can be obtained by more localized measurements made with one or more very small pancake-type (non-enclosing) coils. Consequently, it is recommended that DOE consider funding follow-on work to further explore the potential of the EM methods for characterization of coated particles with respect to key properties.

The RUS work performed in the third year revealed that the resonance modes of a TRISO particle are sensitive to the size and shape of the particle and to the thickness of the SiC layer. Specifically, particles having missing or thin SiC layers were found to have spectra that are distinctly different from normal TRISO particles. Theory suggests that RUS should also be capable of characterizing layers having defects such as cracks or inclusions, but this capability was not demonstrated due to the unavailability of suitable defective particle standards. An inspection throughput rate of about one particle/sec was achieved by considering a narrow spectral range near 3 MHz where the dominant resonance peaks occur for normal TRISO particles. However, greater inspection throughput rates would be possible with a well-engineered particle handling system. Although the unavailability of a suitable transducer until the final

year limited the amount of work performed on the task, the work that was performed indicated that RUS has good potential as an enhanced QC technique. Consequently, it is recommended that DOE fund follow-on work on RUS that would address laser ultrasonic resonance, a non-contact approach that offers improved resolution and sensitivity, reduced scatter in resonance frequencies, and the ability to perform high-speed inspections.

The project also defined digital image analysis methodologies for both off-line laboratory scale optical characterization and in-line optical inspection of coated particles. Methods for digitizing images of particles were developed to support the evaluation of requirements for automated systems, including resolution issues and hardware issues driven by production requirements. The result was a practical approach to digitizing images of individual particles using a digital camera, an optical microscope, and a commercial image processing and analysis software package. Images of particles with diameters in the 700- to 1000-µm range were digitized and processed to provide an extended depth-of-field image at a resolution adequate for features on the order of 5 µm to be easily measured and surface anomalies on the order of 2 µm to be easily detected. Additionally, a coherent anti-Stoke Raman spectroscopy (CARS) microscope was used to acquire a few test images of one particle at very high resolution to illustrate non-scanning electron microscope (SEM) high-resolution optical imaging. An image with sub-micron resolution was achieved, revealing features easily measurable at the sub-micron scale. It is envisioned that these optical inspection techniques could be used for automated off-line inspection of samples of fully-coated TRISO particles to determine the fraction of particles having a defective or missing OPyC layer and for inspection of samples of burned-back particles (particles in which the OPyC layer has been oxidized away by heating the particles in air) for defects in the surface of the SiC coating layer, such as cracks, large open pores, or evidence of impurity attack on the SiC.

A conceptual inspection system was defined and analyzed as part of the in-line optical inspection methods task. Central to the in-line concept is high camera resolution combined with high optical magnification and high frame rate. Components providing these characteristics were identified and a potential implementation arrangement was evaluated.

In addition to supporting the EM methods evaluation task, the micro focus X-radiography work performed at ISU as part of this NERI project demonstrates the capability of X-radiography to measure the diameter of the kernel and the thickness of each of the coating layers in up to about 30 fully-coated TRISO particles at a time. The results of the ISU work suggest that X-radiography with digital image analysis can be automated and deployed to greatly speed up (relative to metallography/image analysis) the inspection of TRISO coated particles for dimensional properties in a batch-sampling mode.

In conclusion, the PNNL-led NERI QA/QC project was successful in demonstrating the feasibility of using automated EM methods (i.e., inductive and capacitive impedance measurements), optical methods, and, to a lesser extent, RUS for enhanced QC inspection of TRISO coated particles. The project also demonstrated the apparent lack of potential of acoustic microscopy for inspection of coated particles at frequencies below 250 MHz, and of air-coupled transmission ultrasound for on-process monitoring of particle size growth within a fluidized bed coater. Although these latter NDE technologies did not prove to have the potential envisioned at the start of the project, the negative results obtained by the project are of value with respect to providing guidance to the direction of future coated-particle enhanced QC methods investigations.

As with any project of this nature, the results and the conduct of the project have provided the participants with insight into additional areas of potentially fruitful investigation. Based on these insights, the authors offer the following recommendations (some of which have been previously mentioned) for future work in the area of advanced coated-particle fuel QC methods development.

- Additional EM method development work to optimize the induction and capacitance sensor frequency for specific coated particle properties.

- Investigation of different induction sensor configurations as a means of detecting cracks or other localized flaws in coated fuel particles.

- Investigation of alternate capacitive sensor designs that reduce stray capacitance and the effects of external factors as a means of reducing measurement uncertainty.

- Investigation of the use of capacitive impedance measurements as a means of detecting individual natural uranium oxycarbide (NUCO) kernels having unacceptable stoichiometry (i.e., relative amounts of uranium carbide and uranium oxide).

- Development of an advanced RUS inspection system using laser ultrasonic techniques.

- Development of the detailed specifications for an automated high-speed optical inspection system, including a fuel particle handling device capable of presenting the fuel particles for imaging at the required precision and speed.

These recommendations are discussed in more detail in Section 6 of this report.

The following table further summarizes the scope, conclusions, and recommendations (for further work) from the NERI QA/QC Project for the convenience of the reader.

Scope, Conclusions, and Recommendations for Further Work		
Method Evaluated	**Conclusions**	**Recommendations**
Electromagnetic methods (inductive and capacitive impedance measurements)	Good potential demonstrated for real-time in-line screening of coated fuel particles having atypical size and coating layer thickness. Potentially useful for detecting particles having other types of coating defects, but this capability not demonstrated during the project.	Optimize sensor frequency for specific coated particle properties. Refine sensor designs as a means of detecting cracks and other non-geometric coating flaws. Optimize sensor design to reduce measurement uncertainty. Determine feasibility of using capacitive impedance measurements to detect NUCO kernels having poor stoichiometry.

Scope, Conclusions, and Recommendations for Further Work		
Method Evaluated	**Conclusions**	**Recommendations**
Resonance ultrasound spectroscopy (RUS)	Good potential for application to off-line, and possibly in-line, inspection of coated particles for geometric (e.g., coating layer thickness) and non-geometric flaws. However, mechanical coupling of a transducer to the small coated particles is problematic for high-speed inspection.	Evaluate laser ultrasonic resonance methods and develop a non contact inspection technique.
Optical surface inspection	Good potential for off-line and, possibly, in-line inspection of coated particles having visual coating defects.	Develop specifications for, build, and demonstrate a prototypic high-speed inspection system.
Acoustic microscopy	No potential for application to coated-particle QC at ultrasonic frequencies below 250 MHz. Must have 1-5 micron resolution to be useful.	None
Transmission and diffuse field ultrasound	Transmission ultrasound did not have the required sensitivity to changes in particle size in the ultrasound frequency range evaluated. Diffuse field ultrasound was not evaluated.	None
X-radiography and computed tomography	Both techniques have good potential for use in off-line inspection of coated particles. Computed tomography work was limited because it was too time consuming to be effective in supporting project objectives.	None

Contents

Figures

Tables

NUCLEAR ENERGY RESEARCH INITIATIVE (NERI) PROGRAM
DE-FG03-99SF0491
FINAL TECHNICAL REPORT

Project Title: *INNOVATIVE LOW-COST APPROACHES TO AUTOMATING QA/QC OF FUEL PARTICLE PRODUCTION USING ON-LINE NONDESTRUCTIVE METHODS FOR HIGHER RELIABILITY*

Covering Period: FY2003 – FY2005

Date of Report: January 30, 2006

Client: U.S. Department of Energy, Office of Nuclear Energy, Science and Technology

Pacific Northwest National Laboratory
Project Manager/Principal Investigator: Allan Pardini
509.375.2525
allan.pardini@pnl.gov

Applied Research Associates
Principal Investigator: Ronald Hockey
505.846.8866
rhockey@ara.com

Collaborators:
Joe Gray, Iowa State University,
 515.294.9745, jgray@cnde.iastate.edu
John Saurwein, General Atomics
 858.455.2485, john.saurwein@gat.com
Leonard Bond, Idaho National Laboratory
 208.526.9150, leonard.bond@inl.gov
James Miller, Oak Ridge National Laboratory
 865.574.5408, millerjh2@ornl.gov
Richard Lowden, Oak Ridge National Laboratory
 865.576.2769, lowdenra@ornl.gov

1.0 Project Introduction

1.1 Objective and Scope

This Nuclear Energy Research Initiative (NERI) project was tasked with exploring, adapting, developing, and demonstrating innovative nondestructive test methods to automate the inspection of coated nuclear fuel particles. The United States (U.S.) requires improved, economical, inspection methods for Quality Assurance and Quality Control (QA/QC) of fuel production for several reactor concepts being proposed for both near-term deployment [DOE-NE & NERAC, 2001] and Generation IV nuclear systems.

Replacing existing QA/QC methods (performed manually and, in most cases, destructively) with higher-speed, automated, nondestructive methods will make fuel production for advanced reactors economically feasible. For successful deployment of next-generation reactors that employ particle fuels, or fuels in the form of pebbles based on particles, extremely large numbers of fuel particles will require inspection at throughput rates that do not significantly impact the proposed manufacturing processes.

This project was focused on nondestructive examination (NDE) technologies that can be automated for production speeds and that can be utilized for either in-line measurements or on-process measurements. The inspection technologies selected for evaluation and development were considered potentially capable of providing a "quality" assessment of an individual particle or group of particles as those particles pass a sensor. A goal was to define a multiple-attribute signature that could be measured and used for qualification or process control decisions. A primary task in addressing that objective was to establish standard signatures for acceptable particles and for the most problematic types of defects.

The technical scope of the project included:

- Establishing a set of test standards representing both acceptable and reject particles.

- Evaluating, developing, and demonstrating new NDE capabilities that will reduce cost and provide improved reliability and uniformity of manufacturing for batches of particle-based fuels.

- Developing the methodology of a multiple attribute "quality index," that describes both single particle and batch conformity to acceptance specifications.

- Identifying NDE design parameters for an integrated in-line "advanced QA/QC system" for next generation large-scale fuel manufacturing inspection systems required to support advanced reactor deployment.

This NERI final report provides an overview of the research efforts during each year of the project. Sections 2, 3, and 4 describe the research accomplished during fiscal years 2003, 2004, and 2005, respectively. Project years 2003 and 2004 are included to provide an historical perspective and insight into some of the early research directions. It should be noted that conclusions from these early phases may be inconsistent with those developed in the last year of the project. As additional data were acquired during the last year, some of the earlier assumptions were proven to be incorrect and new research directions were followed. Section 5 provides the results of the research and a concise set of conclusions. Section 6 provides recommendations for further work considered necessary to fully develop those

inspection methods that have been found to offer effective detection and characterization capabilities. The appendices provide supporting information and justification of the analyses provided as well as general information concerning this final report.

1.2 Background

A diverse range of reactor concepts are being proposed for both near-term deployment [DOE & NERAC 2001] and as Generation IV nuclear systems for deployment in a time window approaching 2030. One family of that diverse set employs gas cooling. The current status and planned future developments of modular high-temperature gas-cooled nuclear reactor technology was reviewed in a recent report [Kendall 2001]. A common and critical technology component in many of the proposed advanced and next generation reactor designs is TRISO (tri-isotropic) "particle" or "pebble" based fuel technologies. In the latter technology, particles with diameters in the range 0.2-2.0 mm are formed into pebbles with a typical diameter of 60 mm. A pebble and a particle are shown in schematic form in Figure 1.1. These types of fuel are being used or proposed in various international programs.
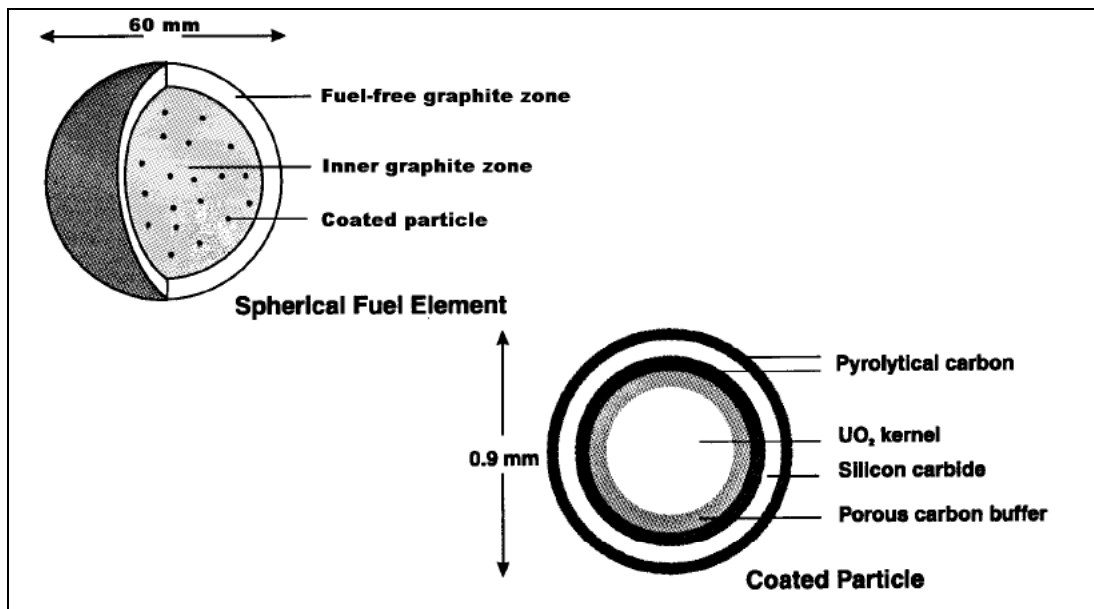
Figure 1.1. A Pebble and a TRISO Particle

The ceramic coated nuclear fuel – TRISO particles – were pioneered in Germany and used in the Arbeitsgemeinshaft Versuchsreaktor (AVR), which operated from 1967 to 1989. Siemens worked on the high temperature gas reactor (HTGR) project from 1972. However, in 1987, a license for construction of a 200 MW Pebble Bed Modular Reactor (PBMR) was denied. The technology, including the fuel technology, was sold to China, which now has an on-going program. A review of the research and development of the fuel element for the Chinese 10 MW (HTGR) was provided by Tang et al. (2000), when criticality of the HTR-10 was scheduled for 2000. The overall QC path for the fuel is described and a sampling-based inspection is reported as the basis for fuel batch acceptance tests, but many details are not provided.

There has also been an extensive Japanese TRISO fuel fabrication program dating back to the late 1960s, that has developed fuel for the High Temperature Engineering Test Reactor (HTTR) [Fukuda et al., 1991]. A series of papers reported aspects of the program, including those needed to improve fuel quality [Minato et al. 1997]. The fabrication of the HTTR first-load fuel was reported by Sawa et al., (1999). Most recently, a summary of the safety criteria and QC for HTTR fuel was provided by Sawa et al., (2001). Only limited details of the QC activities are provided in the various papers that report about this program, but it is apparent that optical measurements, combined with sampling and destructive examinations, are the core of the QC program employed.

In the U.S., General Atomics (GA) provided fuel for generating stations Peach Bottom 1 and Fort St. Vrain and is currently working on the Gas Turbine-Modular Helium Reactor (GT-MHR), which uses TRISO fuel particles set into a compact that is loaded into a hexagonal graphite block to form the fuel element. The methodology for QC used for the Fort St. Vrain program was sampling based, was qualified, and included measurements of 140 attributes of the TRISO particle.

In the early 1990s, a DOE program for coating characterization for the Modular High Temperature Gas Reactor (MHTGR) was supported. The performance of micro-spheres for MHTGRs depends heavily on the properties and performance of the silicon carbide layers. A review of the literature for characterization technologies was prepared by Martin and Martin (1993), including consideration of a range of optical technologies, electronic measurement techniques, and some discussion of magnetic resonance, acoustic and technologies for impurity detection. Current commercial practice for fuel pellet inspection, prior to insertion into zirconium cladding fuel rods, was reviewed by Keyvan et al. (1999). Their conclusion is that the inspection is based on human observation and is essentially a judgment call, prone to error.

An example of a TRISO fuel particle manufacturing process is shown as Figure 1.2. A TRISO particle is shown in Figure 1.3a. The layers are identified in Figure 1.3b. A small quantity of the particles is shown in Figure 1.3c to illustrate some of the challenges of scale and number. It is estimated that there are 20 million particles in a 5-kg batch.
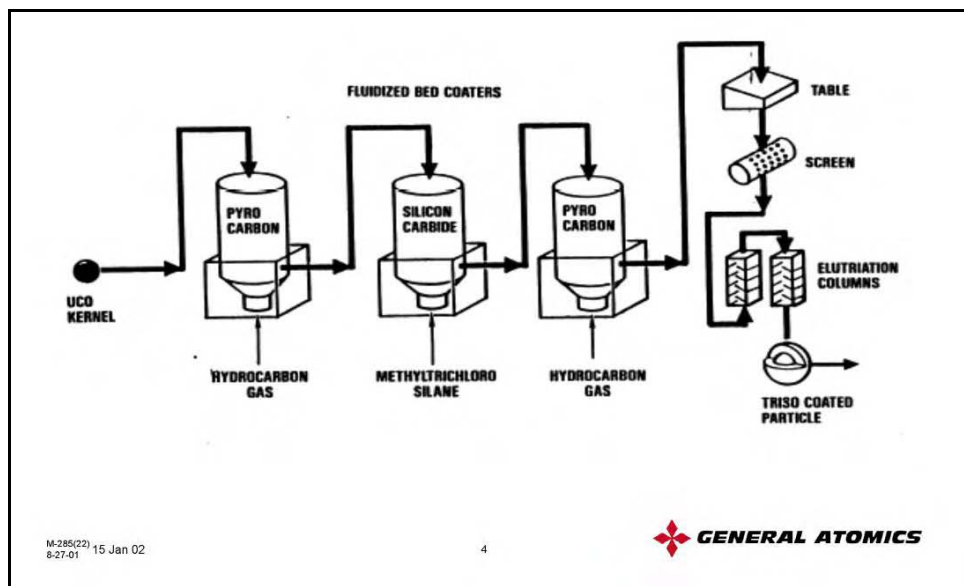
Figure 1.2. Manufacturing Process for TRISO Fuel Particles.
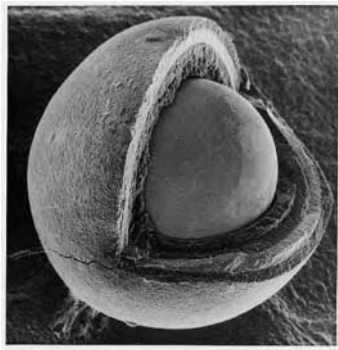
Figure 1.3a. Magnified TRISO Particle.
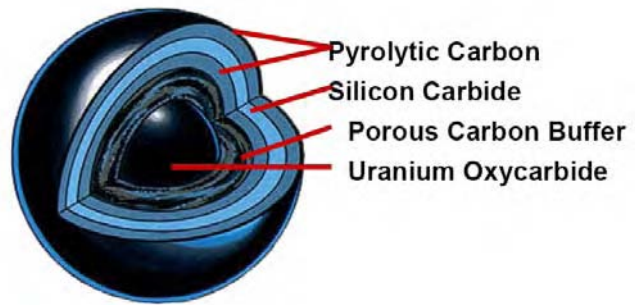
Figure 1.3b. Schematic Drawing of a TRISO Particle

- Pyrolytic Carbon
- Silicon Carbide
- Porous Carbon Buffer
- Uranium Oxycarbide

Figure 1.3c. TRISO Particles

Throughout this document and most of the literature covering this subject, Pyrolytic Carbon is abbreviated as PyC and Silicon Carbide is written as SiC. Most TRISO particles have two PyC layers, commonly referred to as IPyC and OPyC to distinguish between the inner and outer layers.

A summary of the GT-MHR fuel particle and coating thickness data is given as Table 1.1. For such complex requirements, current QC methods employed by GA and other organizations are considered inadequate to support economical fuel production for advanced reactors. Current QA/QC technologies are destructive, inherently time consuming and labor intensive, suitable for only off-line use, and generate too much waste [Saurwein 2001].

Table 1.1. Summary of GT-MHR Fuel Property Specifications Important to Irradiation Performance

Property	Property Type	Mean Value	Critical Region	Defect Fraction
Kernels				
C/U atomic ratio	Variable	0.50 ± 0.20	≤0.01 ≤0.20 ≤0.01 ≥0.80	NA
O/U atomic ratio	Variable	1.50 ± 0.20	NA	NA
Kernel diameter (μm)	Variable	350 ± 10	≤0.01 ≥400	NA
Kernel density (Mg/m^3)	Variable	≥ 10.5	NA	NA
Coated Particles				
Buffer thickness (μm)	Variable	100 ± 10	≤0.01 <50	NA
Missing buffer (≤15 μm)	Discrete	NA	NA	1.0×10^{-5}
IPyC thickness (μm)	Variable	35 ± 5	≤0.01 <20 ≤0.01 >50	NA
IPyC density (Mg/m^3)	Variable	$1.80 – 1.95$	≤0.02 <1.80	NA
IPyC anisotropy (BAF_o)	Variable	1.040	≤0.01 >1.060	NA
SiC thickness (μm)	Variable	35 ± 5	≤0.01 <25	NA
SiC density (Mg/m^3)	Variable	≥3.18	≤0.01 <3.17	NA
SiC integrity – gold spots or visible flaws	Discrete	NA	NA	1.0×10^{-3}
OPyC thickness (μm)	Variable	40 ± 10	≤0.01 <21	NA
OPyC density (Mg/m^3)	Variable	$1.75 – 1.90$	NA	
OPyC anisotropy	Variable	1.040	≤0.01 >1.060	NA
Missing OPyC (≤20 μm)	Discrete	NA	NA	1.0×10^{-4}
OPyC integrity	Discrete	NA	NA	1.0×10^{-2}
Compacts				
U contamination (grams exposed U/gram U)	Variable	NA	NA	1.0×10^{-5}
SiC defect fraction	Discrete	NA	NA	5.0×10^{-5}
IPyC integrity (fuel dispersion)	Discrete	NA	NA	4.0×10^{-5}
OPyC integrity	Discrete	NA	NA	0.01
Iron content outside SiC (μg)	Variable	50	≤0.01 <100	0.01
Cr, Mn, Co + Ni content (ppm)	Variable	NA	≤0.01 <240	0.01

Figure 1.4 is typical of many of the defects observed in destructive evaluation studies. In the left image of Figure 1.4, defects such as radial cracking, disbonding between PyC and SiC layers, and cracks in the SiC layer are clearly shown. In the right image, particles can be seen with disbonding between layers, layers with thin regions, asymmetrical PyC layers, and density discrepancies among particles and within a kernel and its closest coating layer.
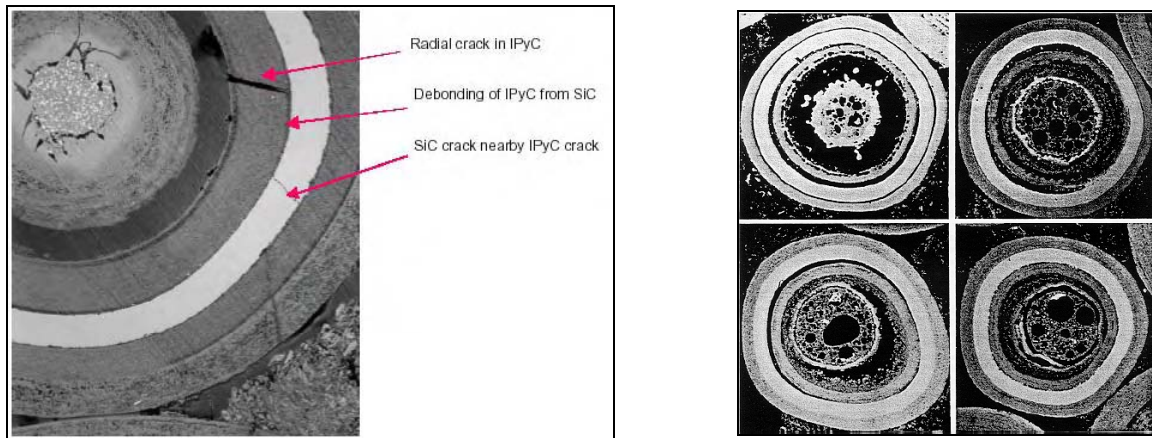
Figure 1.4. Cross-sectional View of Defective Particles

1.3 Participants and Roles

Pacific Northwest National Laboratory (PNNL) led a collaborative team that brings together Applied Research Associates (ARA), General Atomics (GA), Iowa State University (ISU) and Oak Ridge National Laboratory (ORNL).

PNNL served as the lead laboratory and had primary responsibility for coordination of the overall project. This responsibility includes submittal of the initial proposal, administrative duties required by the project (project management plan, quarterly and annual reporting, final project report), cooperating member schedule coordination, and project procurements.

Under a subcontract, ARA provided expertise in the role as principal investigator for portions of the research.

Under a subcontract, GA provided gas-cooled reactor and fuel manufacturing expertise and contributed to the general guidance of the program.

Under a subcontract, staff from the ISU Center for Nondestructive Evaluation (CNDE) performed tasks relating to high-resolution radiographic characterization of fuel particles.

Under a DOE contract, ORNL fabricated coated particles using the same process parameters that would be used for actual fuel. Samples included both acceptable and rejectable particles for each stage in the coating process.

Under the guidance of the principal investigators, this NERI project was structured to meet the project goals through implementation of a PNNL project management plan.

While many laboratory and subcontractor personnel supported and contributed to the three years of intense effort, the core research team is shown in Figure 1.5.

Project Team

Significant contributions to the work were made by:

Ronald Hockey – ARA
Principal Investigator (PI)

Allan Pardini – PNNL
Project Manager/PI

Royce Mathews – PNNL
Electrical Measurements

Joe Gray – ISU CNDE
Radiography

John Saurwein – GA
Consultant

Jim Miller – ORNL Fuel
Fabrication

DOE

Madeline Feltus

Frank Goldner
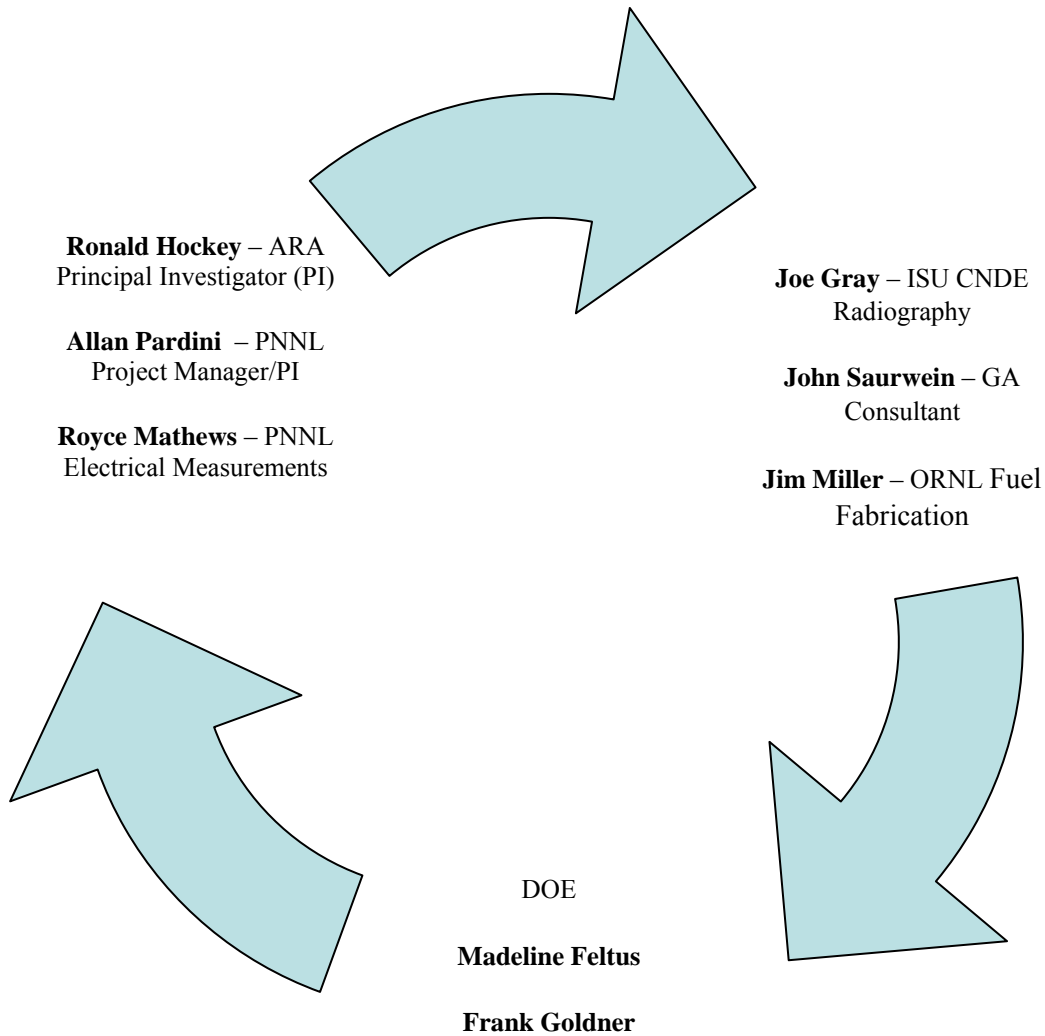
Figure 1.5. NERI Project Core Team

1.4 Project Statement of Work

This section describes the task objectives initiated during the first year of the project, FY2003, and is useful in providing an overall view of the project direction.

To achieve the stated objectives, the project was organized by specific tasks as follows (refer to the PNNL proposal to DOE – 2SF020103, NERI – 2002-103).

Task 1

The first task is to perform a literature review, identifying occurrences where similar materials, used in different applications, have been inspected using similar NDE methods.

Task 2

A limited modeling study will quantify the interaction between various defective TRISO materials and the ultrasonic testing (UT), electromagnetic (EM), and optical sensors identified for this project. For a given defect type, modeling is useful in determining the best technique to obtain optimal flaw signal response for each NDE method. The model results will guide the design of the initial NDE measurement systems.

Task 3

Define a "Quality Index". This task will determine how the measurement data can be used to support QC/QA decisions. The quality index may be derived from multiple measurements, each one of which is determined from several of the properties shown in Table 1.1 above. This is envisioned as a "distribution function" type display combining all the specifications shown in Table 1.1, in the aforementioned background section.

Task 4

Obtain enough reject TRISO surrogate particle fuel, from different processing formulas, to span the full range of defects discussed in the literature, including the most problematic type of defects associated with the SiC containment layer. Once characterized, these particles will form a basis for technology evaluation in the remaining tasks of the project, or until actual fuel particles are tested for equivalence. Initially, ORNL will supply small-quantity samples as available in their particle fabrication program. Eventually, late in the first year or early in the second year, ORNL will coat hafnium kernels to specifications set by GA. These will be used in evaluating several NDE methods for missing coatings, coating thickness variation, density, shape, size, and other microstructure variations found among defective particles.

Task 4a

An important subtask is the nondestructive characterization of the surrogate particles. This subtask will be performed at ISU using three-dimensional, high-resolution, computed tomography. Once characterized, each particle will be carefully handled, avoiding mixture among hundreds of other sub-millimeter-sized particles, and will remain in a standard test sample library for evaluating the various NDE methods.

Task 5

Defects will be induced into particles found to be "defect free". The particles will then be re-characterized. Cracks and 5-μm diameter pits will be the most common defects fabricated into coated layers.

Task 6

Design and develop stationary particle measurements for each NDE measurement method. Each NDE method (UT, EM, and optical) intended for in-line, off-line and on-process type inspection, will be developed for an initial evaluation using the available, characterized, surrogate particles. At this stage in the development process, the particles will be held stationary at the sensor head as each method is assessed for its potential flaw detection capability. The foremost criterion or basis for comparison is flaw detection. The culmination of this task will be several data sets consisting of the NDE measurements on the same set of surrogate fuel particles.

Task 7

Narrow the list of NDE methods and further develop those that show the greatest potential for meeting project objectives. The findings from Task 6 determine which of the initial NDE methods warrant further development and may meet project objectives.

Task 8

Design and develop a system to simulate the particle coating process (inside a coater) and determine the most effective on-process technique for potentially monitoring particle status during the coating process. Ultrasonic scattering techniques are typically used in similar applications.

Task 9

Test flawed particles in the standard particle library using the further refined NDE methods and establish standard signatures characteristic of each flaw type. This information will be used in Task 14 below to develop a Quality Index (QI).

Task 10

In this task, the coated uranium oxide (UO_2) particles specified by GA will be evaluated in the same way as the surrogates of Task 9 to establish signature variations associated with different kernel types. Radiation dose should not be an issue in handling these samples, but the samples will be handled with special care, in a confined work area, to avoid particle loss or coating damage.

Task 11

Design and develop a capillary particle flow tube system to deliver constant particle flow to in-line sensors. The EM-based NDE methods are expected to be the most suitable methods for in-line measurements because of their high-throughput capacity. If, however, other methods show similar promise, they will be considered in this task as well. The particle delivery system will have a wide controllable speed range to satisfy the requirements of Task 15.

Task 12

Establish the relationship between flaw type and in-line measurement signature for particles moving relative to the sensor. This test will determine how the stationary particle signatures of Task 9 change when the same particle moves past the sensor at a given velocity.

Task 13

Determine which particle defects and NDE methods are best suited for off-line testing, where random sampling is a sufficient QA/QC practice. Guidance will come from the modeling study of Task 2.

Task 14

Implement the "Quality Index" defined in Task 3 for all NDE measurements.

Task 15

Determine the particle velocity threshold for in-line NDE methods; i.e., the velocity where flaw detection becomes unreliable.

Task 16

Final laboratory-scale demonstration of each NDE method found to meet the project objectives.

Task 17

Specify NDE design parameters to build pilot-scale systems for effective measurement techniques. This information will be delivered to GA for eventual installation and testing on a fuel manufacturing line.

Task 18

Provide project management. This task will provide for interaction with the DOE NERI Program office, program direction, internal review and coordination with subcontractors, and attendance at programmatic and selected scientific meetings. It will also provide for preparation and delivery of the necessary quarterly and annual reports.

2.0 FY2003 – Project Year 1

October 2002 to September 2003

2.1 FY2003 Summary

This portion of the final report summarizes the activities performed and progress made in FY2003. Various approaches for automating the particle fuel production QC process using on-line nondestructive methods for higher reliability were evaluated. In this first year of a three-year project, surrogate fuel particles, including leftovers from initial coater development runs, were made available for testing. These particles had a high defect fraction and the particle properties spanned a wide range, thereby providing the opportunity to examine worst-case conditions before refining the inspection methods to detect more subtle coating features. Particles specifically designed to evaluate the NDE methods being investigated under this project were specified by GA and PNNL, then fabricated at ORNL. The literature was reviewed for existing inspection technology and identified many of the fuel particle conditions thought to degrade performance. A modeling study, with reasonable assumptions made for material conductivities, showed that the in-line EM methods should provide measurable responses to missing layers, kernel diameter variations, and changes in coating layer thickness. The modeling study for the ultrasonic methods provided the resonant frequencies that should be measurable using the resonant ultrasound technique. The results from these calculations were published in the proceedings of two conferences.

The notion of a particle quality index to relate coating properties to fabrication process parameters was explored. Progress was made in understanding the fabrication process. GA identified key literature in this area and provided a literature review/summary. This literature has been reviewed. An approach previously applied to flexible manufacturing was adopted, and the modification and development of the concepts to meet TRISO particle fuel manufacturing and QA/QC needs was initiated. This approach establishes relationships between key process parameters and part parameters, including defects for each manufacturing step—which, in this case, corresponds to a coating layer. This activity will continue in year two, when an initial evaluation will be made using available process and particle data.

Radiographic (RT) and computed tomography (CT) techniques were developed and refined to examine individual particles and batches of 30-40 particles for kernel diameter, coating layer thickness, and spatial uniformity. These results are essential for developing the defect library of characterized particles that will be used to calibrate the high-speed nondestructive measurement methods that are found capable of automatically detecting particles having properties outside a specified range.

The evaluated in-line inspection methods include the electrical property measurement methods of inductive impedance and capacitive impedance, traditionally referred to as eddy current and capacitance (or dielectric) in the nondestructive test methods literature. An inductive impedance technique was developed and evaluated on stationary particles. Good correlation was found between the inductive measurements and the radiographically determined particle dimensions. Initial measurements on fuel compacts using the inductive impedance approach showed that these materials are amenable to electrical inspection and that significant coil impedance variability can be observed among different samples. A comprehensive evaluation of the capacitance measurement method was deferred until next year due to difficulties in obtaining appropriate sensors.

The resonant ultrasound technique was evaluated using metal spheres with diameters ranging from 1.6 mm to 25 mm. This initial evaluation showed that the measurement system, as configured, could not determine the resonant frequencies for spheres smaller than about 4 mm due to a large background and relatively small sample response. Two potential solutions were identified for overcoming this limitation. The first involved exciting particles with electromagnetic acoustic transducers (EMATs) to avoid contacting the particles. This approach proved to be unsuccessful because of the low energy transfer from the EMAT to the particles. The second approach was to fabricate custom contact transducers that are matched to the mass of the particles to reduce background transducer resonances. This approach was deferred to permit a manufacturer enough time to fabricate and test the custom transducers.

The initial evaluation for using the acoustic microscopy approach to characterize coated surrogate fuel particles has shown that only the extreme high end of the ultrasonic frequency spectrum (i.e., above 250 MHz, and perhaps as high as 1 GHz) was effective for imaging microstructural features in the TRISO fuel. The currently available ultrasonic system is not capable of operating at frequencies above 100 MHz. Therefore, it was recommended that the ultrasonic approach to fuel-particle characterization be refocused toward obtaining a quality signature based on a combination of particle properties rather than toward the imaging of flaws as originally proposed.

On-process measurement technologies were investigated. An initial review identified five technologies that could potentially be applied: 1) transmission ultrasound, 2) pressurized gas-coupled ultrasound, 3) electrical impedance and capacitance measurements, 4) ultrasonic backscatter, scattering and diffuse fields, and 5) process tomography (potentially using various sensing fields). These techniques were evaluated and several were found to have potential merit. Transmission ultrasound was selected for initial development during FY2004 to provide a test bed for this and other ultrasound modalities that could be used to sense in-coater "median" particle diameter as a function of processing time.

Results from this project year appear in four publications.

2.2 FY2003 Research Progress

Task 1. LITERATURE REVIEW

A general literature review, performed as part of the proposal process for this project, revealed over 30 years of work on coated-particle fuels. That initial review covered the relevant topics of advanced gas reactor programs and, in particular, programs reporting the fabrication and testing of TRISO particles, both nationally and internationally. The time frame covered in the initial review was from about 1970 through 2001, and included about 150 papers.

As more recent work became available throughout the project year, periodic updates were made for 2002 and the first half of 2003. Over the summer months, an undergraduate student helped build a searchable electronic database for this literature, making it easier to retrieve specific papers and add new work as it became available. The database currently contains about 200 papers. Accumulating new papers over the remainder of this project will be a relatively small task, using the existing database.

A review article highlighting developments in the characterization and performance evaluation of TRISO fuel particles over the last four decades is being prepared and is expected to be submitted for publication in a journal sometime in 2004.

Task 2. MODELING STUDY

The objective of the modeling activities is to facilitate:

- Development of measurement methods consistent with theory

- Interpretation of measured data

- Prediction of measurement results for a broader range of defect conditions than can be examined experimentally in the time frame of this project.

In the first year, both acoustic and electromagnetic models were developed.

Resonance Computation Modeling

Resonant ultrasound spectroscopy (RUS) is a relatively new technique (A. Migliori and J. L. Sarrao) in which one measures the resonant frequencies of a sample of nearly ideal geometry and with known symmetry, dimensions, and mass. The resonance peaks are amplifications of waves by constructive interference within a solid at specific frequencies. A brief description of the technique is given here, however, more detailed information is available elsewhere (A. Migliori (1997), J. Maynard (1996), J. D. Maynard, (1992), R. B. Schwarz (2000), A. Migliori (1996)). In RUS, a parallelepiped, cylinder, or sphere of the material of interest is suspended between two transducers across opposite edges (in case of the parallelepiped or cylinder). As one transducer excites the specimen by sweeping through a specified range of increasing vibrational frequencies, the opposite transducer monitors the response of the solid to the input signal and converts it to an electrical signal which is fed into a computer for analysis.

In RUS NDE techniques, defects in objects are detected on the basis of changes in the pattern of resonance frequencies relative to the spectrum of the defect-free object. The approach taken in this task was to computationally investigate implementing the XYZ algorithm of (Visscher et al. (1991)) and the suitability of RUS as an NDE tool to detect shape defects and layer imperfections in sub-millimeter sized TRISO particles being considered as fuel for the Generation IV nuclear power plants. The representative material properties of the zirconium oxide (ZrO_2) kernel and the layers of TRISO particles used for this computational study are listed in Table 2.1.

Table 2.1. Representative Material Properties of TRISO Particles

	Density ρ(gm/cc)	Lame constant λ (GPa)	Lame constant μ(GPa)	Thickness/Diameter (μm)
ZrO_2 kernel	5.7	128.19	76.35	500 (diameter)
Porous carbon buffer layer	0.97	2	3.34	65
IPyC layer	1.875	5.5	10.5	35
SiC layer	3.19	77	199	35
OPyC Layer	1.825	5.5	10.5	40

Figure 2.1 illustrates the close agreement between computed results and experimental results for a 3.145-mm aluminum sphere (A. Migliori 1996).
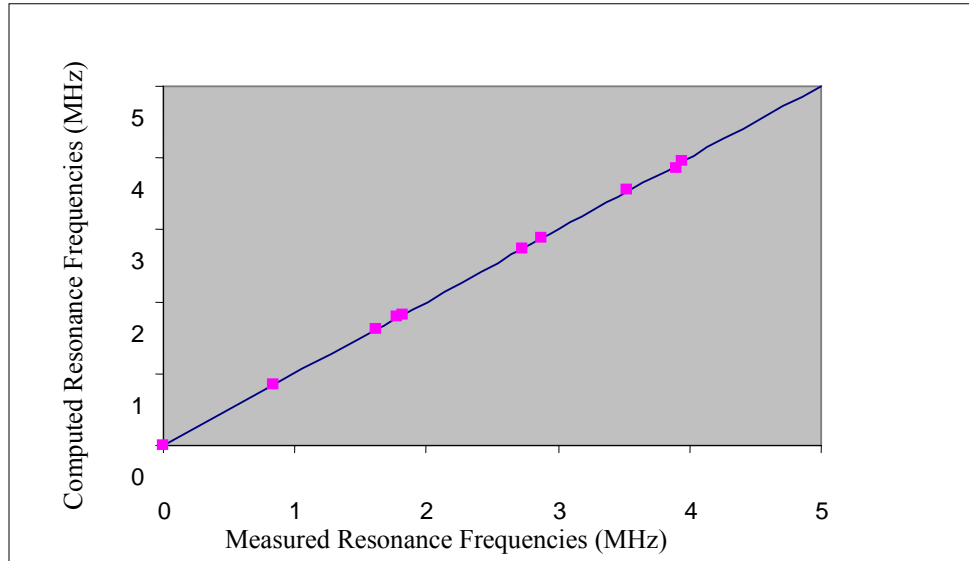
Figure 2.1. Comparison of Measured Resonance Frequencies with Computed Resonance Frequencies for a 3.145-mm Aluminum Sphere

Calculations for different spheroids with the same volume were made to study the effect of shape on the resonance frequencies. The results are shown in Figure 2.2. The x axis represents the aspect ratio between the semi-axes of a general ellipsoid. Notice the massive degeneracy of resonances in the case of perfect spheres (aspect ratio of 1). The reduction in the extent of degeneracy can be utilized as a signature of shape defect.
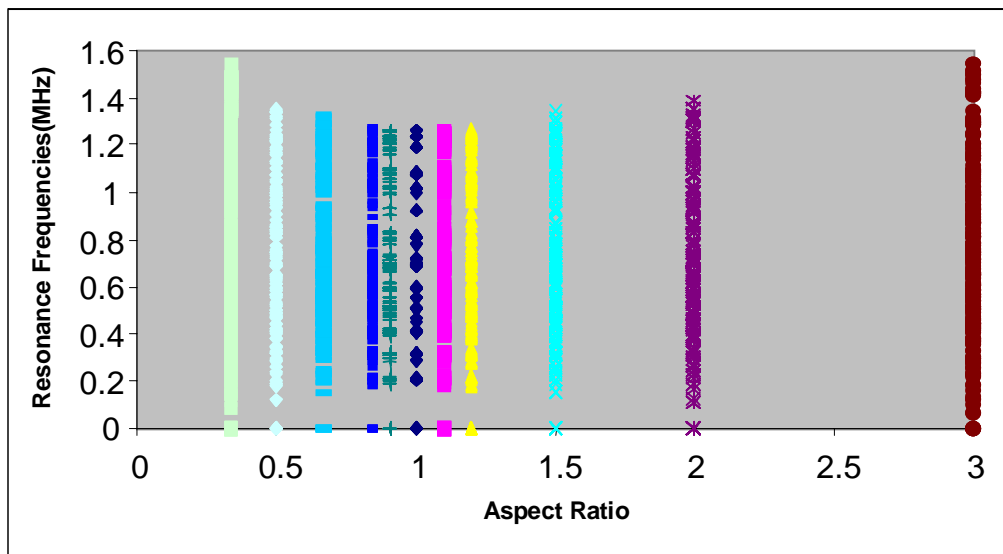
Figure 2.2. Resonance Frequencies for a Family of Spheroids

Figure 2.3 shows the variations of the first 28 free-body resonance frequencies of surrogate TRISO particles caused by a 10-µm decrease in thickness of the porous carbon buffer layer (an overall diameter

reduction of 20 μm). Noticeable differences in the computed frequencies can be seen when compared with those of a "flawless" TRISO particle. It was observed that this type of defect resulted in increased frequencies, relative to the frequencies of the simulated TRISO particle adhering strictly to specifications. Figure 2.4 shows the computed frequencies for the case when the reduction of the buffer layer thickness is offset by increases in the IPyC and the OPyC layers, keeping the diameter of the TRISO particle unaltered. Interestingly, one notices that the resonant frequencies of most of the displayed modes are lowered.
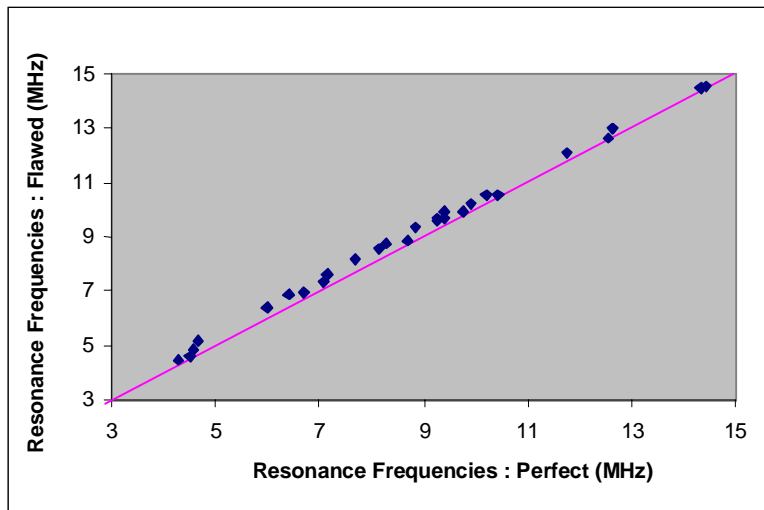
Figure 2.3. Relative Variation of Computed Resonance Frequencies Caused by a 10-μm Decrease in Buffer Layer Thickness
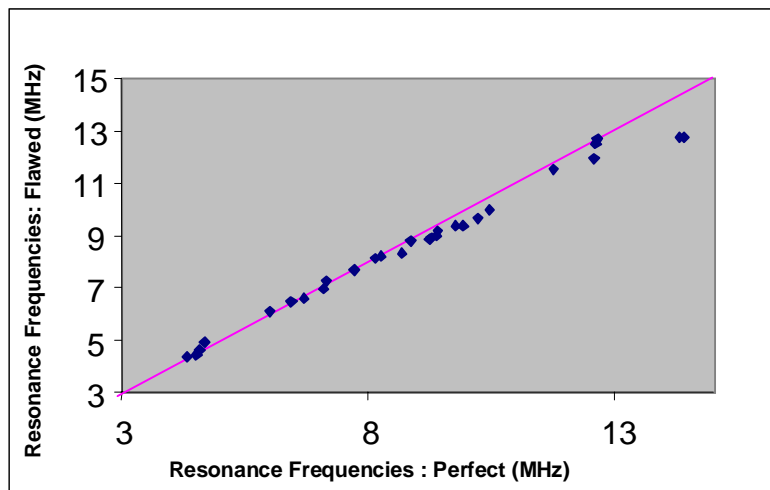
Figure 2.4. Relative Variation of Computed Resonance Frequencies Caused by a 10-μm Decrease in Buffer Layer Thickness Along With a 5-μm Increase in Thickness of Each of the IPyC and OPyC Layers

The results presented here do not distinguish between the different modes of vibrations. It is the surface motions of the elastic object that determine those modes. Although the surface displacement patterns for each vibrational mode have been calculated, the effects of layer defects on vibrational modes have not been studied. The computations indicate that shape defects of spheres have a strong impact on the

resonance frequencies; thus, RUS should provide a viable means of detecting shape defects in TRISO particles. It has also been seen that variations in layer thickness of TRISO particles result in noticeable changes to the normal-mode frequencies. However, further investigations are needed to correlate layer defects with optimally diagnostic normal-mode frequencies.

Acoustic Microscopy Modeling

Since the TRISO particle layers are relatively thin, it would be very difficult to discriminate echoes from different interfaces using ultrasonic pulses when center frequencies are in the 50- to 200-MHz range. However, if the incident wave train is long compared to twice the thickness of the thickest layer, the various transmitted and reflected wave fronts combine in a complex way. This fact has been exploited to compute the reflection coefficient of the layered structure as a function of frequency. The numerical results plotted in Figure 2.5 show that the reflection coefficient is sensitive to layer thickness. Note that when a layer thickness was decreased, another layer thickness was increased by the same amount, leaving the particle diameter unchanged.
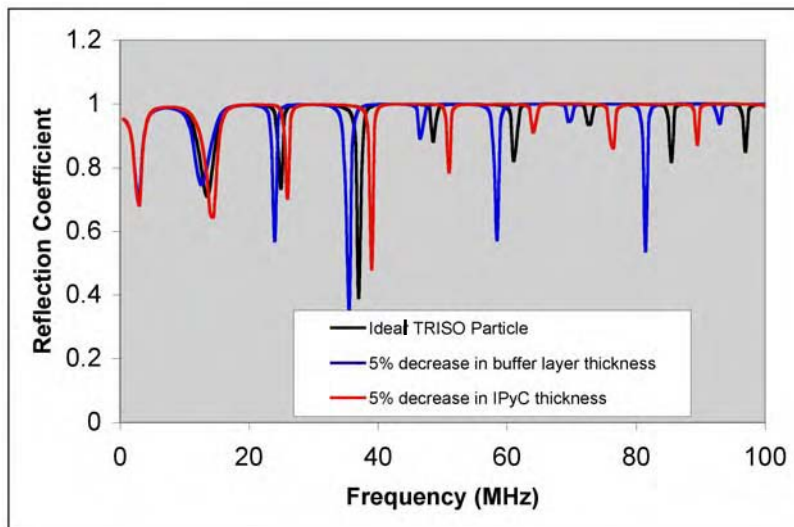
Figure 2.5. Layer Thickness Variation Effect on Frequency-Dependent Reflection Coefficient

Electromagnetic Modeling

Two models were developed to demonstrate how the electromagnetic properties of the TRISO fuel particle respond to an applied electromagnetic field. The first model was used to calculate the complex valued coil impedance for a changing magnetic field applied to a particle of given layer thickness and layer electrical conductivities. The second model focuses on calculating the capacitance change resulting from the addition of each particle coating layer, of a given dielectric constant.

Inductive Impedance Method

The objective of this task was to use a numerical model to predict the inductive impedance response to particle defects (deviations from the specified particle) and to help define the optimal design and operational parameters of appropriate sensors. These results will become most valuable when the experimental measurements are available to verify and calibrate the models.

The software package Electro® by Integrated Engineering Software was purchased to numerically model a capacitive sensor containing a TRISO particle. This software provides a means of numerically solving problems involving two-dimensional or rotationally symmetric geometry. Several different calculations were made to assist in the design of a rotationally symmetric capacitive sensor. However, it was necessary to make several assumptions for the dielectric properties of the various particle layers, since measurement values are not available.

The inductive response of a coil containing a TRISO particle was modeled using the OERSTED® software package, also from Integrated Engineering Software. Values of coil impedance were calculated for rotationally symmetrical particles in which only the outer pyrolytic carbon (OPyC) layer thickness was allowed to vary. Calculated coil impedance variations resulting from this OPyC variation are well above the noise level found in recent measurements and the results are shown below in Figure 2.6.
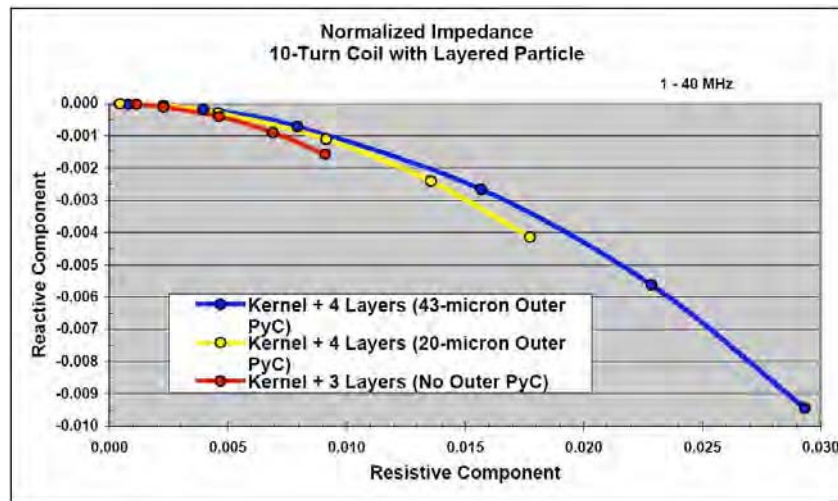
Figure 2.6. Calculated Coil Impedance for TRISO Coated Particles of Various OPyC Layer Thicknesses

The greatest difficulty to be overcome in obtaining relevant information from the model was the large number of unknown electrical properties for each layer, most notably electrical conductivity. Two approaches are planned to overcome this limitation. The first is to investigate particles having a single layer coating of buffer, PyC or SiC over the kernel. The second approach is to use reasonable approximations for the unknown parameters, then use several different characterized particle measurements to adjust the model to fit the measurements.

Capacitance Method

In the capacitance method, a potential difference is applied between two parallel metal plates to establish an electric field. By measuring the voltage across the plates and the current flow, it is possible to determine the change in capacitance and the dielectric constant due to the material, such as a TRISO particle, inserted between the plates.

Using the model shown to the left in Figure 2.7, the change in the capacitance caused by each coating layer was computed, as shown on the right side of Figure 2.7. Notice that the SiC layer produces one of the larger changes because its higher dielectric constant. Therefore, this type of sensor may be well suited for inspecting particles just after application of the SiC coating to determine the SiC layer quality.
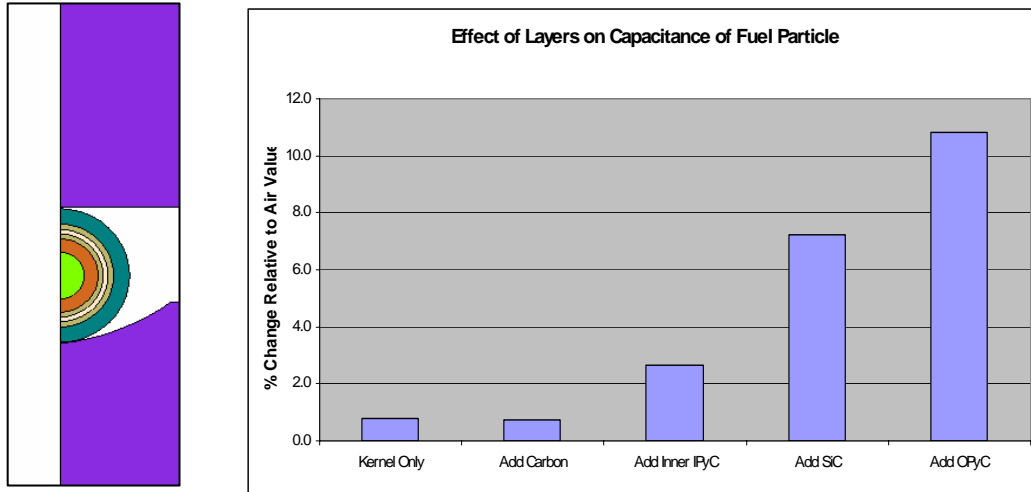
Figure 2.7. Model of a TRISO Particle Inside a Dimpled-Plate Capacitor (left), and the Calculated Capacitance Change Resulting From the Addition of Each Coating Layer (right)

References

A. Migliori and J. L. Sarrao, "Resonant Ultrasound Spectroscopy: Applications to Physics, Materials Measurements, and Nondestructive Evaluation," (1997), John Wiley and Sons, New York.

Maynard, J. 1996. Physics Today, 49, p. 26.

Maynard, JD. 1992. J. Accoust. Soc. Am., 91(3):1754-1762.

Schwarz, RB and JF Vuorinen. 2000. J. Alloys and Compounds, 310, pp. 243-250.

Migliori, A and TW Darling. 1996. Ultrasonics, 34, pp. 473-476.

Visscher, WM, AM Migliori, TM Bell, and RA Reinert. 1991. "On the normal modes of free vibration of inhomogeneous and anisotropic elastic objects", J. Acoust. Soc. Am. 90(4), pp. 2154-2162.

Task 3. DEFINE QUALITY INDEX

The quality of TRISO particles and the methods used to evaluate particles present particular challenges. Current methods (based on sampling) are time-consuming and involve destructive examination of the samples. Better methods, offering fast in-line inspections of large numbers of particles, are needed. For each advanced reactor, up to 15 billion TRISO particles may be required at any one time to give a reactor core fuel load. Refueling cycles can be as often as 18 months. It has been reported that U.S. and German particles exhibit significant performance differences (Petti et al. 2003).

The objective of this task is to develop a "Quality Index" that is based on non-destructive measurements. It is intended that it will be applicable to both individual particles and batches and have batch qualification/acceptance testing capability. The developing methodology seeks to relate properties to fabrication process parameters. Key fuel parameters are summarized in Table 2.2.

Table 2.2. Summary of GT-MHR Fuel Property Specifications Important to Performance

Property	Property Type	Mean Value	Critical Region	Defect Fraction
Kernels				
C/U atomic ratio	Variable	0.50 ± 0.20	$\leq 0.01 \leq 0.20$ $\leq 0.01 \geq 0.80$	NA
O/U atomic ratio	Variable	1.50 ± 0.20	NA	NA
Kernel diameter (μm)	Variable	350 ± 10	$\leq 0.01 \geq 400$	NA
Kernel density (Mg/m3)	Variable	≥ 10.5	NA	NA
Coated Particles				
Buffer thickness (μm)	Variable	100 ± 10	$\leq 0.01 < 50$	NA
Missing buffer (≤15 μm)	Discrete	NA	NA	1.0 x 10-5
IPyC thickness (μm)	Variable	35 ± 5	$\leq 0.01 < 20$ $\leq 0.01 > 50$	NA
IPyC density (Mg/m3)	Variable	$1.80 – 1.95$	$\leq 0.02 < 1.80$	NA
IPyC anisotropy (BAFo)	Variable	1.040	$\leq 0.01 > 1.060$	NA
SiC thickness (μm)	Variable	35 ± 5	$\leq 0.01 < 25$	NA
SiC density (Mg/m3)	Variable	≥ 3.18	$\leq 0.01 < 3.17$	NA
SiC integrity – gold spots or visible flaws	Discrete	NA	NA	1.0 x 10-3
OPyC thickness (μm)	Variable	40 ± 10	$\leq 0.01 < 21$	NA
OPyC density (Mg/m3)	Variable	$1.75 – 1.90$	NA	
OPyC anisotropy	Variable	1.040	$\leq 0.01 > 1.060$	NA
Missing OPyC (≤20 μm)	Discrete	NA	NA	1.0 x 10-4
OPyC integrity	Discrete	NA	NA	1.0 x 10-2
Compacts				
U contamination (grams exposed U/gram U)	Variable	NA	NA	1.0 x 10-5
SiC defect fraction	Discrete	NA	NA	5.0 x 10-5
IPyC integrity (fuel dispersion)	Discrete	NA	NA	4.0 x 10-5
OPyC integrity	Discrete	NA	NA	0.01
Iron content outside SiC (μg)	Variable	50	$\leq 0.01 < 100$	0.01
Cr, Mn, Co + Ni content (ppm)	Variable	NA	$\leq 0.01 < 240$	0.01

Process Characterization

Significant progress has been made in understanding the fabrication process. GA identified key literature in this area and Saurwein (2003a) provided a literature review/summary of much of the historic and recent literature. Significant papers include those by Petti et al. (2003) and a special issue of a journal (Nuclear Technology, September 1977). Recent work, e.g., Sawa and Tobita (2003) considering the behavior of SiC-coated fuel particles in terms of performance, confirmed the significance of the buffer layer and identified other key parameters. Additional input from GA includes "Technical Guidance for Development of Advanced QC Methods Gas-Cooled Reactor Fuel Particles" (Saurwein 2003b) and a "TRISO-Coating Process Summary" (Saurwein 2003c). Additional information is contained in Table 2.6 of the appendix.

Proper fluidization of the particle bed is essential for the production of high-quality coatings. Key process parameters are identified as:

- Total gas flow
- Batch size – mass or volume of particles

- Diameter of the coater (furnace)
- Bed surface area
- Design of gas distributor
- Gas concentrations
- Gas fluidization velocity
- Coating temperature
- Coating rate

For each coating layer, the greatest influence on microstructural properties of the coating has been shown to be variations in temperature and coating gas fractions. Values for the various process parameters are summarized in Table 2.3.

Table 2.3. TRISO Coating Gases, Coating Rates, Active Coating Gas Fractions, and Temperatures

Coating	Diluent and Levitation Gas	Active Coating Gas	Mean Coating Rate (μm/min)(a)	Active Coating Gas Fraction(b) C/(C+L+D)	Nominal Coating Temperature(c)
Buffer	Ar, or Ar and He	C2H2	(d)	(d)	1250
IPyC	Ar	C2H2 and C3H6	≥ 3.0	0.25 – 0.35	1300
SiC	H2	CH3SiCl3	≤ 0.33	0.012 – 0.021	1500
OPyC	Ar	C2H2 and C3H6	≥ 3.0	0.25 – 0.35	1300

Notes:
  a) Mean coating thickness divided by coating deposition time.
  b) C = active coating gas flow rate to coating zone ($C_2H_2 + C_3H_6$ for PyC coatings only), (CH_3SiCl_3 for SiC coatings only). L = levitation gas flow rate to coating zone (Ar for PyC coatings only), (H_2 for SiC coating only). D = diluent gas flow to coating zone (Ar for PyC coatings only), H_2 for SiC coating only).
  c) Normal temperature in the active coating zone of particle bed.
  d) Not defined.

A significant measure of coater performance and effectiveness is the "coating rate." However, the true coating rate is a non-linear parameter with time. In current practice, what is monitored and calculated is the "effective" coating rate, which is defined as the mean coating thickness divided by coating time. This is based on sample physical analysis—post run. Methods for monitoring true median particle diameter during the process were found to be of potentially significant value and could give improved coater control.

Quality Index

A standard distribution (shown in Figure 2.8) can be applied to a single characteristic such as a layer thickness or a particle diameter; thus, a simple metric for quality can be defined for that characteristic. For the TRISO particles, as shown in Table 2.2, many parameters affect quality and must be considered in the definition of an "acceptable" particle.
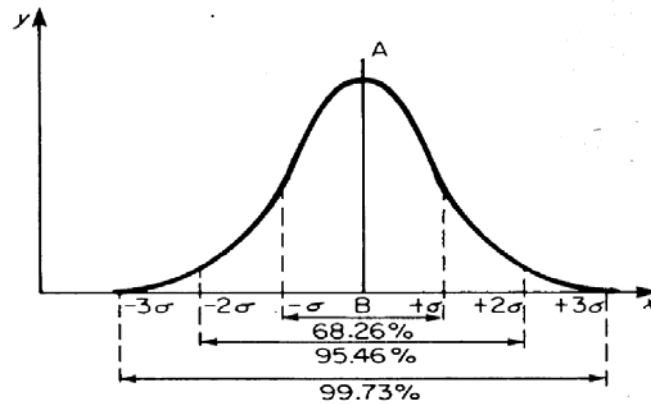
Figure 2.8. Standard Distribution

The primary challenge in developing a metric to define "quality" for the TRISO particle is that there are multiple characteristics, each of which has acceptance bands. For a quantitative relationship to be established, correlations between the key process parameters (summarized in Table 2.2) and resulting particle parameters shown in Tables 2.2, and 2.3 must be established.

An approach was proposed for a quality index relating "process" to "part" parameters. It is developed from a methodology proposed and demonstrated for a flexible manufacturing plant by Seifoddini and Djassemi (2001). For this application, parameters were related to the performance of each specific machine and the quality index was proposed as a part screening mechanism.

A graphical representation for established relationships between "key process parameters" and "part parameters" for each "manufacturing step" is shown in schematic form as Figure 2.9. The data given in Tables 2.2 and 2.3 are then used to define the rows and ranges for acceptable "boxes" for process parameters and these are correlated with directly resulting columns for particle properties, such as a layer thickness resulting from a mean coating rate, gas mixture, temperature and a duration. Each step in the process, layer, is described in terms of a "box". At the minimum for a particular coater run 1:0 are used to define "accept" – "reject" conditions measured for a particle or particles. More probably, each part-process step and desired condition is quantified in terms of deviation from nominal. For example, a thickness may be nominally 200 μm —with acceptable from 190 to 210 μm. A particle with a 200-μm layer would score "10" – for each micron off reduce the score by "1". For a key variable – layer present or missing are scored using a 10:0 scale – and this becomes a multiplier when the quality of the particle is measured.
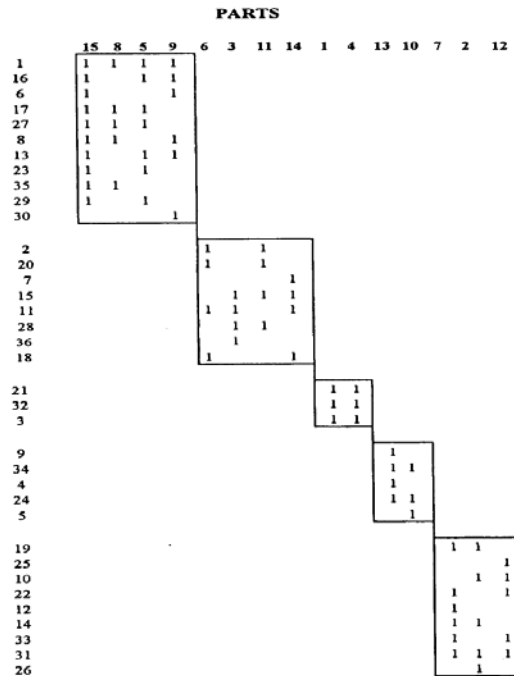
Figure 2.9. Schematic Showing Groupings Between "Process Steps/Machines"—Vertical Axis and "Parts"—horizontal axis. Each Rectangle Represents a Process Step—1 and 0 Represent Part Acceptable and Uaccepatable, Respectively

Table 2.2 and 2.3 specify acceptable ranges for coating processes and TRISO particle layer characteristics. A series of "rectangles" are being developed that bring together these processes and particle parameters.

Each step in the process is used to develop a multi-dimensional "box" for relationships between acceptable process parameters, and acceptable part parameters. The challenge now remains to establish, and demonstrate the relationships between measured parameters, as determined using the NDE tools being developed under other tasks.

In addition, process parameters can potentially be directly measured using on-process measurements that are discussed under Task 8.

The work by GA has identified that, from a performance perspective, the most important defects to detect and characterize are:

- Missing buffer coating

- Heavy metal contamination

- Defective SiC

- Spatial defects penetrating the SiC layer

- Grain size and structure

- Free silicon or free carbon

- Structural flaws, such as inclusions resulting in "gold spots"

- Impurities

- IPyC density

- IPyC thickness

- IPyC anisotropy

- OPyC anisotropy

This defect population will also be used to develop and refine the quality index matrix, similar to Figure 2.9.

Additional defects that are being investigated include the lack of a common centroid for kernel and layers, and other manufacturing defects identified and included in the sample library.

Each "box" of the type shown in Figure 2.9 is then established to define acceptable and rejectable ranges. The "part parameters" are then correlated with proposed metrics obtained from non-invasive measurements (e.g., electrical parameter measures, optical measurements and calibrated against particles characterized using micro-focus radiography and applied to individual particles).

The activity under this task for FY2004 is to obtain integrated experimental data, complete the definition of the "parameter boxes," and perform an initial evaluation of the concept using individual particles, manufactured using known process parameters and characterized using micro-focus radiography.

References

Petti, DA, J Buongiorno, JT Maki, RR Hobbins, and GK Miller. 2003. Key differences in the fabrication, irradiation and high temperature accident testing of U.S. and German TRISO-coated particle fuel, and their implications on fuel performance. Nuclear Engineering and Design, Vol. 222 pp. 281-297.

Saurwein, JJ. 2003a. Reference list: Relationships between coating process parameters and coating properties. May, 2003.

Sawa, K. and T Tobita. 2003. Investigation of irradiation behavior or SiC-coated fuel particle at extended burnup. Nuclear Technology 142 (3):250-259.

Saurwein, JJ. 2003b. Technical guidance for development of advanced QC methods for gas-cooled reactor fuel particles. GA report to PNNL, April 2003.

Saurwein, JJ 2003c. TRISO-coating process summary. September, 2003, Report GA/PNNL-461-03.

Seifoddini, H and M. Djassemi. 2001. The effect of reliability considerations on the application of quality index. Computers & Industrial Engineering, 40 pp. 65-77.

Task 4. OBTAIN SURROGATE PARTICLES

ORNL shipped the surrogate fuel particles listed in Table 2.4 to PNNL in December, 2002. Also within this shipment (but not appearing in the table) was several samples of uncoated ZrO_2 and hafnium oxide (HfO_2) kernels.

Table 2.4. First batch of particles from several of the early coating runs produced at ORNL

Coating Run NT-	Kernel		Layers
	Material	Diameter (μm)	
1	ZrO_2	500	Buffer only
2	ZrO_2	500	Buffer + IPyC
3	ZrO_2	500	Buffer + IPyC
4	ZrO_2	500	Buffer + IPyC
5	ZrO_2	500	Buffer + IPyC
6	ZrO_2	500	Buffer + IPyC + SiC
7	ZrO_2	500	Buffer + IPyC + SiC
8	ZrO_2	300	Buffer + IPyC + SiC
9	ZrO_2	500	Buffer + IPyC + SiC + OPyC
10	ZrO_2	500	Buffer + IPyC
11	ZrO_2	500	Buffer only
12	ZrO_2	500	Buffer only
13	ZrO_2	500	Buffer only
14	ZrO_2	500	Buffer + IPyC
15	ZrO_2	500	Buffer + IPyC
16	ZrO_2	200	Buffer + IPyC + SiC + OPyC
17	ZrO_2	300	Buffer + IPyC + SiC + OPyC
18	ZrO_2	500	Buffer only
19	ZrO_2	500	Buffer only
20	ZrO_2	500	Buffer + IPyC + SiC + OPyC
21	ZrO_2	500	Buffer + IPyC + SiC + OPyC
22	ZrO_2	500	Buffer + IPyC + SiC
23	HfO_2	500	Buffer + IPyC + SiC + OPyC
24	ZrO_2	500	Buffer + IPyC + SiC + OPyC

The research teams at PNNL and ISU used the above surrogate fuel particles to investigate and develop the NDE methods in FY2003. These particles were uncharacterized and found to have a "high defect fraction" as they were produced during the early surrogate coating development phase at ORNL. This simplified the NDE measurement development task by making defective particles more abundant and by providing a wide variety of different defect types. On the other hand, it was difficult to find the ideal particle that could be used as a standard for measuring everything else.

ORNL provided additional surrogate fuel particles late in FY2003. As summarized in Table 2.5 (and defined in greater detail in the appendices), the shipment included 11 different coating runs, including particles with buffer only, buffer+IPyC, and buffer+IpyC+SiC coated on ZrO_2 and HfO_2 kernels. Specific dimensions (like coating thickness) and other properties of these particles were basically unknown, and they were categorized as "available leftovers" from other work. Optical measurements on a small sampling have shown diameter variations in excess of ±5%.

Table 2.5. Second batch of particles from later surrogate coating runs produced at ORNL

		Kernel			
Coating Run	**Cone ID (mm)**	**Material**	**Diameter (μm)**	**Charge In (g)**	**Layers**
NT-52	25	ZrO_2	500	10.008	Buffer + IPyC + SiC
NT-64	25	ZrO_2	500	10.009	Buffer + IPyC + SiC
NT-74	50	ZrO_2	500	54.5	Buffer + IPyC + SiC
NT-75	50	ZrO_2	500	54.5	Buffer + IPyC
AGR-08282003-1	50	ZrO_2	500	54.5	Buffer
AGR-08282003-2	50	ZrO_2	500	54.5	Buffer
AGR-08282003-3	50	ZrO_2	500	54.5	Buffer
AGR-08292003-1	50	ZrO_2	500	54.5	Buffer
AGR-09022003-1	50	ZrO_2	500	54.5	Buffer
AGR-09032003-1	50	ZrO_2	500	54.5	Buffer + IPyC
AGR-09042003-1	50	ZrO_2	500	54.5	Buffer + IPyC
HfO_2, Buffer only	50	HfO_2	500	92.7	Buffer
HfO_2, B + IPyC	50	HfO_2	500	92.7	Buffer + IPyC

A simplified approach to analyzing defects in surrogate TRISO particles is also underway. In this approach, instead of working with the fully coated TRISO, only the kernel with a single layer is investigated. This reduces the number of parameters being investigated simultaneously, for each measurement technique, at any one time. Particles are being designed (beginning next quarter) to have only a single coating layer of either porous carbon buffer, SiC, or PyC. This will focus the measurements on only the simultaneous parameters for a single-layer coating, including thickness and density. Investigating the full TRISO is necessary, but also allows competing effects to confuse or obscure one another. Once the NDE measurement sensitivity to the properties of a single layer is understood, the combined effects from each layer in the full TRISO will become easier to deconvolve.

Task 4a. PARTICLE CHARACTERIZATION

Initially, the plan for characterizing particle density distribution was to use three-dimensional computed tomography (CT) to sort each particle. After processing the large volumes of high-resolution CT data (~1 GB) for each particle and considering the 90 minutes it takes to mount, scan, and reconstruct an image for a single particle, it quickly became apparent that a faster and more efficient method was necessary to obtain the full spectrum of defect types necessary for a QA/QC project involving over one hundred different types of defects. Even though CT techniques can also provide detailed three-dimensional information for more than one particle, as shown below in Figure 2.10, this much information is not necessary in the initial screening phase, where many particles from several different coating runs must be examined for defects in their coating layers. The CT analysis is more suitable to gaining a comprehensive, multidimensional view of a particular particle once an estimate of the type and magnitude of its defects are established.
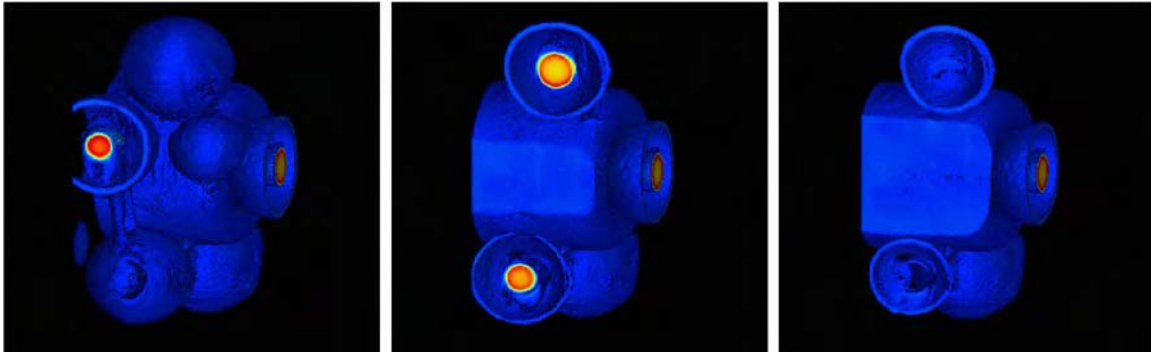
Figure 2.10. Three Different Slices Through a three-Dimensional Image of a CT Scan of Several Particles Attached to the Tip of a Glass Pipette

Digital radiography was found to be a faster and more efficient approach to rapidly assessing a batch of particles and selecting only those with the most representative features or defects thought to degrade particle fuel performance in a reactor. The radiographic presorting approach can scan 20-30 particles in only a few minutes and produce images similar to the photo of Figure 2.11 below. Also, by presorting with digital radiography at high geometric magnification, typically 30X, images with a 3.0-µm pixel size are possible using the system developed for this purpose at ISU's Center for NDE. As the radiograph of Figure 2.11 shows, many particles are stacked in a thin-wall tube, making it possible to track each particle's identity relative to the resulting digital radiograph.
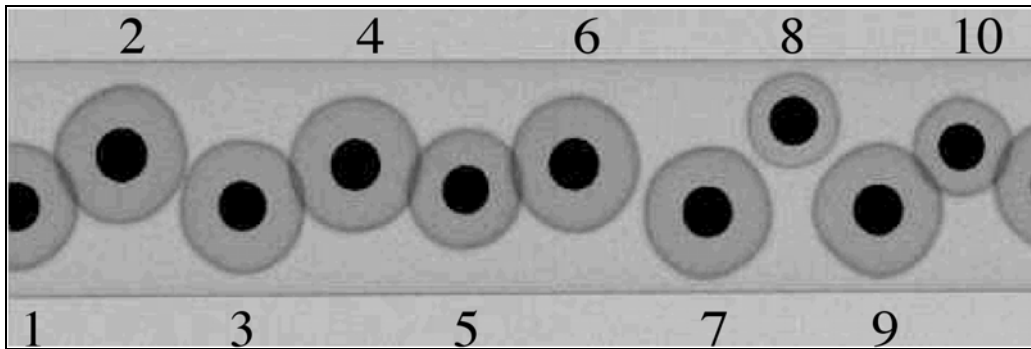
Figure 2.11. Digital Radiograph of Ten Particles in a Horizontal Glass Pipette (of 10-µm Wall Thickness) Illustrates the Use of Digital Radiography as an Initial Sorting Tool for Finding Anomalous Particles. Notice that Particles 5, 8, and 10 are Relatively Small and that Particle 9 has an Irregular Shape

Several particles with different coating layer defect types were found using the digital radiographic presorting approach, and now that the coating capability support at ORNL is becoming routine, faster characterization is becoming essential to keeping pace with the increase in production. The following figures contain specific examples of a few selected coating defect types discovered using the radiographic presorting approach.

The particle images in Figure 2.12 were flagged as anomalous by the radiographic sorting technique because of their dissimilar sizes. A digital image analysis of this figure shows that the OPyC layers of the two particles are about the same, whereas the particle to the left has a thinner buffer and thinner SiC coating. Furthermore, comparing this image with others reveals that the SiC coating on the particle to the right is thicker than normal.
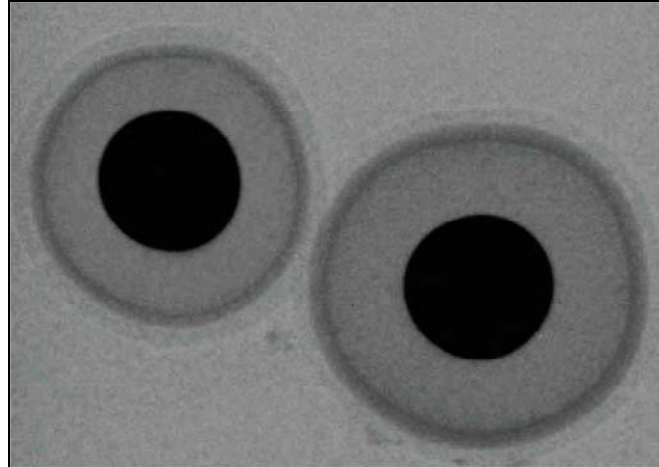
Figure 2.12. The Left Particle in this Image Shows a Thick OPyC, Thin Buffer and SiC, while the Particle to the Right Shows a Relatively Thick SiC

Another important observation from radiographic presorting was that measuring the average diameter is not always a valid approach to finding missing (or thin) layers. Figure 2.13 is an example of a defect where the overall diameters of two particles are normal, but their OPyC and SiC layers are thin or missing. Therefore, each layer must be taken into consideration, not just the outer diameter as is done in a sieving process.
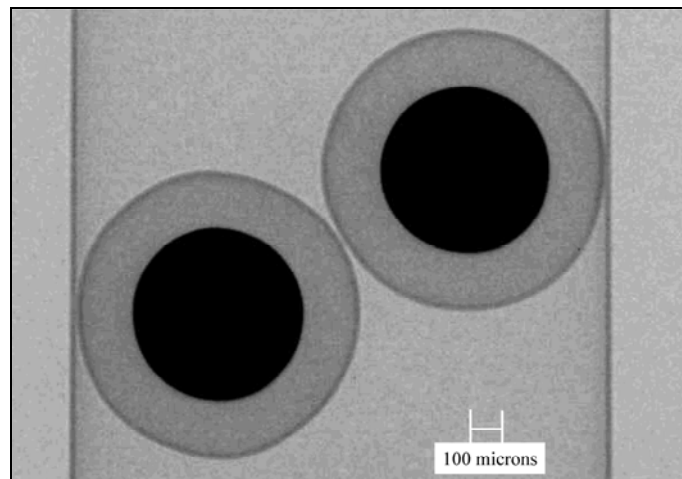
Figure 2.13. Both Particles are About the Correct Size, 900 μm. However, the Outer Carbon Layer is Missing and the SiC Layer is Thin. These Represent Defects that Would Go Undetected by a Sieving Operation

Another common feature observed by radiographic imaging was non-uniform coating thickness, which typically results in a nonspherical particle. In many cases, the buffer coating is applied non-uniformly to a small fraction of the particles, resulting in images similar to the one shown in Figure 2.14.
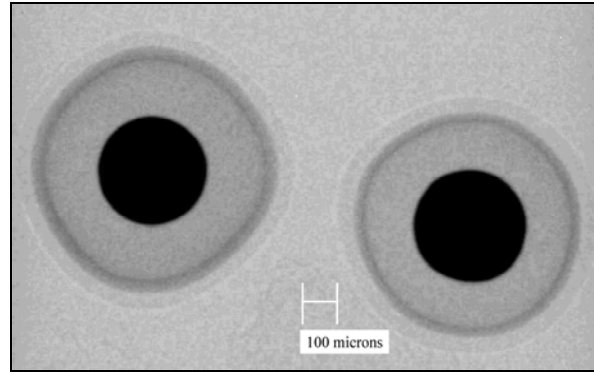
Figure 2.14. Irregular Shaped Particles. This Defect May Result in Unsafe Stress and Strain Relationships Among the TRISO Layers Under Reactor Conditions

This same micro-focus radiographic technique as described here will be continually used throughout the project in building the flaw library of Task 9.

Task 5. INTRODUCE DEFECTS IN SURROGATE PARTICLES

Although initially scheduled to begin in July, 2003, this task has been deferred until particles can be coated with flaws better representing those most likely to occur in fabricating TRISO fuel. Surrogate particles now being defined for coating will contain many of the defects found in particles known to fail under test reactor conditions. Examples include a thin or missing coating layer, and variations in the density and microstructure of the PyC layers.

This task will, however, be evoked as necessary further into the project to make particles available with defects that cannot be found (or fabricated) but are needed to develop a standard library of defects known to affect fuel performance. Appropriate defects may be produced, for example, by using compression to induce cracking in the SiC layer or by using a pulsed laser to "drill" micro-pores in the SiC layer.

Task 6. DESIGN, DEVELOP STATIONARY-PARTICLE NDE METHODS

The purpose of this task is to investigate four different NDE methods and to develop the most promising of those for demonstrating in-line QA/QC for each step in the TRISO fuel coating sequence. The four methods include:

- EM method
- UT resonance method
- Acoustic microscopy
- Optical method

Each of these methods uses a different physical principal to interrogate characteristic material properties within the TRISO particle.

The optical and EM methods use electromagnetic energy to interrogate particles and are capable of functioning at the high throughput speeds (approaching 200 particles/s) required for 100% inspection.

The optical method uses light reflected from the surface to provide diameter, shape and surface breaking features like cracks and pits. The EM method includes techniques using electromagnetic induction and capacitance to interrogate coating properties below the surface, including coating thickness and microstructural features associated with unique electrical conductivity signatures.

The ultrasonic methods (RUS and acoustic microscopy) were chosen to interrogate the microstructure of each coating layer. These methods operate at inspection speeds slower than the optical and EM methods and, therefore, could possibly be used in a batch sampling inspection mode (less than 100% inspection) to provide a statistical measure of total defect fraction.

The following is a progress summary for each of these NDE methods.

Electromagnetic

Progress in the first half of this reporting period focused on designing, developing, and characterizing the sensors thought to provide the greatest sensitivity to the various defect conditions known to occur in particle fuel. Essential to the performance of each design is the test procedure used in the evaluation. One of the foremost challenges in making each design functional was developing a procedure to insert and eject sub-millimeter-sized particles without disturbing the sensor, making it possible to accurately demonstrate measurement repeatability. Approximately ten different sensor designs (including both inductive and capacitive sensors) were evaluated and refined before arriving at a technique that provides the level of accuracy necessary to reliably detect some of the relevant differences among the available particles.

One of the earliest inductive sensor designs showed that this technique is clearly sensitive to particle diameter. However, at this early phase in the project the available particles were basically uncharacterized, with the outside diameter being the only known property. An example impedance plane plot, showing the inductive coil response, is shown in Figure 2.15. The particle labels in the legend of Figure 2.15 distinguish between large- and small-diameter particles by the beginning letter "L" or "S", respectively.

As the development of X-ray analysis techniques advanced, the inspection analysis time to determine particle density distribution diminished significantly, primarily in the second half of this reporting period. The radiographic results provided sufficient information to begin relating the inductive impedance measurements to internal particle properties.

Figure 2.16 shows how the dimensional results derived from radiography relate to the coil resistance measurements. Neglecting one or two outliers, a linear relationship can be seen between the induction coil resistance and either the particle size or the combined buffer/IPyC coating thickness.
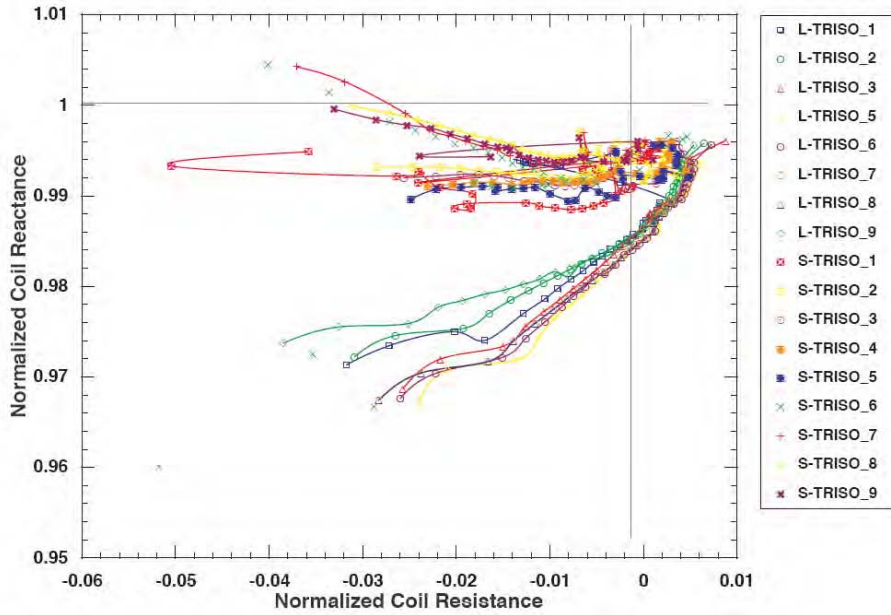
Figure 2.15. Normalized Coil Impedance of 18 Different TRISO Surrogate Fuel Particles, Separately Placed in the Center of the Test Coil
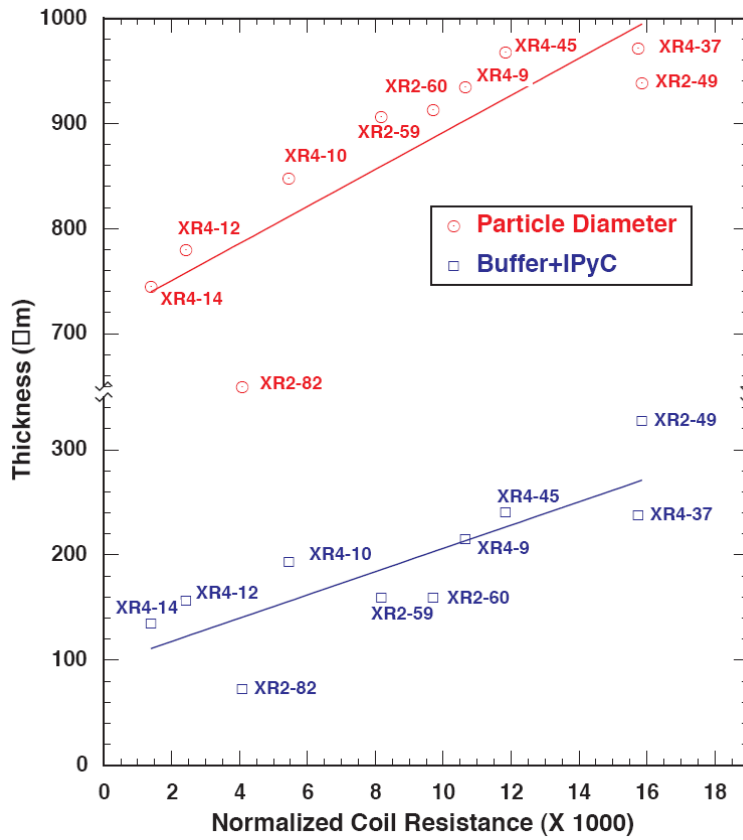
Figure 2.16. Normalized Coil Resistance Plotted Against Particle Diameter and the Combined Buffer Plus IPyC Layer in Fully Coated ZrO_2 Surrogate TRISO Particles

The next step is to calibrate the inductive impedance method and establish signatures for each flaw type expected to affect particle fuel performance. The effect that each individual layer, and combinations of various layer properties, may have on the coil impedance will be fully investigated in the first quarter of FY2004. This investigation will include missing (or thin) layers and layers of different densities. The first activity in conducting this investigation will be to specify the coating parameters for a matrix of coating runs required to produce the necessary particles. This activity is discussed further under Task 9, developing the standard flaw library.

The inductive impedance technique was also used to assess the electrical properties of fuel compacts–elements containing TRISO fuel particles inserted into a reactor in the form of fuel bundles. Fuel compacts are constructed from thousands of TRISO particles bound together in a carbonaceous matrix. Three different fuel compacts were available for this evaluation. The compacts came in three different lengths, two were several times longer than the sensor coil and one was approximately twice the coil length. Each fuel compact was placed inside a coiled wire having an inside diameter slightly greater than that of the compact, as shown in the photograph of Figure 2.17. The coil was excited over a broad range of frequencies as denoted in Figures 2.18 and 2.19.
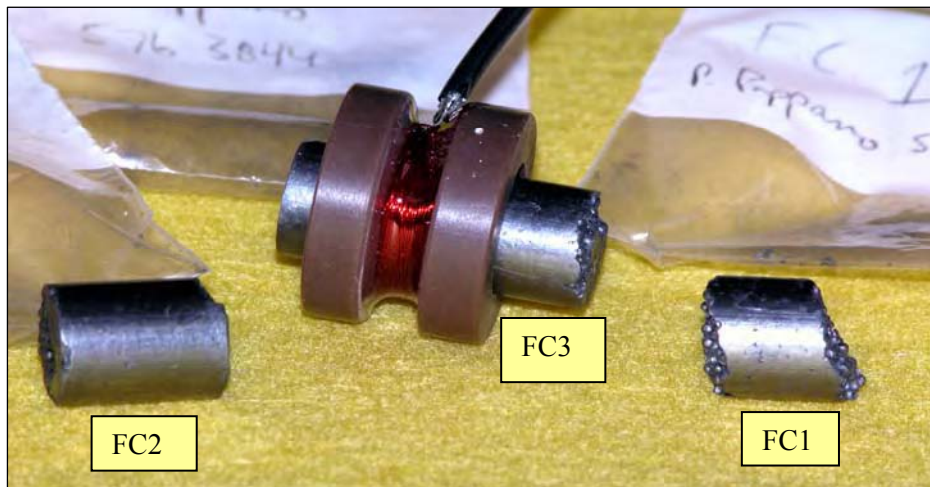
Figure 2.17. Fuel Compacts Assessed Using an Inductive Coil. Moving the Coil along the Length of a Full-Size Compact Allows the Coil to Interrogate the Electrical Properties as a Function of Position

The coil impedances (shown in Figures 2.18 and 2.19) for the three compacts are distinctly different. In the case of sample FC1, its relatively low coil impedance could be partially due to its short length (approximately 1 cm), which would allow end effects to influence the result more strongly than for the longer pieces. However, the lengths of samples FC2 and FC3 should not have affected the coil impedance measurement because they were both several times longer than the coil. The impedance of a coil surrounding a fuel compact is expected to depend on many different material properties of the compact. The most dominate properties include: compaction density, chemical composition of the matrix material, TRISO particle density (number of particles per unit volume), void-fraction, cracking, and depending upon the conductivity ratio between the matrix material and the TRISO particles, the average TRISO particle conductivity. Without additional testing, using radiography and perhaps destructive metallographic techniques, it will not be possible to determine the principal cause(s) of these observed differences.
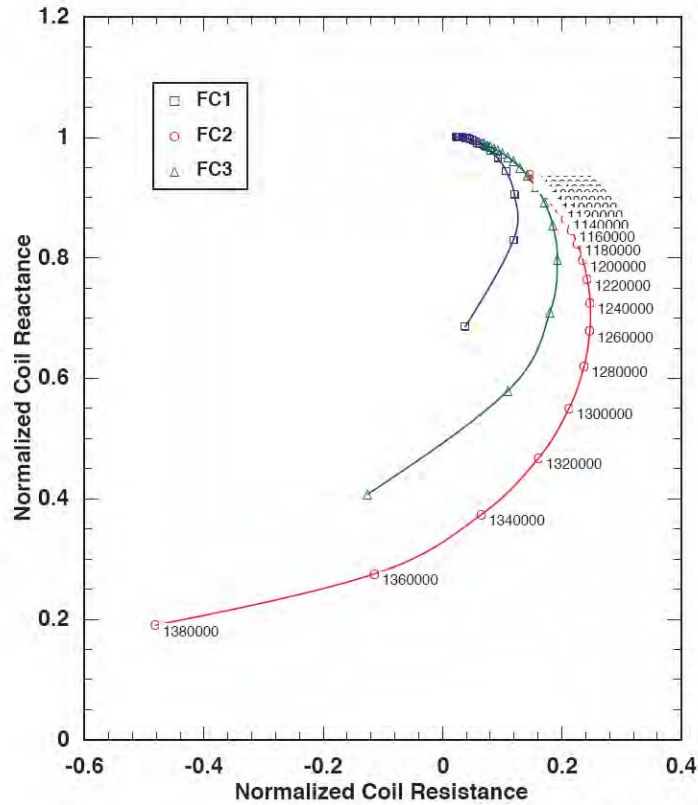
Figure 2.18. Coil Impedance Normalized to the Empty Coil as a Function of Frequency Ranging from 1 to 1.38MHz
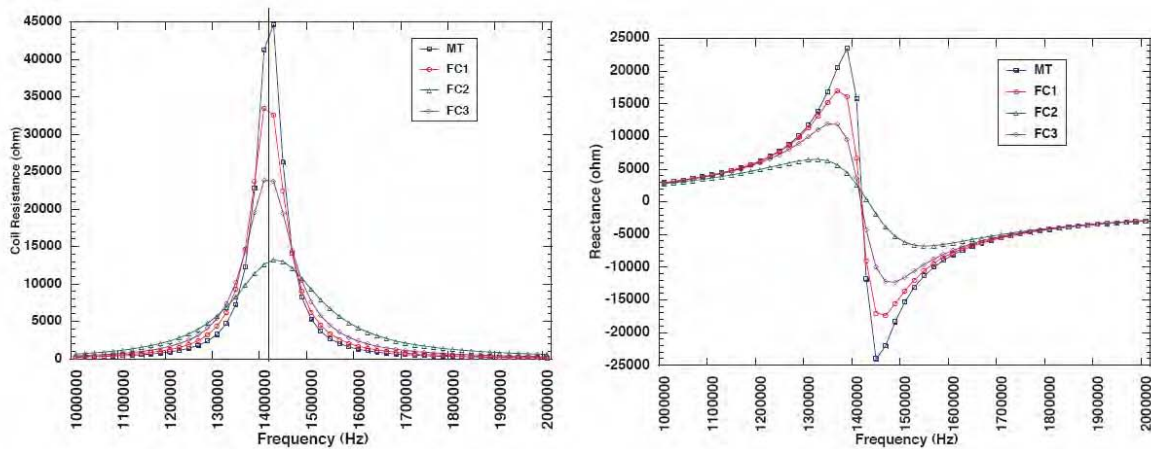
Figure 2.19. Coil Resistance (left) and Reactance (right) as a Function of Frequency for Three Different Surrogate Fuel Compacts

In addition to the inductive impedance techniques mentioned above, a capacitive measurement technique is also being evaluated to determine the extent to which it can provide the dielectric constant of a TRISO particle that is coupled through the electric field. The development of this technique progressed slower than that of the inductive impedance technique because of the experimental difficulties involved in measuring such a small impedance change associated with mm-sized particles, relative to a large

background signal associated with the test assembly. A new design, requiring the purchase of a custom sensor, is expected to circumvent this troublesome measurement problem and will be evaluated early in next reporting period.

UT Resonance

The goal of this subtask is to determine the feasibility of utilizing resonance measurements to determine the physical properties of TRISO particles. The characteristic resonances of rigid bodies contain information regarding the structural properties and shape of the bodies. As part of these properties, the structure and make up of layers affects the characteristic resonance frequencies. In addition, the elastic moduli contribute to the resonant frequencies of the body. In principal, all of these parameters can be determined. However, if several parameters change simultaneously or affect the resonant frequency in the same way, then determining the specific property that changed can be problematic. For QA/QC, the resonance technique may be ideal, due to its high sensitivity to several important properties of the TRISO particles such as thickness of layers and the composition of each layer. The results will be utilized to help determine the quality of TRISO particles during production.

This task has three activities:

- A literature review to assess current resonance theories for predicting the resonant frequencies of spherical particles.

- Calculations of the resonant frequencies of TRISO particles to predict the expected changes in frequency for various changes in the particle layers.

- Experimental measurement of the resonant ultrasound spectra of spherical particles to determine the limits of the current system and to provide guidance in developing alternate measurement methods if needed.

Activities 1 and 2:

The literature review was completed under Task 1 and the modeling work is described as part of the modeling study of Task 2.

Activity 3, Experimental Measurements:

In FY2003, studies were performed to determine the sensitivity and frequency limits of the current ultrasonic resonance system at PNNL using the standard configuration. Steel ball bearings were used with diameters of 1/16 in., 1/8 in., 1/4 in., 3/8 in. and 1 in. The resonances for the 1/16 in. (1.5 mm) sphere were barely visible due to background from the transducers and the electronic system. The intermediate conclusion from this initial look shows that the system, as configured, will have difficulty obtaining resonant spectra for the smaller TRISO particles due to a large background and the relatively small size of the particles.

Two paths were pursued to overcome this limitation of the commercial system:

1. The use of electromagnetic acoustic transducers (EMATs) to eliminate contact effects.

2. Custom fabrication of contact transducers to eliminate or reduce background from transducer resonance.

Path 1. EMAT Transduction

Several specimens were sent to Dr. Ward Johnson of the National Institute of Standards and Technology (NIST) in Boulder, CO for analysis. This approach was to eliminate the cost associated with establishing this EMAT Resonance measurement capability at PNNL. These transducers rely on the interaction between the eddy currents on the surface of the materials and a static magnetic field. Results showed that the electronic resonance of the system overshadowed the potential resonances of the surrogate TRISO particles. The question still remains that even if the conductivity is high enough will it be possible to take advantage of this transduction mechanism?

Path 2. Custom Contact Transducers

Contact has been made with researchers at LANL (Albert Migliori) and at the University of Tennessee at Knoxville (Veerle Keppens) to determine how to push the limits of the commercial system that is currently available at PNNL for resonance measurements. Both scientists indicated that specific transducer configurations can be constructed to minimize the interference from transducer resonances. Custom designs from LANL and the University of Tennessee have been considered as well as commercially available transducers from Dynamic Resonance Systems.

Future development work on this method of inspection was deferred until the acquisition or manufacture of custom transducers and measurements on surrogate TRISO particles have demonstrated adequate extension of the capability of the commercial device owned by PNNL.

Acoustic Microscopy

This task was designated to evaluate an acoustic microscopy approach to characterizing coated surrogate fuel particles (i.e., determining the feasibility of acquiring measurements of layer thickness, material properties, and localized changes in microstructure. Initially, before coated particles were available, glass spheres were examined using this method. Working at 50 MHz, it was possible to see gross feature differences between a damaged and an undamaged glass sphere. The diameter of the sphere was also determined to within about 50 μm.

As surrogate fuel particles became available, they were ultrasonically imaged both at PNNL and at Matec Micro Electronics. A 100-MHz transducer was used at PNNL, and a 105-MHz transducer was used at Matec. The PNNL system had a 30-μm lateral resolution and the Matec resolution was unspecified. Matec pursed PNNL's suggestion of using 60°C water to couple the transducer to the particle. The transducer used by PNNL was a 100-MHz Panametrics V3346, with a 3-mm-diameter aperture and a 6-mm focal length in water. The measured peak frequency from the samples was at 98 MHz. The transducer used by Matec was described as having a peak frequency of approximately 105 MHz and a 4.3-mm focal length in water. C-scan images obtained by PNNL and Matec had step sizes of 12 and 5 mm, respectively. These experiments demonstrated good penetration into the buffer layer; however, it was also determined that more work would be necessary to image features of interest.

As this work progressed, preliminary measurements confirmed the need to work at the extreme high end of the frequency range for ultrasonics (above 250 MHz, and perhaps as high as 1 GHz). It may be possible to work in this frequency range, but such an effort requires a larger investment than was proposed for this task. The reason it is necessary to work in this higher frequency range is to have wavelengths short enough to image and resolve the tens-of-micron-size defects important to the reliability of TRISO coated particles.

However, it may be possible to obtain valuable results by removing the defect imaging requirement and just detecting conditions indicative of a deviation of material properties from those of a standard. This position is based on calculations suggesting that measurements using currently available techniques at 50 MHz. This approach will be evaluated early in the next reporting period.

Optical

The first task objective was to review the commercially available systems for high-speed optical surface characterization systems for both batch and single-stream particle flaw inspection. A second objective was to explore the characterization capabilities that optical image analysis may offer if state-of-the-art technology were combined with emerging technology to potentially fill any existing gaps in realizing the imminent high-speed fuel particle inspection requirements.

An extensive review looking for existing commercially available optical inspection systems was completed. This review established that commercial, high-speed particle size and shape characterization systems are inadequate for TRISO fuel particle inspection. Dr. John Hunn (at ORNL) came to the same conclusion in his quest for an existing high-speed particle counting and sizing system. Dr. Hunn is now developing a system to meet his immediate requirements regarding sizing, based on off-the-shelf components.

To provide for the more advanced needs of the future, where high-speed flaw detection and surface characterization will become essential, an investigation into a method that uses automated digital image analysis was initiated at PNNL. This type of inspection is expected to automatically detect surface features such as micro-pores and fissures that have been found to develop during fabrication and reported to degrade particle fuel performance. Activities in this reporting period were limited to planning and system design. At the conclusion of this task, the capability of this inspection method will be established along with estimates for further development and demonstration.

Task 8. ON-PROCESS MEASUREMENTS

This task has been considered as two elements: a review and assessment of potential on-process measurement technologies, and preliminary measurements using transmission ultrasound on a model coater.

An initial review of technologies was performed. The assessment started from two published reviews by Workman et al. (1999), which looked at process chemometrics, and one by Tayebi et al. (2001), which considered measurement techniques for validating CFD models for multi-phase reactors. In addition, various books on the emerging topic of process tomography were reviewed (Williams and Beck 1995, Plaskowski et al. 1995). The techniques identified were then investigated further using the database "Web of Science."

Five technologies that could potentially be implemented to give on-process monitoring for a coater-system of the type used for TRISO particle fabrication were identified:

- Transmission ultrasound

- Pressurized gas-coupled ultrasound

- Electrical impedance and capacitance measurements

- Ultrasound backscatter, scattering, and diffuse field

- Process tomography (using various sensing fields)

Transmission Ultrasound

Transmission ultrasound has been successfully demonstrated on an autoclave, fluidized beds, and other reactors by Soong (1995-2000) and other groups (e.g., Bond, 1998). This work has demonstrated that high temperature operation is feasible and that radiation resistant materials for transducer fabrication have demonstrated performance in various nuclear applications. For example, acoustic emission sensors, based on piezoelectric elements, have been deployed on the primary pressure vessels of nuclear submarine power reactors. A schematic diagram of an ultrasound system on an autoclave reactor is shown in Figure 2.20.

Fig. 1. Schematic diagram of the autoclave reactor.
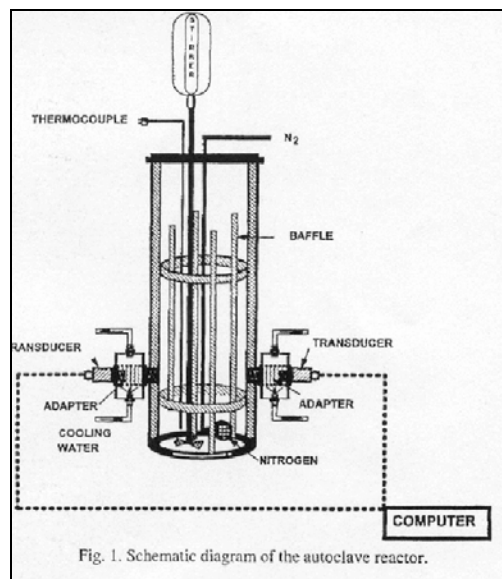
Figure 2.20. Example of an Autoclave Reactor with Transmission Ultrasound (from Soong et al., 1997)

In addition, there is significant literature that reports attenuation of sound in gas-solid suspensions (Gregor and Rumpf, 1976), velocity of sound in fluidized beds (Gregor and Rumpf, 1974, Roy et al., 1990), and various sensor implementations for in-line particle size measurements and characterization of granular materials in flowing bulk solids (Weir 2001, Tallon et al., 2003).

Pressurized Gas-Coupled Ultrasound

The use of high-pressure inert gas has been demonstrated for a limited number of demanding non-contact inspection systems. The use of gas removes the requirement for a liquid couplant and, at elevated pressure, gives a factor of five improvement of resolution, when compared with the same frequency operating in water. Reflection, gas-coupled, acoustic-microscopy was demonstrated by Wickramasinghe and Petts (1980), and a transmission microscope was developed by Bond (1992). More recently, gas-coupled ultrasound has been implemented for the characterization of compaction responses for porous membranes (Reinsch et al., 2000). Facets of this technology are illustrated in Figures 2.21 and 2.22, which show a gas-coupled microscope image of a coin and a graph showing the variation of attenuation as a function of pressure in nitrogen.
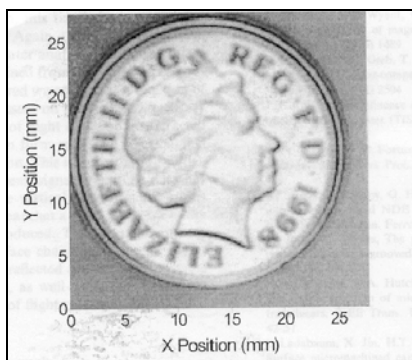
Figure 2.21. Coin Image Using Gas-Coupled Ultrasound (Robertson et al. 2002)
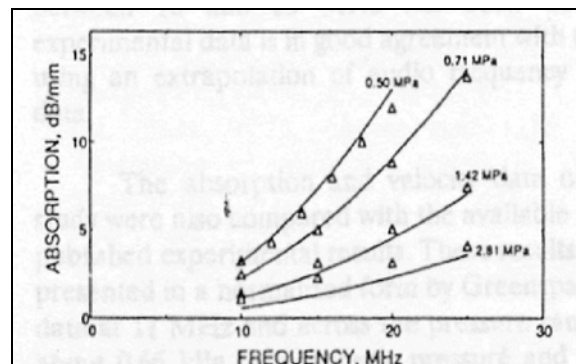
Figure 2.22. Attenuation as a Function of Pressure in Nitrogen (Bond 1992)

Electrical Impedance – Capacitance Measurements

Electrical impedance measurements have been successfully used in geophysics, seismology, nondestructive testing (NDT), and medicine. Conductive variations have been used to both characterize and image fluid flow. Recently, an example of electrical-impedance microscopy was reported by (Xiang and Gao, 2002). An image from that paper (Figure 2.23) shows a response from a small reference notch and corresponding frequency/impedance data from a line scan across the same feature.
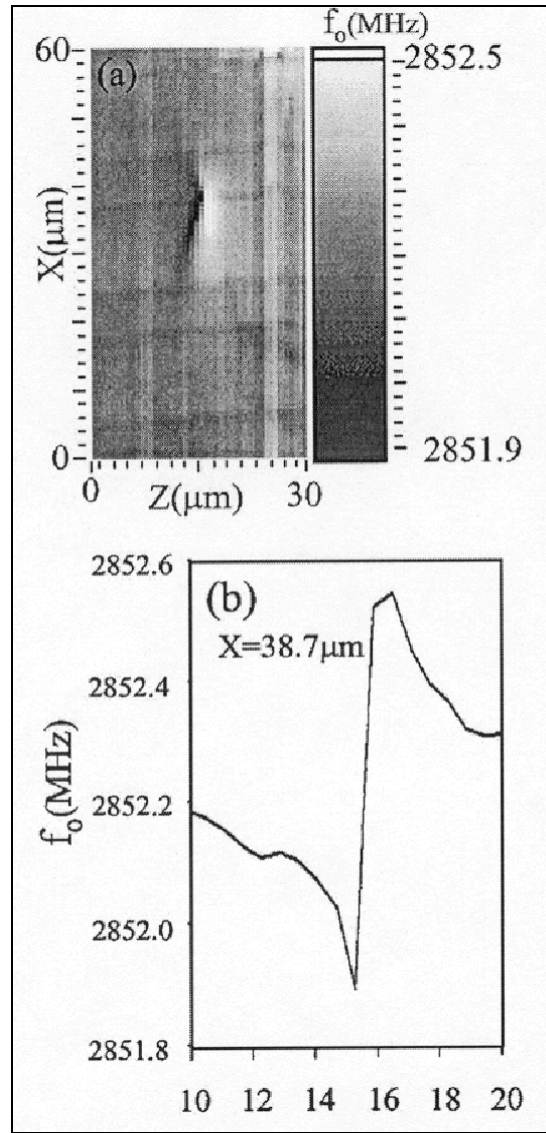
Figure 2.23. Example of Electrical Impedance Microscopy Image (Xiang and Gao, 2002)

Ultrasound Backscatter, Scattering and Diffuse Field

Ultrasound has been implemented in several forms for the characterization of multi-phase systems (Tayebi et al., 2001). Diffuse fields have been monitored in glass-bead slurries (Weaver and Sachse, 1995), and there have been numerous studies of the response of "hard" targets that result in multiple scattering of sound (ultrasound). This literature was recently reviewed by Tourin et al. (2000). An example of the complex time-domain and spectral responses for diffuse transport of acoustic waves in glass beads in water is shown in Figure 2.24 (Page et al., 1999). Conventional pulse-echo or transit-time measurements involve a primary pulse, attenuation, and arrival time. In diffuse-field/backscatter, the signature results from multiple scattering at amplitudes that may be several orders of magnitude less than that of the primary pulses.
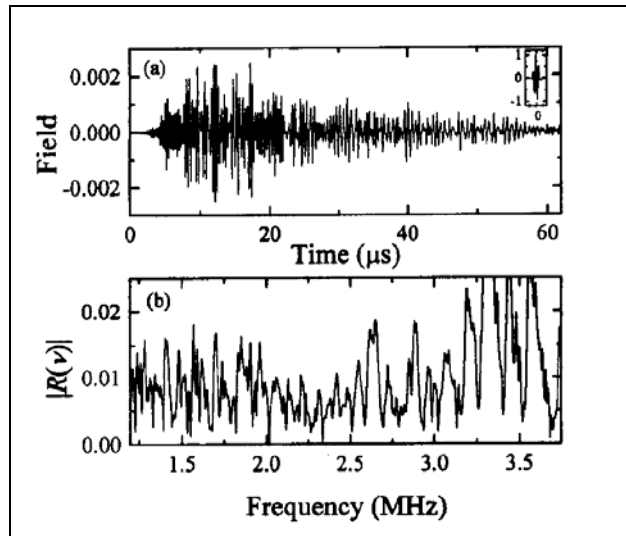
Figure 2.24. Example of Time Domain and Spectral Responses for Diffuse Transport of Acoustic Waves in Glass Beads in Water (Page et al., 1999)

Tomography

There has been a growing interest in the application of tomography for the imaging of process chambers and flows (Williams and Beck, 1995, Plaskowski et al., 1995). Tomography can be performed in both reflection and transmission as illustrated in Figure 2.25. The largest challenge in tomography is to get an adequate range of viewing angles, although some work has been successfully performed in reflection using relatively small viewing angles.
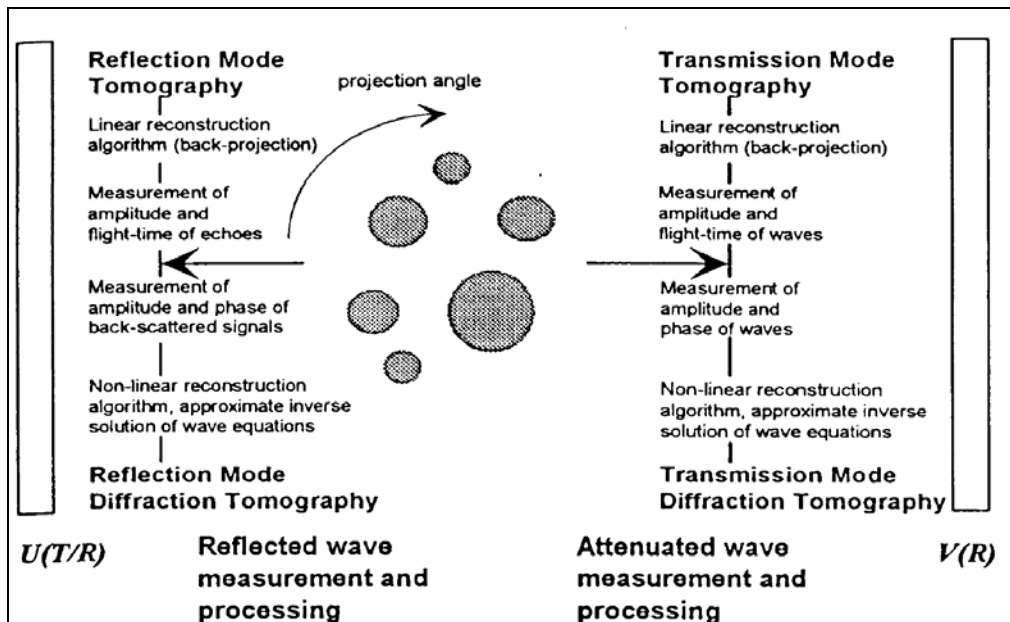
Figure 2.25. Concepts Involved in Tomography (from Plaskowski et al., 1995)

Method Assessment Summary

The technology assessment identified transmission and back-scatter based ultrasound measurements to be the two approaches that could potentially be implemented in a high-temperature vessel with limited access. These ultrasound techniques have the potential to be expanded and developed for implementation in a form of tomography.

In support of ultrasonic transmission and reflection measurements, the theory for multiple scattering from "hard" targets is well developed, including applications to gas-particle systems and fluidized beds.

The greatest challenges seem to be in quantifying the results of ultrasound measurements and in achieving the required sensitivity to dimensional variations in a batch of particles.

A model coater, based on an ORNL design, was fabricated and used to investigate the effects of particle size and concentration on measured parameters. The coater-transducer system was modified in two ways. First, windows were provided for the installation of the acoustic transducers. This improved the acoustic signal-to-noise ratio by more than 20 dB. Second, copper coating was added to the vessel to provide grounding and to eliminate static problems. The photograph in Figure 2.26 shows the fully functional model coater at PNNL after being modified.
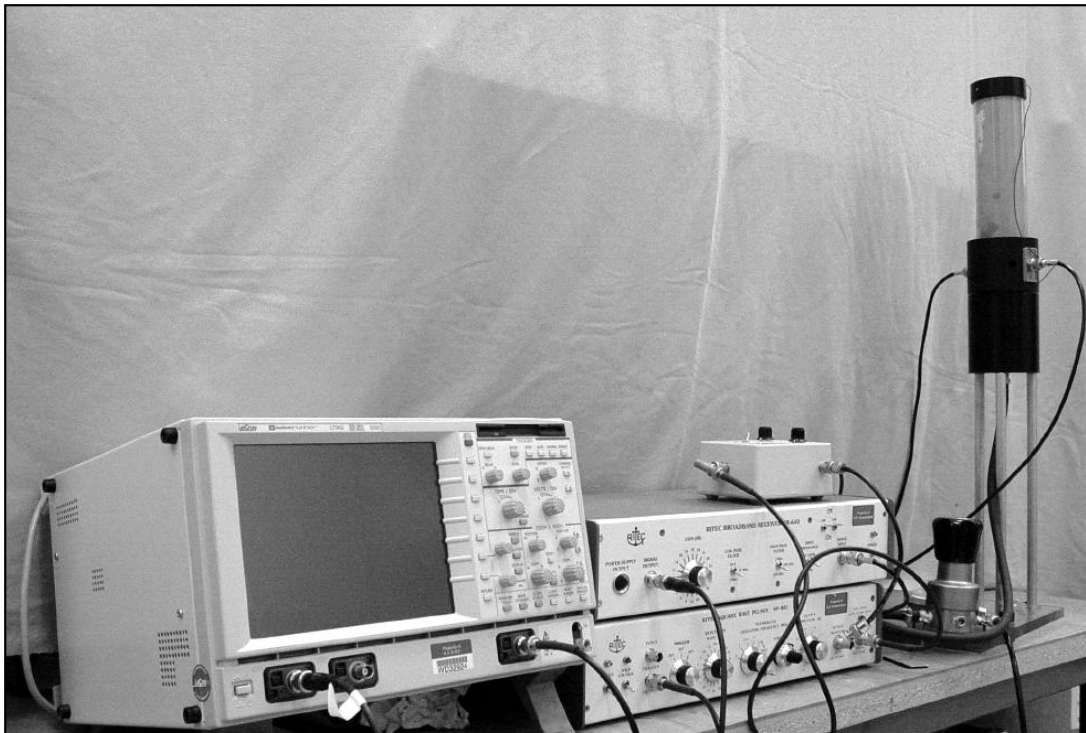
Figure 2.26. Model Coater and Measurement System

The dependence of the ultrasonic response on operating pressure and particle size is illustrated in Figure 2.27. The dependence of the measured time-of-flight on operating pressure and particle size is shown in Figure 2.28.

Amplitude(pressure, particle diameter) PC and PE
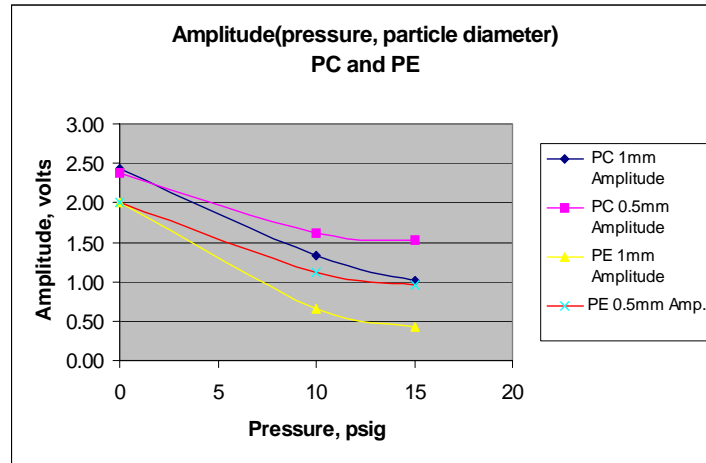
Figure 2.27. Example of Changes in Normalized Amplitude Response Seen With Particle Size and Coater Operating Pressure

TOF(pressure, particle diameter) PE
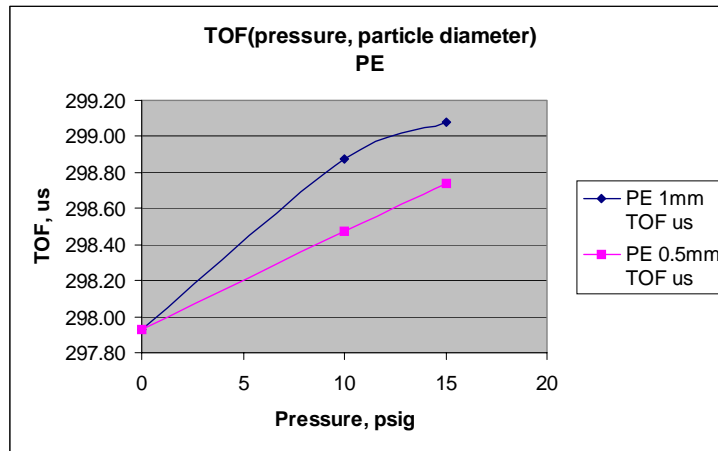
Figure 2.28. Example of Change in Measured Time of Flight (µs) With Two Different Particle Sizes and Operating Pressures

Data from the literature and preliminary data from this study demonstrate that ultrasonic methods have the potential to give on-line in-process dimensional monitoring in the coater. It is now necessary to determine if this technique can provide the required sensitivity to particle parameters to monitor the coating of TRISO particles during fabrication.

Next Steps

During FY2004, batches of coated particles will be obtained and trials will be performed to further investigate the capabilities for transmission ultrasound on-process measurements. In addition, further work will be performed to review and apply models that have been used to predict ultrasound response in fluidized beds.

References

Workman J, DJ Veltkamp, S Doherty, BB Anderson, KE Creasy, M Koch, JF Tatera, AL Robinson, LJ Bond, LW Burgess, GN Bokerman, AH Ullman, GP Darsey, F Mozayeni, JA Bamberger, and MS Greenwood. 1999. Process analytical chemistry, *Analytical Chemistry*, 71(12):121R-180R JUN 15 1999.

Tayebi D, HF Svendsen, HA Jakobsen, and A Grisingas. 2001. Measurement techniques and data interpretations for validating CFD multi-phase reactor models, *Chemical Engineering Communications* 186 pp. 57-159.

Williams RA and MS Beck. 1995. Process Tomography, Butterworth-Heinemann (Oxford).

Plaskowski A., MS Beck. R Thorn, and T Dyakowski. 1995. Imaging industrial flows, Institute of Physics Publishing (Bristol).

Soong Y, IK Gamow, AG Blackwell, KR Mundorf, FW Harke, RR Schehl, and MF Zarochak. 1997. Ultrasonic measurement of solids concentration in an autoclave reactor at high temperature. *Chemical Engineering Journal* 67(3):175-180.

Soong Y, IK Gamow, AG Blackwell, and EP Ladner. 1999. Ultrasonic characterization of slurries in a bubble column reactor. *Industrial & Engineering Chemistry Research* 38(5):2137-2143.

Bond LJ. 1998. Ultrasound measurements on three-phase chemical reactor. Denver Research Institute.

Gregor W. and H Rumpf. 1976. The attenuation of sound in gas-solid suspensions. *Powder Technology* 15 pp. 43-51.

Gregor W and H Rumpf. 1975. Velocity of sound in two-phase media. *Int. J. Multiphase flow*. 1 pp. 753-769.

Roy R, JF Davidson, and VG Tuponogov. 1990. The velocity of sound in fluidized beds. *Chemical Engineering Sciences* 45(11)3233-3245.

Weir GJ. 2001. Sound speed and attenuation in dense, non-cohesive air-granular systems. *Chemical Engineering Science* 56 pp. 3699-3717.

Tallon S, CE Davies, and M Kirkegaard. 2003. An acoustic method for in-line particle size measurement in flowing bulk solids. Proc. Inst. Mech. Eng. 217 Part E: *J. Process Mechanical Engineering* pp. 33-40.

Wickramasinghe HK and CR Petts. 1980. Acoustic microscopy in high pressure gases. Proceedings, IEEE Ultrasonics Symposium, pp. 668-671

Bond LJ. 1992. *Through transmission gas and pulsed water-coupled microscopy of electronic packaging and composite materials.* Report to NIST. University of Colorado at Boulder, Boulder, CO.

Reinsch VE, AR Greenberg, SS Kelly, R Peterson, and LJ Bond. 2000. A new technique for the simultaneous real-time measurement of membrane compaction and performance during exposure to high-pressure gas. *J. Membrane Sci.* 171 pp. 217-228.

Robertson TJ, DA Hutchins, DR Billson, JH Rakels, and DW Schindel. 2002. Surface metrology using reflected ultrasonic signals in air. *Ultrasonics* 39 pp. 479-486.

Xiang XD and C Gao. 2002. Quantitative complex electrical impedance microscopy by scanning evanescent microwave microscope. *Materials characterization* 48(2-3):117-125.

Weaver RL and W Sachse. 1995. Diffusion of ultrasound in a glass bead slurry. *J.Acoust. Soc. A.* 97(4):2094-2102.

Tourin A, M Fink, and A Derode. 2000. Multiple scattering of sound. Waves in random media. 10 pp. R31-R60.

Page JH, IP Jones, HP Schriemer, ML Cowan, P Sheng, and DA Weitz. 1999. Diffusive transport of acoustic waves in strongly scattering media, *Physica B*. 263-264 pp. 37-39.

Seifoddini H, and M Djassemi. 2001. The effect of reliability consideration on the application of quality index. *Computers & Industrial Engineering* 40 pp. 65-77.

Task 9. ESTABLISH STANDARD SIGNATURES AND FLAW LIBRARY

This task will develop a library of standard particles representing the full range of conditions known to degrade fuel performance. It will also include particles deemed to provide optimal fuel performance. Multiple particles will be selected for each standard to enable statistical analyses. The standard particles will form a basis for developing and calibrating the NDE techniques for automated defect detection. For each NDE technique, a signature will be established for each particle in the flaw library.

In FY2003, considerable effort went into developing the NDE methods. The measurement results from the NDE methods showing the greatest potential for automated defect detection were evaluated using surrogate TRISO particles obtained from another program that was in the early stages of developing the coating processes. The coating facilities at ORNL were unable to provide the specific needs of this task in FY2003. Therefore, large numbers of particles with highly variable coating conditions were sorted to select the few particles with defects considered capable of degrading fuel performance in a reactor. These particles were used predominately in finding trends between X-ray characterization and an electromagnetic measurement technique.

One of the outcomes from this effort was a clear definition of the type of particles that a flaw library must contain to fully develop, assess, and calibrate the NDE methods. The matrix of coating runs and associated parameters to achieve the necessary standard particle library will be submitted to ORNL for review in October, 2004. Even without particles coated specifically for this project, strong correlations were found between the particle diameter and the induction coil impedance; however, the multitude of undetermined parameters that could be varying among these early particles made it difficult to draw conclusions as to which parameters the NDE methods were most sensitive to and to sort out the various

effects. The coating runs to be developed early next year will simplify this problem by eliminating many of the simultaneously varying parameters and by systematically focusing on a limited parameter set.

One of the biggest challenges faced by this task (and other programs as well) is particle characterization. To date, there are a very limited number of methods available to facilitate characterization at ORNL's coating facility and to verify that specified coating parameters actually result in particles with particular properties. Calibration of the NDE methods being developed for automated inspections requires independent calibration of each particle in the standard library. Micro-focus radiography and CT X-ray techniques were developed under Task 4a of this project for providing kernel size, layer-thickness, and density distribution. Additional methods for characterizing coating layer porosity, density, and crystal structure are expected to become available at ORNL in FY2004.

2.3 FY2003 Presentations and Publications

Four presentations on work completed under this project were given this year, in addition to the annual program review in Rockville, MD.

40th WANTO Meeting (Weapons Agencies Nondestructive Testing Organization) held at PNNL and titled "Micro-NDE", presented by Dr. Leonard Bond on April 22-24, 2003. The material presented at this meeting generated interest within the NNSA community as techniques to assist NIF Target characterization.

R Hockey, L Bond, M Good and J Gray, 2003. "QA/QC for Advanced Fuel Particle Production," Transactions of the American Nuclear Society, Advances in Nuclear Fuel, Vol. 88, TANSAO 88 1–938 (2003), ISSN: 0003-018X. Presented at the 2003 ANS Annual Meeting, June 1–5, 2003; San Diego, California, pp. 412–413.

Ahmed S and RL Hockey. 2003. "Effects of Shape and Layer Defects on Resonance Frequencies of Spheres," presented in the NDE 2003 Conference, December 11-13, 2003, India.

Ahmed S and PD Panetta. 2003. "Effects of Layer Properties on the Ultrasonic Resonance of Composite Spheres," Review of Progress in Quantitative NDE. KI Convention Center – Green Bay, Wisconsin, July 27 – August 1, 2003.

2.4 FY2003 Financial Summary

Cumulative Cost Performance

	Oct	Nov	Dec	Jan	Feb	Mar	Apr	May	Jun	Jul	Aug	Sep
Cum Actual ($K)	$10.4	$21.7	$37.0	$63.1	$97.8	$155.3	$192.0	$233.9	$300.3	$350.6	$423.4	$540.1
Cum Budget ($K)	$35.6	$41.4	$124.2	$206.8	$267.7	$305.0	$372.8	$436.3	$484.1	$530.9	$546.4	$570.5

Annual Cost Performance:

Expenditures of $540.1K were incurred during FY2003 of the $570.5K received in funding. Spending lagged in the first four months of the year while two subcontracts and non-disclosure agreements with Iowa State University and General Atomics were negotiated and established. Spending accelerated continuously over the next eight months peaking in September due to lagging subcontract invoicing and accruals of estimated cost for the last quarter.

During the second quarter, funds were deobligated due to the closure of the DOE Oakland Operations Office at the end of FY2003 and reinstated in the fourth quarter by DOE HQ.

A change request to carry over approximately $30K of FY2003 scope and associated funding was requested and approved during the month of September.

Funding for FY2004 arrived at PNNL during the fourth quarter, allowing planning for FY2004 and subcontract actions to be initiated.

2.5 FY2003 Project Milestones

Milestone & Deliverables	Planned Completion	Revised Completion	Actual Completion	Percent Complete
Place subcontract with ISU	Oct—02		Dec-02	100
Place subcontract with GA	Oct—02		Dec-02	100
Nondisclosure Agreements	Nov—02		Nov-02	100
Complete Initial Literature Review	Jan—03		Jan-03	100
Quality Index Defined FY2003	Jun—03		Jun-03	100
Particle Batch No. 1 & CT Received	Apr—03		Aug-03	100
Additional Particles & CT	Jun—03		Dec-03	100
Stationary NDE Method Development Complete	Sep—03	Dec-03	Jan-04	100
Standard Signature Flaw Library Complete	Apr—04	Jun-04		5
FY2003 Annual Report Complete	Sep—03	Mar-04		90

The tasks involving the development of NDE methods for stationary particles and the construction of a standard signature library are behind schedule due to delays in obtaining surrogate particles with the coating properties necessary for testing and calibrating the NDE methods. Measurement data from the in-line NDE measurement methods will be necessary to develop the quality index. Particles appropriate for completing these milestones are expected to become available in the first quarter of FY2004, barring further delays in the coating development work at ORNL.

2.6 FY2003 Appendices

Appendix to Task 4:

General Atomics deliverable #1.

**General Atomic's Deliverable No. 1: Derived From the report
"Criteria for Developing Advanced QC Methods for Gas-Cooled Reactor Fuel Particle."**

Table 2.6. Recommended Coated Particle Standards for QC Methods Development and Qualification

Key Property	Priority(1)	Potential Method	Particle Type Needed	Particle Standards Required(3)	Comments
Kernel stoichiometry	2		Kernel	UO_2 kernels, UCO kernels, and UC_2 kernels. Alternately, UCO kernels having different O/U and C/U ratios, if these ratios can be established in individual kernels	Availability of UC_2 kernels is doubtful. O/U and C/U may be determinable in individual kernels by X-ray diffraction
Missing (or thin(2)) buffer coating	1			Particles with nominal buffer density and the following buffer coating thickness: - no coating - 20 μm - 40 μm	Determine actual buffer coating thickness by radiography
Buffer coating density	3			TBD	Possible to characterize buffer void volume as a verification of both buffer coating thickness and density?
IPyC microstructure	1			Particles with high, moderate, and low anisotropy and nominal IPyC thickness and density: - IPyC deposited with CGR = 0.15 - IPyC deposited with CGR = 0.25 - IPyC deposited with CGR = 0.35	Characterize anisotropy with optical OAF measurement
IPyC thickness	2			Particles with low anisotropy and the following coating thickness: - 35 μm - 20 μm	35-μm standard is also one of the IPyC microstructure standards
IPyC density	3			TBD	
Missing or thin SiC	1			Particles with following SiC coating thickness: - 15 μm - 25 μm - 35 μm	Determine actual SiC coating thickness by radiography

Key Property	Priority(1)	Potential Method	Particle Type Needed	Particle Standards Required(3)	Comments
Cracks or pores penetrating the SiC layer	1			Particles with pores in SiC - Laser drilled surrogate particles - Particles with SiC deposited on an IPyC-coated substrate having a highly permeable IPyC - Particles with cracked SiC	Verify presence of pores using burn-leach test Create cracked SiC by applying a compressive load to particles
Lenticular flaws in SiC coating	3			Particles with small, medium, and large "gold spots"	Fabricate by running a SiC batch with excessive particle fluidization
Metallic impurities in SiC coating	1			Particles with metallic inclusions - At IPyC/SiC interface - At SiC/OPyC interface	Fabricate by introducing metallic impurities into surface of IPyC prior to SiC coating and into surface of SiC prior to OPyC coating
SiC microstructure	1			Particles with SiC deposited at: - 1400C (globular structure, α-SiC, and free Si) - 1550C (small grains, β-SiC) - 1750C (very large columnar grains, β-SiC, and free C)	Characterize particle batches by ceramography (structure) and Raman spectroscopy (SiC structure and presence of free Si and C)
OPyC microstructure	2			Particles with high, moderate, and low anisotropy and nominal OPyC thickness and density: - OPyC deposited with CGR = 0.15 - OPyC deposited with CGR = 0.25 - OPyC deposited with CGR = 0.35	Characterize anisotropy with optical OAF measurement
OPyC thickness	3			Particles with low OPyC anisotropy and the following coating thickness: - 40 µm - 20 µm	40-µm standard is also one of the OPyC microstructure standards
OPyC density	3			TBD	

(1)1 is highest priority and 3 is lowest

(2)A buffer coating is considered to be "thin" if the thickness is less than 20 µm

(3)Particle standards in bold type will be available from coating runs performed under the AGR Program. However, all of these particles will contain depleted or natural uranium kernels

3.0   FY2004 – Project Year 2

October 2003 to September 2004

3.1 FY2004 Summary

This document summarizes the activities performed and progress made in FY2004. Various approaches were evaluated for automating quality control in the particle-fuel production process using nondestructive methods adaptable to in-line inspection. In the first-year of this three-year project, surrogate fuel particles available for testing included leftovers from initial coater development coating runs. These particles had high defect fractions and widely ranging particle properties, providing an opportunity to examine worst-case conditions before refining the inspection methods to detect more subtle coating features.

In this second project year, it became necessary to have fully and partially coated surrogate particles without defects (standard particle) and particles with specific variations from the standard particle to evaluate the NDE methods for defect detection. A matrix of 14 different coating specifications was developed for this purpose, requiring over 40 specific coating runs at ORNL to fabricate. In addition to surrogate-coated particles, the planning process was completed for obtaining uranium-based materials with similar coatings.

Radiographic techniques for characterizing the dimensional properties of coated particles were further developed and refined at ISU to examine more particles in less time. The only particle characterization method available to this project has been radiography, therefore defect conditions associated with the dimensional properties of the TRISO particle have been a major focus in developing high-speed defect detection techniques for automating particle inspection.

The notion of a particle quality index to relate coating properties to fabrication process parameters was defined further.

The nondestructive evaluation (NDE) inspection methods were further developed and evaluated for defect detection. An inductive impedance method was found to discriminate between a normal and a thin buffer coating in both partially and fully coated surrogate TRISO particle. Radiographic layer thickness values were highly correlated with the inductive impedance measurements when only a buffer or a single PyC layer is deposited on a surrogate kernel. As additional TRISO coating layers were deposited, layer diameter was also found to correlate well with inductive impedance measurements. The capacitive impedance measurement technique was seen to detect the absence or presence of a thin or missing SiC layer—a key defect in TRISO coated fuel because of the ability of the SiC layer to confine fission products. Based on these findings, an example particle inspection system, employing both an inductive and a capacitive sensor, is recommended for a specific coating process to significantly improve QC.

Several optical techniques were evaluated for detecting surface defects. Findings suggest that an optical inspection system could be developed at a reasonable cost with the capability to detect 1-µm pits, which are expected to occur under certain fabrication conditions.

The ultrasonic techniques being evaluated in this project have not proven to be effective for detecting particle defect conditions and require more development. Therefore, it was suggested that evaluation of these methods be suspended.

Progress this year was broadly discussed and disseminated through several presentations at meetings, seminars and conferences, in addition to the annual program review held in Gaithersburg, MD.

3.2 FY2004 Research Progress

Task 1. LITERATURE REVIEW

A general literature review performed as part of the proposal process revealed over 30 years of work on coated particle fuels. This initial review spans topics relevant to advanced gas reactor programs, with particular focus on the reporting of fabrication and testing of TRISO particles, both nationally and internationally. The 1970-2001 period covered by this initial publication review yielded over 150 publications.

Task 1 was completed in project year one, per the original statement of work; however, the list of publications was updated through mid-2004 as more recent work became available. Some of the more recent works shown below were added to the searchable electronic database developed under this project, simplifying the retrieval and dissemination of information specific to coated-particle fuels. The database currently contains over 250 publications.

References

Pain CC, MD Eaton, JLMA Gomes, et al. 2003. "The fission power of a conceptual fluidized bed thermal nuclear reactor", ATW-INT, J Nucl Power 48 (10): 613-+.

Talamo A, W Gudowski, and F Venneri. 2004. "The burnup capabilities of the deep burn modular helium reactor analyzed by the Monte Carlo continuous energy code MCB", *Annual Nucl Energy* 31 (2):173-196.

Plukiene R, D. Ridikas. 2003. "Modelling of HTRs with Monte Carlo: from a homogeneous to an exact heterogeneous kernel with microparticles", *Annual Nuclear Energy* 30(15):1573-1585.

Task 2. MODELING STUDY

The objectives of the modeling activities are threefold:

1. Develop the measurement methods consistent with the theory

2. Better analyze and interpret measurement results

3. Predict measurement results for a broader range of defect conditions, beyond those that can be fabricated in the time frame of this project.

Per the original statement of work, both acoustic and electromagnetic models were developed in project year one. In the second project year, the numerical models were not refined or developed further. They

were used to estimate detection thresholds for various particle properties and in refining the sensors and instrumentation.

Results from the numerical modeling are discussed in Task 6, where a closer comparison with the measurement results is presented.

Task 3. DEFINE QUALITY INDEX

Quality control in a production setting is typically implemented in the form of a measurement process that is fast enough to prevent non-conforming material from entering the final product stream. A pass/fail criterion is programmed into the decision logic of the test and becomes the central part of such a procedure. There are several quality measures that can be used for such a pass/fail criterion. In past acceptance plans, the average value, or the average deviation from a target value, was often used as the quality measure. However, the use of the average alone provides no measure of variability, and it is now recognized that variability is often an important predictor of performance. Several quality measures, including percent defective (PD) and percent within limits (PWL), have been preferred in recent years because they simultaneously measure both the average level and the variability in a statistically meaningful way.

One of the objectives of this NERI project is to develop a measure of quality based on NDE measurements. The two primary reasons for this objective are: 1) nondestructive measurements are necessary for inspecting a high particle fraction before use; and 2) NDE methods may be fast enough to accommodate the high throughput rates required to keep pace with frequent refueling cycles required by next-generation nuclear power systems, each requiring more than 10^9 particles.

Thus,the quality index is based on relationships among statistical distributions empirically formulated from high-speed NDE measurement results, coating production process parameters, material properties within the coated TRISO particles, and the performance of the particles.

The PWL Quality Measure

The PWL quality measure uses the sample mean and the sample standard deviation to estimate the percentage of the population (batch) that is within the specification limits. This is called the PWL method, and is similar in concept to determining the area under the normal curve.

In theory, the use of the PWL (or PD) method assumes that the population being sampled is normally distributed. In practice, it has been found that statistical estimates of quality are reasonably accurate provided the sampled population is at least approximately normal, i.e., reasonably bell-shaped and not bimodal or highly skewed.

Conceptually, the PWL procedure is based on the normal distribution. The area under the normal curve can be calculated to determine the percentage of the population that is within certain limits. Similarly, the percentage of the batch that is within the specification limits can be estimated.

Instead of using the Z-value and the standard normal curve, a similar statistic, the quality index, QI, is used to estimate PWL. The QI value (a measurement value derived from a sensor) is used with a PWL table (defined from acceptance criteria) to determine the estimated PWL for the batch.

The statistic Z, therefore, measures distance above or below the mean, μ, using the number of standard deviation units, σ, as the measurement scale. This is illustrated in Figure 3.1 and 3.2.
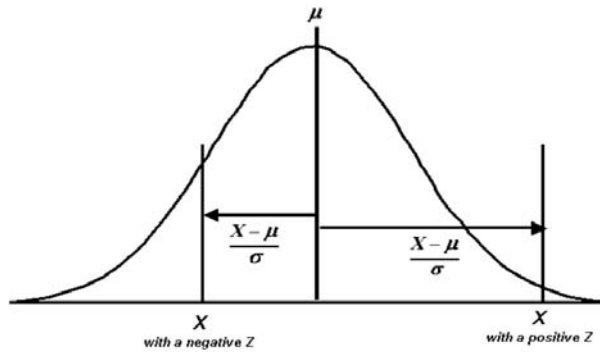
Figure 3.1. Illustration of the Calculation of the Z Statistic
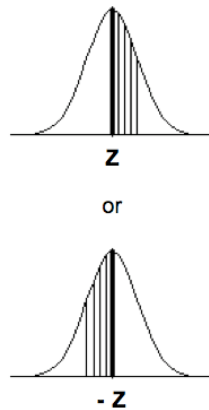
Figure 3.2. Distribution of a Single Attribute, Both Positive and Negative.

The Z-statistic that is used with the standard normal table uses the population mean as the point of reference from which the area under the curve is measured:

$$Z = \frac{X - \mu}{\sigma}$$ (3.1)

Quality Index

A *Quality Index* approach is a convenient way of organizing and implementing a statistical measure of quality, particularly on a high-speed measurement basis relating a large number of parameters.

The process for coating next-generation nuclear particle fuel involves hundreds of different parameters, each having a (unique) limited range of values that result in the most favorable performance. A quality index that relates NDE measurement results to coating process parameters that yield acceptable coatings and particles would be well suited to automated inspections. A quality index of this type could be developed for both batch sampling and 100% inspection methods and could provide a statistical basis for acceptance/rejection of a particle batch.

Currently, the NDE methods showing promise for quantifying a unique statistical relationship between the NDE measurement values, particle properties, and the process parameters used in their fabrication are

inductive and capacitive electrical measurements. The combination of these two techniques has the potential to inspect individual particles at inspection speeds approaching those required for 100% (or a large fraction of each coating run) inspection. Radiographic methods, also under development, are showing promise for providing a more direct measure of layer dimensions, at lower inspection rates.

Per the original statement of work, Task 3 (Defining the Quality Index) was completed during project year one. Up to this reporting period, particles, characterization data, and reactor performance measures have not become available in sufficient quantity to develop and demonstrate a quality index for a given coating flow sheet. The particles and characterization data satisfying these three requirements were expected to become available in the third year of this project.

Task 4. OBTAIN SURROGATE PARTICLES

The objective of this task is to specify the properties of surrogate particles to obtain those particles in sufficient quantities to evaluate, refine, and calibrate the high-speed NDE measurement methods being developed by this project. Many different particle-coating conditions are considered to be defects. A defect is defined as a physical particle property that deviates from specifications and adversely affects reactor efficiency, safety, or maintenance costs. Both nominal and defective particles are needed to demonstrate the ability to detect the various coating defects. The primary outcome of this task will be a particle defect library (structured in Task 9) to be used throughout the remainder of this project in evaluating each inspection method.

Defects occur for various reasons. The defective fraction of an entire coating run is dependent upon many variables in the manufacturing process. The primary focus of defect characterization in this project is detecting dimensional defects-- kernel diameters and coating layer thickness out of specification. Although other properties of TRISO particles are important, dimensional attributes have been found to play a key role in fuel performance. Deviant dimensional parameters are found to occur more often than other types of defects. The NDE methods to detect those defects must be evaluated against another, independent, means of particle characterization. X-ray techniques were the best available method for that purpose. In particular, micro-focus radiography has been shown to provide dimensional parameters to within a few microns.

The NDE methods developed in this project must apply to fueled particles as well as to the surrogate particles being used in the evaluation phase for reasons of convenience and cost reduction. It should be demonstrated as early as possible in the project that this is the case. This is the objective of Task 10. In that task, depleted uranium will be coated and evaluated to determine what effect the chemistry of the kernel may have on detection and discrimination of the high-speed NDE methods.

Defective Coatings

Project team members from PNNL, ORNL, and GA jointly developed a particle coating specification matrix for establishing a surrogate-particle defect standards library. This approach creates particles with specific defects that can be used to evaluate the NDE methods, primarily electromagnetic measurements. The particles produced using this matrix were the first batch coated specifically for developing and calibrating the NDE measurement methods at PNNL. All prior work had been conducted using particles coated for other projects. The full matrix of coating conditions designed at the beginning of this project

year is included in this report under the appendix to Task 4. This matrix includes particle-coating specifications to establish:

1. Single layers of buffer, PyC, and SiC material coated at various thicknesses on surrogate kernels of different sizes.

2. NDE signature variations about a "standard" TRISO particle on a bimodal distribution of kernel sizes ranging from 275 μm to 450 μm.

3. NDE response to variations in PyC density/microstructure relative to the nominal value.

4. NDE response to a metal coating-layer impurity.

5. Effect of SiC thickness.

6. Effect of laminar defects.

Programmatic delays at the ORNL coating facility impacted this task by deferring production of the above particles until late into the second quarter. Downtime on one of two furnaces and a lack of characterization are the primary causes for the delay. In the meantime, on December 19, ORNL did ship particles coated for the Advanced Gas Reactor (AGR) project as follows:

1. AGR-11172003-2—100-μm buffer on, 500-μm (diameter) ZrO_2 kernels.

2. AGR-11122003-1—100-μm buffer and 40-μm IPyC on 500-μm ZrO_2 kernels.

3. AGR-10132003-2—100-μm buffer, 40-μm IPyC, 35-μm SiC, and 40-μm OPyC on 500-μm ZrO_2 kernels.

4. NT-64—buffer, IPyC and SiC on 500-μm ZrO_2 kernels found to have "gold spots[a]"

5. Uncoated ZrO_2 200-, 300-, 400-, 500-, 650-, and 800-μm kernels.

Particles from item No. 4 above will be used to evaluate the optical imaging methods under Task 6. The kernels of various sizes listed as item No. 5, with the specific tolerances displayed in Table 3.1, were used to evaluate size effects in the on-process NDE method of Task 8 and the sensitivities of the EM methods to kernel properties in Task 6.

Table 3.1. YZT – ZrO_2 Kernel Specifications

Diameter (mm)	Tolerance* (mm)		Diameter (μm)	Tolerance* (μm)		Current Batch Specs
0.10	-0.02	0.03	100	-20	30	
0.20	-0.03	0.07	200	-30	70	
0.30	-0.01	0.07	300	-10	70	300 μm < 100% < 350 μm
0.40	-0.05	0.10	400	-50	100	
0.50	-0.05	0.15	500	-50	150	35% ~ 500 μm, 65% > 500 μm
0.65	-0.10	0.15	650	-100	150	
0.80	-0.10	0.15	800	-100	150	
* Manufacturer supplied tolerances						

(a) Gold spot defects are described further in Task 6 under optical methods. They have been found to occur during the application of SiC onto the IPyC layer.

In producing the initial 14 coating variations outlined in the coating matrix as shown in appendix to Task 4, Table 3.9, some of the runs required several iterations to attain particles having the desired properties. To complete the requirements of this initial coating specification, 29 separate coating runs were performed at ORNL. The specifications for these coatings are presented in terms of the AGR (Advanced Gas Reactor) specifications. A few particles from each coating run were destructively tested at ORNL to estimate how far selected coatings properties may have deviated from the specification.

The only characterization results available to correlate with the NDE methods being evaluated at PNNL is the X-ray analysis conducted at ISU under Task 4a. A small fraction of particles from each coating run were shipped to ISU to allow parallel characterization and development of the inductive impedance measurements being performed at PNNL.

In a meeting held at ORNL on April 14, 2004, two additional coating runs were identified as necessary to assist in the EM measurement method development task. They include a single buffer layer of ~400 μm in thickness and another run of a PyC layer thickness of ~ 400 μm, both applied to ~200-μm ZrO_2 kernels. The process parameters used to produce these coatings are shown in Table 3.2. The request for these particles arose from a need to answer a question considering the electrical conductivity difference between the denser PyC material and the less dense buffer material.

Table 3.2. Coating parameters for developing particles with extra-thick, buffer and single PyC layers

Run Number	**15-A**
Date Shipped	6/7/04
Desired particle dia (μm)	200
Particle batch(s) to use	200
Buffer	
Run Segment 1	
Measured Thickness (μm)	80
Temperature	1300
C2H2/Ar	1.5
Time	18
Run Segment 2	
Measured Thickness (μm)	130
Temperature	1300
C2H2/Ar	1.5
Time	18
Run Segment 3	Batch from run segment 2 split in half. Run Segment 3 only has half as many particles as run segment 2.
Measured Thickness (μm)	250
Temperature	1300
C2H2/Ar	9
Time	18
Run Segment 4	Batch from run segment 3 split in half. Run Segment 4 only has half as many particles as run segment 3.
Measured Thickness (μm)	390
Temperature	1300
C2H2/Ar	9
Time	18

Table 3.2. (contd.)

Run Number	16-A
Date Shipped	6/7/04
Desired particle dia (μm)	200
Particle batch(s) to use	200
IPYC	
Run Segment 1	
Measured Thickness (μm)	Did not record
%HC	30
Temperature	1300
%C2H2 in HC	44
%C3H6 in HC	56
Time	60
Run Segment 2	
Measured Thickness (μm)	Did not record
%HC	30
Temperature	1300
%C2H2 in HC	44
%C3H6 in HC	56
Time	60
Run Segment 3	Batch from run segment 2 split in half. Run segment 3 only has half as many particles as run segment 2.
Measured Thickness (μm)	375
%HC	50
Temperature	1300
%C2H2 in HC	44
%C3H6 in HC	56
Time	90

Discussing the results of this NERI project at the April meeting at ORNL introduced some new thoughts as to why the IPyC layer properties may have been altered after applying SiC layer. This concept had not been considered before PNNL requested the application of IPyC material without other successive TRISO layers.

To resolve this issue, ORNL team members suggested adding a SiC layer to the particles coated in runs 7 – 9. PNNL sent most of the remaining particles from those runs back to ORNL for SiC coating in the third quarter of this year. Several additional coating runs were completed at ORNL to further investigate the coating conditions necessary to control the density and anisotropy of PyC coatings. The resulting particles were shipped to PNNL during of the fourth quarter reporting period. This was in support of a more thorough analysis being conducted at ORNL to better understand their coating process. Table 3.3 is a summary of the coating runs made to optimize the PyC coating process.

Table 3.3. Coating parameters used to produce variations in the PyC properties

AGR #	PNL-NERI	Temp (C)	Coatings	C3H6/C2H2	Total Gas Flow (l/min)	Active Gas Fraction	Nominal IPyC Thickness (μm)	IPyC Coating Time (min)	Nominal IPyC Coating Rate (um/min)
AGR0122 2004-1	007-A		IPyC and SiC on 500-μm ZrO₂	1.2		0.15	45	15	3.0
AGR0122 2004-2	008-A			1.3	7000	0.28	40	6.5	6.2
AGR0122 2004-3	009-A			1.3		0.40	40	5	8.0
NA	017-B		Buffer and IPyC on 500-μm ZrO₂	10.6	11408	0.48	40	6	6.7
NA	018-C	1300		10.9	13144	0.67	40	4	10.0
NA	019-A			13.2	16450	0.81	50	5	10.0
NA	017-E			1.2		0.15	40	15	2.7
NA	018-F			1.3	7000	0.28	40	9	4.4
NA	019-C			1.3		0.40	40	8	5.0
NA	020-A			1.3		0.15	40	22	1.8
NA	021-A			1.3	5000	0.28	40	12	3.3
NA	022-B			1.3		0.40	40	9	4.4

Most of the particles produced using the conditions displayed in Table 3.3 were evaluated with the inductive and capacitive sensors before and after adding a SiC coating layer.

Task 4a. PARTICLE CHARACTERIZATION

Many different particle characterization methods were contemplated for this project. Only radiography was available as a practical option. Other options such as electron microscopy (SEM and TEM) and several related methods were too time consuming, unavailable, or too costly. However, radiography did provide dimensional information at resolutions sufficient for evaluating the sensitivity of other NDE methods to particles having dimensions that are outside of nominal specifications.

The two-dimensional radiography techniques used in the first year underwent further refinement to meet the specific requirements of this project, primarily higher throughput, without sacrificing accuracy. Progress includes the development of a more efficient particle handling procedure, software tools for quickly measuring dimensions from the digital radiographs, and more sharply defined specifications of essential characterization requirements.

Finding sufficient quantities of particles having a particular defect among the vast quantities of particles being coated is a major challenge. This challenge was partially overcome using two approaches. The first approach simultaneously surveys a 30-40 particles to quickly identify anomalous particles requiring additional characterization. This approach was found to be more efficient than obtaining higher-resolution images of only a few particles at a time. The second approach looks at over 30 particles by first funneling them into a thin-walled pipette, then using micro-focus radiography at 25X magnification (5-μm pixel size). After observing anomalous particles among 30+ similar particles, the challenge then becomes sifting out those of interest. A tray, suitable for loading and unloading the particles into a hollow tube, was developed for this purpose (Figure 3.3).
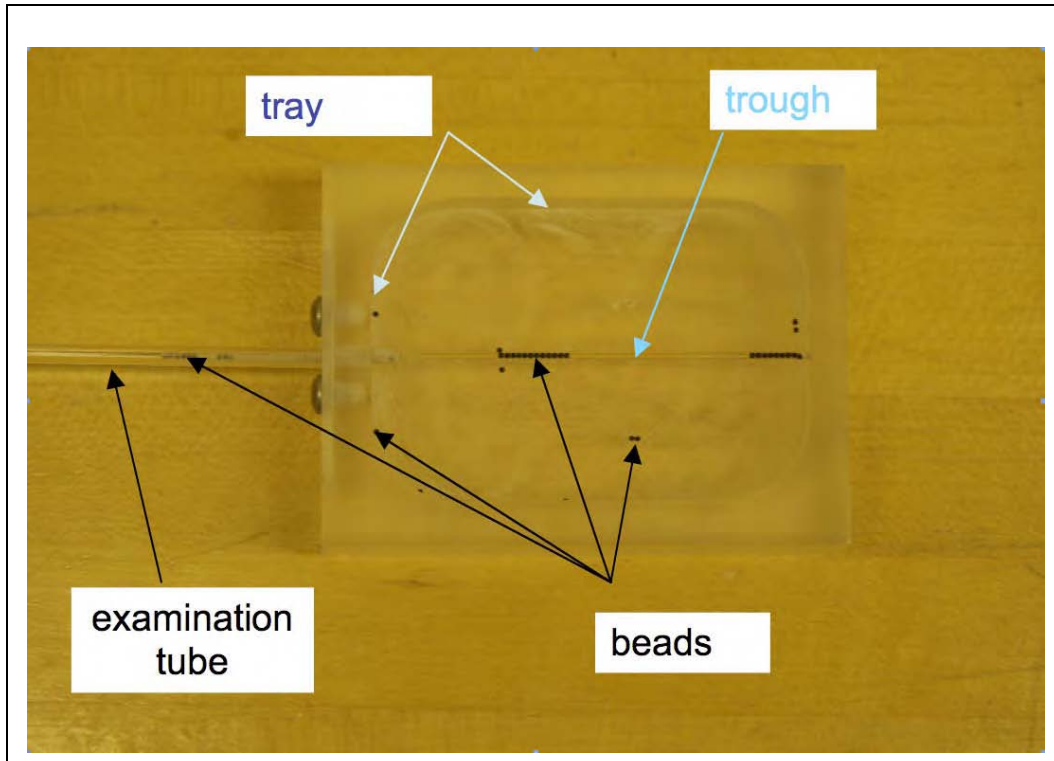
Figure 3.3. A Plastic Tray With a Trough Feeding the Examination Tube Allows Easy Loading of Particles. After an Initial Survey Using Micro-Focus Radiography, Tilting the Examination Tube and Pouring the Particles Out Into the Trough Can Remove Selected Particles. The Anomalous Particles Can Be Easily Picked Out of the Line and Placed in Separately Labeled Tubes

Example radiographs of particles sorted by this approach are shown in Figure 3.4. Figure 3.5 zooms in on an area of the leftmost image in Figure 3.4. The particle shown has a large kernel and is without a SiC shell. A clear interface is seen at the outer carbon layers. Note that the bright ring on the particle perimeter is due to an X-ray refraction effect.
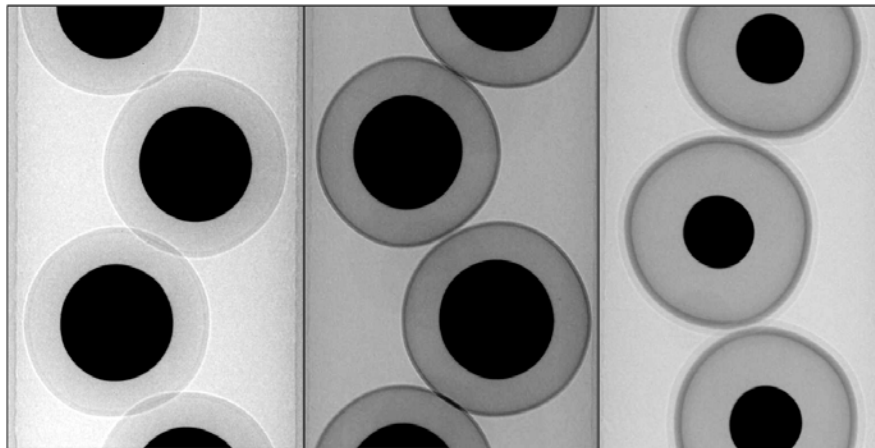
Figure 3.4. The Left Image is of the Particles Without SiC or OPyC. The Middle Image Shows the Particles With the SiC Layer and No OPyC. The Right Image Shows the Full TRISO Particles. Note the Two Left Images Have Larger Kernels
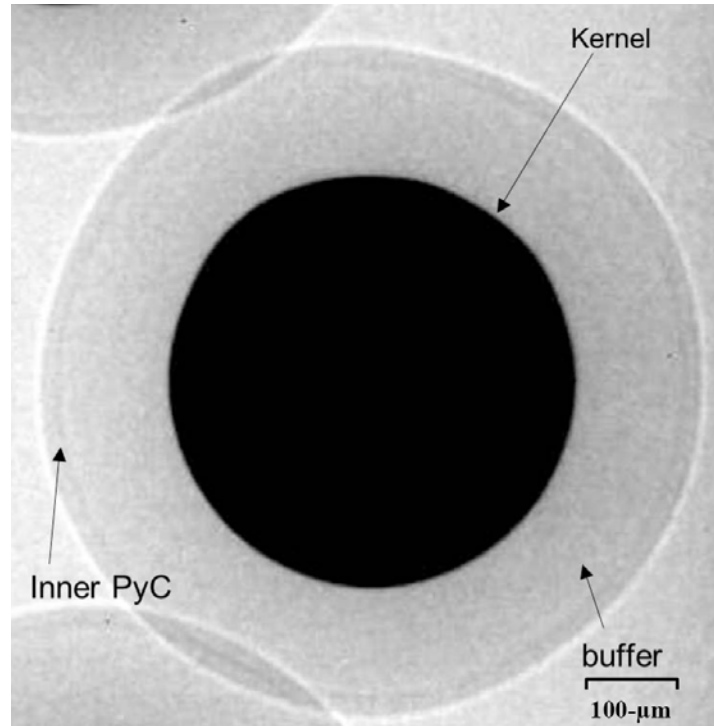
Figure 3.5. An Enlarged Image of the Particles Without a SiC or OPyC Layer

Figure 3.6 is an enlarged image of a particle with a large kernel and a SiC layer. The high-density SiC layer is easy to see in comparison with the underlying lower-density IPyC layer.
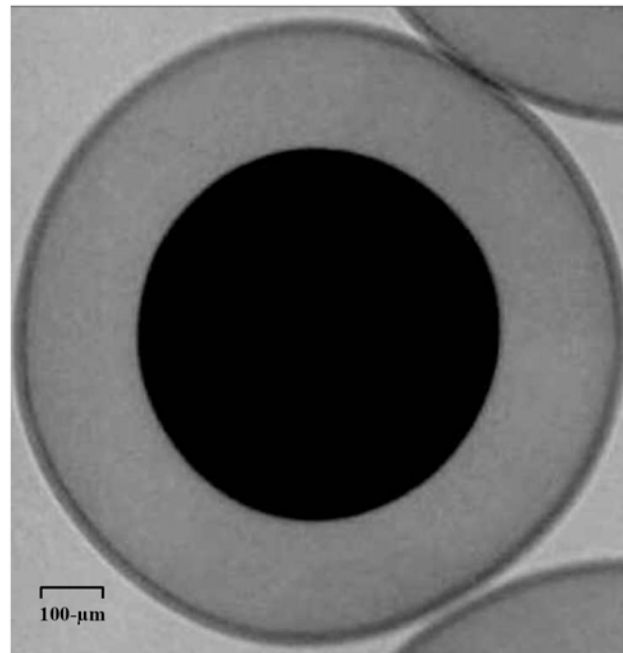
Figure 3.6. An Enlarged Image of a Particle With a SiC Shell (no OPyC Layer)

3.11

Finally, from this series of images, Figure 3.7 shows a TRISO particle with all of its layers. The light blue line shows the kernel diameter. The dark blue line shows the interface between the buffer and the inner PyC. The pale lavender line shows the inner diameter of the SiC shell. Finally, the red line shows the inner diameter of the outer PyC.
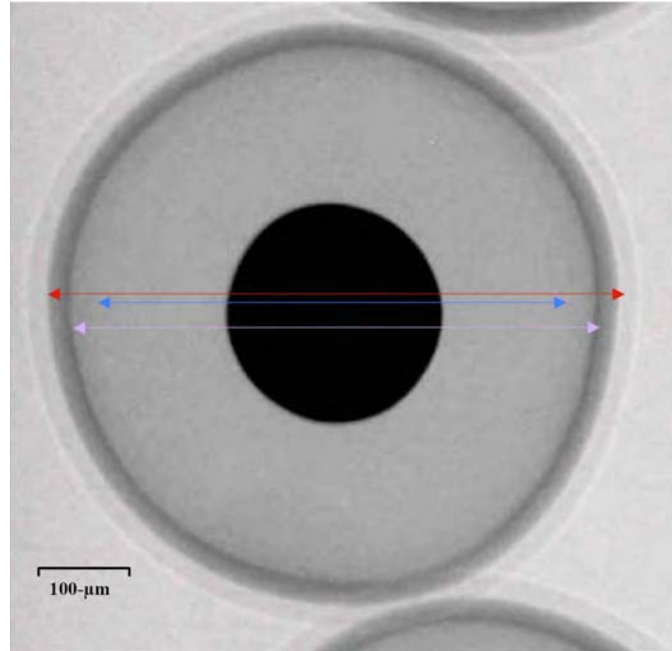
Figure 3.7. Fully Coated TRISO Particle Image

The second approach to achieving higher-speed particle sorting was to radiographically image only those particles that exhibited EM signatures within specific impedance ranges. Both approaches—the radiographic survey and EM-based sorting—were implemented in parallel to quickly determine which approach provided the more effective sorting method.

General Radiographic Characterization

In this second project year, selected samples from all 15 batches of intentionally flawed surrogate particles have been examined to varying degrees, depending upon coating conditions. Particles from some of the coating runs will require additional radiographic examination. The radiographic images were taken using a micro-focus X-ray source with a pixel size typically at 2.5 µm. Standard image mapping was applied to present the 14-bit data in a form suitable for viewing on an 8-bit monitor (typical computer monitor). The X-ray imaging system is further described below appendix to Task 4a.

The characterization process for the first set of particles uses an image manipulation program written at ISU. The dimensions of the particles were measured by averaging 6-10 measurements of the kernel and layers present in a batch. The diameters of the layers were measured and the individual layer thicknesses were independently characterized. Figure 3.8 shows an example of the type of measurements that are made.
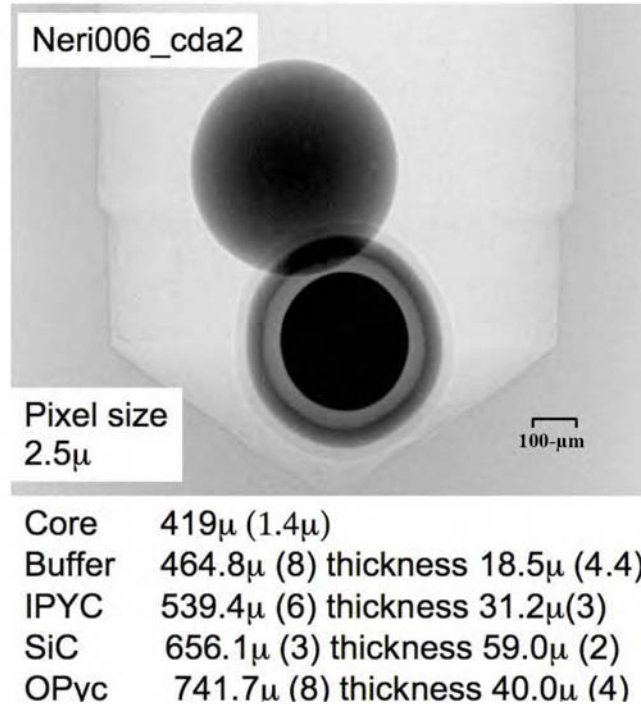
Figure 3.8.   The Upper Object is a Calibration Sample, in this Case a Glass Sphere with a Known Diameter. The Dimensions of the Sphere are Noted

The other type of measurement that is being made is a sorting measurement. In this case, a detailed analysis on each particle is not made; rather each particle is categorized by kernel size into groups labeled as large, medium, and small. Many of the sample batches were made with a wide distribution of sizes about two dominant kernel diameters. There are two important points that directly depend on the kernel diameters. First, the inductive impedance measurements depend on the amount of each layer present. Second, the amount of each layer depends on the initial diameter. Sorting can be done much more rapidly than quantitative sizing; therefore, examining 100-125 particles from each batch is possible. Another example of the image made for sorting purposes is shown in Figure 3.9. The particles are rolled out of the tube and placed in a tray where they are separated into different vials. Sets from batch 5, consisting of ~100 particles sorted into three groups were sent to PNNL.
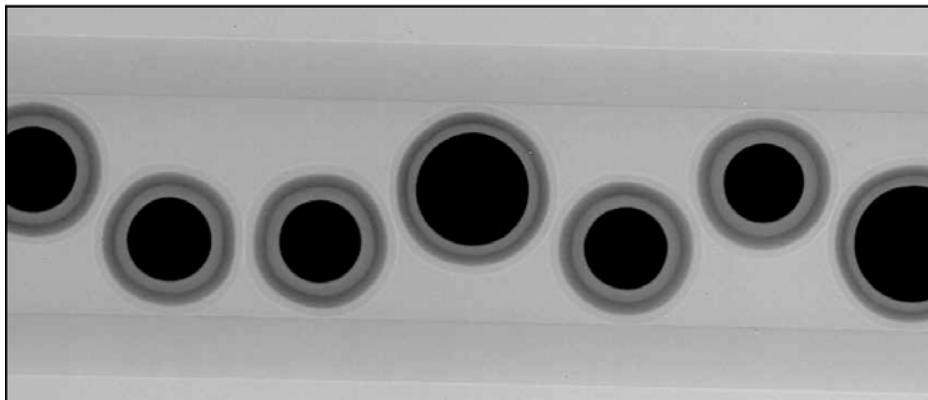
Figure 3.9.   An Example Image Used for Separating Particles by Kernel Size

ISU's image display program was modified for this project. Additions to the program included: 1) a function to compute the distance between two points and to apply a calibration, and 2) a function to calculate the statistical averages and standard deviations. The overall efficiency of layer characterization has improved, increasing throughput by decreasing the time to examine each particle.

More-detailed measurements were performed on several particles from coating runs 3, 5, 6, 12, and 13. Those particles were radiographically analyzed for kernel size and coating layer thickness. Tables 3.4 through 3.7 show kernel diameters and coating layer thickness for particles found to have the inductive impedance signatures that deviated significantly from the norm.

Table 3.4. Dimensions of Selected Particles From Coating Runs 5 (Standard TRISO) and 13 (Thin SiC)

Particle	Kernel (μm)	buffer (μm)	IPyC (μm)	SiC (μm)	OPyC (μm)
r13A1	422.9	85.4	30.2	30.5	30.3
r13A17	340.6	116.4	31.8	28.4	33.3
r13A18	337.9	101.5	29.6	31.9	37.4
r5B2	401.7	101.2	32.8	47.8	36.4
r5B5	393.6	73.4	26.4	47.5	35
r5B10	388.4	112.8	29.9	48.4	27.7
r5B11	335.3	111.6	36.2	54.9	37
r5B18	385.7	103.7	34.4	52.4	38.8
r5B20	327.2	98.2	37.8	56.2	37

Table 3.5. Dimensions of Selected Particles From Coating Run 3 (Standard Buffer and IPyC)

Particle No.	kernel (μm)	buffer (μm)	IPyC (μm)
B11	396	100	28
B12	309.6	111.3	28
B13	397.3	102	25.8
B15	438.9	104.6	23.1
B16	334.3	112	27.2
B17	400.6	106	29.2
B18	378	105.7	27.2
B19	314.8	112.4	55
B20	407	108	27.8

Table 3.6. Dimensions of Selected Particles From Coating Run 6 (Standard TRISO With Thin Buffer)

Particle	Kernel (μm)	Buffer (μm)	IPyC (μm)	SiC (μm)	OPyC (μm)
CD-A2	419	18.5	31.2	59	40
CD-A3	543.2	15.3	26.1	49.4	39.9
CD-A5	507.8	18.1	27.2	53.9	43.5
CD-A9	399.8	26.6	34.1	56.3	41.5
CD-A10	489.1	18.8	24.2	50.1	40
CD-A19	532.6	14.9	23.7	50.4	42.8
CD-A20	423.5	17.9	26	56.1	40.1

Table 3.7. Dimensions of Selected Particles From Coating Run 12 (Standard TRISO With Thin Missing SiC)

Particle	Kernel (µm).	Buffer (µm)	PyC (µm)
012-B1	322.5	124	64.8
012-B3	451.5	120	56.8
012-B4	400	105.8	58.6
012-B5	334.8	116.6	57.9
012-B8	345.4	122.6	68.3
012-B15	287.9	117	56.7
012-B17	340.3	107	59
012-B19	447	111	59

Task 5. INTRODUCE DEFECTS IN SURROGATE PARTICLES

Although initially scheduled to begin in the first project year, this task was deferred until particles with flaws representing those most likely to occur in the coating process have been fully evaluated. The research focus of this second project year was on dimensional defects involving abnormalities in kernel diameter and layer thickness. It is now recognized that surrogate particles offer a sufficient number and range of these kinds of defects without the intentional introduction of additional defects. Examples of existing defects include a thin or missing coating layer and variations in the density and microstructure of the PyC layers.

This task will, however, be evoked as necessary further into the project to produce additional particles with specific defects needed to complete the standard flaw library with multiple particles representing each defect type known to affect fuel performance. Flaws may be produced by using compression to induce cracking in the SiC layer or by using a pulsed laser or ion beam to "drill" micro-pores in the SiC layer.

Task 6. DESIGN, DEVELOP STATIONARY PARTICLE NDE METHODS

The purpose of this task is to evaluate four different NDE methods for their ability to provide 100% in-line inspection. The four methods are:

- Electromagnetic

- UT Resonance

- Acoustic Microscopy

- Optical

The method(s) showing feasibility for meeting the requirements of this application will be further refined, and techniques will be developed for demonstrating in-line QA/QC for each step in the TRISO coating sequence.

Each of these methods uses a different physical principal to interrogate characteristic material properties within the TRISO particle. The optical and EM methods use electromagnetic energy and are capable of functioning at the high throughput speeds (approaching 200 particles/s) required for 100% inspection. The optical method uses light reflected from the surface to provide diameter, shape, and surface-breaking features like cracks and pits. The EM method introduces electromagnetic energy to measure coating

properties below the surface, including coating thickness and microstructural features associated with electrical conductivity signatures. The inductive and capacitive sensors being evaluated use electromagnetic signals at a frequency of approximately 50 MHz. At this frequency, measurements represent the response of the whole particle rather than the signature of a localized flaw within the particle.

The ultrasonic methods (UT Resonance and Acoustic Microscopy) were chosen to interrogate the microstructure of each coating layer. These methods operate at inspection speeds slower than the optical and EM methods so are considered to be potentially most effective in a batch sampling inspection mode (less than 100% inspection) to provide a statistical measure of total defect fraction.

The following is a progress summary for each of these NDE methods.

Electromagnetic

EM Modeling

Inductive and capacitive impedance signatures are expected to respond to defects such as missing layers, layers that are too thick or too thin, asymmetrical layers, and fractures. However, because of the wide range of potential characteristics and combinations of such defects, it is virtually impossible to make a fully representative set of experimental measurements or to interpret the responses of the sensors without the aid of computer modeling. Therefore, this task involves the use of numerical models to: 1) assist in the design and evaluation of appropriate electrostatic and electromagnetic sensors, 2) provide comparative and predictive estimates of sensor responses for a wide range of ideal and flawed particles, and 3) assist in the development of data analysis methods.

The commercial software packages Oersted® and Electro® (from Integrated Engineering Software, Inc.) have been used to examine layer-thickness anomalies that can be oriented such that they are symmetrical about the measurement axis. Off-axis measurements and the detection of asymmetrical flaws were not considered, but can be evaluated using the 3-D versions of the aforementioned software.

Several experimental coil-particle configurations were modeled in FY2003. These involved coils of various sizes, wire dimensions, and numbers of turns. The principal difficulty in obtaining good agreement between measured and computed values of coil impedance for these various configurations is dealing with the effects of the distributed capacitance present in the measurements, but not included in the model. The combination of resistance, inductance, and capacitance leads to a strong resonance in the sensor coil that cannot be directly modeled with the available software. An effective approach is to combine the numerical EM model with an analytical equivalent circuit that includes capacitance. The model is then used to compute the frequency-dependent resistance and inductance of the coil or the coil-particle combination. These values are then used, together with a best-fit estimate of the coil and lead capacitance, to compute the true complex impedance throughout the frequency range of the measurement. Figure 3.10 shows examples of computed and measured impedance curves of a 72-turn coil. One curve shows the impedance of the empty coil; the others show the impedance of the coil containing aluminum balls of sizes consistent with fuel particles.
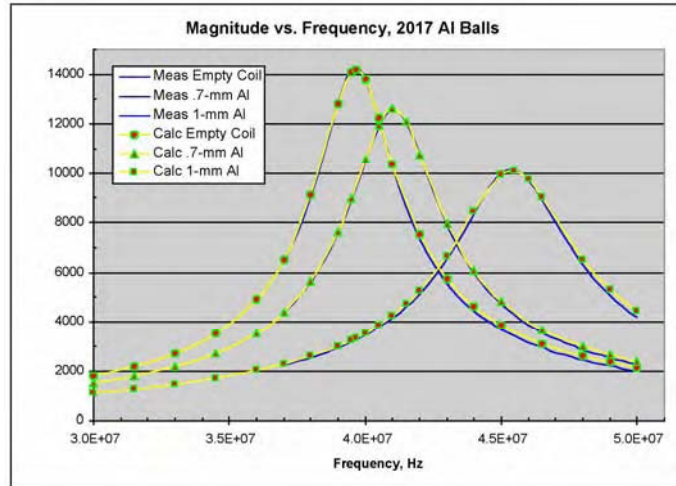
Figure 3.10. Computed and Measured Coil Impedance for the Empty Coil and the Coil Containing Aluminum
Spheres

The numerical model was used to determine the effect on coil impedance when the volume of the carbon
buffer in a fuel particle is held constant while the diameter of the kernel is varied. Results from this
simple example, illustrated in Figure 3.11 shows how numerical modeling can be used to examine issues
that are impractical to investigate experimentally.
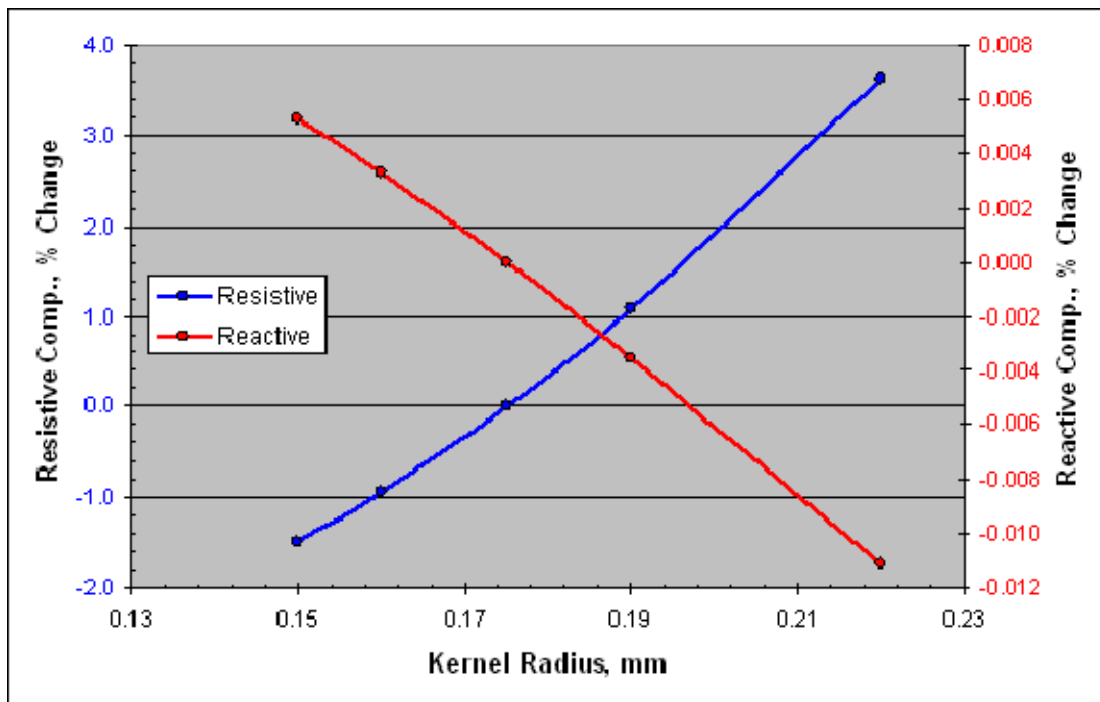
Figure 3.11. Both Coil Impedance Components as a Function of Kernel Radius, Computed at 50 MHz

EM Measurements

Progress in the first half of FY2004 focused on developing and characterizing the sensors found to be sensitive to the wide-ranging variability in the physical properties of particles selected from the initial coating runs at ORNL. Particles obtained last year (in the first year of this project) were coated for other projects, such as coater qualification, but offered a good opportunity to evaluate the initial sensor designs. In this initial evaluation the inductive impedance measurements showed a high degree of sensitivity to particle dimensions, shown by a ratio of sensor volume to the volume constituent materials within a particle—sensor fill fraction. At this early phase of the project, most of the available particles came mostly uncharacterized, the outside diameter being the only property known with certainty.

The inductive sensors were characterized using several different techniques. One technique was to independently measure the coil response to the size and the electrical resistivity of small metal spheres. The results of this procedure are shown in Figure 3.12. The magnitude of coil impedance, measured using an Agilent 4294A impedance analyzer[a], is plotted as a function of frequency for four types of 1-mm metal spheres. Note that the amplitude and frequency of the resonance peak are greatest for the most conductive spheres. This information was useful in observing how the inductive sensor responds to the electrical properties of the coated particles.
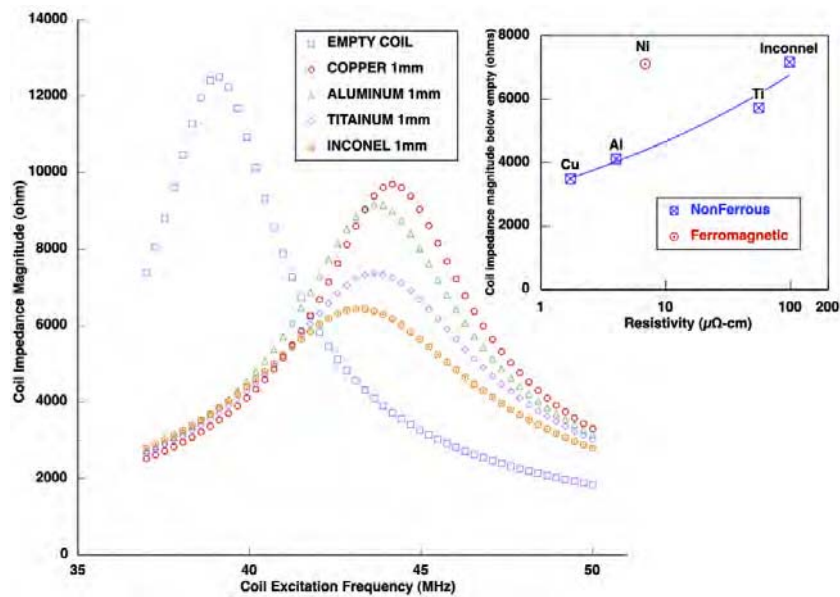
Figure 3.12. Coil Impedance Magnitude Measured as a Function of Excitation Frequency With 1-mm Spheres of Different Metals Inserted into the Coil Sensor. The Inset Plot Shows Change in Coil Impedance Versus Electrical Resistivity

---

(a) The Agilent 4294A precision impedance analyzer was the primary impedance measurement device used for electrical impedance measurements. Its features include measurement over an impedance range from 3 mΩ to 500 MΩ, a frequency range from 40 Hz to 110 MHz, with a basic impedance accuracy of ± 0.08%.

In another series of tests to characterize the inductive sensor for size effects, aluminum spheres were varied in size. The empty coil and the coil loaded with 1-, 0.8-, and 0.7-mm aluminum spheres were measured at coil excitation frequencies ranging from 35 MHz to 50 MHz. The resulting coil impedance components (magnitude and phase) are plotted in Figure 3.13. A uniform monotonic trend toward lower amplitude and greater resonant frequency can be seen as the volume of metal within the sensor increases.
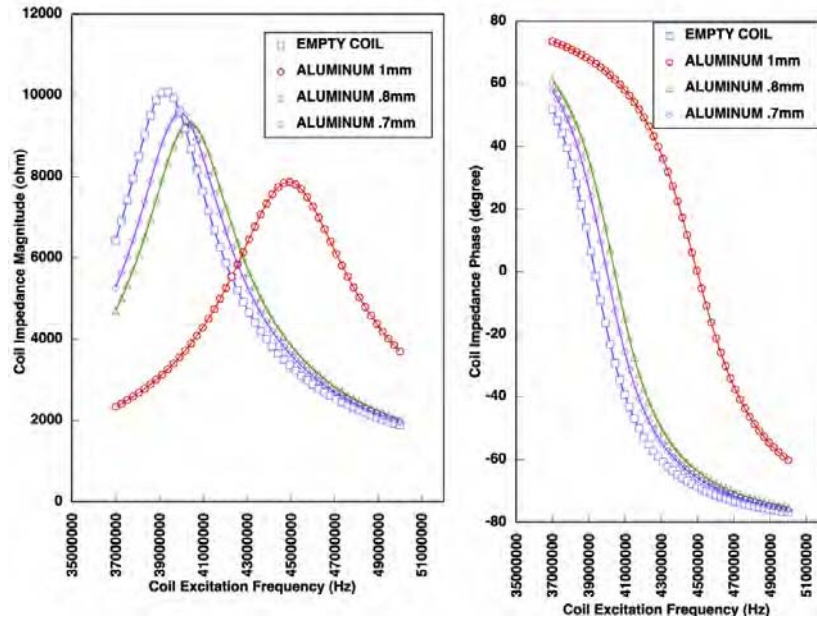
Figure 3.13. Coil Impedance Magnitude (Left) and Phase (Right) Measured as a Function of Excitation Frequency When Aluminum Spheres of Three Different Sizes are Inserted

Separately, these two tests using metal spheres show how the inductive sensor responds to samples of different resistivity and varying size. The results plotted in Figures 3.12 and 3.13 show that both resistivity and size affect the coil response. However, because the relatively conductive layers (buffer and PyC) used to coat TRISO particles are expected to vary over a narrow resistivity range, centered at about 1000 times greater resistivity than the metals used in this characterization test, only the results in Figure 3.13 showing size effects are of primary importance. Furthermore, conductive layer size variation in TRISO particles are expected have much less of an effect on the sensor coil than for a metal since the conductive PyC layers are amorphous semi-metals.

The final coil-sensor evaluation test involved a comparison of various metal spheres with a solid graphite spheroid. Graphite was chosen for this test because it is reasonably comparable to the carbon coating materials in a TRISO particle. The results from this comparative test are plotted in Figure 3.14. As expected, the graphite, with electrical properties roughly similar to some of the layers in TRISO particles, produces a much smaller frequency shift at significantly lower amplitude than metals placed in the same sensor coil.
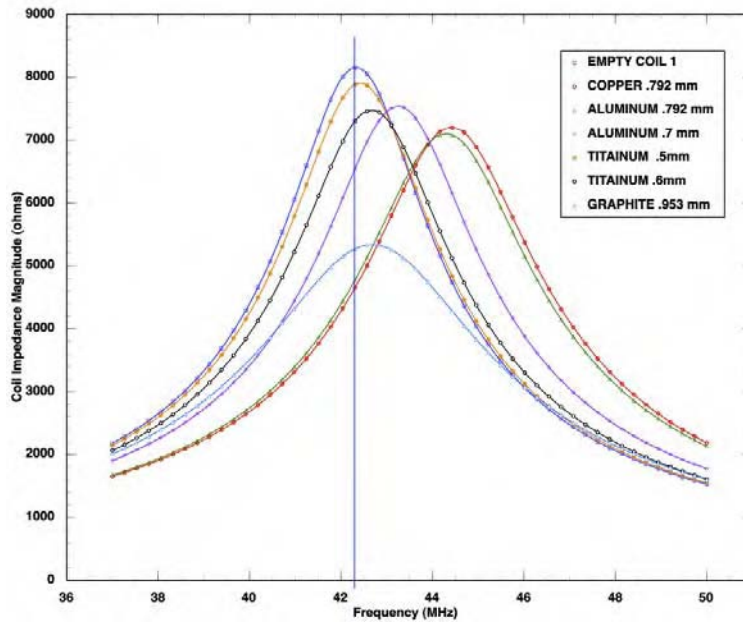
Figure 3.14. Coil Impedance Magnitude Measured as a Function of Excitation Frequency for a Graphite Spheroid and Metal Spheres of Different Sizes and Types

A significant portion of Task 6 was devoted to evaluating the performance of the inductive sensor and refining the capacitive sensor. The basis for this evaluation was flaw detection and discriminating between the standard coating condition and various deviations represented in the defect particle library. Table 3.8 contains a summary of the particles developed at ORNL specifically for this task.

The inductive sensor developed in the first year of this project (and further refined this year) was used to evaluate each batch of particles coated on ZrO_2 kernels, as summarized in Table 3.8. More detailed coating information can be found in the appendix to Task 4.

Table 3.8.   Coating Runs Developed Specifically for This Project at ORNL to Evaluate the NDE Sensors

Run Number	Date Shipped	Desired ZrO$_2$ Kernel Dia. (µm)	Objective
1-B	21-Jan-04	250-450	Compare full buffer with thin Buffer with other layers absent
2-B	23-Jan-04	350-550	
3-B	20-Jan-04	250-450	Compare full buffer with thin Buffer beneath normal IPyC
4-A	23-Jan-04	350-550	
7-A	23-Jan-04	480-520	IPyC coating variants on Kernel
8-A	23-Jan-04	480-520	
9-A	23-Jan-04	480-520	
10-B	10-Feb-04	480-520	Thin IPyC on kernel
14-B	9-Feb-04	620	SiC on Kernel
5-B	17-Feb-04	250-450	Normal TRISO
12-B	20-Jan-04	300-400	Normal TRISO, missing SiC
13-A	17-Feb-04	300 and 400	Normal TRISO, thin SiC
6-CD	23-Feb-04	350-550	Normal TRISO, thin buffer
11-E	11-Mar-04	350	Normal TRISO w/Metal Inclusions

The background colors in this table help to categorize the different basic objectives.

Runs 1 and 2 were coated to evaluate sensitivity in distinguishing missing or thin buffer layers in the presence of large variations in kernel diameter. The inductive sensor was used for this purpose. The procedure developed for this measurement includes placing each particle inside a coil, measuring the maximum impedance magnitude at the coils resonant frequency, and repeating the process after removing the particle. Then the fractional coil impedance magnitude was computed as

$$(Z_0 - Z)/Z_0,$$ a unitless ratio quantifying the change in coil impedance.

Figures 3.15 and 3.16 show the inductive impedance response for 10 different particles from coating runs 1 and 2, respectively. It is clear from these results that thick buffers yield large coil impedance shifts. A 3-9% shift in coil impedance was measured for particles having the full 100-µm buffer coating, whereas particles with less than about 20 µm of buffer coating produced less than a 1% shift. The different groups of curves shown in Figure 3.15 are most likely the result of coating a bimodal distribution of ZrO$_2$ kernel sizes. The larger kernels are expected to produce a larger impedance shift than the smaller kernels because, for a given coating thickness, they have larger buffers. As shown by measurement in Figure 3.13, as the volume of conductive material increases, so will the shift in coil impedance.
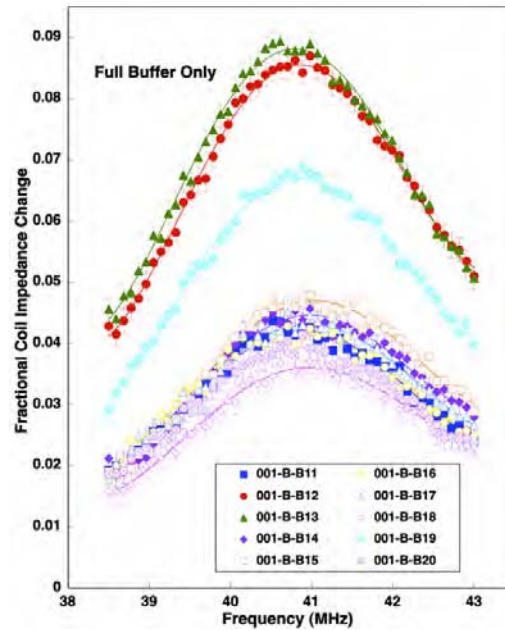
Figure 3.15. Fractional Change in Coil Impedance Magnitude for Particles From Run 1 (Full Buffer Only) Measured as a Function of Excitation Frequency
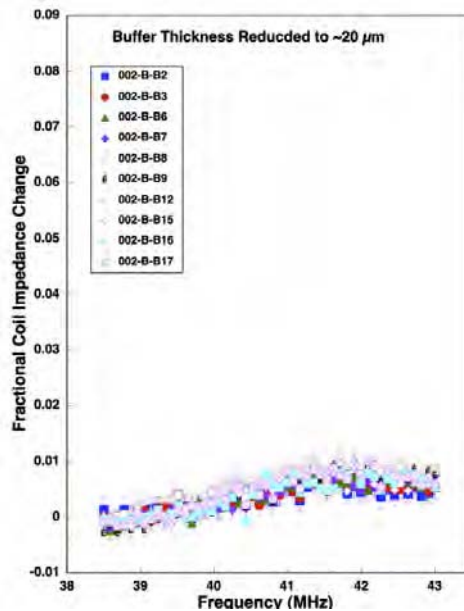
Figure 3.16. Fractional Change in Coil Impedance Magnitude for Particles From Run 2 (Reduced Buffer) Measured as a Function of Excitation Frequency

The particles produced in coating runs 3 and 4 of Table 3.8 were also evaluated using the inductive sensor to determine if a thin buffer could be detected beneath a normal IPyC coating. The plots shown in Figure 3.17, compared with those of Figure 3.18, show that coil impedance is reduced when there is a thin buffer beneath the normal IPyC coating. Again, for both coating conditions, a bimodal distribution of impedance curves resulted from the 50/50 mixture of two difference average kernel sizes into the coating process.
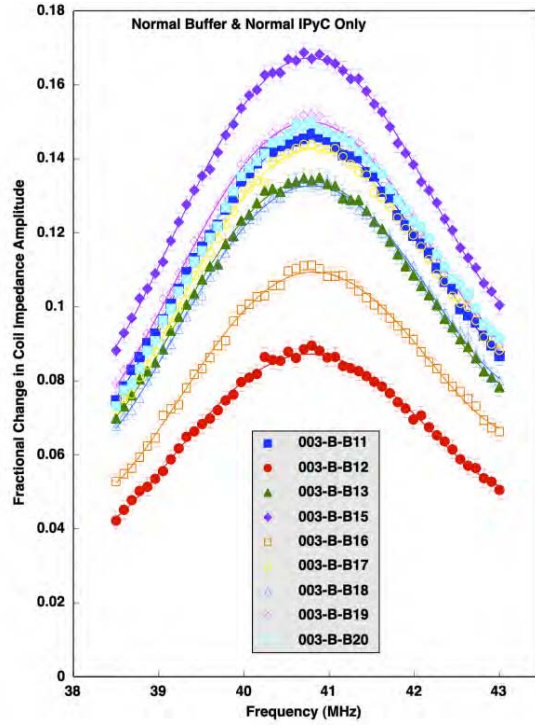
Figure 3.17. Fractional change in coil impedance magnitude for particles from run 3 (full buffer beneath full IPyC) measured as a function of excitation frequency
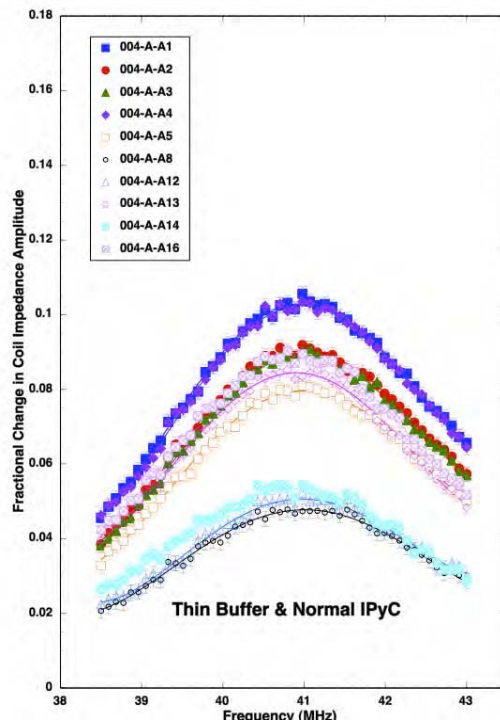
Figure 3.18. Fractional Change in Coil Impedance Magnitude for Particles from Run 4 (Thin Buffer Beneath Full IPyC) Measured as a Function of Excitation Frequency

In comparing the results from Figure 3.18 (thin buffer beneath normal IPyC) with Figure 3.15 (full buffer with no IPyC), it is noted that the results overlap. This could cause an automated inspection system to confuse the two conditions. However, particles would typically be inspected either after each coating is applied or after all coatings have been applied. In either case, a unique coil impedance is expected. In the first case, the thin buffer would be detected as suggested by the results shown in Figures 3.15 and 3.16. In the latter case, the thin buffer condition would most likely also result in smaller-diameter SiC and OPyC layers as well. Therefore, the overall diameter would be reduced and the effects of less SiC and OPyC should be detected by an abnormal value of inductive impedance, capacitive impedance, or overall physical size.

The bar chart of Figure 3.19 compares the coil impedance values for coating run 3 with those for run 4. Overlap does exist for this particular set of two coating conditions. However, it occurs only because such a wide-ranging set of kernel diameters was chosen. In a production setting, the kernel size would be controlled for much tighter tolerances.
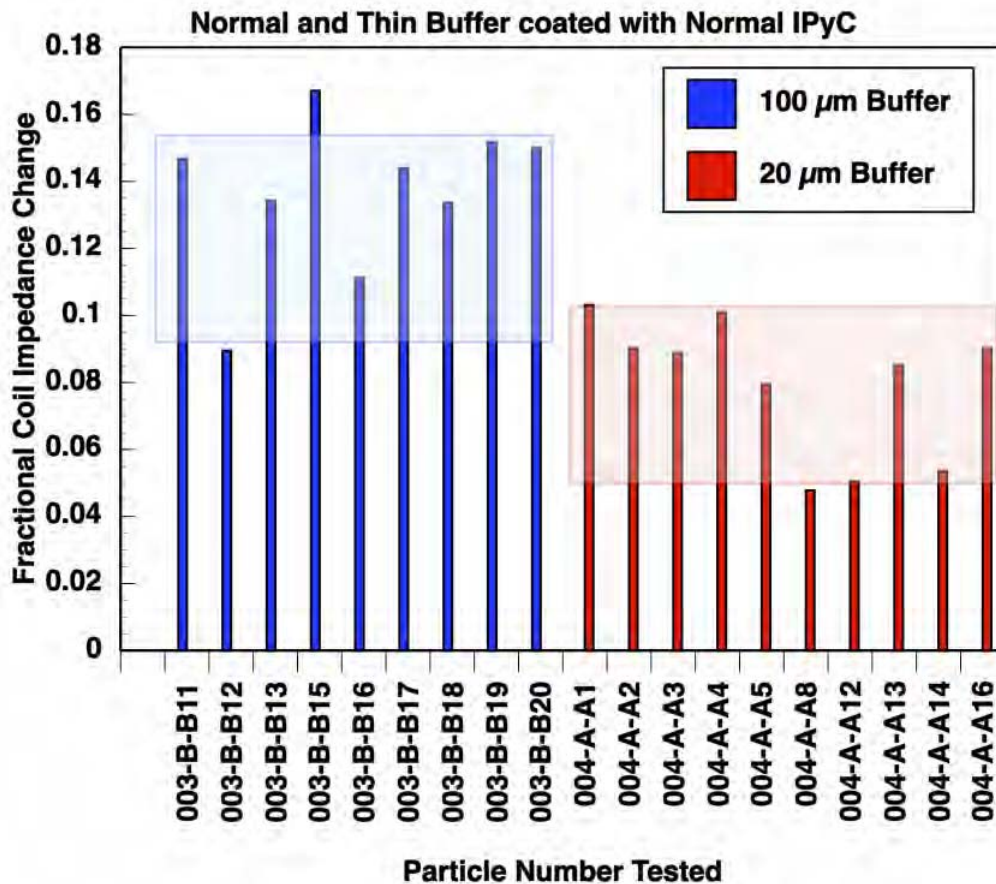
Figure 3.19. Maximum Fractional Change in Coil Impedance Magnitude for Particles in Run 3 (Full Buffer Beneath Full IPyC) Plotted Side-by-Side With Particles from Run 4 (Thin Buffer Beneath Full IPyC)

Radiographic images were obtained for several of the same run-3 particles that were analyzed in the inductive sensor. This was an effort to discover the relationship between inductive impedance and layer dimensions. The results of this investigation are graphically displayed in Figure 3.20, where the kernel

and layer diameters are plotted against the fractional inductive impedance values. The radiographic images provided the diameters of the kernel, buffer, and IPyC layers. As shown in Figure 3.20, linear regression between these two sets of measurements gives R^2 correlation coefficients of 0.491 for the kernel diameter, 0.533 for the buffer diameter, and 0.926 for the IPyC diameter. The relative magnitude of the correlation coefficient for each diameter suggests that the coil is most sensitive to the IPyC layer for this particular coating condition. This may not necessarily be the case for thinner IPyC layers, thicker buffer layers, or different sized kernels.
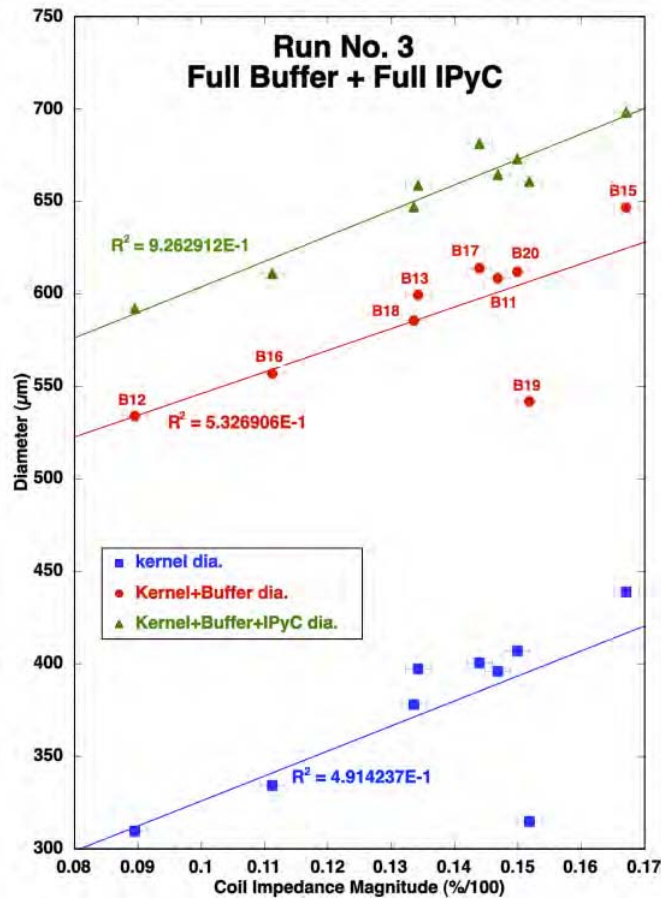
Figure 3.20. Maximum Fractional Change in Coil Impedance Magnitude for Particles from Run 3 (Thin Buffer Beneath Full IPyC) Plotted Versus Radiographic Kernel and Coating Layer Diameters

Coil impedance measurements were performed on particles from coating run 10 with limited success. The IPyC coatings, purposely thinned to about half the normal value of 40 μm, had difficulty adhering to the ZrO_2 kernel and tended to flake off inside the coil or when they were handled.

Particles from coating run 14, with a SiC layer deposited directly on the ZrO_2 kernel, were examined using the inductive sensor. The measured impedance shift was within the noise for this technique, indicating that virtually no impedance shift occurs in the presence of either of these two nonconductive materials.

Several measurements were performed on particles from coating run 11—particles coated to introduce iron impurities. These measurements are part of a study to determine if in-line measurements of the electrical properties of a TRISO fuel particle can reveal the presence of the iron (metal) compounds found in the coating process and in irradiated particles. The impedance values observed for particles from run 11 were the same as those from run 5. Two possibilities could account for this finding. Either the iron/metal component is below the detection threshold, or, the iron was present in a nonconductive/nonmagnetic phase.

Results from SEM and TEM analyses conducted at ORNL on several fractured particles indicated that no iron was present, consistent with the null result obtained using the inductive impedance sensor. Additional coating runs, further refined to produce particles having iron defect impurities are necessary to evaluate the ability of the NDE methods to detect such flaws. However, the importance of this particular defect, relative to the other more common defects, must be balanced against project resources. Considering the fact that defects resulting from metal impurities are of a lesser concern than those arising from dimensional irregularities, the remaining efforts of this project will focus primarily on developing methods for automated detection of dimensional defects.

A series of four coating runs produced particles to simulate the standard TRISO particle and three coating variations considered to be defective. Coating run 5 supplied the standard TRISO surrogate particles, with variations only in the kernel size. In run 6, normal IPyC, SiC, and OPyC layers were deposited on a thin buffer. The SiC layer was deliberately not applied to particles in run 12, and was applied at only half the normal thickness in run 13.

Inductive measurements were recorded for 20 randomly selected particles from each of these four coating runs. Figure 3.21 shows the peak inductive impedance responses for those particles in. The particles with thin buffers yielded lower values of coil impedance than the normally coated TRISO particles. However, some of the particles with missing SiC layers (and a few with half-thickness SiC layers) exhibited coil impedance values falling within the range found for the normally coated particles. This occurred because kernel size has a large effect on the coil impedance, as seen in the 7% deviation among run 5 particles. In all of these coating runs, the same bimodal kernel size distribution was used. If kernel size were held to within ±8 µm of a central value, then the four coating conditions would be expected to produce four unique groups of impedance values.
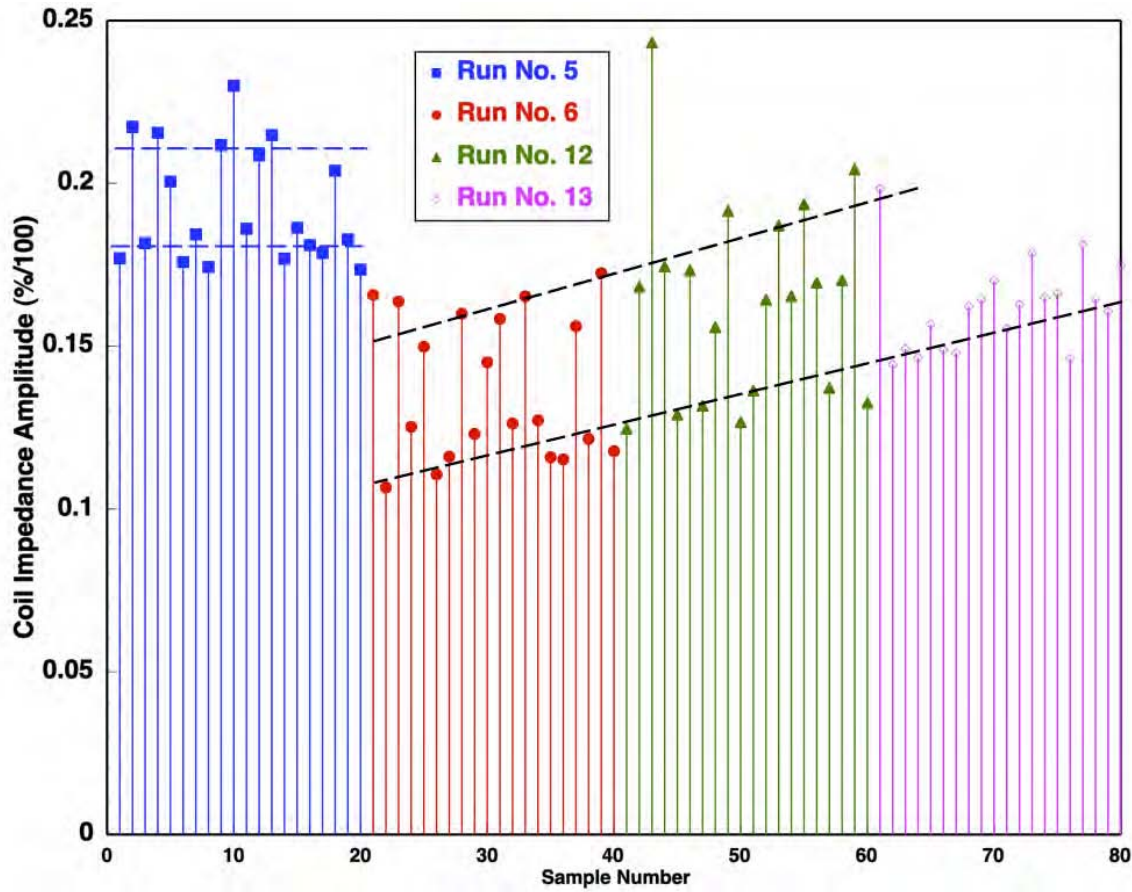
Figure 3.21. Maximum Fractional Change in Coil Impedance Magnitude for 20 Particles from Each of Run 5 (Standard TRISO Surrogate), 6 (Thin Buffer), 12 (No SiC), and 13 (Thin SiC)

About five particles from each of runs 5 and 13, displaying the average and most extreme impedance responses in Figure 3.21, were radiographically analyzed to obtain their dimensions. The relationship between the inductive impedance response and the diameter of each coating layer is shown graphically in the plots of Figure 3.22. The inductive impedance appears to be more strongly related to the buffer and IPyC diameters than to other dimensional parameters.
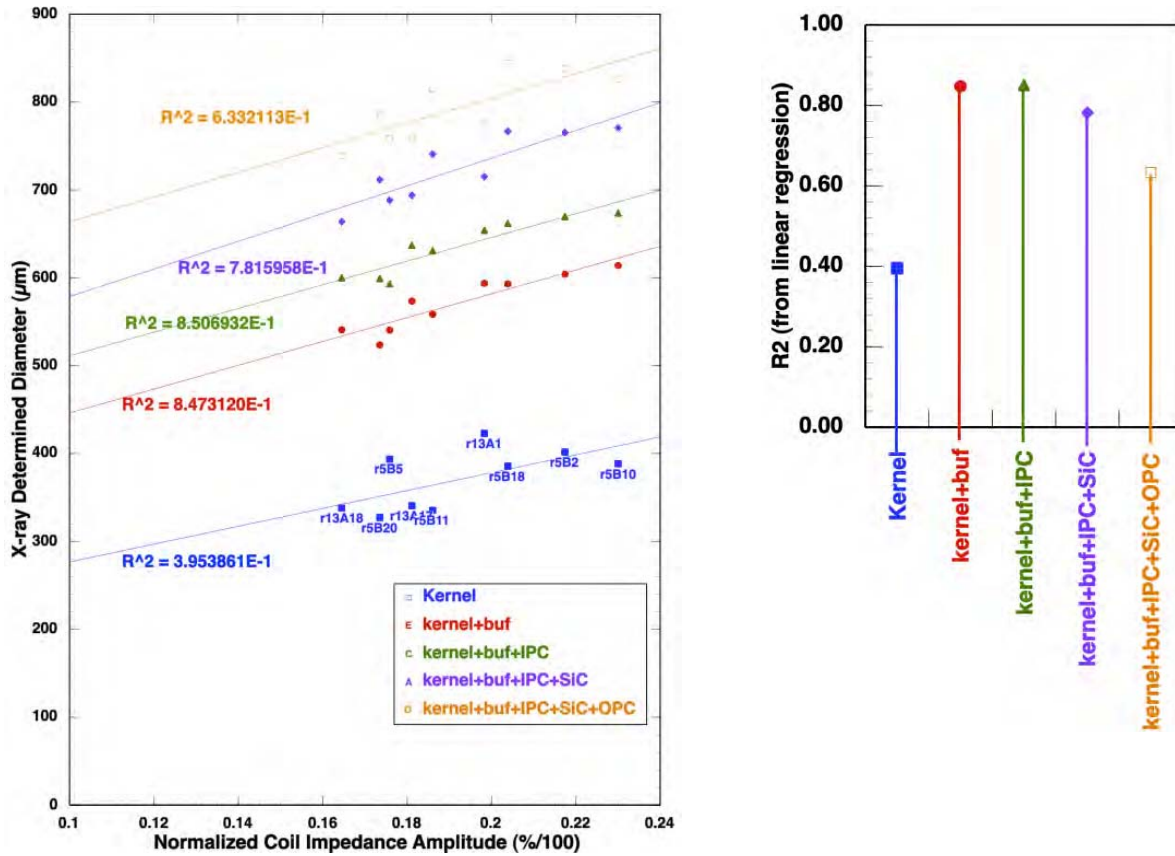
Figure 3.22. Peak Coil Impedance Versus Each Coating-Layer Diameter from Coating Runs 5 and 13 (left). Run 5 is Designed to the Standard Values for TRISO Fuel, and 13 Has a Thin SiC Layer. The Plot to the Right Compares R^2 Values Computed from a Linear Regression Analysis of Coil Impedance Amplitude and Each Layer Diameter

Coating runs 7, 8 and 9 were designed to evaluate the ability of NDE methods to detect variations in PyC coating properties such as porosity (density) and anisotropy. The coating gas fraction typically controls these physical properties. This parameter was varied, as shown in Table 3.11, in producing these three coating runs. Coil impedance measurements, obtained for several particles selected from these three coating runs, are shown in Figure 3.23. The average measured coil impedance amplitude was larger for particles from run 7 than for particles from runs 8 and 9. The percentage variation in kernel size was small compared with the percentage changes in PyC coating thickness among the three runs.

When the process parameters (gas fractions) were selected for these three runs, the intent was to produce coatings having diminishing density (increasing void volume) and crystallite anisotropy. However, measured values of density and anisotropy are inconsistent with the expected results and appear to indicate that all three runs produced PyC layers of about the same density and anisotropy. One hypothesis currently being explored at ORNL proposes that the buffer and SiC layers must be present before the expected density and anisotropy changes in the IPyC layer will occur.

The lower average coil impedance amplitude seen for particles from runs 8 and 9 (compared to run 7 seen in Figure 3.23) is most likely due to a thinner PyC coating. It may also be possible that particles from run

8 or 9 do have a PyC coating of slightly lower density. Without additional density measurements of higher accuracy, it is not possible to determine how density variation affects the coil impedance measurement.
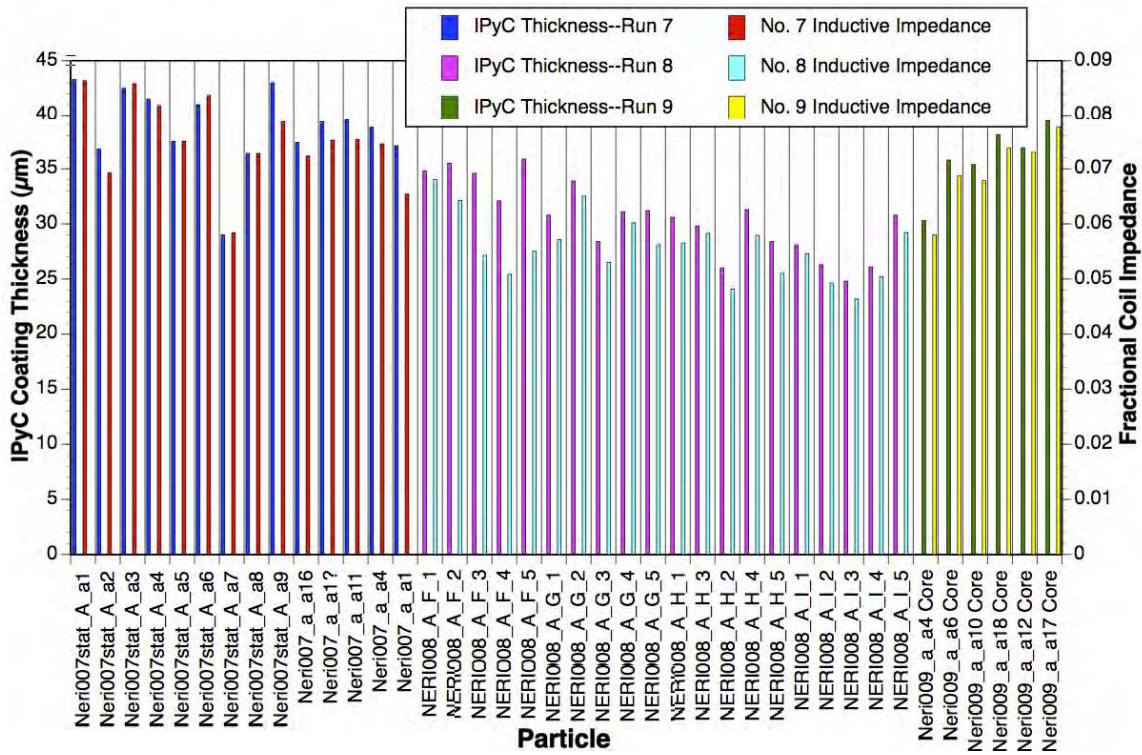
Figure 3.23. Fractional Coil Impedance Measurements (right axis) and Radiographic IPyC Coating Thickness (left axis) Are Compared for a Random Selection of Particles From Coating Runs 7, 8, and 9

Note in Figure 3.23 how the measured values of IPyC coating thickness and fractional coil impedance measurements follow the same trend. This trend is explored further by linear regression in Figure 3.24. This is one of the few examples where coating thickness is highly correlated with an impedance measurement. Measurements from runs 7 and 9 have R^2 correlation coefficients of 0.84 and 0.98, respectively. In most other cases, only the coating diameter is found to correlate with the impedance measurements. This is due to the presence of only one conductive coating layer being present to interact with the coil. When more layers are present, the overall coil response is the sum of the contributions of all of the layers. The weaker correlation between the measurements for particles from run 8 may be a result of another material property affecting the coil impedance values.
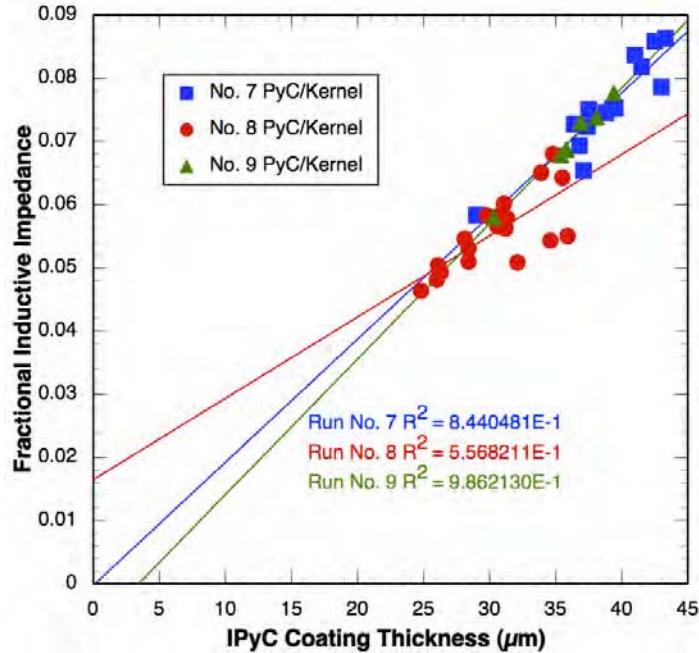
Figure 3.24. IPyC coating Thickness Measurements Plotted Against Coil Impedance. The R^2 Values From Linear Regression are Shown

In coating run 14, SiC was deposited with a target thickness of 35 µm. Figure 3.25 shows that about 35 particles from this coating run had an average SiC thickness above this value, at 41.3 ± 2.4 µm. A possible cause for the SiC thickness reaching values above the target value could be related to a larger-than-expected kernel diameter. The coating process parameters were selected assuming a kernel diameter of 650 µm, whereas the average kernel diameter was measured to be 692.5 ± 2.5 µm. This conclusion is consistent with the trend shown in Figure 3.25, where, on average, SiC layer thickness appears to increase with kernel diameter.
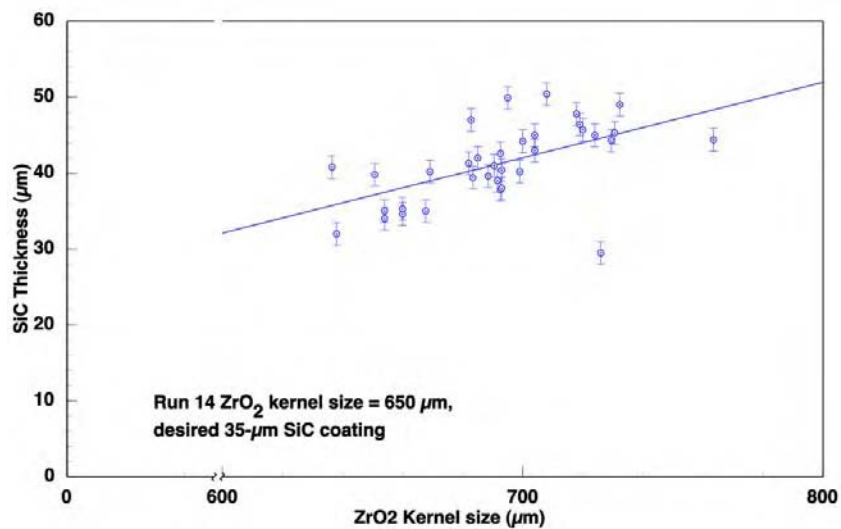
Figure 3.25. Radiographic Measurements of Both Kernel Diameter and SiC Coating Thickness Plotted Against Each Other

The in-line sensor method being evaluated for interrogating the nonconductive materials in the TRISO particles relies primarily on the electric field introduced by a capacitor. A very simple sensor design has shown results consistent with theory.

The measured values of capacitive impedance plotted in Figure 3.26 show that this method is sensitive to the diameters of both the kernel and the SiC coating. The capacitive impedance produced by the uncoated kernel is much lower than that produced by a kernel coated with SiC.

The measured capacitance is also increased by a dielectric kernel, but the increase is less than that produced by a conductive body or shell of the same volume. This is demonstrated by the data plotted on the right side of Figure 3.26. As the ZrO2 kernel diameter decreases toward 300 μm, the impedance decreases, as it should. The fact that it appears to decrease to zero at a kernel diameter of 300 μm is the result of measurement error/uncertainty and a small number of data points.
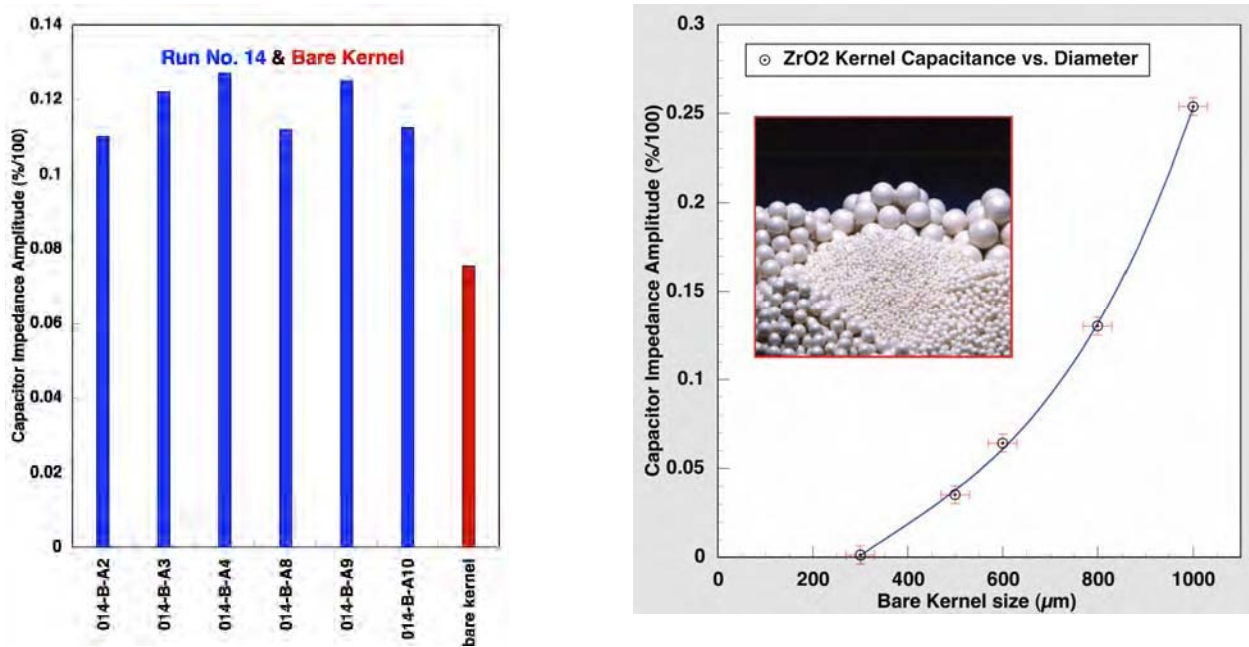
Figure 3.26. Fractional Capacitive Impedance Measurements of a Bare 650-μm Kernel Compared with Several 650-μm Kernels of Coating Run 14 Coated with SiC (left), and ZrO_2 Kernels Ranging is Size From 300 μm to 1000 μm (Right)

More than 10 particles from each of coating runs 5 and 12 were measured using both the inductive and capacitive sensors. The results from these measurements are plotted in Figure 3.27. Even though the kernel size effects can be seen throughout all four measurement groups, it is interesting to note that the capacitive impedance measurements diminished by a larger amount between particles from run 5 to run 12 than did the inductive impedance measurements between particles from these same two coating runs.
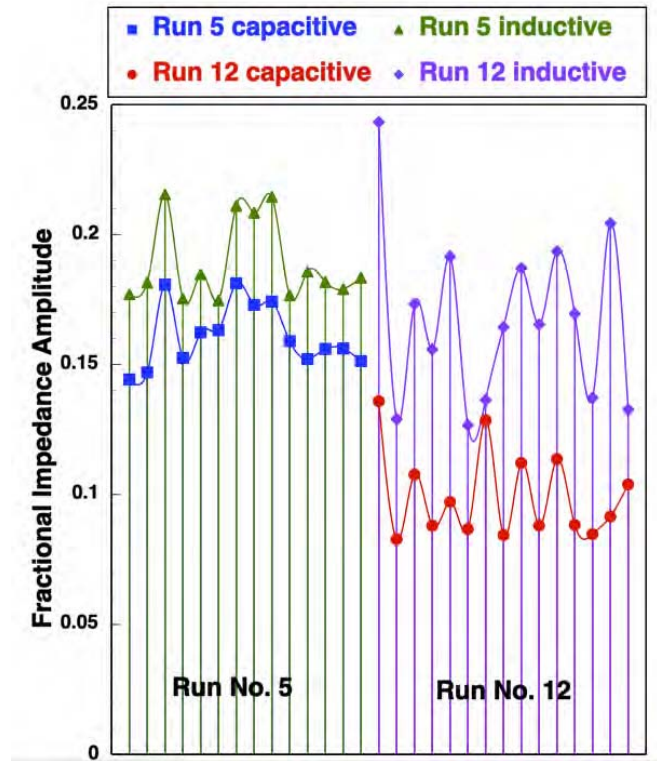
Figure 3.27. Fractional Capacitive and Inductive Impedance Measurements for Particles From Coating Run 5 (Standard TRISO) and Coating Run 12 (No SiC)

A modification of the original coil design was implemented to simplify the high-speed particle inspection process and to provide greater resolution. The primary improvement includes a capacitive sensor, positioned side-by-side with the inductive sensor. A drawing of this newer concept is shown in Figure 3.28. This design improved the sensitivity and accuracy of the capacitive volume measurements.
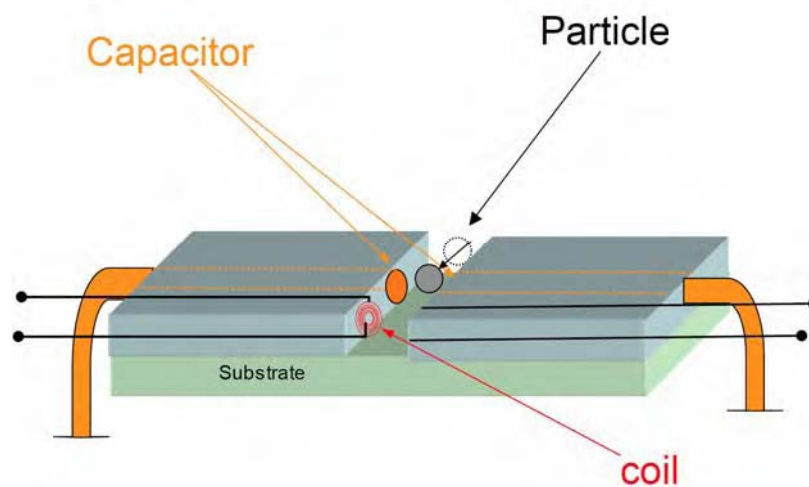
Figure 3.28. Capacitive and Inductive Impedance Sensor Design Where Both Measurements Take Place Sequentially as Particles Flow Through a Groove

Conclusions from EM Measurement Methods

The electrical impedance measurements obtained on surrogate-coated particles suggest several conclusions:

1. Significant reductions in buffer coating thickness can be detected either with or without a PyC coating layer present using the inductive impedance measurement. See results from coating runs 1, 2, 3, and 4.

2. PyC coating layer thickness correlates with inductive impedance measurements. See results from coating runs 3.

3. Although sensitive to kernel size, the inductive sensor can detect a thin buffer layer or a thin or missing SiC layer in the fully coated TRISO particle when these conditions occur separately. This may not be the case if multiple defects occur simultaneously. The inductive impedance response due to a reduction in SiC layer is most likely caused by a reduction in the OPyC layer diameter.

4. The buffer and PyC layer diameters are highly correlated with the inductive impedance measurements.

5. When kernel diameter is held relatively constant, a single buffer or PyC layer thickness is highly correlated with inductive impedance measurements.

6. The addition of a SiC layer to the kernel significantly increases the capacitive impedance measurement.

7. The absence of the SiC layer has a sizeable effect on the capacitive impedance of fully coated TRISO particles. See results from coating runs 5 and 12 in Figure 3.27.

The results from electrical impedance measurements also suggest that if the kernel size is held constant (using the capacitive impedance measurement in a sorting operation before coating) that it is likely to detect deviation in one of the dimensional parameters. Using both inductive and impedance measurements, it may even be possible to detect a thin SiC layer in the presence of a thin carbon layer. However, if there are three or more dimensional parameters simultaneously out of control, then even the combined inductive and capacitive impedance measurements may not be enough to detect all defects. One potential solution that avoids having to detect multiple interfering defects is to perform the inspection after applying each coating layer, or at least after every two coating layers.

An example coating/inspection operation would be to:

1. Sort kernels into bins by size (±5 μm) using capacitive impedance measurement.

2. Coat kernels with buffer, IPyC, and SiC then perform 100% inspection with inductive and capacitive measurements.

3. Finally, apply OPyC layer and inspect 100% with inductive impedance measurement.

The distribution width of the electrical impedance measurements for a large batch of particles may also prove to be a useful quantitative measure of batch uniformity and quality.

UT Resonance

The goal of this subtask was to evaluate the feasibility of utilizing an ultrasonic resonance technique to measure the physical properties of TRISO particles. The characteristic resonance of rigid bodies contain information regarding their structural properties and shape. As part of these properties, the structure and make up of each layer affects the characteristic resonance frequencies that develop when a particle is excited with acoustic energy. In addition, the elastic moduli are expected to contribute to the resonant frequencies of a particle. In principle, all of these parameters can be determined. However, if several parameters were to change simultaneously or affect the resonant frequency in the same way, then determining the specific properties that have changed can be problematic. For QA/QC, the resonance technique may be ideal due to its high sensitivity to several important properties of the TRISO particles such as the thickness and composition of each layer. These results will be utilized to help determine the quality of TRISO particles during production.

This task has three activities:

1. A literature review to assess current resonance theories for predicting the resonant frequencies of spherical particles.

2. Calculations of the resonant frequencies of TRISO particles to predict the expected changes in frequency for various changes to the particle layers.

3. Experimental measurement of the resonant ultrasound spectra of spherical particles to determine the limits of the current system and to provide guidance in developing alternate measurement methods if needed.

Literature review and modeling

The literature review was completed under Task 1 and the modeling work was completed under Task 2, both in the first year of this project.

Experimental measurements:

In FY2003, studies were performed to determine the sensitivity and frequency limits of the current ultrasonic resonance system at PNNL using the standard configuration. This study found that the existing sensor did not have sufficient resolution to measure the material properties of interest. The mass ratio between the transducer and TRISO particles is too large. Two paths were pursued in FY2004 to overcome this limitation:

1. Investigate the use of electromagnetic acoustic transducers (EMATs) to eliminate contact effects. Initial attempts to explore this option showed a very low probability for success due to the low electrical conductivity of the PyC in the TRISO particles. The electrical conductivity is a necessary requirement for coupling energy between the particle and the transducer, so insufficient energy coupling can occur to interrogate TRISO particles. Therefore, this option was deemed infeasible.

2. Evaluate custom contact transducers. Interactions with several other laboratories suggested that a commercial system currently available to this project could be fitted with a smaller, less massive

transducer. A transducer arrangement thought to be appropriate for this task was located, and particles having various coating conditions were sent to the manufacturer for a preliminary, pre-purchase evaluation. The test results showed apparent spectral features that may be unique to each coating combination; however, background noise and multiple particle testing will be required before conclusions can be drawn.

Progress has been limited by having to request time on equipment owned by other laboratories. A one-day limited test was conducted to determine if the abundant, but variable, spectral features observed among multiple particles were repeatable for a single particle. The results were uncertain due to the constraints on modifying equipment owned by another laboratory. The fixture is the same as the one previously used at DRS International, LLC.

Acoustic Microscopy

The objective of this task was to evaluate an acoustic microscopy approach to characterizing coated surrogate fuel particles—determining the feasibility of acquiring measurements such as layer thickness, material properties, and detecting localized changes in microstructure. Initially, before coated particles were available, glass spheres were examined using this method. Working at 50 MHz it was possible to see gross differences between a damaged and an undamaged glass sphere. The diameter of the sphere was also determined to within about 50 μm.

As this work progressed, preliminary measurements confirmed the need to work at the extreme high end of the frequency range for ultrasonics -- above 250 MHz, and perhaps as high as 1 GHz -- to have wavelengths short enough to image and resolve the tens-of-micron-size defects in the TRISO coated particles. It may be possible to work in this frequency range, but such an effort requires a larger investment than was proposed for this task.

However, calculations suggest that by removing the requirement to image defects and focusing on detecting flaws, it may be possible to obtain valuable results at 50 MHz.

An ultrasonic experiment was performed to evaluate the defect detection concept using the following:

1. A reference experiment (immersion) was performed on a 12.93-mm thick glass slab and the reflected signal was obtained. Sampling rate for the digitized signal was 1 GHz. A 50-MHz broadband transducer was used. The water path was adjusted so that the focus was at the surface of the slab. The water temperature was maintained at 50°C to reduce the attenuation of the ultrasonic beam. Let $\beta(f)$ be the frequency dependent transducer efficiency and $D(f)$ be the frequency dependent diffraction correction for the beam, with Γ_{ref} being the received signal from the front surface of glass slab. Then $\Gamma_{ref}(f) = \beta R_{w,g} D(f) e^{-i2k_w z_w - 2\alpha_w z_w}$. Here k_w is the wave number in water, $R_{w,g}$ is the reflection coefficient of plane waves at the water-glass interface, and α_w is the frequency dependent attenuation in water.

2. Under identical experimental conditions and equipment settings, a front surface reflection signal was obtained for a representative 0.81-mm TRISO particle. It is well known from the theory of reflection and transmission of acoustic waves through layered media that if $h < c\Delta t / 2$ (h is the thickness of a layer, c is the speed of sound in that layer, and Δt is the width of the pulse), the reflection coefficient

is a function of both layer thickness and frequency. The received signal can be described as $\Gamma_{TRISO}(f) = \beta R_{w,TRISO} D(f) e^{-i2k_w z_w - 2\alpha_w z_w}$. Thus, $R_{w,TRISO} = R_{w,g} \times \Gamma_{TRISO} / \Gamma_{ref}$. Since we know $R_{w,g}$ and also $R_{w,TRISO}$ from theoretical analysis, we have a quantitative relationship between measured Γ_{TRISO} and properties of the layers inside the TRISO particles.

3. Representative experimental data are provided in Figure 3.29. The depressions in the received signals are a function of layer elastic properties and thickness.
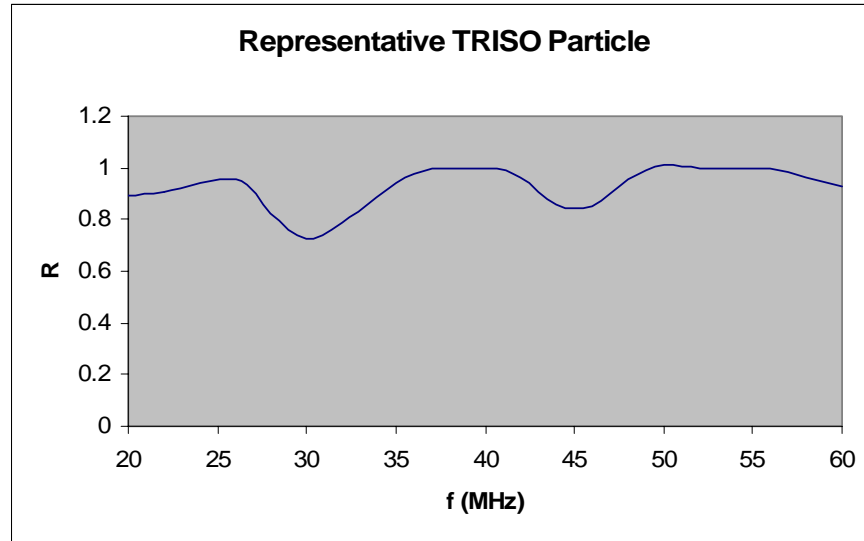
Figure 3.29. Reflection Coefficient as a Function of Frequency

Although the data contain interesting features, no conclusive evidence was found to support further development of this subtask in the sub-200-MHz frequency range. Measurement results on particles with known defects do not seem to vary enough from corresponding results on particles without defects to provide detection. Therefore, this task is being suspended in favor or the other tasks showing evidence for achieving the project objective.

Optical

The objective of this task is to investigate and develop instrumentation, algorithms and procedures for characterization/inspection of fuel particles using optical imaging methods. Two parallel paths of investigation had originally been proposed within the scope of optical inspection 1) profilometry and 2) image analysis. Optical profilometry was set aside upon learning of other NERI projects (at ORNL) developing a similar capability. The image analysis approach is being investigated along two parallel paths at PNNL aimed at automated characterization. One path focuses on off-line (static) laboratory scale characterization, and the other focuses on in-line inspection.

Methods for static image digitization of particles were developed to support the evaluation of requirements for automated systems, including resolution issues and hardware issues driven by production requirements. The result was a practical approach to digitizing images of individual particles

using an available optical microscope with images recorded using a "prosumer" digital camera, and image processing with a commercial image processing and analysis software package. Images of particles in the 700-1000-µm diameter range were digitized and processed to provide an extended depth-of-field image at a resolution adequate for features on the order of ≤ 5 µm to be easily measured, and for surface anomalies on the order of a micron or two to be easily detected.

The methods used for the initial results were refined, and following a decision to emphasize off-line automated characterization, hardware was identified and algorithm development started towards an off-line automated digital camera/microscope system for image digitization and automated characterization of particle surface features. An idle Leica Egolux microscope (computer controlled X-Y-Z axes) procured for a previous project was identified and steps were taken to prepare it for use in this task.

Since depth-of-field decreases as magnification increases, and increased magnification is needed to achieve higher resolution with a fixed pixel-count sensor, achieving sharp enough focus over a 0.5-mm depth at moderate magnifications is a challenge. A CARS (coherent anti-Stoke Raman spectroscopy) microscope was found to be available for use on this project. A few test images of one particle were made at very high resolution to illustrate potential (non-SEM) high-resolution optical imaging. An image with sub-micron resolution was achieved, revealing features easily measurable at the sub-micron scale.

High-speed in-line inspection was investigated in parallel with other activities. Detectors were researched and identified for use in a multi-camera, multi-line-of-sight concept for providing high-resolution images of particles on the fly, at speeds sufficient for parallel lines to achieve a throughput of 200 particles/sec. Actual resolution requirements for inspection are not yet defined.
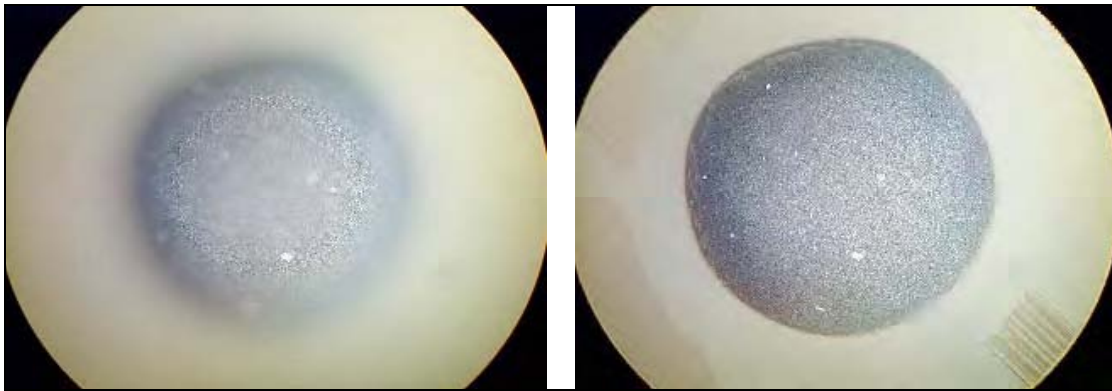
Figure 3.30. TRISO Particle with 10X Optical Microscope. a) A Slice at a Depth From the Top of About 1/3 the Radius – Notice Anular Ring of In-Focus Surface. b) A 28-Image Composite. The Image Dimensions are 1280 x 960 Pixels, or 1675 µm x 1256 µm. The Largest White Feature is About 35 µm x 31 µm
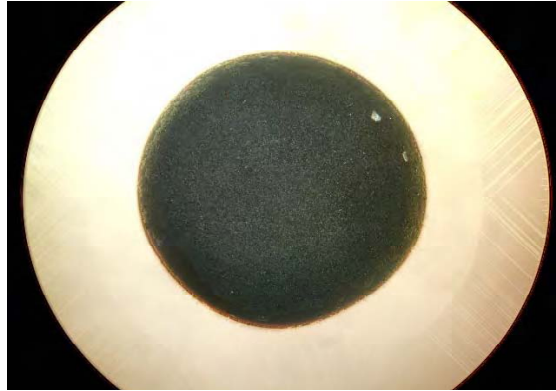
Figure 3.31. TRISO particle under 10X objective and optimized illumination; composite image includes 35 image slices. The image dimensions are 2560 x 1920 pixels

Improved image capture

Illumination and exposure were refined to capture images at the camera's full resolution of 2560 x 1920 pixels. Figure 3.31 shows an example of a composite particle image with the optimized capture settings. The 30 to 35 image slices used for the composites include many redundant slices because the in-focus region overlaps among the slices. Throughput can be increased, while retaining image quality in the extended depth-of-field image, by selecting as few slices as possible. In this case, the number of image slices was reduced by selecting a sharp first image slice at the top surface, a sharp image slice at the mid-height of the particle (to provide a sharp edge of diameter measurements) and as few as two or three additional intermediate slices.

With the improved illumination and exposure, images were also made of groups of particles to demonstrate multiple particle capture at lower magnification. The image shown in Figure 3.32 is a composite image including four particles.
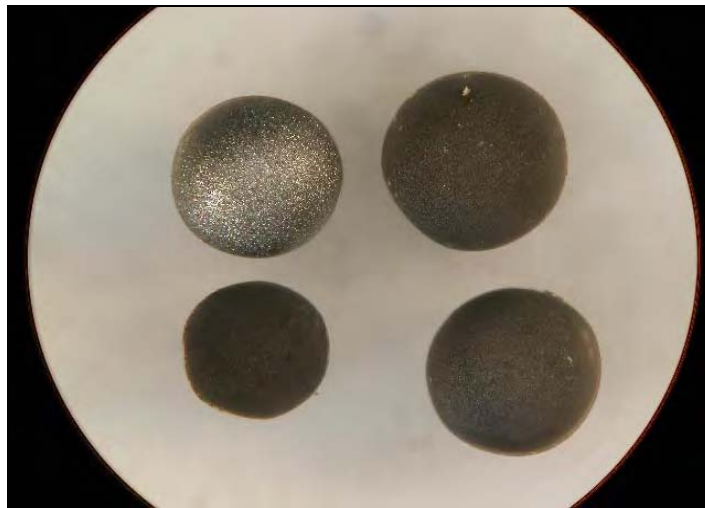
Figure 3.32. Composite Image of Four Particles at 5X, Including a SiC Coated Particle (upper-left) and the Particle Shown in Figure 3.31 (upper-right). Notice That the Image is 2X the One in Figure 3.31, so That the Appearance of the 10X in Figure 3.31 and the 5X in Figure 3.32 is the Same

CARS high-resolution surface imaging

Figure 3.33 shows the surface of a particle captured using the CARS microscope. The randomly distributed white dots are presumably instrument noise, and the red areas are saturated areas resulting from instrument calibration.

The surface texture appears only as a grainy, sandpaper-like surface in the optical microscope images. Also note the ripple-like structure in the large, slightly brighter grain at the top-center. Periodicity of the ripples is about 1.2 µm.
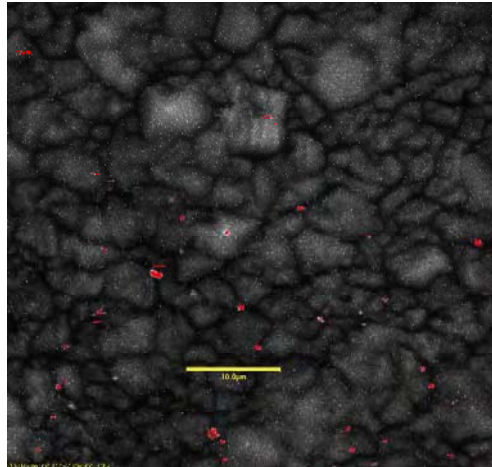
Figure 3.33. CARS Microscope Image Showing a Small Area of the Surface. The Yellow Scale Bar Represents 10 µm

Hardware implementation for off-line characterization

Hardware identified and/or acquired to implement automated, off-line characterization includes the following:

- Lieca Egolux microscope with computer controlled X-Y-Z translation, 5X, 10X, 20X, 50X and 100X objectives, with existing control software

- Desktop PC

- Canon EOS 1Ds digital SLR camera, memory cards, card reader

- Canon remote controller for computer controlled capture

On-line characterization/inspection

The scope of high-speed in-line characterization included defining a concept, then investigating available instrumentation for implementation. A handling system concept had been defined in prior work and the image acquisition concept was intended to be compatible with the handling concept. One or two cameras were envisioned, capturing images of individual particles as they passed through the camera's

line-of-sight. Central to the in-line concept is high camera resolution combined with high optical magnification and high frame rate. This concept was defined and analyzed. Components were identified and a potential implementation arrangement was evaluated.

Canon EOS 1Ds Digital SLR Camera with Canon 65 mm MP-E 1X-5X Macro Lens.

This configuration consists of a Canon EOS 1Ds digital SLR camera with Canon 65 mm MP-E 1X-5X macro lens attached. This lens is a dedicated macro lens that can only be used at 1X to 5X conjugates. At 5X, the FOV is ~7-mm wide because the CCD is 36-mm wide. The camera has a format that is 4064 x 2704 pixels so that at 5X, the 863.8-µm mean diameter particle would have a pixel diameter of ~488 pixels, or a resolution of ~1.8 µm/pixel.

Canon EOS 1Ds Digital SLR Camera with Leica Microscope.

Another configuration consisted of the same Canon camera as in the previous configuration, but mounted on the camera port of a Leica microscope, and using the Leica's 5X and 10X objectives. This configuration is of particular importance since it includes a computer-controlled X-Y-Z stage to provide automated multiple particle image acquisition, and multiple Z-height image stacks for each particle.

With this configuration, the 5X objective gives a particle image of about 1244 pixels, or ~0.69 µm/pixel. At this magnification it would be possible to digitize an image of an array of 3 x 2 particles. At 10X, the particle image diameter is ~2361 pixels, or ~0.37 µm/pixel. At 10X, the particle slightly under fills the frame; therefore, this is the maximum magnification usable for a full-particle image. Only one image can be digitized at a time. In both cases, as in previous configurations, multiple Z-slices are necessary to allow synthesizing an extended DoF composite. For 5X, seven images were used for synthesizing the composite. For 10X, 14 images were used. In either case, analyzing the minimum number of slices needed for a good enough composite is desirable. Previous studies have shown that as few as three or four might suffice at 5X. Figure 3.34 shows the composite image from the 5X configuration, and Figure 3.35 shows the composite from the 10X configuration.
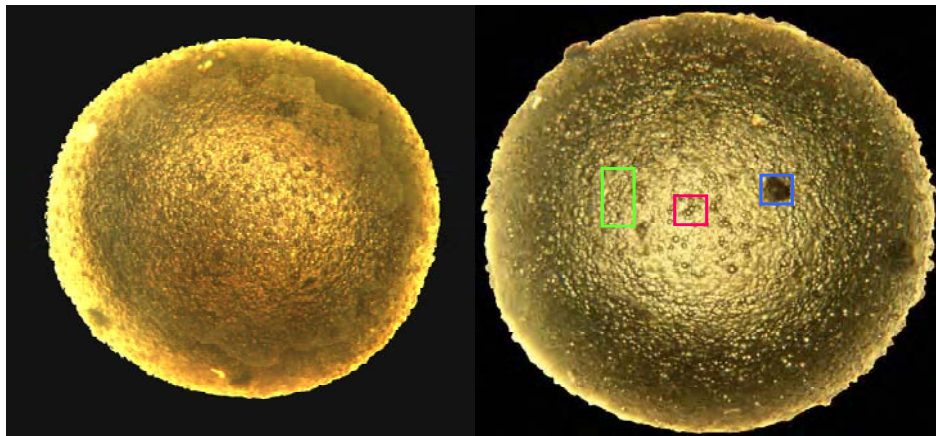
Figure 3.34. Composite particle image from seven Z-slices acquired with the 5X microscope configuration. This is the raw digital image with no color correction, so color is not significant. Sharp, elongated edge features are artifacts of the extended DoF processing. Resolution is about 0.69 µm/pixel

Figure 3.35. Composite particle image from seven Z-slices acquired with the 10X microscope configuration. Resolution is about 0.35 µm/pixel

The composite image in Figure 3.35, captured at 10X, probably represents the best full-particle image achievable with a straight optical microscope and digital camera. While higher microscope objective power can be used to achieve greater magnification, the greater apparent resolution – for example proportionally on the order of 0.17 µm/pixel at 20X – would be wasted magnification because the theoretical resolution for visible light (assume green light at about 0.55 µm) is ~0.67 µm for a 1-mm microscope objective aperture. Effectively, the 10X image in Figure 3.35 already has a higher pixel resolution than the image projected onto the CCD by the microscope optics. Some improvement might be possible, but nothing significant.

Figure 3.36 shows three enlargements of small areas of the image in Figure 3.35. These illustrate the resolution of the image in terms of actual surface features. Each of the images is keyed to Figure 3.35 by a colored circle defined in the caption. Each has a 10-µm scale bar.

Figures 3.36a and 3.36b are areas about 53-µm square – one centered on an area of blister-like features near the center of the image and thus likely to have the highest image quality – and one centered on a dark feature slightly above and to the right of center. The dark feature is likely to be a "gold spot" flaw because this particle is one of a batch with that flaw. The smallest features resolved appear to be the circular granular features comprising the clusters, which appear to be blister-like features in the full image. These are ~1.3 µm in diameter with the clusters ~5- to 10 µm in diameter.

When looking carefully at the full-size image, one notices occasional extended features, which, on closer scrutiny, appear to be linear groupings of clusters or granules. Figure 3.36c shows these at greater magnification. The feature of interest, diagonally crossing Figure 3.36c, is ~100 µm long.
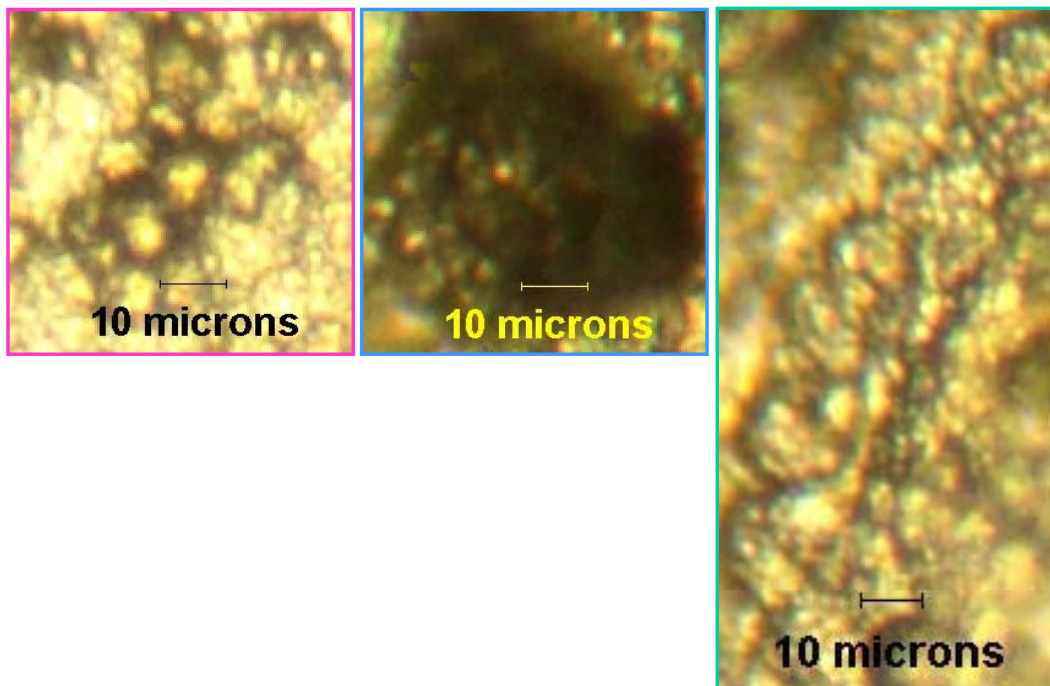
Figure 3.36. a) Red Box in Figure 3.35; b) Blue Box in Figure 3.35; c) Green Box in Figure 3.35

Summary of off-line configuration resolution

The following summarizes and compares the resolutions of the tested configurations:

- Nikon/Olympus (previous report) – 1.6 µm/pixel

- Nikon/Nikkor macro – 2.6 µm/pixel

- Canon/5X macro – 1.8 µm/pixel

- Canon/Leica 5X – 0.69 µm/pixel

- Canon/Leica 10X – 0.35 µm/pixel.

Task 7. NARROW LIST AND FURTHER DEVELOP REMAINING NDE METHODS

In this task, the NDE methods are evaluated to determine which have the best chance of meeting the project objectives.

Electromagnetic

The method(s) showing most promise for meeting the requirements of this project are the electromagnetic inductive and capacitive measurements. These have been chosen to be further refined and will be developed for demonstrating in-line QA/QC for each coating process of the TRISO fuel coating sequence.

UT Resonance

The attractive spectral features reported in FY2003 prompted further investigation into this method. Progress was limited by having to request time on equipment owned by other laboratories. The results were uncertain. The fixture is the same as the one previously used at DRS International, LLC. To progress further, it will be necessary to purchase the necessary transducer. This acquisition is planned for next year.

Acoustic Microscopy

No conclusive evidence was found to support further development of this subtask in the sub-200-MHz frequency range. Therefore, this task was suspended in favor of the other tasks showing evidence for achieving the project objective.

Optical

An evaluation of this method, demonstrating the potential capability for in-line coating inspection, was completed. Further development of this method is being weighed against the potential benefit relative to the other methods under evaluation.

Task 8. ON-PROCESS MEASUREMENTS

An on-process method is being investigated because it could potentially offer significant QA/QC benefits to the coating process, in real-time. As particles are being coated, measurements, if sensitive to particle diameter, could provide real-time feedback for maintaining coating thickness within specifications.

This task is divided into two elements: a) a review and assessment of potential on-process measurement technologies, and b) preliminary results obtained with transmission ultrasound on a model coater.

The review and assessment phase of this task was completed in FY2003.

A model coater was used to evaluate the potential for using air-coupled ultrasonic measurements as an in-situ coating thickness monitor. The two primary measurement techniques under investigation were:

1. Acoustic attenuation – a measure of energy loss between the sending and receiving transducers, mounted on opposite sides of the model coater.

2. Acoustic impact energy – a passive technique sensitive to the average energy (proportional to the mass) of the particles impacting the transducer face.

The transmission ultrasound measurement system and the model coater were refined and evaluated using surrogate particles. First, the ultrasonic transducer-mounting fixture attached to the model coater was improved for a more stable and repeatable measurement. The ultrasonic transducers are now held in place to tight tolerances, avoiding movement that could lead to measurement error. The time-of-flight distance between transducers is now much more consistent and repeatable. In Figure 3.37, the new fixture is shown in black with cables extending from opposite sides.
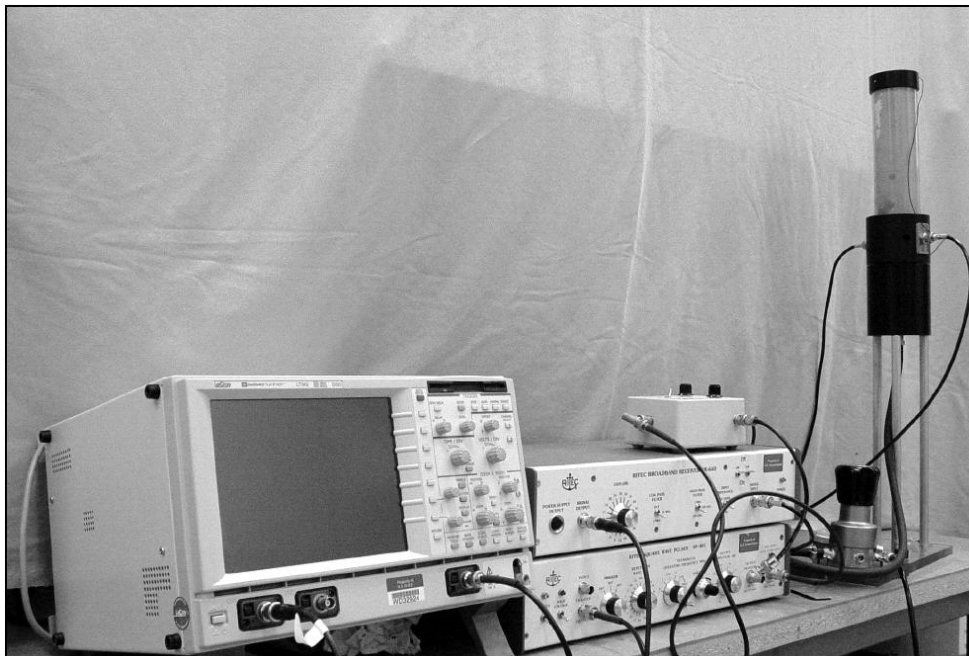
Figure 3.37. Model Coater and Measurement System

Preliminary results using glass spheres show consistent trends between average particle size (diameter) and measured attenuation. Measurements using three different sphere sizes show that attenuation[a] increases with particle diameter as in the plot of Figure 3.38.
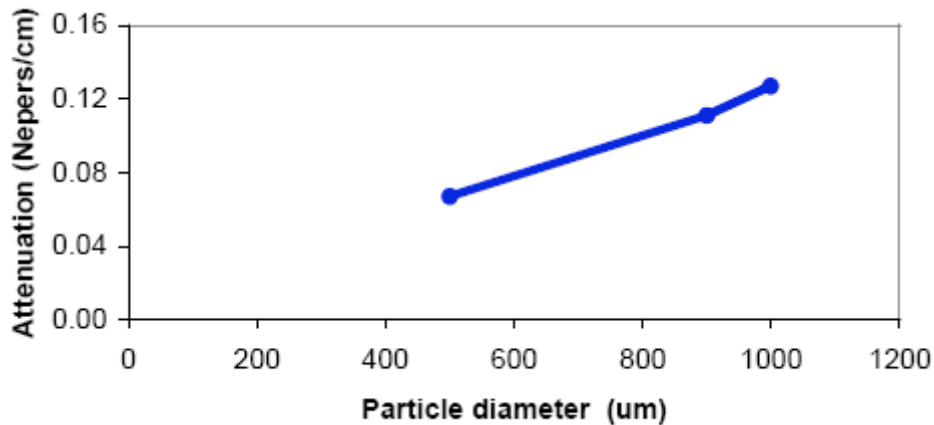
Figure 3.38. Acoustic attenuation through a fountain of glass spheres. Three different sphere sizes were evaluated separately in the model coater

These measurements indicate that the acoustic techniques are sensitive to particle size; however, determining the overall accuracy of the measurement requires additional refinement of the experimental setup. Several experiments this year suggested that the measurements also depend on the number of particles, gas pressure, and gas temperature. Additional measurement results using ZrO_2 surrogate kernels, although varying with particle size, are not showing the expected linear, monotonically increasing behavior seen for glass spheres.

The published theories on particles in a fluidized bed suggest that the frequency of the ultrasonic sound field is an important measurement parameter. The existing theories are derived by assuming the ratio of particle size to ultrasonic wavelength is either much greater than or much less than unity. In this work, only ultrasonic frequencies near 500 kHz have been used, due to their immediate availability. However, for fluidized particles of sizes between 100 μm and 1000 μm, in sound fields near 500 kHz, a new theory is necessary to explain the non-linear behavior exhibited in recent experiments.

This task has been reduced in scope to resolving the inconsistencies between existing theories and the experimental difficulties in working in a different frequency range.

Task 9. ESTABLISH STANDARD SIGNATURES AND FLAW LIBRARY

This task will develop a library of standard particles containing the full range of conditions known to degrade fuel performance, as well as particles with deemed to result in optimal fuel performance.

(a) The units of the attenuation value in nepers/length can be converted to decibels/length by dividing by 0.1151. Decibels are a more common unit when relating the amplitudes of two signals.

Multiple particles will be selected for each standard to enable statistical analyses. The standard particles will form a basis for developing and calibrating the NDE techniques for automated defect detection. For each NDE technique, a signature will be established for each particle in the flaw library.

In FY2003, considerable effort went into developing the NDE methods. The measurement results from the NDE methods showing the greatest potential for automated defect detection were evaluated using surrogate TRISO particles developed from another program, also in the early stages of developing the coating processes. The coating facilities at ORNL were unable to meet the specific needs of this task in FY2003. Therefore, large numbers of particles, having highly variable coating conditions, were sorted to select the few particles with defects representative of those considered to degrade fuel performance in a reactor. These particles were used predominately in finding trends between X-ray characterization and an electromagnetic measurement technique.

In this second year, several inductive impedance responses from unspecified surrogate particles coated at ORNL for another program were added to the flaw library. In addition, spheres made of copper, aluminum, titanium, inconel, and carbon were obtained and inductively measured. These spheres range in size from 1-mm down to about 0.5-mm. Their signatures are important because they offer a repeatability and calibration standard for the inductive impedance technique being evaluated for in-line inspection. The signatures offer a way to better define the relationship between material properties in absolute terms, and the NDE measurements cannot be done using coated particles having physical properties of higher uncertainty.

As outlined in Task 4, significant progress was made in developing a particle flaw matrix that resulted in 14 defect conditions in particles coated at ORNL for this project using surrogate kernels. See Task 4 and the appendices to Task 4 for details. Inductive signatures were obtained for all of these particles. Capacitive signatures were also obtained for several of them.

Although somewhat lagging behind the impedance measurements in quantity, at least a few micro-focus radiographic images have been obtained on particles with impedance signatures. Radiographs have been obtained for 10-50 particles for each of several selected coating runs. For several of the coating runs, radiographic and impedance measurements were obtained in parallel. Thus, the data cannot be used to compare techniques on a specific particle, but they can be used to draw conclusions about the entire batch.

This task will conclude with a few more coating run variations, measurements on DUO_2 coated particles at ISU, and filling a few gaps that exist in the current signature library. The largest gaps are in the capacitive sensor measurements. This is a consequence of technical challenges found in refining the capacitive sensor, which is now in the final phase of construction.

Task 10. EVALUATE ELECTRICAL PROPERTY EQUIVALENCE BETWEEN DUO_2 AND ZrO_2

To date, most of the sensor development and flaw detection sensitivity assessment work has been conducted using unfueled (surrogate) particles. Surrogate material was selected for initial evaluations to save the time and cost associated with handling radioactive materials. However, measurements similar to those performed on surrogate particles must also be performed on fueled particles to determine if the kernel chemistry may have an effect on the inspection methods developed using surrogate particles. This

task is to explore differences in how the NDE sensors react to the same coatings applied to ZrO_2 and DUO_2.

In the third quarter of this year, the kernel and coatings needed to evaluate electrical property differences between uranium based materials and ZrO_2 were selected. A six-page document was prepared, summarizing why this material is necessary, the material and coatings required, the health safety guidelines at ISU, and the test procedures to be followed. A significant amount of effort went into planning the category, shipment, and storage of the uranium-based materials for testing at ISU. All documentation for this shipping request was submitted to ORNL and to DOE for approval. A table showing the requested particle parameters is in the appendix to this task.

Task 11. DESIGN AND DEVELOP CAPILLARY PARTICLE FLOW TUBE SYSTEM

This task evaluates the feasibility and techniques required for dynamic flaw detection in particles having statically acquired signatures. The electrical in-line measurement methods being developed for this project typically have a potentially fast (micro-second to milli-second) response time, so measurement speed is not likely to be a limitation. However, the details of implementing techniques developed under static conditions to operate at production speeds may require particular consideration.

To demonstrate the in-line EM inspection measurement concept the inductive impedance sensor was put in a particle flow loop. Particles were allowed to pass through the inductive sensor as the measurement system continuously recorded the coil impedance. Initial results, plotted in Figure 3.39, are consistent with the stationary measurements, but span a wider range. A wider range of inductive impedance values were observed because the measurement rate of the impedance analyzer was not fast enough to always attain a measurement at the instant that each particle was centered longitudinally in the sensor coil.
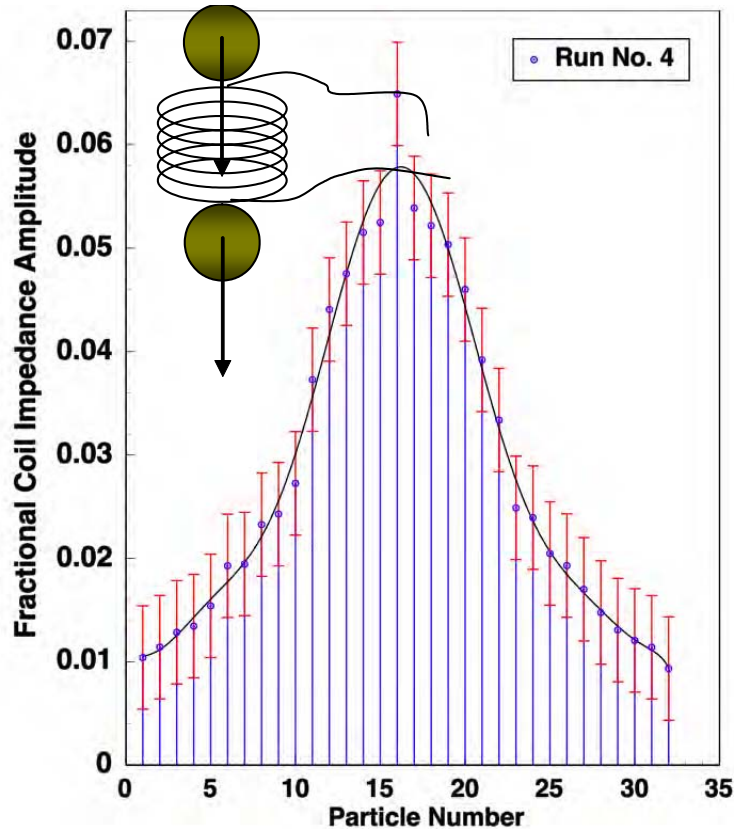
Figure 3.39. Fractional coil impedance measurements from several particles from coating run 4 passing through the coil sensor

At the relatively slow measurement rate used in this evaluation, some of the particles were closer to the top or bottom of the coil at the time a measurement was recorded. The impedance analyzer was set at about 30 ms between measurements, and the coil sensor was about 2 mm in length. By substantially increasing the measurement rate, it will become possible to acquire a sufficient number of measurements on each particle when its center is collocated with (within one third of a particle diameter) the sensor coil's center, where a maximum in the coil response occurs. Commercial inductive impedance measurement instruments are available with recording rates orders of magnitude faster than that used in this initial evaluation.

The results obtained in this task suggest that dynamic electrical impedance measurements will agree with static measurements when using instrumentation with sufficient measurement frequency. Several commercial instruments have this capability.

3.3 FY2004 Presentations and Publications

Progress this year was broadly discussed and disseminated through several presentations at meeting, seminars, and conferences, in addition to the annual program review in Gaithersburg, MD.

A paper was accepted for publication and presented at the 2004 International Congress on Advances in Nuclear Power Plants (ICAPP '04) meeting held June 13–17, 2004, in Pittsburgh, PA, at the Omni William Penn Hotel and Sponsored by ANS, SNE, SFEN, AESJ and KNS.

- A technical project team review meeting was held at ORNL on April 14.

- The status of this project was presented in detail at the 2004 Annual NERI program review meeting held at the Hilton, Washington DC North/Gaithersburg conference center on June 2–3.

- The project team participated in monthly conference calls.

- A paper entitled "Combining X-ray, Eddy Current, and Electric Field Techniques for Automating Particle Fuel Characterization" was presented at the 2004 review of progress in QNDE in Golden, CO, on July 29, 2004.

3.4 FY2004 Financial Summary

Cumulative Cost Performance
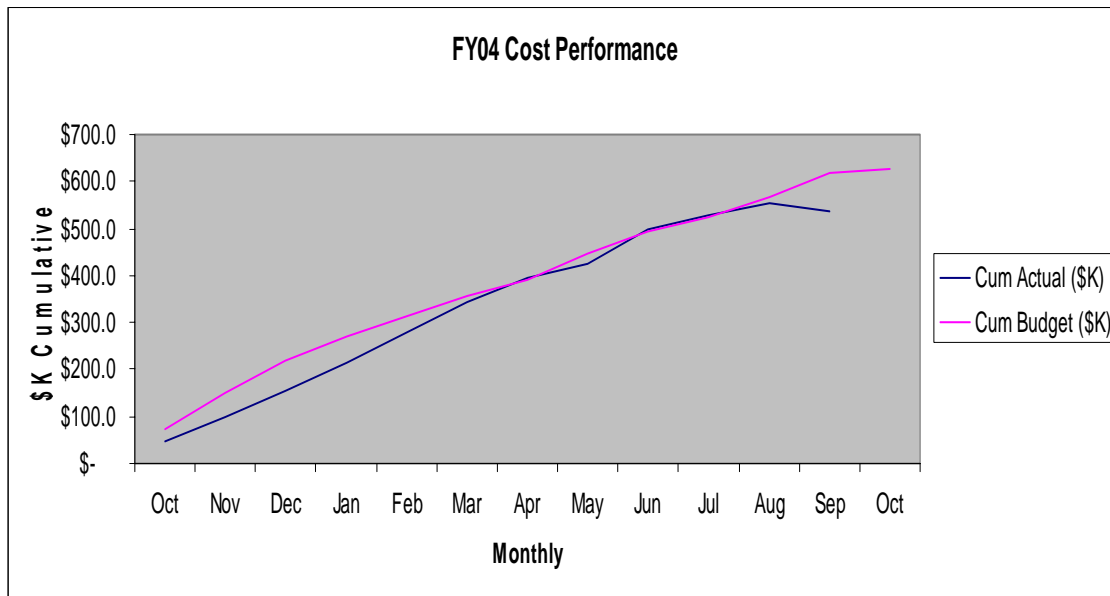
	Oct	Nov	Dec	Jan	Feb	Mar	Apr	May	Jun	Jul	Aug	Sep	Oct
Cum Actual ($K)	$ 47.6	$ 99.8	$ 155.3	$ 215.1	$ 277.2	$ 341.6	$ 396.5	$ 426.7	$ 496.1	$ 528.0	$ 555.4	$ 538.2	
Cum Budget ($K)	$ 72.6	$ 150.5	$ 217.6	$ 269.2	$ 312.7	$ 357.3	$ 390.5	$ 445.7	$ 494.9	$ 526.0	$ 565.2	$ 617.8	$ 626.9

Annual Cost Performance:

FY2004 ended with a dip in spending during the final month because of a favorable variance allowing a pass back to projects. Of the $618K of planned work, the final actual cost was $538K. Although spending was slow in the first quarter, improvement was seen in the second, third, and fourth quarters, with the final month dipping as a result of the pass-back funding received in the final days of the fiscal year. While PNNL was on track with completing the year on budget, the final pass back changed that position. GA finished the year under budget with scope remaining, and ISU completed the year over budget for commensurate scope.

Testing of uranium-based materials was not completed in FY2004, aligning with the AGR program schedule. A request to complete associated activities is planned for the final year of the project. Remaining PNNL scope included final-quarter and FY2004 annual report preparation, on-process measurements testing, and NDE method verification of the depleted uranium samples. GA was unable to prepare documentation of the effects of QC methods on fuel due to insufficient data generated thus far. Incomplete ISU scope included radiographic work and characterization of depleted uranium particles. A change request is in preparation for completion of activities remaining at the end of September for PNNL and GA with remaining carryover funding.

3.5 FY2004 Project Milestones

Milestone & Deliverables	Planned Completion	Revised Completion	Actual Completion	Percent Complete
FY2003 Annual Report Complete	Sep—03	Dec-03	Mar-04	100
FY2004 Annual Report Complete	Oct—04	Jul-05	Nov-05	99

3.6 FY2004 Appendices

Table 3.9. Coating Parameters Used in Developing Surrogate "Standard" and Defective TRISO Coated Particles

Run Number	1-B	2-B	3-B	4-A
Standard Number	1	2	3	4
Date Shipped	1/20/04	1/23/04	1/20/04	1/23/04
Desired particle dia (μm)	250-450	350-550	250-450	350-550
Particle batch(s) to use	300 and 400	400 and 500	300 and 400	400 and 500
Kernal size spilt by SA	50/50	50/50	50/50	50/50
Approx Batch Surface area (cm^2)	1046	1046	1046	1046
Buffer				
Desired Thickness (μm)	100	20	100	20
Measured Thickness (μm)	100	20	101	20
Temperature	1300	1300	1300	1300
C2H2/Ar	1.5	1.5	1.5	1.5
Time	11	50 sec.	11	50 sec.
IPYC				
Desired Thickness (μm)			40	40
Measured Thickness (μm)			37	40
%HC			30	30
Temperature			1300	1300
%C2H2 in HC			44	44
%C3H6 in HC			56	56
Time			13	9
SiC				
Desired Thickness (μm)				
Measured Thickness (μm)				
Temperature				
% MTS in H2				
Time				
OPYC				
Desired Thickness (μm)				
Measured Thickness (μm)				
%HC				
Temperature				
%C2H2 in HC				
%C3H6 in HC				
Time				

Run Number	7-A	8-A	9-A	10-B
Standard Number	7	8	9	11
Date Shipped	1/23/04	1/23/04	1/23/04	2/9/04
Desired particle dia (µm)	480-520	480-520	480-520	480-520
Particle batch(s) to use	500	500	500	500
Kernal size spilt by SA				
Approx Batch Surface area (cm^2)	1046	1046	1046	1046
Buffer				
Desired Thickness (µm)				
Measured Thickness (µm)				
Temperature				
C2H2/Ar				
Time				
IPYC				
Desired Thickness (µm)	40	40	40	20
Measured Thickness (µm)	45	40	40	20
%HC	15	28	40	28
Temperature	1300	1300	1300	1300
%C2H2 in HC	44	44	44	44
%C3H6 in HC	56	56	56	56
Time	15	6.5	5	2.5
SiC				
Desired Thickness (µm)				
Measured Thickness (µm)				
Temperature				
% MTS in H2				
Time				
OPYC				
Desired Thickness (µm)				
Measured Thickness (µm)				
%HC				
Temperature				
%C2H2 in HC				
%C3H6 in HC				
Time				

Run Number	12-B	14-B	5-B	13-A	6-CD	11-E
Standard Number	13	16	5	14	6	12
Date Shipped	1/20/04	2/9/04				3/11/04
Desired particle dia (µm)	300-400	620	250-450	300 / 400	350-550	350
Particle batch(s) to use	300 / 400	650	300 / 400	50/50	400 / 500	300-400
Kernal size spilt by SA	50/50		50/50	1046	50/50	50/50
Approx Batch Surface area (cm^2)	1046	1046	1046		1610	1610
Buffer						
Desired Thickness (µm)	100		100	100	20	20
Measured Thickness (µm)	107		105	100	20	120
Temperature	1300		1300	1300	1300	1300
C2H2/Ar	1.5		1.5	1.5	1.5	1.5
Time	11		11	11	50 sec	10
IPYC						
Desired Thickness (µm)	40		40	40	40	40
Measured Thickness (µm)	37		40	37	40	40
%HC	30		30	30	30	30
Temperature	1300		1300	1300	1300	1300
%C2H2 in HC	44		44	44	44	44
%C3H6 in HC	56		56	56	56	56
Time	13		15	15	9	15
SiC						
Desired Thickness (µm)		35	35	20	35	35
Measured Thickness (µm)		42	45	20	40	30
Temperature		1500	1500	1500	1500	1500
% MTS in H2		1.7	1.7	1.7	1.7	1.7
Time		45	240	120	180	120
OPYC						
Desired Thickness (µm)	40		40	40	40	40
Measured Thickness (µm)	36		40	40	40	40
%HC	30		30	30	30	30
Temperature	1300		1300	1300	1300	1300
%C2H2 in HC	44		44	44	44	44
%C3H6 in HC	56		56	56	56	56
Time	15		13	13	7.5	13

Table 3.10. ORNL Particles Supplied September 9, 2003, Left Over From the AGR Program

| Coating Run NT- | Cone ID (mm) | Kernel | | Charge In (g) | Layers |
		Material	Diameter (μm)		
52	25	ZrO$_2$	500	10.008	Buffer + IPyC + SiC
64	25	ZrO$_2$	500	10.009	Buffer + IPyC + SiC
74	50	ZrO$_2$	500	54.5	Buffer + IPyC + SiC
75	50	ZrO$_2$	500	54.5	Buffer + IPyC
AGR-08282003-1	50	ZrO$_2$	500	54.5	Buffer
AGR-08282003-2	50	ZrO$_2$	500	54.5	Buffer
AGR-08282003-3	50	ZrO$_2$	500	54.5	Buffer
AGR-08292003-1	50	ZrO$_2$	500	54.5	Buffer
AGR-09022003-1	50	ZrO$_2$	500	54.5	Buffer
AGR-09032003-1	50	ZrO$_2$	500	54.5	Buffer + IPyC
AGR-09042003-1	50	ZrO$_2$	500	54.5	Buffer + IPyC
HfO$_2$, Buffer only	50	HfO$_2$	500	92.7	Buffer
HfO$_2$, B + IPyC	50	HfO$_2$	500	92.7	Buffer + IPyC

Appendix to Task 4a:

X-ray Facilities and resources at ISU: Hardware requirements for a high resolution CT system.

The high-resolution CT system at ISU consists of a 130-kVp micro-focus X-ray source (with spot size ~2 μm), a 4-axis precision motion stage (x-y-z-θ) and an amorphous silicon array (gadolinium oxysulphide scintillator screen with a 127-μm pixel size). The approach of this CT system is to utilize geometric magnification to reduce the pixel size. The geometric magnification is limited with the present cabinet to ~50X resulting in a minimum pixel size of ~2-3 μm. The control software for the data acquisition was developed at ISU, and includes interfaces with the detector and the motion controller. The system can be used in both a CT configuration and a digital radiography mode. The three-dimensional CT reconstructions are preformed on a Linux cluster made up of 54 nodes running at 2.8 GHz with 1-GB RAM. The reconstruction can be done with both parallel-fan-beam and cone-beam algorithms. The hardware cost of this system is ~$150K.
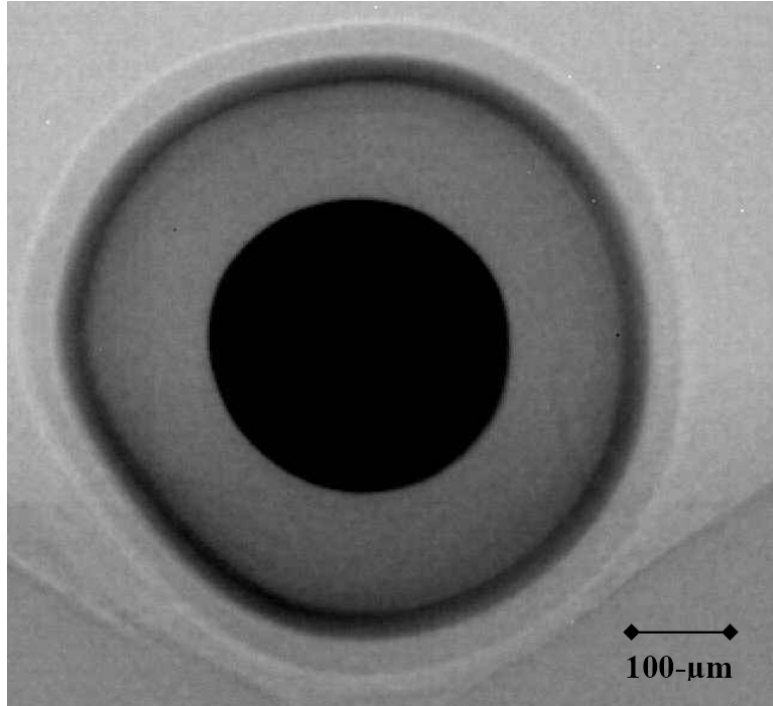
Figure 3.40. A Typical Image From the Digital Radiography System. The Mapping Has Been Selected to Show the Outer Carbon Layer and Not to Illustrate the Inner Carbon Buffer and the Inner Pyrolytic Carbon Layer
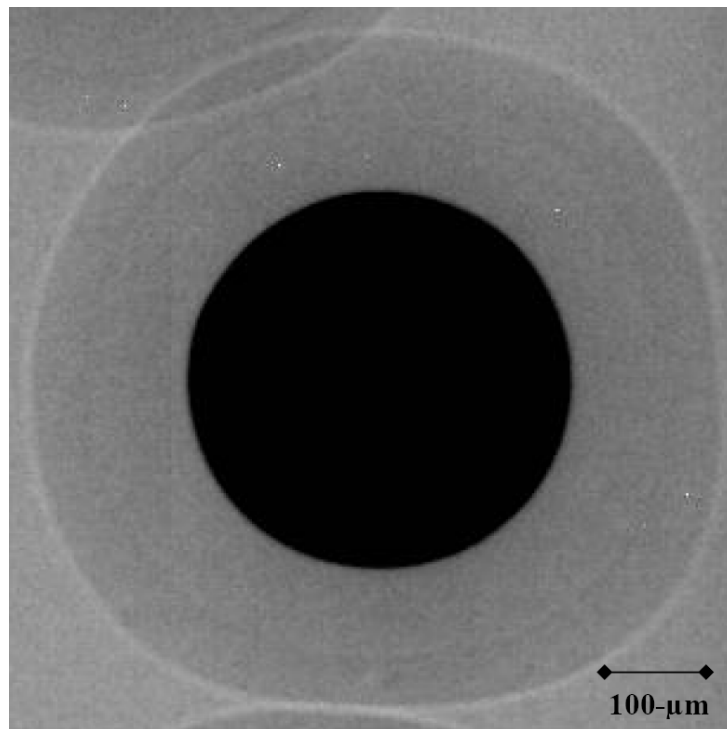
Figure 3.41. This Image Shows the Mapping Function Selected to Show the Contrast Difference Between the Two Inner Carbon Layers. This Sample was Extracted From the Fabrication Process Before the SiC Layer was Added

This system can produce high-resolution images suitable for characterization of layers in fuel particles either by digital radiography or by three-dimensional CT scans. In Figure 3.41, a digital radiograph illustrates the detail produced in the images of a particle. Several issues need to be pointed out in viewing such data, particularly data having more than 8 bits of dynamic range -- in this work, 12 bit resolution is standard. A typical monitor can only display 8 bits of grey scale or 255 shades of grey. The detectors used on digital radiography typically range from 12 to 16 bits. The mapping procedure of this high-dynamic-range data onto the lower dynamic range of a video monitor is a key factor in viewing the data collected by these systems.

The three-dimensional CT scanner has the ability to show the regularity of the particle layers. Figure 3.42 shows a particle with flat surfaces in the SiC layer. The transparency of the three-dimensional visualization was set to make the low-density carbon layers transparent, showing the SiC layer and the ceramic kernel. (Most of the particles are more spherical than this example, specifically chosen as atypical.)
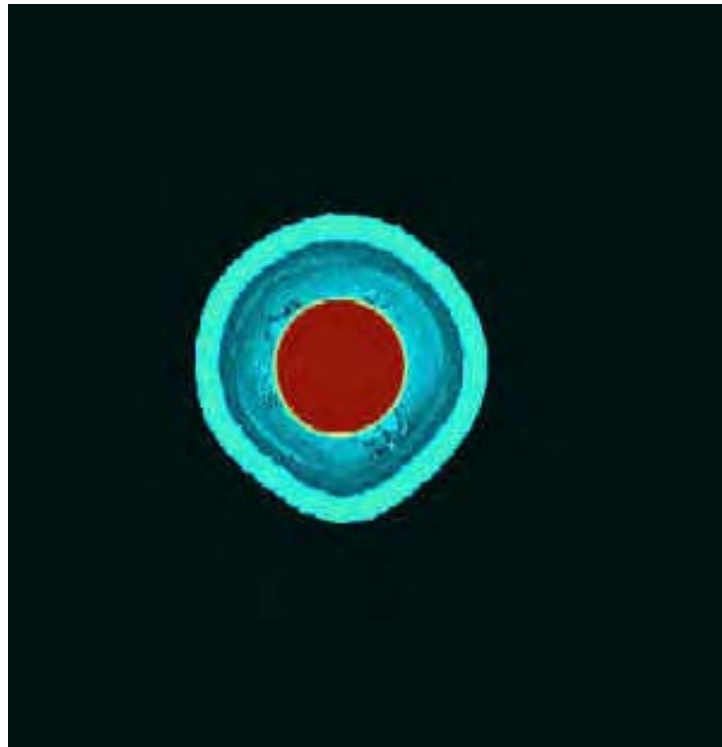
Figure 3.42. An Example of a Profile From the Three-Dimensional CT Data Set Showing the Flattened Surfaces on the SiC Layer. The Three-Dimensional Visualization Tool Has Set Densities Less Than the SiC and Kernel to be Transparent. The Red is the Kernel and the Cyan is the SiC Layer

3.55
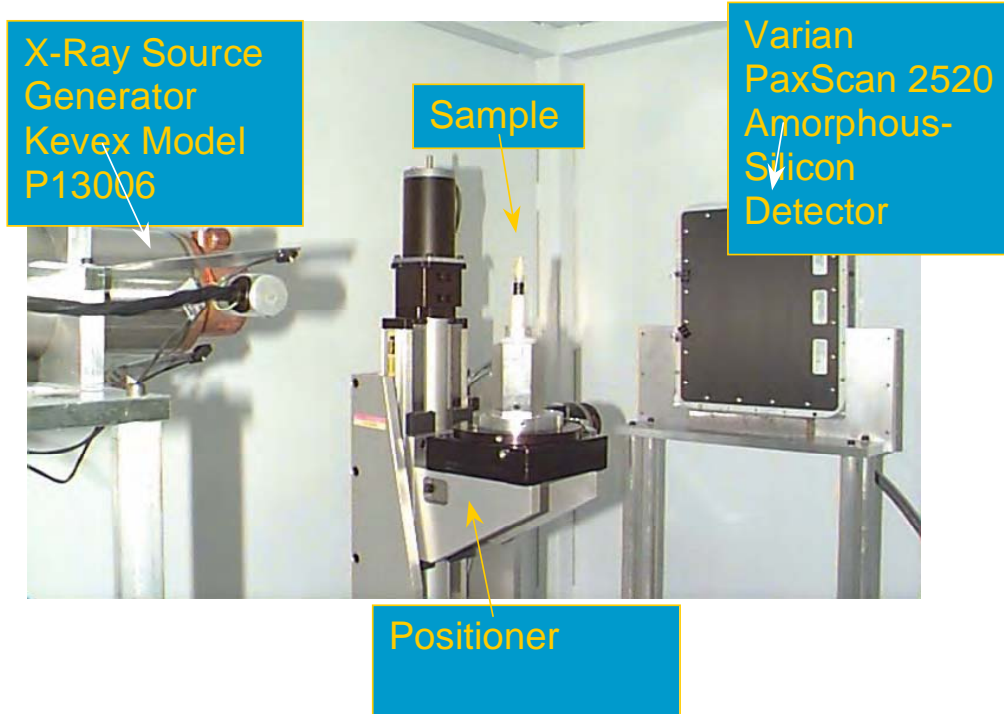
Figure 3.43. Photograph of the Inside of the Cabinet Housing the High-Resolution CT System

The measurements are placed together with the raw data files for the images and a viewer program on a CNDE anonymous ftp site.

Appendix to Task 6:

Table 3.11   Coating Run Conditions to Evaluate Relationships Between Physical Property Changes Expected From Variations in Gas Fraction and Coating Time on Electrical Properties

Parameters	7-A	8-A	9-A
Standard Run Number	7	8	9
Date Shipped	1/23/04	1/23/04	1/23/04
Desired particle dia (μm)	480-520	480-520	480-520
Particle batch(s) to use	500	500	500
Kernal size spilt by SA			
Approx Batch Surface area (cm^2)	1046	1046	1046
PyC			
Desired Thickness (μm)	40	40	40
Measured Thickness (μm)	45	40	40
%HC	15	28	40
Temperature	1300	1300	1300
%C2H2 in HC	44	44	44
%C3H6 in HC	56	56	56
Time	15	6.5	5

Table 3.12. Kernel Diameter and PyC Coating Thickness (in µm) Derived from Radiography

Particle No.	Kernel Dia. (µm)	PyC Run 7	PyC Run 8	PyC Run 9
Neri007stat_A_a1	501.3	43.3		
Neri007stat_A_a2	531	36.8		
Neri007stat_A_a3	495	42.5		
Neri007stat_A_a4	507	41.5		
Neri007stat_A_a5	500	37.5		
Neri007stat_A_a6	490	41		
Neri007stat_A_a7	497	29		
Neri007stat_A_a8	500	36.4		
Neri007stat_A_a9	547	43		
Neri007_a_a16	517.1	37.4		
Neri007_a_a1	522.4	39.3		
Neri007_a_a11	524.2	39.5		
Neri007_a_a4	520.6	38.8		
Neri007_a_a1	567.1	37.1		
NERI008_A_F_1	511.3		34.8	
NERI008_A_F_2	552.5		35.5	
NERI008_A_F_3	637.2		34.6	
NERI008_A_F_4	631.2		32.1	
NERI008_A_F_5	652.2		35.9	
NERI008_A_G_1	538.9		30.8	
NERI008_A_G_2	521.2		33.9	
NERI008_A_G_3	535.5		28.4	
NERI008_A_G_4	516.6		31.1	
NERI008_A_G_5	555.1		31.2	
NERI008_A_H_1	541.3		30.6	
NERI008_A_H_3	511.2		29.8	
NERI008_A_H_2	539.9		26	
NERI008_A_H_4	540.3		31.3	
NERI008_A_H_5	556.5		28.4	
NERI008_A_I_1	514.8		28.1	
NERI008_A_I_2	533.4		26.3	
NERI008_A_I_3	534.8		24.8	
NERI008_A_I_4	517.5		26.1	
NERI008_A_I_5	527.1		30.8	
Neri009_a_a4	522.2			30.3
Neri009_a_a6	521			35.8
Neri009_a_a10	521.7			35.4
Neri009_a_a18	516.2			38.1
Neri009_a_a12	505.5			36.9
Neri009_a_a17	507.4			39.4
Ave. kernel dia.		511.74	550.43	518.95
Average PyC coat		36.64	30.51	35.3

Appendix to Task 10:

Table 3.13. Requested Uranium-based Particles to Evaluate Electrical Property Equivalence with the Coated Surrogate Particles

Attachment A
NE Radioactive Shipment Request:

The following NE radioactive shipments are requested to be approved for the week of : Week of December 13, 20, or 27, 2004, or January 3 or 10, 2005

Shipping Site	Isotope or Material	Transportation Mode	Receiving Location	Quantity	Package Type	Values A₁ or A₂ (mCi)
UT-Battelle, LLC Oak Ridge National Laboratory Bethal Valley Rd. Oak Ridge, TN 37830 Attn: J. H. Miller (865)574-5408	0.5139g of 500μm DUO₂ kernels 0.5200g of 350μm DUO₂ kernels 0.5242g of TRISO coated 500μm DUO₂ kernels 0.5072g of 350μm NUCO kernels Subtotals: 1.0625g of DU 0.4566g of NU 0.0055g of U-235 All masses +/- 0.0001g	Federal Express	Joe Gray log # 040520 Iowa State University 216 Nuclear Engineering Ames, IA 50011 (515)294-9745	Approx 1.0625g of DU and 0.4566g of NU with a combined total of 0.0055g of U-235 (0.855 μCi total) All masses +/- 0.0001g	- Each sample packed in a screw top gasket sealed glass vial with each vial individually wrapped in "Chem-pack" fabric packing material to provide mechanical isolation. - Packaged within 1 mechanically sealed metal isotope can - Packaged within a fiber board box - Limited quantity, excepted package. (Packaging is type A compliant.)	A₁ (Normal Form) unlimited mCi

To ensure the safety of the DOE shipments of radioactive material, we verify that we have implemented the following procedures

FOR TRUCK SHIPMENTS[1]

☐ Required a list of the drivers that will be entering the DOE facilities be provided to the site prior to the pickup of the shipment

☐ Verified that each driver is a citizen of the United States

☐ Required a copy of the driver's Commercial Drivers License with proper hazardous materials endorsement.
☐ Conducted safety/security inspections of all incoming and outgoing shipments, such as for explosives and other devises, as detailed in Measure 18 of DOE Notice 473.6, Security Conditions.
  ∠ Available communication for carrier:
  ∠ Qualcomrn satellite tracking
  ∠ TRANSCOM satellite tracking
  ∠ Mobile telephone

FOR ALL SHIPMENTS[1]

☐ Shipment contains Highway Route Controlled Quantities of radioactive material under the regulation of NRC. NRC's November 8, 2001, advisory has been met.
☐ Check here if additional information is attached

_____   _____
Signature and Title of Requesting Official   Signature and Title of Approving Official

4.0   FY2005 – Project Year 3

October 2004 to January 2006*

* Note: Project year 3 includes work performed during the four-month no-cost time extension that was requested by PNNL. Appendix A to the final report provides the no-cost extension request.

4.1 FY2005 Summary

This portion of the final report summarizes the activities performed and progress made in FY2005.

In the first-year (FY2003) of this three-year project, surrogate fuel particles available for testing included leftovers from initial coater development coating runs. These particles had high defect fractions and widely ranging particle properties, providing an opportunity to examine worst-case conditions before refining the inspection methods to detect more subtle coating features. In the second project year (FY2004), it became necessary to have fully and partially coated surrogate particles without defects (standard particles) and particles with specific variations from the standard to evaluate the NDE methods for defect detection. A matrix of 14 different coating specifications was developed for this purpose, requiring over 40 specific coating runs at ORNL to fabricate. In addition, the planning process was completed for obtaining uranium-based materials with similar coatings. The third project year (FY2005) began with a scope redirection based on a 27% ($97K) funding reduction. This caused the project to be re-scoped (reference appendix to Task 12-17, PNNL NERI 005-001, October 13, 2004). Consequently, the original Tasks 12-17 were condensed into a single task, similar to the original Task 16 (Final Laboratory Scale Demonstration of Each NDE Method Found to Meet the Project Objectives).   For the remainder of this project, the primary objective is to demonstrate technical feasibility for using electrical (inductive and capacitive impedance) sensor measurements for high-speed defect detection and sorting.

During the course of FY2005, the capacitive sensor went through a final design revision and is now fully functional. The results compared to the previous design show a significant improvement. The complementary inductive sensor was modified for integration into a single package with the capacitive sensor and the integrated design was completed, fabricated, and demonstrated to show potential for making high-speed electrical measurements. The two sensors were integrated into a prototypical particle delivery system for the inspection of TRISO particles.   A demonstration video of the prototypical system was produced.

Work this fiscal year included the evaluation of the effects of kernel chemistry on the electrical measurement techniques. Initial review of an ORNL report provided guidance in selecting suitable particles for determining those effects. Two requests were submitted for obtaining coated and uncoated DUO_2 kernels. The first batch of uranium bearing particles was shipped to ISU in December, 2004, and electrical measurements were made in March, 2005. The second batch of uranium bearing particles was shipped in August 2005, and electrical measurements were made in October, 2005.

An additional analysis was performed this year to ascertain whether the bulk measurement capabilities of the air-coupled ultrasonic technologies were applicable to the TRISO particle examination. Preliminary work was carried out in FY2003, but with inconclusive results. Based on these new test results, the air-coupled ultrasonic approach to measuring average particle size for the next-generation nuclear fuels does not appear to have the required sensitivity needed for this process-monitoring application. If the nuclear fuel particles were to be transferred through a liquid medium, where a higher frequency ultrasonic setup

could be used, determination of average particle size would be much more feasible using both velocity and attenuation parameters.

In FY2003, a RUS system was acquired and initial measurements were made. This initial evaluation determined that the RUS system, as configured, could not determine the resonant frequencies for spheres smaller than about 4 mm. Two approaches were identified that could overcome this limitation. The first approach involved particle excitation with electromagnetic acoustic transducers (EMATs), which proved unsuccessful. The second approach involved fabricating custom contact transducers matched to the mass of the particles. This approach was deferred until the third year of the project (FY2005). In FY2005, special transducers were procured and customized for use with sub-millimeter particles. The data indicate that resonance modes of TRISO particles are sensitive to internal defects, including thin layers, missing layers, and metal inclusions, as well as to the size and shape of the particles. Even though there is variability in the location, number, and shape of the resonant peaks for nominally identical particles, the defective particles are clearly distinguishable from normal TRISO particles.

Establishment of the particle library as an analysis tool proved useful this year. All of the particles examined to date were included, along with process parameters, radiographic data, and electrical measurements. The particle library was utilized to perform further statistical and physical property modeling.

A presentation given at the University of Michigan entitled "Nondestructive Characterization of TRISO Coated Particle Fuel" described this multidisciplinary research effort to enable production and safe use of coated particle fuels in next-generation nuclear reactors.

4.2 FY2005 Research Progress

Task 1. LITERATURE REVIEW

A general literature review performed as part of the proposal process revealed over 30 years of work on coated particle fuels. This initial review spans topics relevant to Advanced Gas Reactor programs, with particular focus on the reporting of fabrication and testing of TRISO particles, both nationally and internationally. The time frame included in this initial review includes publications from 1970 through 2001, and contains over 150 publications.

Although Task 1 was completed in project year one in accordance with the original statement of work, some additional related papers were added to the database. However, no new papers on particle fuel inspection were input into the database this year.

Task 2. MODELING STUDY

The objectives of the modeling activities were threefold:
1. Develop the measurement methods consistent with the theory.
2. Better analyze and interpret measurement results.
3. Predict measurement results for a broader range of defect conditions, beyond those that can be fabricated in the time frame of this project.

Per the original statement of work, both acoustic and electromagnetic models were developed in project year one. In the second project year, the numerical models developed in the prior year were utilized but

were not refined or developed further. The models were used to estimate detection thresholds for various particle properties and to refine the measurement sensors and instrumentation. Some additional modeling of inductive and capacitive sensors was performed this fiscal year to provide a more complete understanding of the particle properties that were being measured by the sensors.

This extended modeling, described in Section 5, more clearly defined the capabilities and limitations of the inductive and capacitive sensors. The results showed that, for both complete and incomplete TRISO particles, the inductive sensor measures only the total volume (or mass) of the conductive material (buffer, IPyC, and OPyC layers) present in the particle. The dimensions of the kernel and SiC layer have almost no effect on the inductive signature of a particle except by affecting the volumes of overlying layers. It was also determined that the capacitive sensor provides a sensitive measure of the outer diameter or volume of a particle, but offers no direct information about the thicknesses or properties of the inner layers. The electrical conductivities of the buffer and PyC materials are so large that, when present at the outer surface of a particle, they have the same effect as a metal. All of the inner layers of the particle are effectively shielded by the outer layer, so the capacitive sensor can measure only the total volume of the particle. Even the conductivity of the SiC material is high enough to produce this effect when the SiC layer is the outermost layer of the particle.

Task 3. DEFINE QUALITY INDEX

The objective for developing a quality index is to relate the NDE measurement results to the process parameters and the physical properties for each TRISO particle coating condition. Per the original statement of work, Task 3 (Defining the Quality Index) was completed during project year one.

Task 4. OBTAIN SURROGATE PARTICLES

Two additional coating runs were completed at ORNL and shipped to PNNL. The SiC layers produced in original coating runs 5-B and 13-A were found to have average thickness of 50 µm and 29 µm, respectively. Upon recoating, in runs 5-D and 13-C, the SiC layers were reduced to about 48 µm and 24 µm, respectively.

Some new thoughts on why the IPyC layer properties may have been altered after applying a SiC layer were discussed in FY2004. This concept had not been considered before PNNL requested the application of IPyC material without the addition of successive TRISO layers. To resolve this issue, ORNL team members suggested the application of a SiC layer to coating runs 7-9. PNNL sent most of the remaining particles from those coating runs back to ORNL for SiC coating in the third quarter of FY2004. Particles from several additional coating runs were shipped to PNNL in the first quarter of FY2005 to further investigate the coating conditions necessary to control the density and anisotropy of PyC coatings. This was done in support of a more thorough analysis being conducted at ORNL to better understand their coating process conditions. Table 4.2 is a summary of those coating runs.

Particles from coating runs 7, 8, and 9 were returned to ORNL last year. A SiC layer was added and the particles were returned to PNNL. Particles from several the AGR program coating runs were also shipped to PNNL. The AGR particles had batches with and without SiC applied. These particles were evaluated in FY2005 with the capacitive impedance sensor.

Table 4.1.   Original Coating Runs were recoated to Bring SiC Layer within Specifications

Run Number	5-D	13-C
Date Shipped	10/22/04	10/22/04
Desired particle dia (μm)	400	400
Particle batch(s) to use	400	400
Approx Batch Surface area (cm^2)	1100	1100
Buffer		
Desired Thickness (μm)	100	100
Measured Thickness (μm)	77*	81*
Temperature	1300	1300
C2H2/Ar	1.5	1.5
Time	5	5
IPYC		
Desired Thickness (μm)	40	40
Measured Thickness (μm)	40*	40*
%HC	30	30
Temperature	1300	1300
%C2H2 in HC	44	44
%C3H6 in HC	56	56
Time	9	9
SiC		
Desired Thickness (μm)	40	20
Measured Thickness (μm)	48*	24*
Temperature	1500	1500
% MTS in H2	5.5	5.5
Time	60	30
OPYC		
Desired Thickness (μm)	40	40
Measured Thickness (μm)	52*	56*
%HC	30	30
Temperature	1300	1300
%C2H2 in HC	44	44
%C3H6 in HC	56	56
Time	9	9
* Measured Thickness from ISU Data		

Table 4.2. Particles Shipped December 28, 2004 to Explore the Effect of SiC Deposition on the IPyC Layer

AGR #	PNL-NERI	Deposition Temp (C)	Coatings	C3H6/ C2H2	Total Gas Flow (l/min)	Active Gas Fraction	Nominal IPyC Thickness (μm)	IPyC Coating Time (min)	Nominal IPyC Coating Rate (μm/min)
AGR012 22004-1	007-A		IPyC and SiC on 500 um ZrO$_2$	1.2		0.15	45	15	3.0
AGR012 22004-2	008-A			1.3	7000	0.28	40	6.5	6.2
AGR012 22004-3	009-A			1.3		0.40	40	5	8.0
NA	017-B	1300	Buffer and IPyC on 500 um ZrO$_2$	10.6	11408	0.48	40	6	6.7
NA	018-C			10.9	13144	0.67	40	4	10.0
NA	019-A			13.2	16450	0.81	50	5	10.0
NA	017-E			1.2		0.15	40	15	2.7
NA	018-F			1.3	7000	0.28	40	9	4.4
NA	019-C			1.3		0.40	40	8	5.0
NA	020-A			1.3		0.15	40	22	1.8
NA	021-A			1.3	5000	0.28	40	12	3.3
NA	022-B			1.3		0.40	40	9	4.4

Note: Flow meter malfunction on runs 17-B, 18-C, and 19-A; might give interesting results.

The possibility that uranium-based kernels and the surrogate kernels might produce different responses in the inductive and capacitive sensors was investigated in FY2005. The uranium-based kernels of Table 4.3 were shipped to ISU in December 2004 and plans were made to perform X-ray and electrical measurements on these particles in the 2nd quarter of FY2005.

Table 4.3. DUO$_2$ and NUCO Particles Shipped to ISU for X-ray and Electrical Measurements

Shipping Site	Isotope or Material	Transportation Mode	Receiving Location	Quantity	Package Type	Values A$_1$ or A$_2$ (mCi)
UT-Battelle, LLC Oak Ridge National Laboratory Bethal Valley Rd. Oak Ridge, TN 37830 Attn: J. H. Miller (865)574-5408	0.5139g of 500μm DUO$_2$ kernels 0.5200g of 350μm DUO$_2$ kernels 0.5242g of TRISO coated 500μm DUO$_2$ kernels 0.5072g of 350μm NUCO kernels Subtotals: 1.0625g of DU 0.4566g of NU 0.0055g of U-235 All masses +/- 0.0001g	Federal Express	Joe Gray log # 040520 Iowa State University 216 Nuclear Engineering Ames, IA 50011 (515)294-9745	Approx 1.0625g of DU and 0.4566g of NU with a combined total of 0.0055g of U-235 (0.855 μCi total) All masses +/- 0.0001g	- Each sample packed in a screw top gasket sealed glass vial with each vial individually wrapped in "Chem-pack" fabric packing material to provide mechanical isolation. - Packaged within 1 mechanically sealed metal isotope can - Packaged within a fiber board box - Limited quantity, excepted package. (Packaging is type A compliant.)	A$_1$ (Normal Form) unlimited mCi

In the final quarter of FY2005, a second group of uranium-bearing particles was produced at ORNL and sent to ISU for examination in August, 2005 (Table 4.4).

Table 4.4. Second Batch of Particles Shipped to ISU for X-ray and Electrical Measurements

a. Shipping Site	b. Description of Material	c. Transportation Mode	d. Receiving Location	e. Quantity (Ci)	f. Package Type/Model	g. A₁ or A₂ Values (Ci)
UT-Battelle,LLC Oak Ridge National Laboratory Bethal Valley Rd. Oak Ridge, TN 37830 Attn: J. H. Miller (865)574-5408	<1.5g natural uranium (<0.011g U-235) combined total in 5 samples of un-irradiated coated fuel particles: 1. <0.55g of TRISO coated particles from compaction qualification lot 2. <0.55g of carbon buffer coated particles from buffer density determination lot 3. <0.55g of carbon buffer/IPyC coated particles from IPyC density determination lot 4. <0.55g of carbon buffer/IPyC coated particles from lot # NUCO350-IPyC-5 5. <0.55g of carbon buffer/IPyC coated particles from lot # NUCO350-IPyC-6	Federal Express	Joe Gray log # 050312 Iowa State University 216 Nuclear Engineering Ames, IA 50011 (515)294-9745	<1.1 µCi total (<1.5g NU) (<0.011g U-235)	• Each sample packed in screw top gasket sealed glass vial. Each vial individually wrapped in "Chem-pack" fabric packing material to provide mechanical isolation. • Packaged within one mechanically sealed metal isotope can • Packaged within a fiber board box • Limited quantity, excepted package. (Packaging is type A compliant.)	A1 (Normal Form) unlimited mCi

Batches 39T and 41T were selected as reasonably representatives of AGR program fully-coated TRISO particles. 58B and 66BI were selected as representative of AGR buffer-coated and buffer-IPyC coated particles, and IPyC-5 and IPyC-6 are buffer/IPyC coated particles that were selected because they have similar size kernels and coating thickness, but significantly different IPyC densities (i.e., 1.75 g/cc and 1.96 g/cc, respectively).

A PNNL staff member traveled to ISU to assist in the electromagnetic measurements on these particles. Both inductive and capacitive measurements were made and the results have been included in the particle library. Additionally, selected particles from batch 39T were radiographed and analyzed. Those data were also included in the particle library.

Task 4a. PARTICLE CHARACTERIZATON

Radiographic measurements performed during this project year included several particles from coating runs 5-D, 6CD, 007AA, 008AA, 009AA, 012B, 013A, 013C, 014B, AGR, and 39T. All of these new characterization data are shown in the particle library in Appendix B.

Task 5. INTRODUCE DEFECTS IN SURROGATE PARTICLES

Although initially scheduled to begin in the first project year, this task was deferred until coated particles with flaws representative of those most likely to occur in TRISO fuel have been fully evaluated. The focus was on dimensional defects involving kernel diameter and layer-thickness abnormalities. However, it was determined that surrogate particles offered a sufficient number and range of these kinds of defects to make this task unnecessary as originally planned. Examples of existing defects include a thin or missing coating layer and variations in the density and microstructure of the PyC layers.

The project scope changes approved at the beginning of FY2005 narrow the focus of this project down to demonstrating the in-line detection of defects associated with dimensional variations in coated particles. This task was redefined to involve seeking naturally occurring dimensional defects intrinsic to the coating process.

Task 6. DESIGN, DEVELOP STATIONARY PARTICLE NDE METHODS

Progress on this task was focused on two areas for completing the in-line electromagnetic measurement methods evaluation. The first focus area was evaluating a dual impedance measurement concept—a combination of inductive and capacitive measurements—to determine the feasibility of detecting coating defects. The inductive sensor alone has been found to provide only a partial solution for this purpose. The second focus area was to validate the use of ZrO_2 coated kernels as surrogates for uranium-based particles in establishing flaw detection capability. The kernel equivalence assessment is reported in Task 10.

Electromagnetic

The inductive sensor is insensitive to the slightly conductive SiC confinement layer and the nonconductive oxides that make up the kernel. It does respond to thickness changes in these materials, but only because of their volumetric effects on the surrounding electrically conductive materials. The large variation in kernel diameter in the particle defect library has shown that the inductive sensor impedance values are indeed sensitive to kernel size. Even when the conductive layer thicknesses do not vary, kernel diameter has been observed to have a significant effect on the inductive impedance. This observation can be explained by noting how the kernel size affects the volume fraction of each coating layer in comparison with the total particle volume, as plotted in Figure 4.1. In this analysis, each coating layer thickness is held constant at the value specified for the AGR design, and allowing only the kernel diameter to vary. Notice that for relatively small kernel sizes the OPyC layer dominates the overall particle volume, but as the kernel size increases above about 400 μm the buffer volume becomes the dominant material. A similar analysis, independently varying each coating layer thickness while holding all other dimensional parameter constant, will show that each dimensional parameter can affect the volume of all subsequently applied materials.
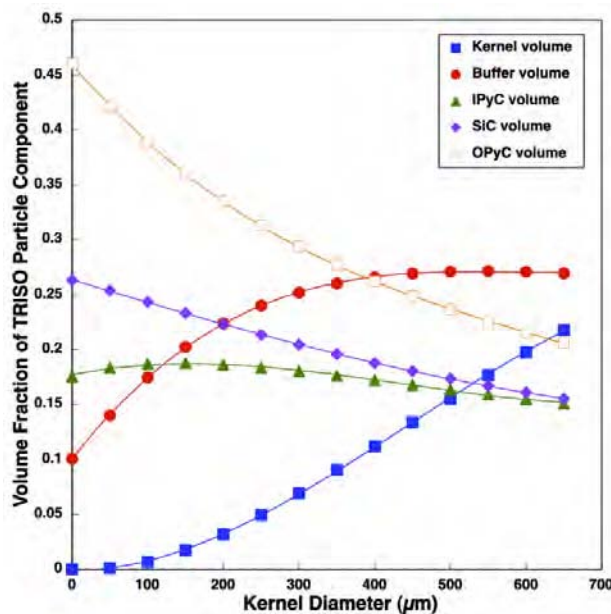
Figure 4.1. Volume Fraction of Each TRISO Particle Component Computed and Plotted as a Function of Kernel Diameter

To separate this mutually dependent size effect, it is necessary to have another independent measurement sensitive to an independent material property, like the dielectric strength of the SiC and kernel.

A new capacitor design and fabrication was completed, as shown in Figure 4.2. The latest design is similar to that shown previously as part of the sensor in Figure 3.28 and is 5 to 10 times more sensitive to particle dielectric properties than previous designs. Measurement repeatability and signal-to-noise ratios are also much improved.

Particle is placed here for measurement
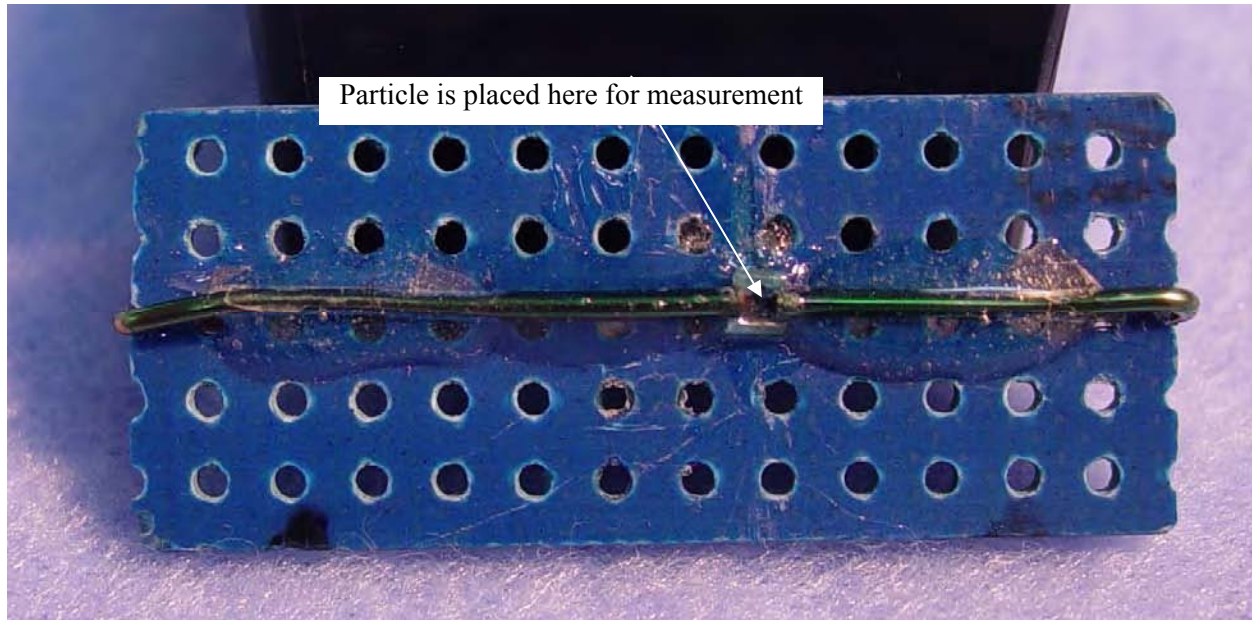
Figure 4.2. Capacitive Sensor

The results plotted in Figure 4.3 were obtained using the improved capacitor design. Clear separation can be seen between measurements from particles selected from the three different coating runs.
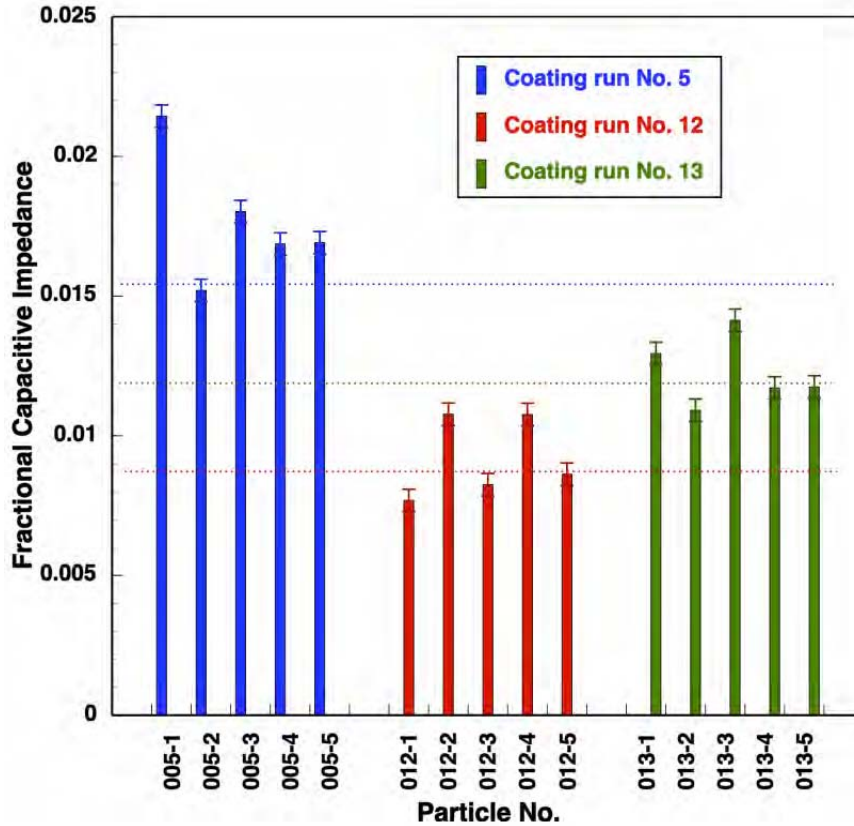
Figure 4.3. Capacitive Impedance Measurements From Five Randomly Selected Particles From Coating Runs 5 (Fully Coated TRISO), 12 (Missing SiC Layer), and 13 (Thin SiC Layer)

The improved capacitive measurement technique is providing results that suggest a combination of the inductive and capacitance impedance measurements will make it possible to detect deviation from the standard TRISO dimensional parameters. The combined impedance measurements were performed on particles from the following coating runs to evaluate the specific objectives listed in Table 4.5.

Table 4.5. Coating Run Conditions Used to Evaluate Measurement Methods. For a More Complete Description of the Coating Conditions, Refer to ORNL Fabrication Specifications.

Coating Condition*	Coating Run
Thin buffer, full TRISO	6
PyC variations	7,8,9
"Normal" TRISO	5
SiC variations, missing & thin	12,13
Uranium-based AGR materials	
Buffer+IPyC+(SiC)	17,18,19,20,21,22

* Coatings were applied to ZrO_2 kernels having a bimodal
size distribution, centered about 300 and 400 μm, to also
evaluate expected variability in kernel size.

Particles from coating runs 7, 8, and 9, defined in Table 4.6 to evaluate relationships between the PyC coating process parameters, were further analyzed using the dual impedance sensor concept. When particles from each of these coating runs were analyzed using the inductive coil sensor, the only observable impedance variation was attributed to IPyC layer thickness and kernel diameter, in agreement (for the most part) with characterization studies performed at ORNL to determine PyC layer density and anisotropy variation among these three coating runs. On fully coated particles, ORNL has observed density and anisotropy variation in the IPyC layer using the same coating conditions as originally applied to runs 7, 8, and 9. To explain the apparent lack of density and anisotropy variation in these three coating runs, there was speculation that the SiC coating process might alter the IPyC coating properties. Therefore, most of the particles from these three coating runs had a subsequent SiC layer applied in an attempt to observe how the process of applying a SiC layer may affect the underlying IPyC layer. At any rate, the addition of a SiC layer offers another opportunity to quantify detection criteria and variations in SiC coating thickness on a partially coated particle.

Capacitive measurements were performed on different particles from the same three coating runs both before and after the SiC layer was applied. The fractional impedance change measured with the capacitive sensor for these particles is plotted in Figure 4.4. Note that the red values, taken before depositing SiC, have about the same average value for particles from all three coating runs. The relatively small variation between measurements is most likely the result of kernel size effects. However, the same measurements taken from different particles from the same coating runs, after applying a SiC layer (blue symbols) show a decrease for particles from run 8, similar to what was observed using the inductive sensor. This decrease is most likely caused by a lower SiC volume, resulting from the IPyC coating layer thickness reduction (see Table 4.6).
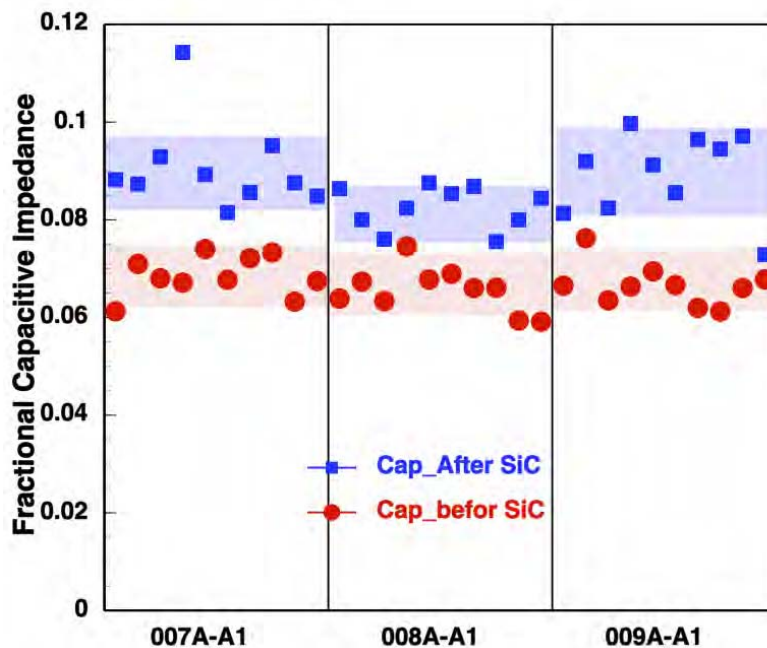
Figure 4.4. Capacitive Impedance Measurements of 10 Different Particles from Each of Coating Runs 7, 8, and 9, Both Before and After Applying a SiC Layer. A Total of 60 Particles Were Analyzed Using the Capacitive Sensor

Table 4.6. Kernel Diameter and PyC Coating Thickness (in µm) Derived From Radiography Before SiC Was Applied

Particles No.	Kernel Dia(µm)	PyC Run 7	PyC Run 8	PyC Run 9
Neri007_a_a1	567.1	37.1		
Neri007_a_a4	520.6	38.8		
Neri007_a_a11	524.2	39.5		
Neri007_a_a14	522.4	39.3		
Neri007_a_a16	517.1	37.4		
Neri008_a_a1	507.1		33.8	
Neri008_a_a10	516.4		36.0	
Neri008_a_a15	509.1		34.2	
Neri008_a_a16	506.1		35.5	
Neri008_a_a19	531.3		34.7	
Neri009_a_a4	522.2			30.3
Neri009_a_a6	521			35.8
Neri009_a_a10	521.7			35.4
Neri009_a_a12	505.5			36.9
Neri009_a_a17	507.4			39.4
Neri009_a_a18	516.2			38.1
Ave. kernel dia.		530.3	514.0	515.7
Average PyC coat		38.42	34.84	35.98

Figure 4.5 compares the impedance values from each sensor before and after SiC application and compares the impedance values between different sensors before and after SiC application. The most interesting attribute to note is how little the inductive impedance changes by adding the SiC layer. However, the capacitive impedance does increase notably after adding the SiC layer. This implies that the capacitive sensor does respond to the SiC layer, whereas the inductive sensor does not.
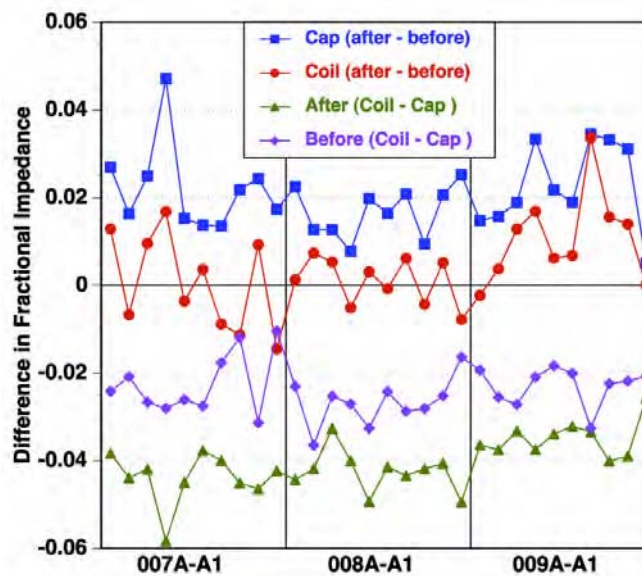
Figure 4.5. Comparisons Between Capacitive and Inductive Impedance, Before and After SiC Application

Coating Runs 5, 13, and 12

Another set of measurements suggesting that a relationship between inductive and capacitive measurements may provide insight into the internal layer structure of the fully coated TRISO particle was observed from coating run 5-B. Five particles from coating run 5-B were examined with both sensors, inductive and capacitive. The results are plotted in Figure 4.6. In some cases, the inductive impedance is greater than the capacitive impedance, and in others, just the opposite was observed. Furthermore, there also seems to be some correlation between the two measurements. These two observations suggest that perhaps the difference between the two measurements may provide a useful measure of variation in particle dimensional properties.
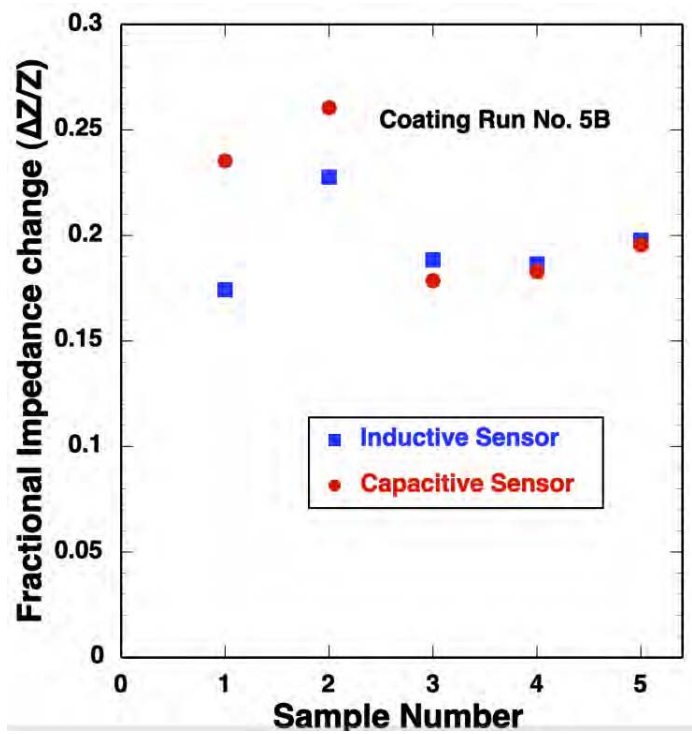
Figure 4.6.   Fractional Impedance Change Measured for Five Particles From Coating Run 5-B Using Both Inductive and Capacitive Sensors

Coating runs 5-B and 13-A were recoated to reduce the SiC layer thickness; in both cases this layer was thicker than specified. Coating run 5 was designed to have a SiC thickness of about 40 μm and run 13 was supposed to be about 20 μm. Radiography has shown coating run 5-B to have a SiC thickness of about 50 μm and run 13-A to have about 42 μm of SiC. These radiographic values were obtained from about 20 independent measurements and should represent a value characteristic for each coating run. The new coating runs produced particles with SiC layer thicknesses of about 48 μm and 38 μm, in runs 5-D and 13-C, respectively. However, the radiographic layer thicknesses derived from runs 5-D and 13-C were from a much smaller number of measurements, and therefore have lower confidence. The electrical measurements plotted in Figure 4.7 indicate that the SiC layer thickness didn't change much between coating runs 5-B and 5-D and may have increased from 13-A to 13-C. However, the capacitive impedance values from particles in coating run 12 are consistent with no SiC layer.
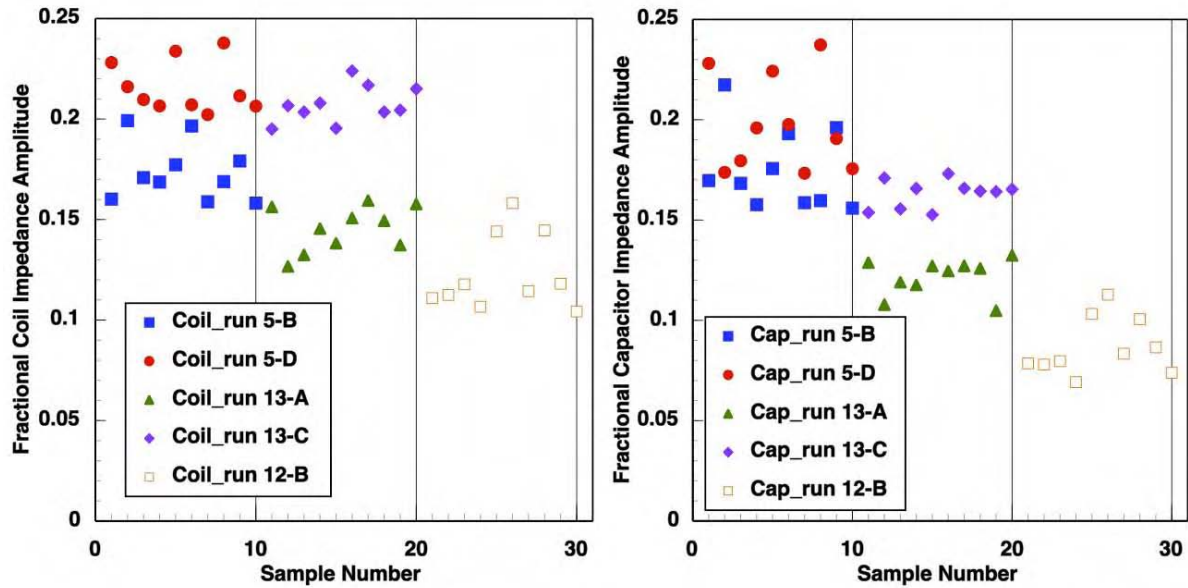
Figure 4.7.   Inductive and Capacitive Impedance Measurements from Particles in Coating Runs 5-B, 5-D, 13-A, 13-C, and 12-B.

Another way to compare these results is to compare the capacitive impedance values between 5-B and 13-A, then 5-D with 13-C. In this comparison it can be seen that the capacitive impedance is reduced in both cases when the SiC layer is reduced.
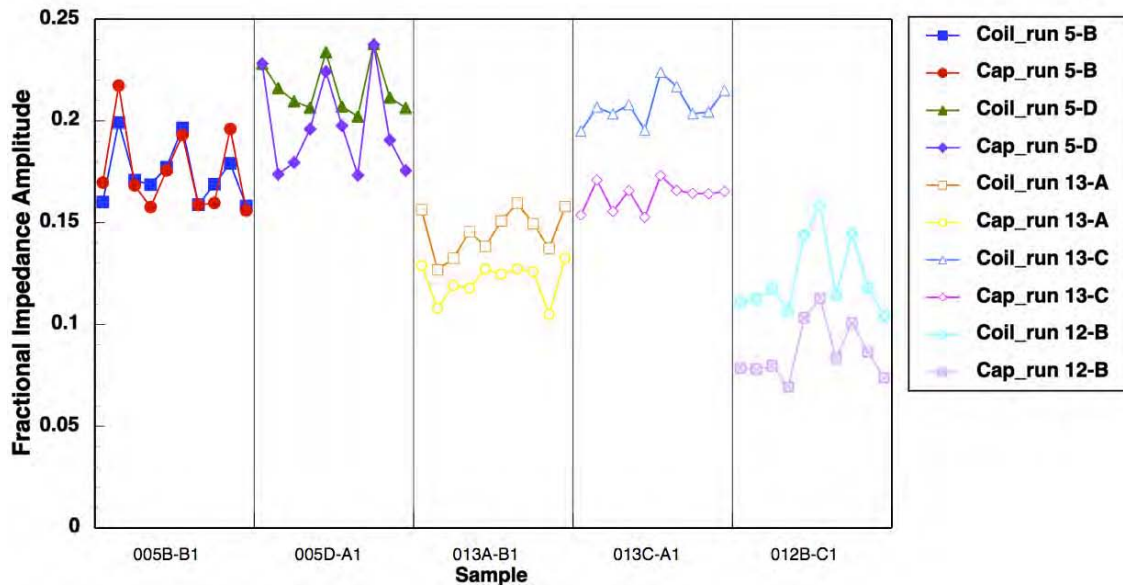
Figure 4.8.   Inductive and Capacitive Impedance Measurements from Particles in Coating Runs 5-B, 5-D, 13-A, 13-C, and 12-B Plotted on a Single Axis

The difference in impedance between the inductive and capacitive impedance is shown in Figure 4.8. Note that the difference between these two measurements increases as the SiC layer is reduced. For both coating runs, the difference between inductive and capacitive impedance for run 5-B and 5-D is smaller

than for the other coating runs with less SiC applied. This difference is seen best in Figure 4.9, where the vertical axis is the difference between inductive and capacitive impedance. The impedance difference may be diminished somewhat for coating run 12 because the sensor fill-fraction is reduced as a result of a reduction in particle size.
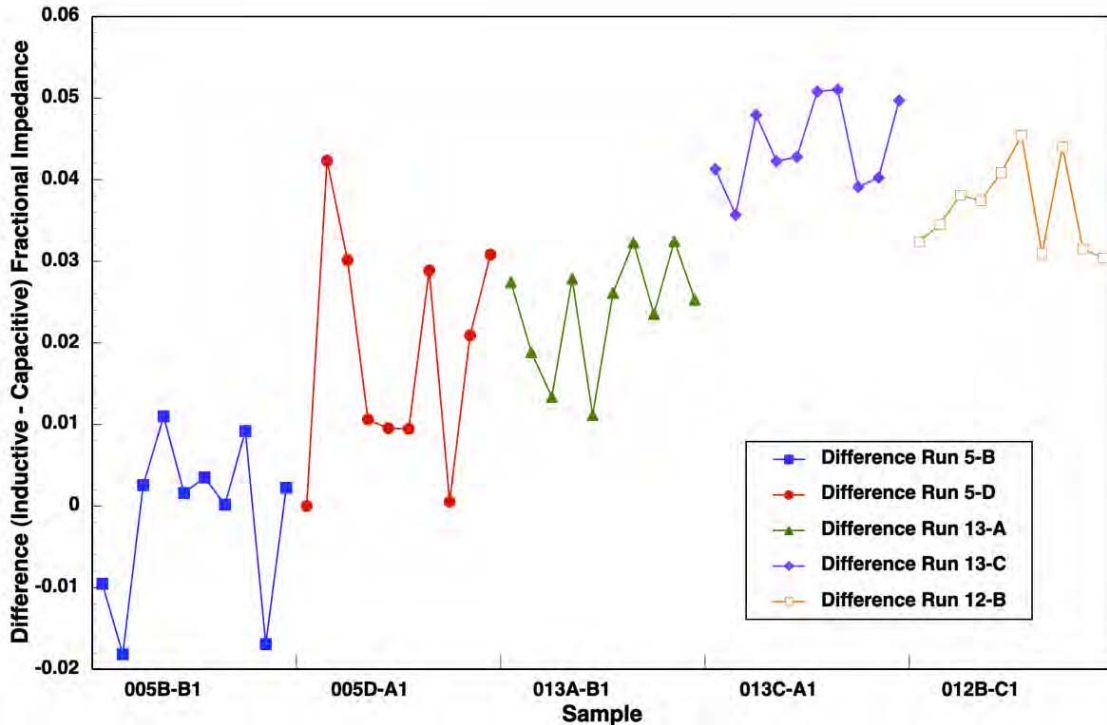
Figure 4.9. Difference in Inductive and Capacitive Impedance Measurements From Particles in Coating Runs 5-B, 5-D, 13-A, 13-C, and 12-B Plotted on a Single Axis

Coating Run 6

Particles from coating run 6—the full TRISO coating, but with a thin buffer—were also examined using the dual-sensor measurement method. Measurement results from this assessment are plotted in Figure 4.10 as the fractional impedance and the fractional impedance difference between the capacitive and inductive sensors. It should be noted that the inductive impedance is less than the capacitive impedance, unlike coating runs 5, 13, and 12, where the inductive impedance is either the same or greater than the capacitive impedance. This reduction in inductive impedance is most likely due to less conductive material is present and interacting with the coil sensor.

The impedance measurement values from both methods appear to be highly correlated. This becomes clearer when plotting the same measurements against each other, as in Figure 4.11. The R^2 correlation coefficient is 0.959. This indicates that both sensors are mostly sensitive to the effects caused by the same physical property. The kernel diameter has been found to be the most widely varying parameter for the particles being evaluated by this project. As discussed above, the kernel diameter can have a significant effect on the diameter (and therefore the volume) of all coating layers. Similarly, thickness variation in any single coating layer can also affect the volume of all successive layers, but typically, individual coating layers do not vary in thickness as much as the kernel diameter for the particles under consideration here.
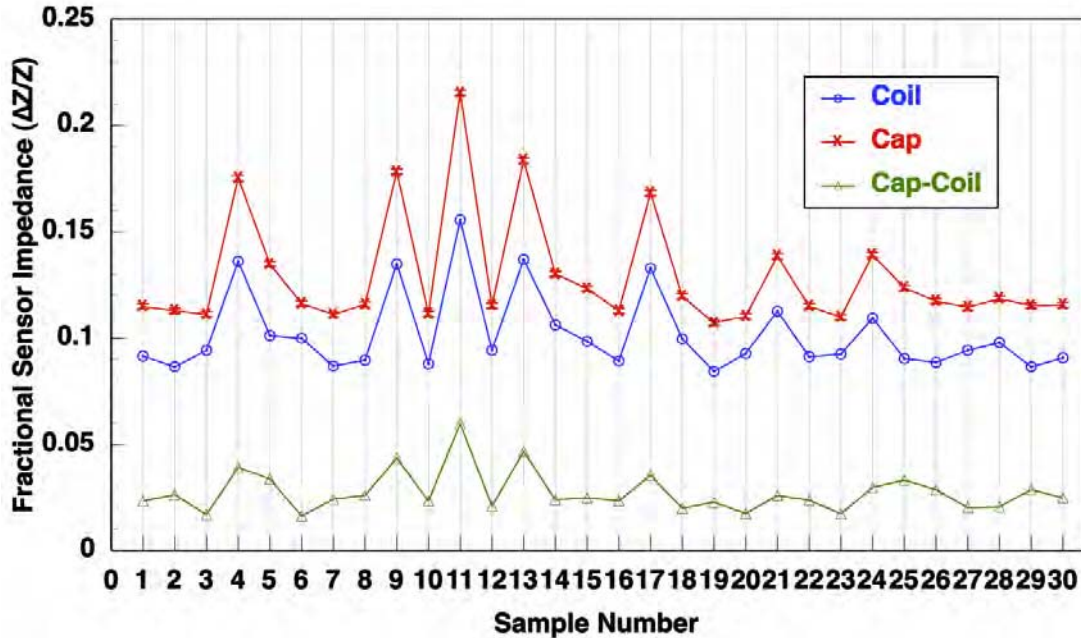
Figure 4.10. Both Inductive and Capacitive Measurements on Particles From Coating Run 6 (Full TRISO with Thin Buffer), a Total of 60 Measurements. The Fractional Impedance and the Difference in Fractional Impedance are Plotted for 30 Different Particles
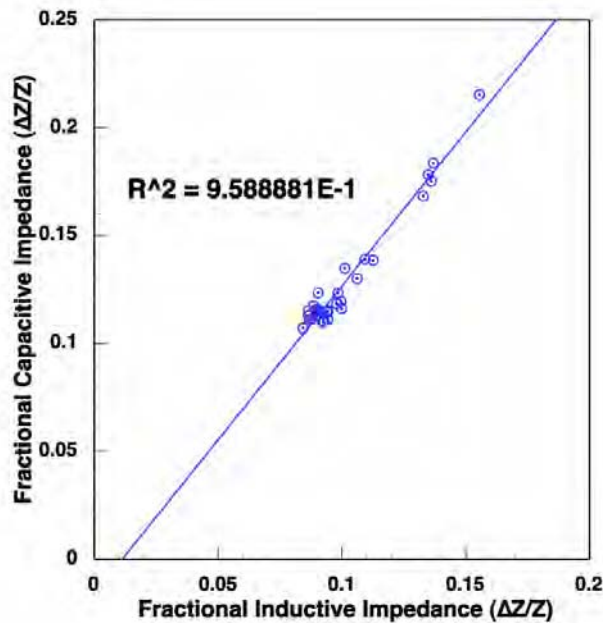
Figure 4.11. Fractional Inductive Impedance Plotted Against Fractional Capacitive Impedance for the Measurements in Figure 4.10. A Linear Curve Fit Shows the Results to be Highly Correlated

Figure 4.12, which is a plot of fractional inductive and capacitive impedance against the fractional impedance difference of these two measurements, indicates that the difference has a higher correlation with the capacitive impedance. This suggests that variation in the kernel diameter and SiC layer thickness most likely account for the difference seen between the two types of electrical impedance measurements.
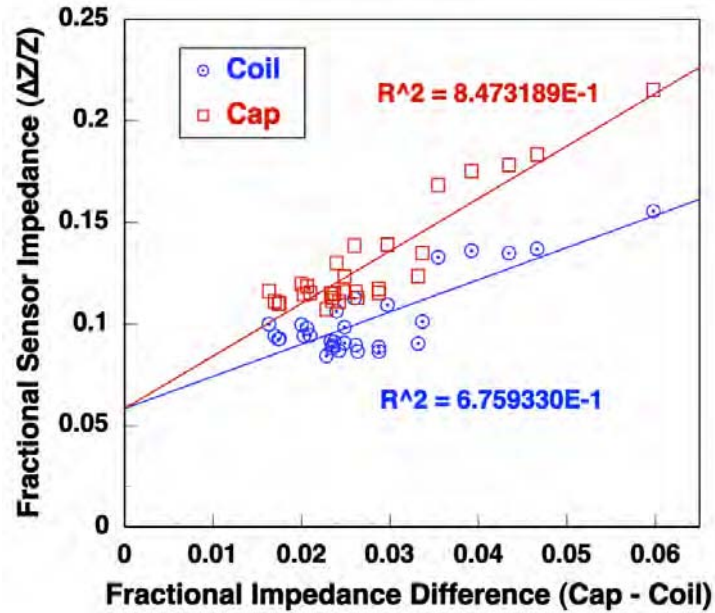
Figure 4.12. The Difference in Fractional Impedance Between the Two Sensors Plotted Against Fractional
Capacitive and Inductive Impedance for the Measurements in Figure 4.10

Coating Run 17

Coating runs 17-B, 17-BB, 17-E, and 17-EE were analyzed using the dual in-line impedance sensors.
This coating series was developed at ORNL to evaluate variations in the IPyC coating parameters applied
over a 500-µm ZrO_2 kernel and a standard buffer in runs 17-B and 17-E. Coating runs 17-BB and 17-EE
had a SiC layer applied to runs 17-B and 17-E.

Figure 4.13 shows the average impedance sensor measurements plotted for each coating run. The error
bars in the plot of Figure 4.13 are the standard deviations derived from measurements of 20 different
particles. These relatively large standard deviations should be attributed more to a large variation in
kernel diameter than to measurement uncertainty. Interestingly, the coil impedance is seen to increase
when the SiC layer was applied to run 17-B, as if there were some kind of annealing process occurring to
decrease the anisotropy or to increase the electrical conductivity. This was not observed for run 17-E. An
increase in capacitive impedance was observed for both runs after the SiC layer was applied, as expected.
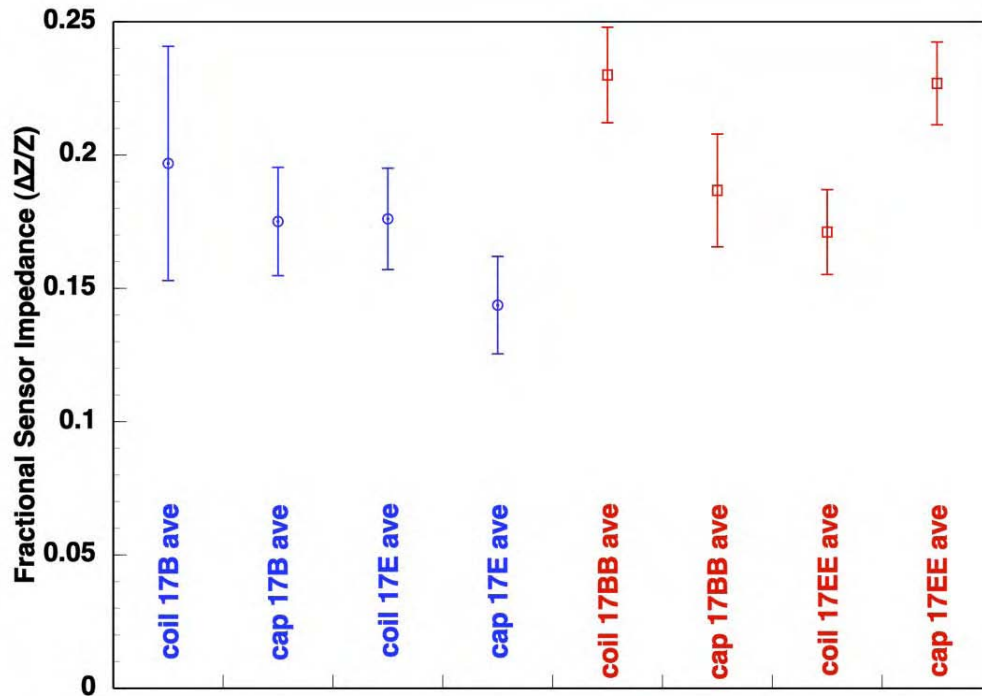
Figure 4.13. The Average Inductive and Capacitive Impedance Values Measured for Four Different Coating Runs. The Error Bars Designate the Standard Deviations from Measuring 20 Different Particles

UT Resonance

When an object is excited mechanically, it resonates at specific frequencies, which are controlled by properties including size, shape, composition, mechanical properties, and temperature. The technique where a specimen is mechanically excited over a range of frequencies has been termed RUS and is very sensitive to material properties. Because of its sensitivity to material properties and shape, RUS is commonly utilized to determine elastic constants of single crystal and polycrystalline materials and for QA/QC on finished parts.

The investigation of RUS centered on the feasibility of utilizing resonance measurements to determine the physical properties of TRISO particles. This investigation involved three main activities:

1. A literature review of current theories for predicting the resonant frequencies of spherical particles.

2. Calculations of the resonant frequencies of TRISO particles to predict the expected changes in frequency for various changes to the particle layers.

3. Experimental measurement of the resonant ultrasound spectra of spherical particles to determine the limits of the current system and to provide guidance to develop alternate measurement methods if needed.

In the first year (FY2003), a RUS system was acquired and initial measurements were made on metal spheres with diameters from 1.6 mm to 25 mm. This initial evaluation determined that the RUS system as configured could not determine the resonant frequencies for spheres smaller than about 4 mm because

of the large background resonance and relatively small sample responses. Two approaches were identified that could overcome this limitation. The first approach proposed particle excitation with EMATs. This proved to be unsuccessful because of low energy transfer from the EMAT to the particle. The second approach required the fabrication of custom contact transducers matched to the mass of the particles. This approach was deferred until this year (FY2005), when special transducers were procured and customized for use with sub-millimeter particles. Shown in Figure 4.14 are the original transducers and the new customized version. The customization included the removal of a buffer extension on the transducer face. Once this was removed, the transducer performed extremely well, as anticipated.

Figure 4.14. Modified and Original RUS Transducers

Figure 4.15 shows the transducer assembly and the system configuration. The particle is placed between the transmitting transducer and the receiving transducer during data acquisition.

Particle is placed between transducers.
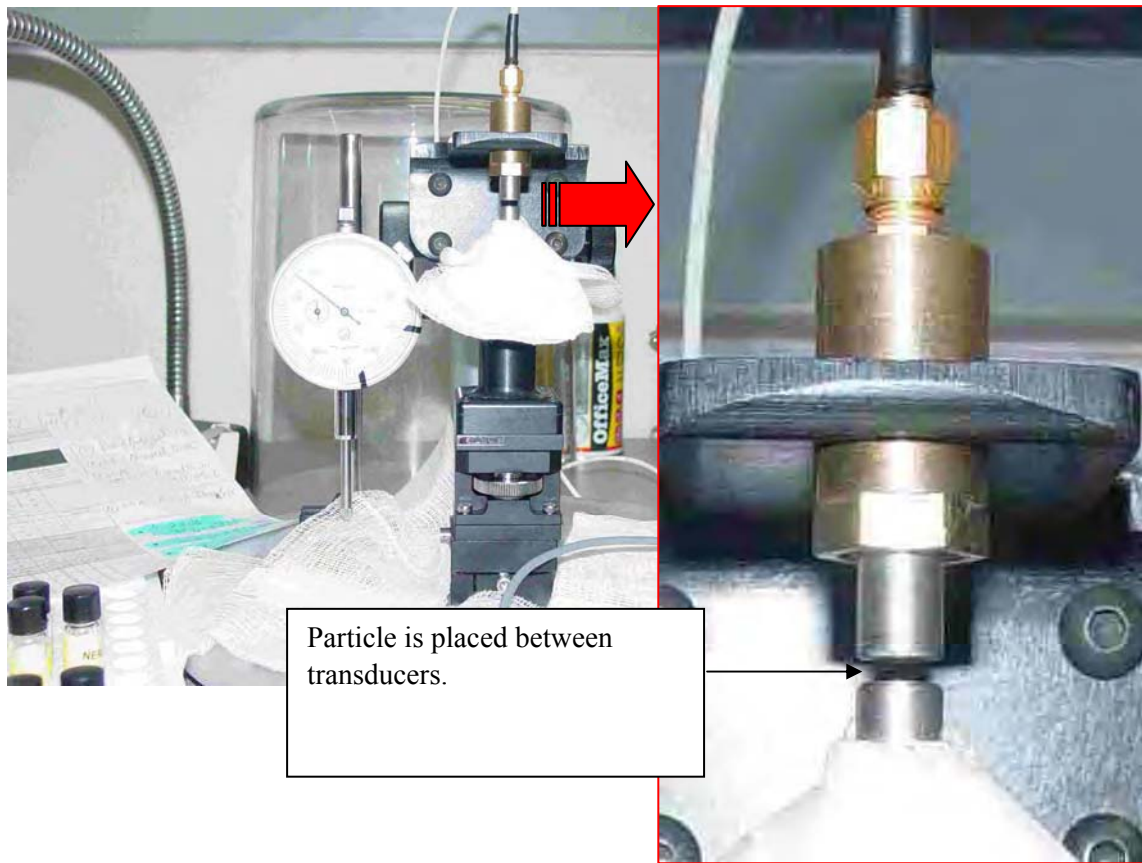
Figure 4.15. Resonant Ultrasound Spectroscopy System

A typical frequency scan is shown in Figure 4.16, where the resonant frequencies are indicated by peaks in the spectrum. As displayed in the image, the resonant peaks stand out clearly from the background.
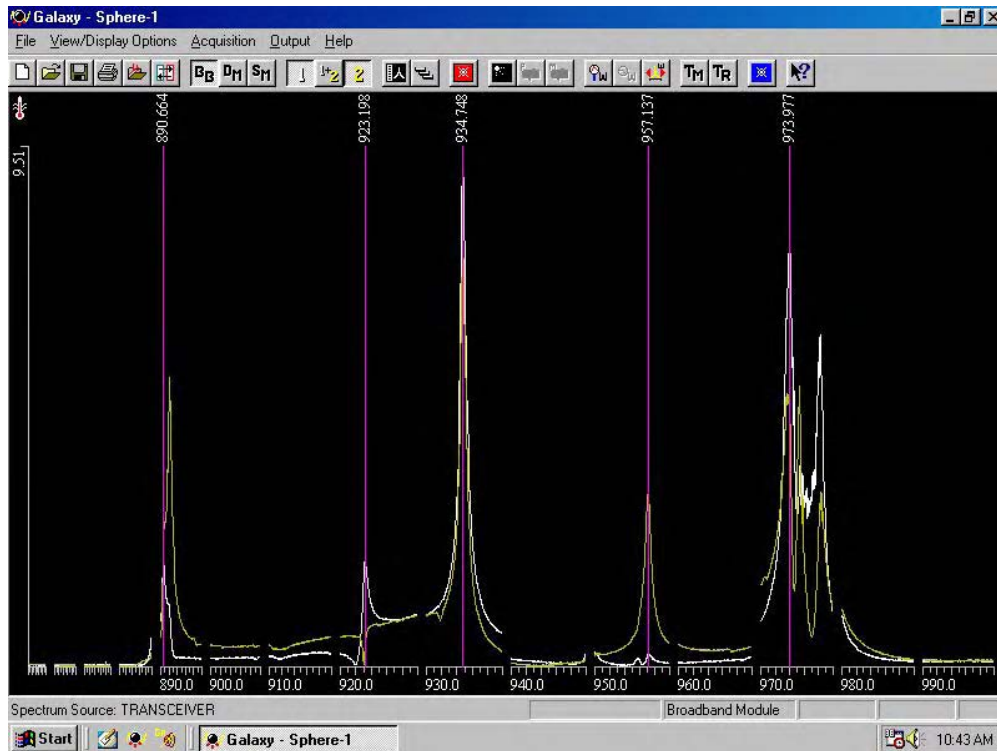
Figure 4.16. Typical RUS Frequency Scan

Studies performed during the project's first year showed that the signal-to-noise ratio was suitable for characterizing the surrogate TRISO particles and that there was a possibility to distinguish between a full TRISO particle and one with a missing SiC layer. Using knowledge of the particle dimensions from the radiography data in the particle library, multiple particles were chosen from several different batches. Repetitive RUS measurements were performed on these batches. Table 4.7 provides a list of the particles measured with the RUS system.

Table 4.7. Particles Measured with RUS

Batch Number	Objective
14-B	SiC on Kernel
5-B	Normal TRISO
12-B	Normal TRISO, missing SiC
13-A	Normal TRISO, thin SiC
6-CD	Normal TRISO, thin buffer
11-E	Normal TRISO, possible metal inclusion

Systematic measurements were made to determine the reproducibility and precision of the resonant measurements. Several resonance spectra were acquired on the particles listed in Table 4.8, with repetitive measurements performed on several particles from each batch. The resonance spectra of a single "normal" TRISO particle are shown in Figure 4.17.

4.20
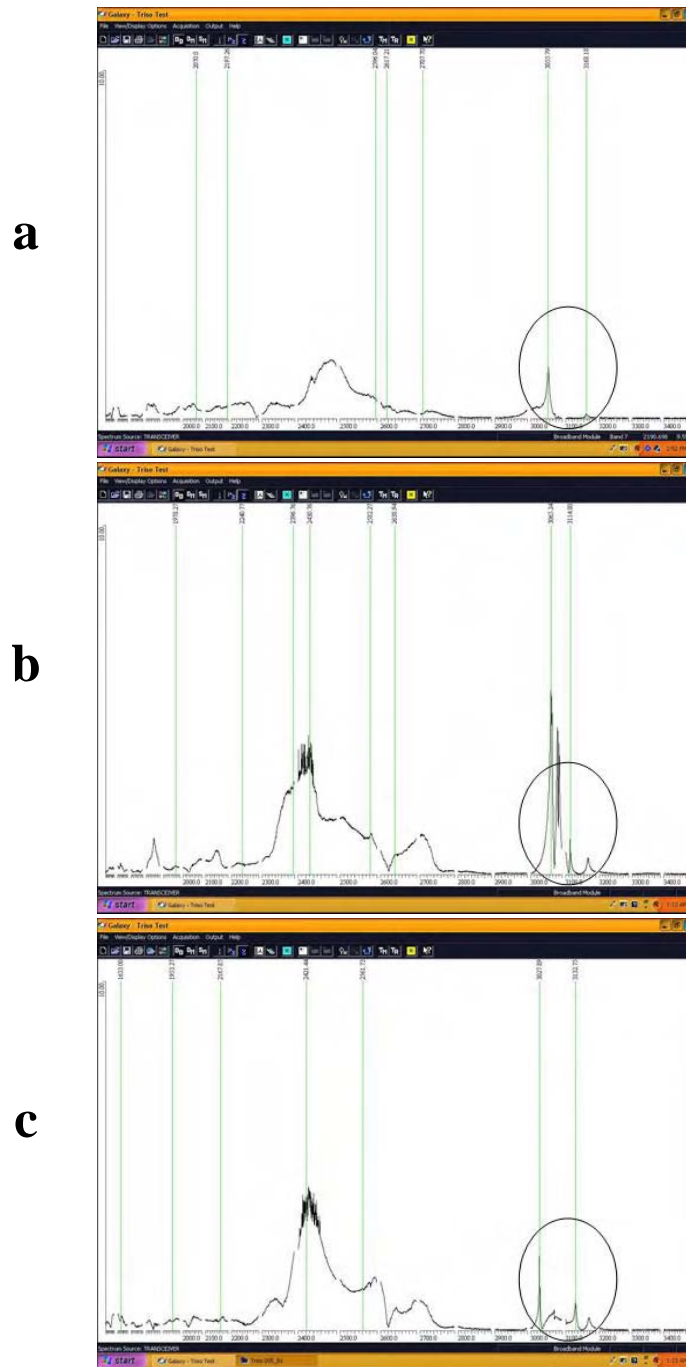
Figure 4.17. Resonance Spectra for Normal TRISO Particle 005 B-1: a) Run 1, b) Run 2, c) Run 3

The particle was removed from the testing apparatus between resonance spectrum measurements to determine the reproducibility of the measurements. The region near 3 MHz is circled to indicate resonant peaks that are above the background noise level. The resonance spectrum with no particle is shown in Figure 4.18.
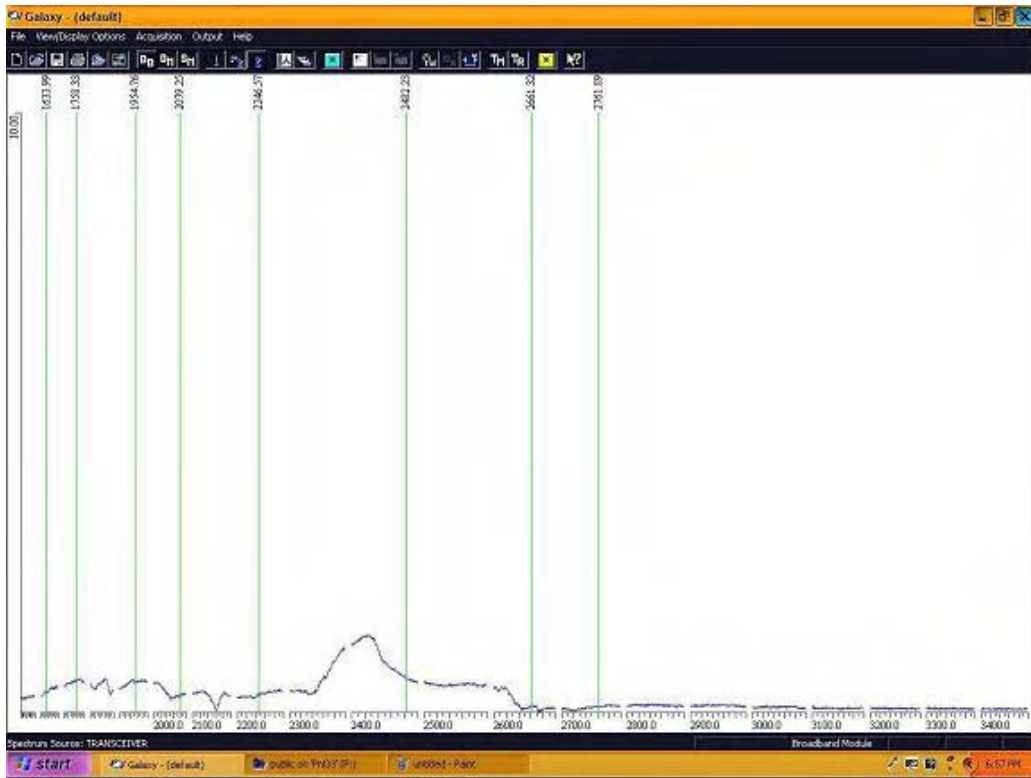
Figure 4.18. Background with Small Air Gap

While the structure and number of peaks in this region varies between runs and particles, the dominant peaks above the background are centered in the region near 3 MHz. These peaks are well above the measurable noise level. These results indicate that the RUS system is capable of measuring the resonance spectrum on sub-millimeter particles. While multiple runs on all the particles were measured, only representative data will be presented to conserve space.

The resonance spectra for two additional normal TRISO particles are shown in Figure 4.19. Again there is some variability between the location, number, and shape of the peaks; however, the general location is similar and well above the noise level.
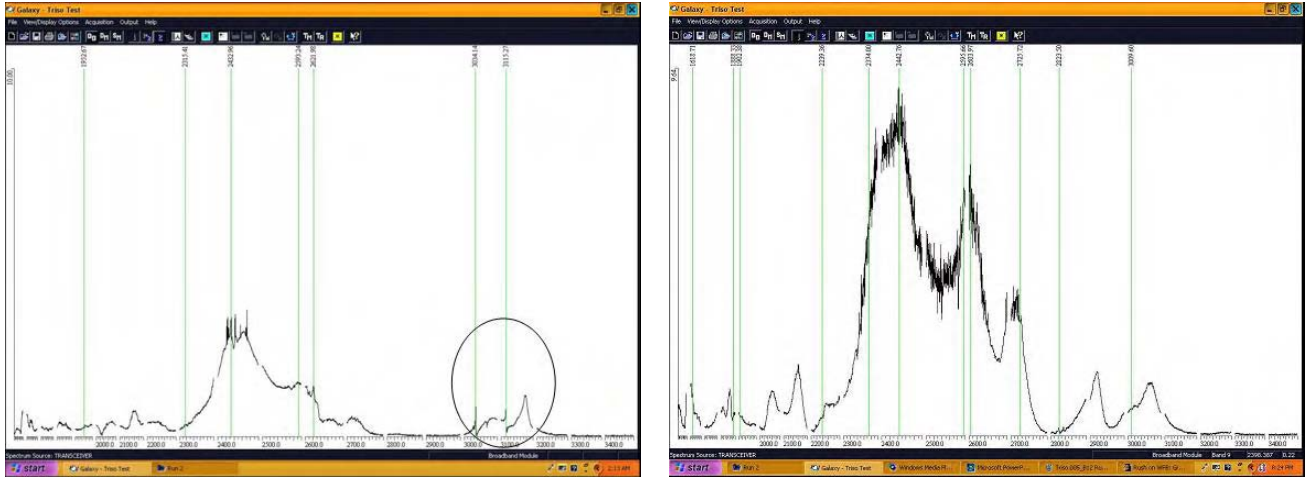
Figure 4.19. Resonance Spectra For normal TRISO Particles 005 B-8 and 005 B-12

Several particles with defects were measured to determine if the resonance of particles with defects could be distinguished from those produced by normal particles. Representative spectra for a TRISO particle with a thin SiC layer are shown in Figure 4.20.
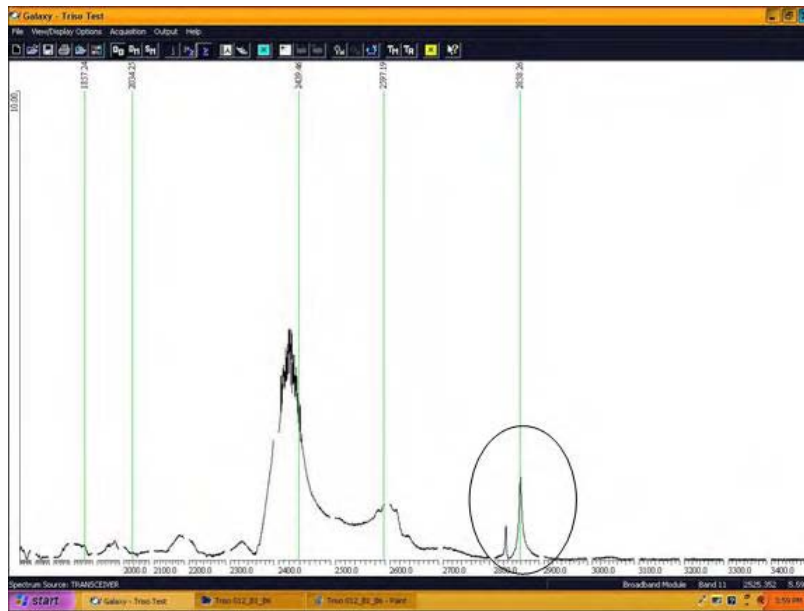
Figure 4.20. Resonance Spectra for Thin-SiC TRISO Particle 013 A-3

The dominant peaks above the background noise were shifted to the 2.8-MHz region, as indicated by the highlighted circle in the figures. The dominant peaks are distinctly separate from the peaks from the normal TRISO particle, indicating the sensitivity of the resonant modes to small changes in the internal structure of small particles. As a further indication of the power of RUS to distinguish defective TRISO particles, Figure 4.21 shows the resonance spectra for TRISO particles with no SiC layer. In this case, the dominant peaks are shifted down into the 2-MHz range, as indicated by the circled region. These particles can easily be separated from the particles with thin SiC layers and the normal TRISO particles.
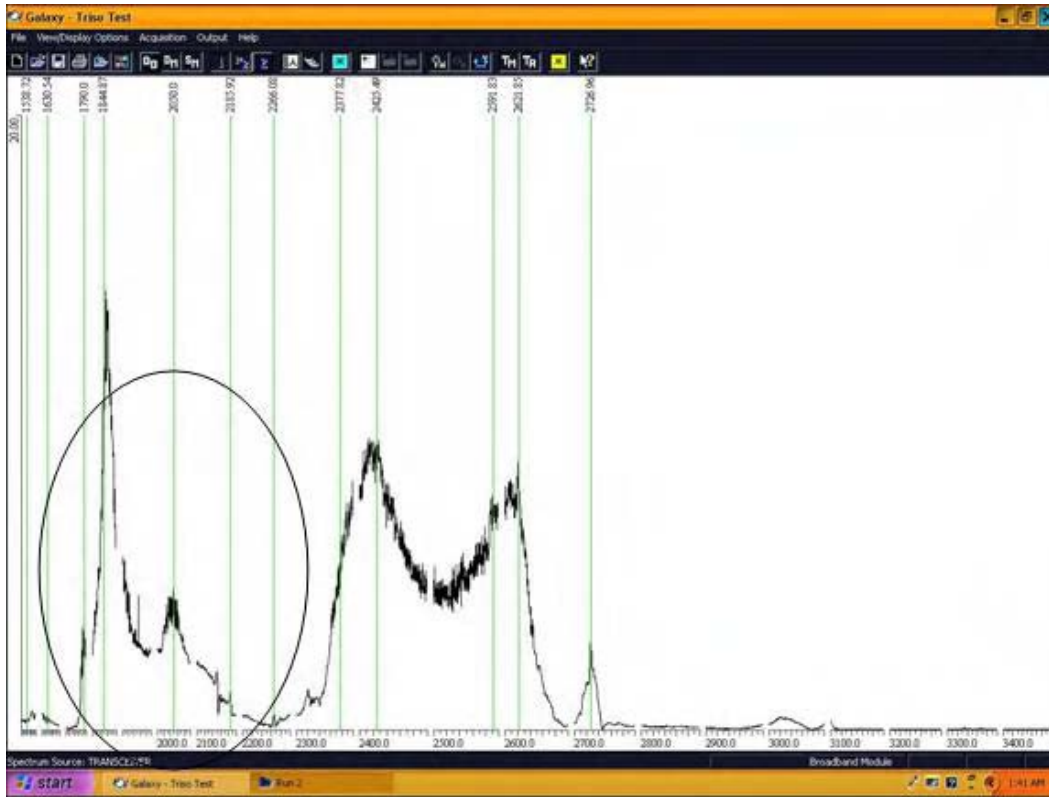
Figure 4.21. Resonance Spectra for No-SiC TRISO particle 012 B1-B6

To further test the sensitivity of the resonant modes to internal defects, the resonance spectra from particles with metal inclusions (although not verified by destructive analysis) are shown in Figure 4.22. Even though, there is variability in the resonant modes, these particles with possible metal inclusions are distinctly separable from normal TRISO particles and from those with thin or missing SiC layers.

A-1
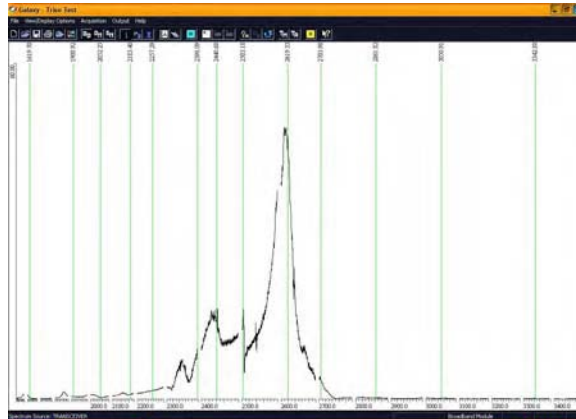
A-2
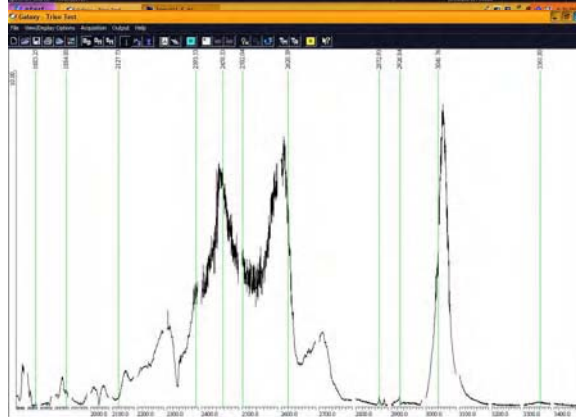
A-3
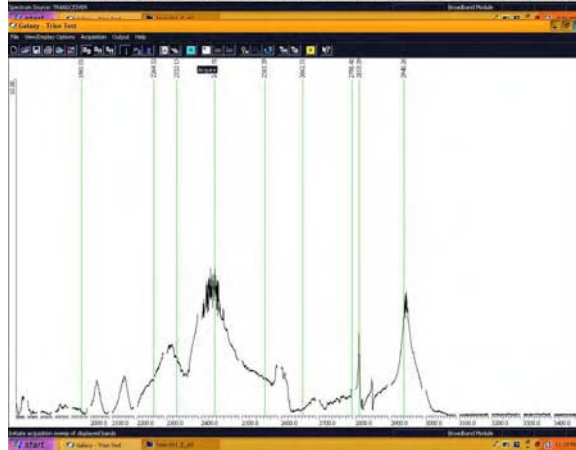
Figure 4.22. Possible Metal Inclusion 11-E A-1, A-2, A-3

Acoustic Microscopy

This task was suspended to divert efforts to the in-line flaw detection methods that showed greater potential for developing future automated flaw detection systems.

Optical

An evaluation of this method, demonstrating the potential capability for in-line coating inspection, is complete. The method was not considered suitable for continued development.

Task 7. NARROW LIST AND FURTHER DEVELOP REMAINING NDE METHODS

Electromagnetic

Inductive and capacitive measurements have shown the most promise for meeting the requirements of this project. These methods were chosen to be further refined this fiscal year.

Ultrasonic Resonance

The attractive spectral features reported in earlier phases of this project prompted further investigation into this method. New transducers were procured to support this activity this year and are discussed in Task 6.

Acoustic Microscopy

This task was suspended in favor of other tasks showing more promise for achieving the project objective.

Optical

An evaluation of this method, demonstrating the potential capability for in-line coating inspection, was completed. Further development of this method was weighed against the potential benefit relative to the other methods under evaluation. No further work was performed this year.

Task 8. ON-PROCESS MEASUREMENTS

Further work was done in FY2005 to establish whether the bulk measurement capabilities of the air-coupled ultrasonic technologies were applicable to TRISO particle examination. The original purpose of this task was to evaluate the feasibility for air-coupled ultrasonic technologies to monitor particle size of next-generation nuclear fuel particles during coating processes. Preliminary work was carried out in FY2003, but with inconclusive results. In this specific case, a need for determination of average particle size during the coating process was identified for process monitoring purposes. As the particles are being manufactured, layers are applied by temporarily suspending the particles in air while spraying the coating material. Thus, there exists a need for an effective, rapid, non-invasive, non-contact method for evaluation of average particle size while the particles are suspended in air. The specific requirements include monitoring changes in the coating thickness as small as 2 µm for a 1000-µm diameter particle.

The use of air-coupled ultrasonic measurements was evaluated for in-situ measurements of particle properties. This approach requires a correlation of measurable ultrasonic parameters such as acoustic speed of sound (time-of-flight), attenuation (amplitude), and frequency response information, to the conditions, geometry, and physical properties of the material under test. For this evaluation, glass spheres of three average sizes were used as surrogates to the nuclear fuel particles. An air-coupled ultrasonic pulse-compression technique was used to ensonify the glass spheres with sufficient energy to measure the

speed of sound and attenuation. Based on the results from this testing, the air-coupled ultrasonic technique does not appear to have the required sensitivity to changes in coating thickness for the frequency range and particle sizes of interest.

Technical Background

This section describes the operation principles of the ultrasonic data acquisition system used to conduct preliminary trials on the surrogate glass spheres. It covers technical background information and issues relating to the data acquisition methodology.

Ultrasonic sensors are used in a wide variety of applications. New fields of ultrasonic sensor and system applications include process monitoring and control, automotive examination techniques, chemical analysis, medical imaging, material property measurements, etc. These applications have enjoyed a rapid increase in interest in recent years. The development of new ultrasonic sensors and technology platforms has been accelerated by progress in electronics, availability of new piezoelectric and piezocomposite materials, exploitation of new technologies, and the need for new or more accurate analysis methods in the industrial sector. The low-frequency ultrasonic data acquisition platform uses ultrasonic sensors, or transducers, which transform an electrical signal into an ultrasonic wave and vice versa. They actively transmit and/or receive acoustic energy. Piezoelectricity is the most commonly used physical mechanism for generating and receiving sound in nondestructive evaluation applications. In this application, however, air-coupled, electrostatic membranes were used to generate and receive the acoustic waves. The system operates in a pitch-catch (through-transmission) mode, where one transducer is used as a source and the other is used to receive the sound. As the sound field propagates through the glass spheres used in this study, the acoustic wave is modified by the geometry, microstructure, and material properties of the spheres. The ultrasonic signals carry information about the physical parameters of the material.

The laboratory system used in this study is capable of efficient operation over a wide range of frequencies. Low frequencies from just above the audible range (around 20 kHz) to the lower ultrasonic range (around 2 MHz) can be employed using this bench-top system. Lower ultrasonic frequencies allow for increased penetration of highly attenuative materials, while higher frequencies provide increased resolution and greater measurement sensitivity for less attenuative, materials. The use of ultrasonic energy enables the data acquisition system to be non-invasive and non-intrusive as the acoustic wave is capable of penetrating through materials. The air-coupled configuration allows the sensors to be employed without the use of an acoustic wetting agent, gel, or water for coupling purposes. The ultrasonic technology is based upon the use of compressional (or longitudinal) wave energy and generates the ultrasonic energy by utilizing piezoelectric, piezocomposite, and electrostatic materials.

A poor signal-to-noise ratio (SNR) is very common in air-coupled ultrasonic testing due to impedance mismatches between air and most other materials. Traditional ultrasound may improve the SNR by simply using high-power pulse transmission, commonly using tone-burst excitation techniques. A long-duration tone burst can efficiently transmit large amounts of energy into air or any other medium. However, tone bust excitation generally results in poor time-of-flight (TOF) accuracy and provides a narrow-band response in the frequency domain. A long-duration frequency sweep (chirp) can also efficiently transmit energy into a medium; however, as will be discussed later, signal processing techniques can be used to convert a long chirp into a compressed broadband pulse for extremely accurate TOF measurements and a correspondingly broadband response in the frequency domain.

Pulse compression is a technique that has been employed in both radar and medical ultrasound. It is used to transmit large amounts of energy over a long period of time without sacrificing temporal resolution. A wide-bandwidth, long-duration frequency chirp is commonly used to excite the source (transmitting transducer). This pulse is received by one or more receiving transducers. Cross-correlation between the transmitted pulse and the received pulses results in a waveform containing the same time, amplitude, and spectral information as the received pulse. Pulse compression has recently been used with broadband air-coupled transducers, where energy transmission, SNR, and TOF accuracy are relatively low compared with conventional direct-coupled ultrasound. Previous researchers found that pulse compression provided the air-coupled system with the ability to detect received pulses even when they were well below the noise floor due to the frequency encoded transmitted pulse. In addition, they were able to resolve closely-spaced return echoes from various reflection sources with high accuracy, which was not possible with typical ultrasonic tone-burst or square-wave excitation technologies. The pulse compression technique has also been used in conjunction with air-coupled ultrasound to interrogate food containers and detect foreign objects within food materials.

Pulse compression is a signal processing technique carried out by cross-correlating a transmitted chirp with a received signal. The cross correlation function effectively locates the specific frequency pattern within the received waveform and outputs a compressed waveform containing information associated with the frequency-dependent amplitude and transit time of the transmitted pulse. This procedure is extremely useful when trying to locate echoes within a signal whose amplitude is well below that of the noise floor. The energy associated with the compressed cross correlation signal is directly related to the duration of the transmitted chirp pulse. Therefore, a longer-duration pulse is employed to achieve a higher SNR.

As stated earlier, the pulse compression technique results in accurate TOF measurements. This is directly related to the frequency bandwidth of the transmitted and received pulses, where a larger bandwidth results in higher TOF resolution. Effectively, the cross-correlation output (also known as deconvolution) will appear as a broadband pulse with a width inversely proportional to the bandwidth of the transmitted chirp. The broadband pulses in the cross-correlation result contain not only TOF information, but also frequency-dependent amplitude information that is used to calculate attenuation of the ultrasonic signals. Another advantage of the pulse compression technique is the discrimination of multiple, closely-spaced echoes. A traditional ultrasonic tone burst measurement technique cannot discriminate between closely spaced echoes, but the deconvolution of a long-duration, broadband, transmitted chirp results in a compressed cross correlation function having multiple narrow-width pulses, allowing multiple echoes to be easily resolved in time.

Specimens Used in this Evaluation

Glass spheres were used as surrogates for the next-generation fuel particles. Three size distributions (Figure 4.23) of particles were chosen with average particle diameters of 550 μm, 800 μm, and 1100 μm. These sizes were chosen to determine if current state-of-the-art ultrasonic test methods are capable of discriminating different-sized particles while the particles are suspended in air.
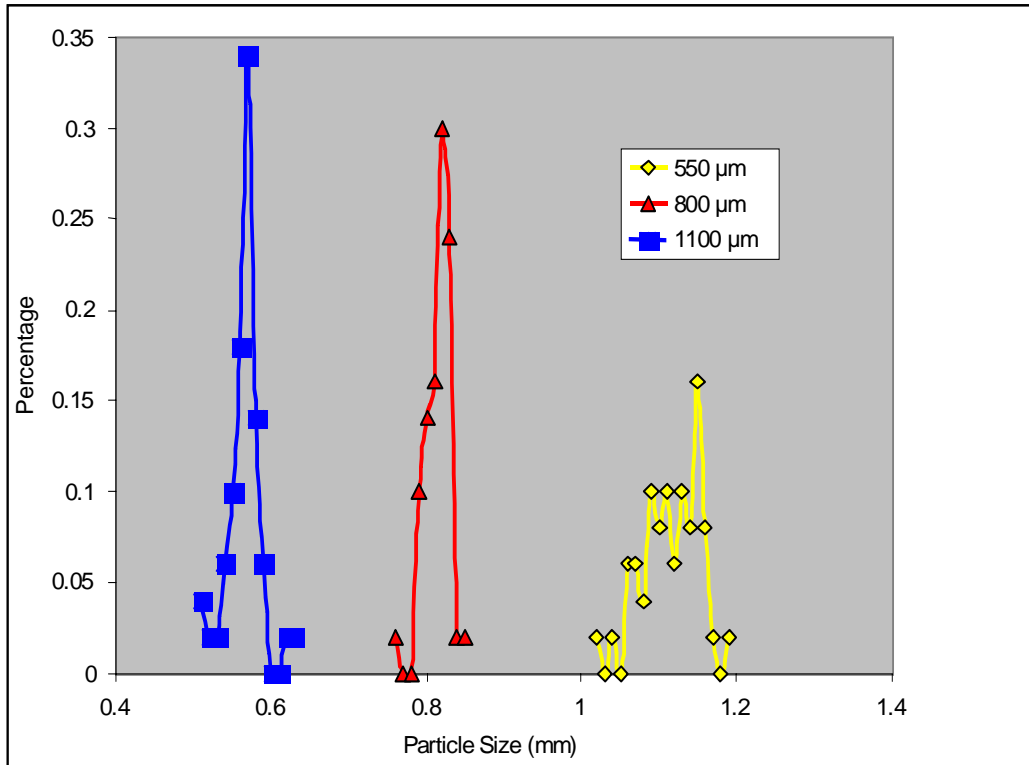
Figure 4.23. Size Distribution of Surrogate Glass Spheres as Provided by Manufacturer

Technical Objective

The objective of this work was to assess if a non-contact, air-coupled, ultrasonic technique was capable of detecting differences in average particle diameter. Specifically, there was a desire to detect changes of 2 μm for a 1000-μm-diameter particle.

Approach/Concept

The ultrasonic properties of the glass-sphere specimens were characterized using low-frequency ultrasound, (i.e., frequencies between 20 kHz and 2 MHz). PNNL utilized specialized transducers and ultrasonic equipment to attempt to penetrate the spheres in a pitch-catch (through-transmission) mode. The effects of frequency, sound-field propagation, transducer characteristics, transmitter excitation methods, and signal processing algorithm optimization were evaluated using existing equipment and methodologies. The glass spheres were contained in a plastic cylinder of known height and suspended on a #240 mesh screen sieve (0.066-mm square opening). This configuration allowed for a consistent volume of particles, consistent boundary effects, and a known propagation distance. Broadband ultrasonic waves were propagated through the volume of glass spheres by orienting the transmitting transducer below the suspended particles and the receiving transducer above the particles. The experimental setup is shown in Figures 4.24 and 4.25.
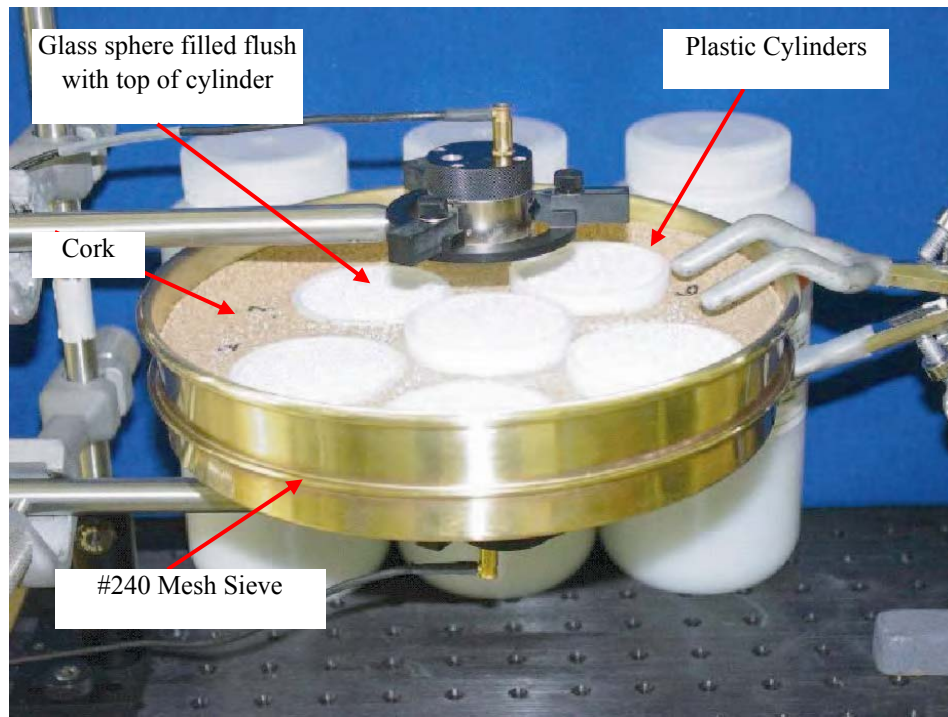
Figure 4.24. Experimental Setup for Ultrasonic Interrogation of Surrogate Glass Spheres
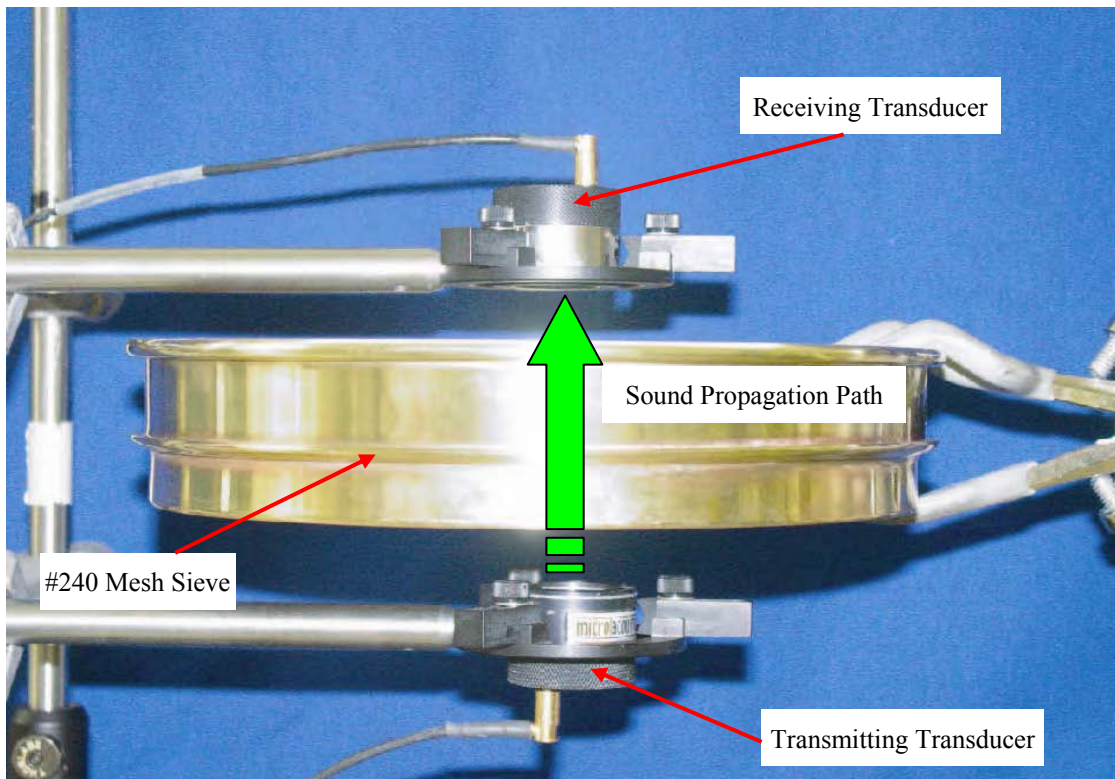
Figure 4.25. Experimental Setup Showing Ultrasonic Propagation Path Through the Sieve and Cylindrical Volume of Glass Spheres

Results

The speed and relative attenuation of the propagating sound wave were measured using the results from the broadband pulse compression technique. Although the signals were highly attenuated, deconvolution allowed the received waveforms to be located and analyzed for TOF, amplitude, and frequency content. Wave speed through each of the different-size glass sphere volumes was calculated based on the average TOF from several repeated measurements. As can be seen in Figure 4.26, spheres with an average diameter of 800 µm exhibited the highest wave speed of 1034 m/s, while the 550-µm and 1100-µm spheres exhibited wave speeds of 1008 m/s and 929 m/s, respectively. These results contradict the anticipated results that the 550-µm spheres would have the highest wave speed due to a higher mass of glass spheres within the same volume. One possible reason for this phenomenon is the dependence of wave speed on more than one variable such as: 1) glass mass per volume, 2) air-glass interactions per volume, or 3) varying material properties (diameter dependent) for different-size spheres. Although the material make-up of the glass spheres should be identical, there could be density or elastic property differences between particle sizes. Again, the results presented here are contradictory to expected behavior, but there could be some variables that have not been taken into account.
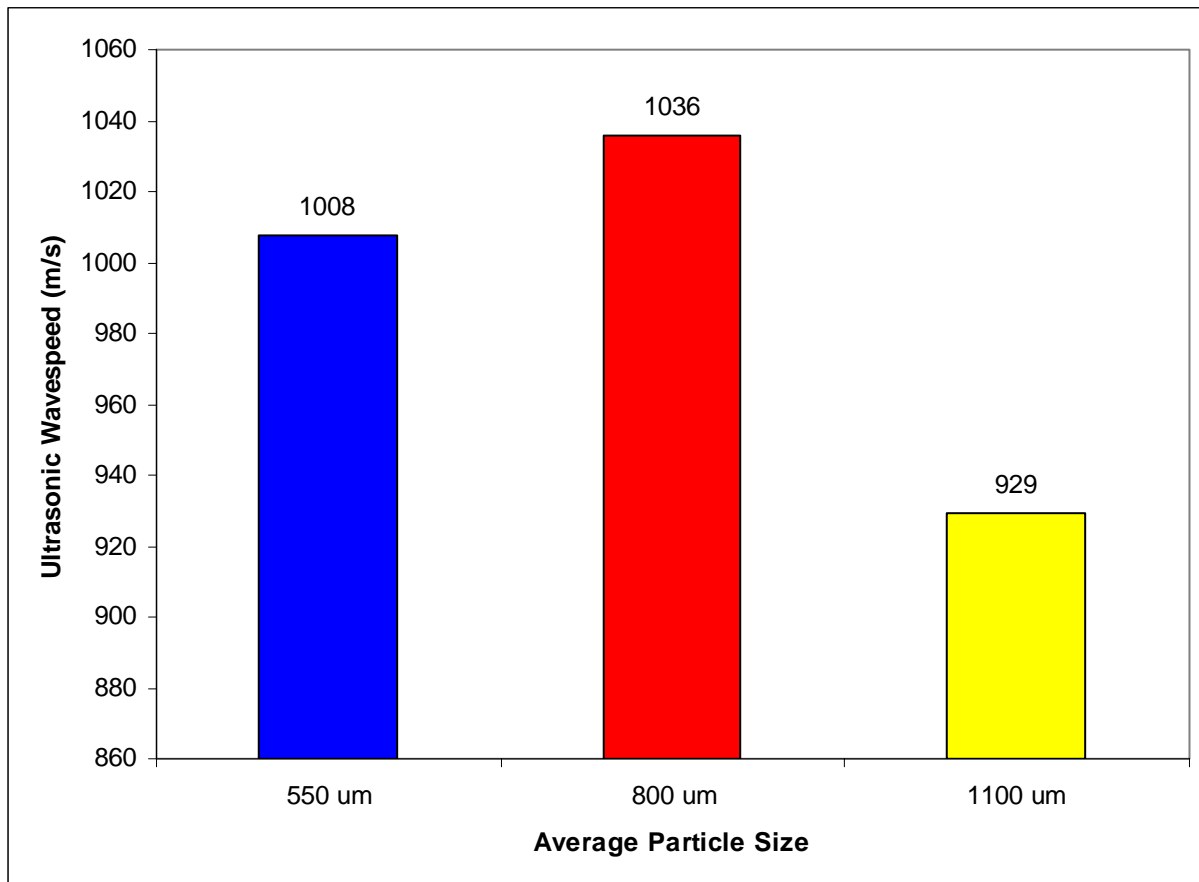
Figure 4.26. Comparison of Ultrasonic Velocity Through Glass Spheres

Relative attenuation measurements were made by comparing the frequency-dependent signal amplitude through two different wave propagation paths, thus minimizing the effects of acoustic impedance and

various other factors that affect ultrasonic wave propagation. Using the data from multiple measurements, analysis of variance was performed on the data and 95% confidence limits were calculated for amplitude at each frequency. As can be seen in Figure 4.27, the differences in attenuation spectra from each sphere size are small when compared to the actual particle size distributions. For the frequency range presented here, the wavelengths varied from 2 cm down to 0.5 cm in the glass spheres. Therefore, the wavelengths varied from 5 to 40 times the average particle diameter. The average sphere sizes could possibly be distinguished by focusing on attenuation measurements in localized frequency ranges. Another possible size discrimination method would be to use frequency-dependent attenuation patterns. The latter approach would require additional measurements to determine the frequency response of these materials and the sensitivity to layer thickness and potential feasibility for in coater measurements. Further advances in resolution may be accomplished by employing alternative post-processing techniques such as chemometric analysis.
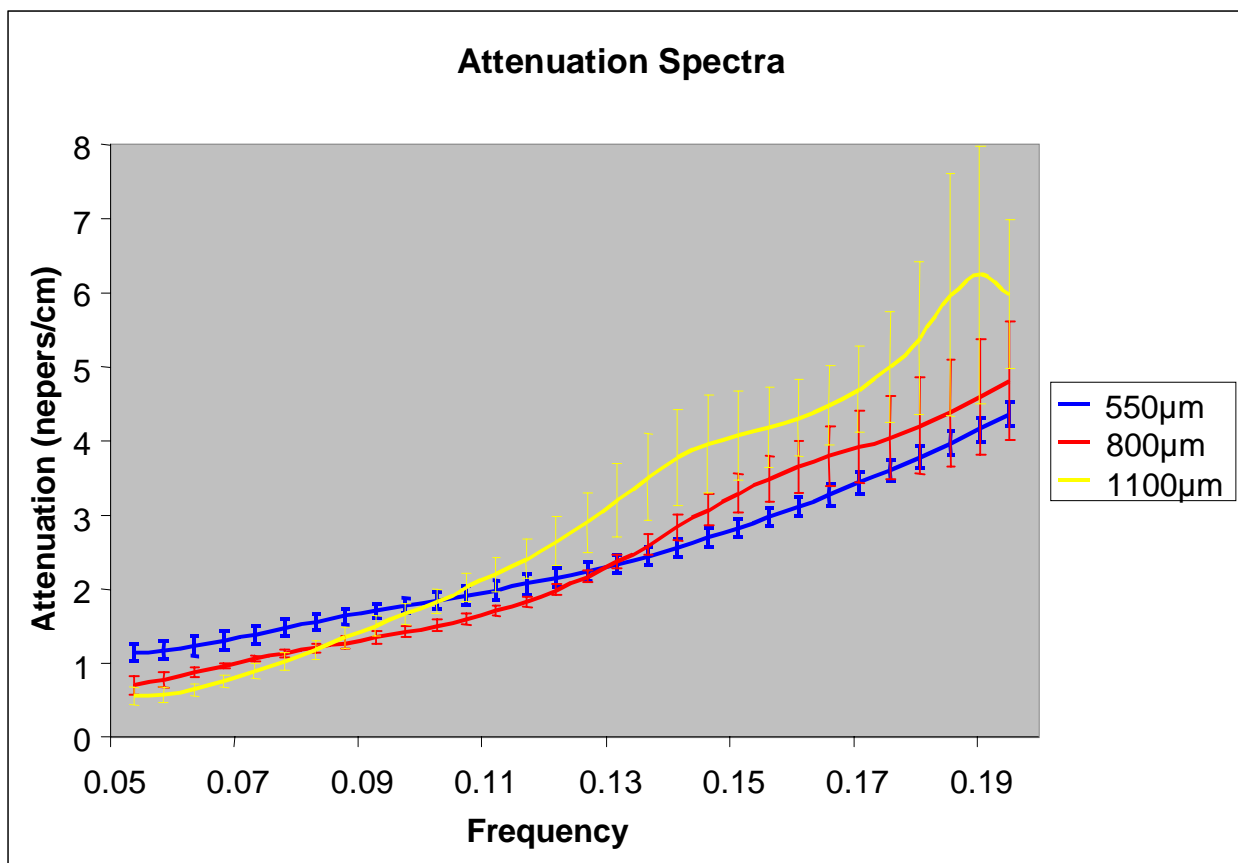
Figure 4.27. Comparison of Frequency-Dependent Attenuation of Glass Spheres

Task 9. ESTABLISH STANDARD SIGNATURES AND FLAW LIBRARY

This task developed a library of data characterizing both nominal and flawed particles. These data formed a basis for developing and calibrating the NDE techniques considered in this project for automated defect detection.

Populating the flaw library was done using the radiographic and electromagnetic techniques. The physical dimensions of the particles were measured at ISU by X-ray radiography aided by a software measurement tool. After measurements using the stationary eddy current coil configuration shown in Figure 4.28, the inductive impedance values were calculated in terms of fractional impedance relative to the empty-coil impedance. The stationary capacitive sensor shown in Figure 4.3 was used to measure capacitive impedance values, then fractional values were calculated relative to the impedance of the empty capacitive sensor.
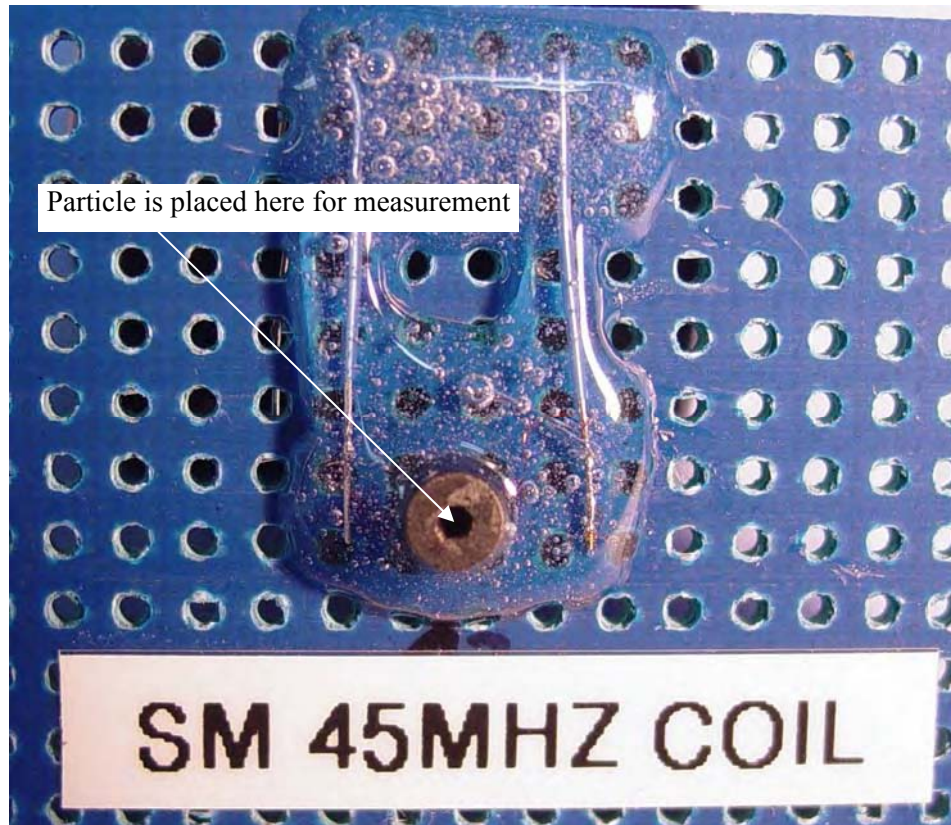
Figure 4.28. The Stationary Induction Coil

Figure 4.29 provides a small sample of the particle library. Particle batches are listed with each of the parameters measured. This list provides a basis for the statistical analysis developed in the final phase of the project and is described in depth in Section 5 of this final report. The entire particle library is provided in Appendix B of this final report.

Run Number	Date Shipped	Kernel dia (µm)	Particle batch(s) to use	Kernal size spilt by SA	Buffer Thickness (µm)	IPYC Thickness (µm)	SiC Thickness (µm)	OPYC Thickness (µm)	Objective	Inductive Impedance Samples	Capacitive Impedance Samples	Radiography Samples	Set #1	Set #2	RT Kernel dia (µm)	RT Buffer Thickness (µm)	RT IPYC Thickness (µm)	RT SiC Thickness (µm)	RT OPYC Thickness (µm)	Inductive Excitation Frequency (MHz) [older]	Inductive Impedance (Fractional) [older]	Capacitive Excitation Frequency (MHz) [older]	Capacitive Impedance (Fractional) [older]	Inductive Excitation Frequency (MHz) [opt]	Inductive Impedance (Fractional) [opt]	Capacitive Excitation Frequency (MHz) [opt]	Capacitive Impedance (Fractional) [opt]
6-CD	23-Feb-2004	350-550	400 and 500	50/50	20	40	35	40	Normal TRISO, thin buffer	20	0	7	006-CD-A1							42.500	1.657E-01			45.000	1.297E-01		
													006-CD-A2		419	18.5	31.2	59.0	40.0	42.500	1.066E-01			45.000	9.944E-02		
													006-CD-A3		543	15.3	26.1	49.4	39.9	42.500	1.637E-01			45.000	9.229E-02		
													006-CD-A4							42.500	1.252E-01			45.000	1.296E-01		
													006-CD-A5		508	18.1	27.2	53.9	43.5	42.500	1.498E-01			45.000	1.370E-01		
													006-CD-A6							42.500	1.106E-01			45.000	9.731E-02		
													006-CD-A7							42.500	1.161E-01			45.000	9.656E-02		
													006-CD-A8							42.500	1.600E-01			45.000	9.253E-02		
													006-CD-A9		400	26.6	34.1	56.3	41.5	42.500	1.230E-01			45.000	1.049E-01		
													006-CD-A10		489	18.8	24.2	50.1	40.0	42.500	1.450E-01			45.000	9.936E-02		
													006-CD-A11							42.500	1.584E-01						
													006-CD-A12							42.500	1.262E-01						
													006-CD-A13							42.500	1.653E-01						
													006-CD-A14							42.500	1.272E-01						
													006-CD-A15							42.500	1.159E-01						
													006-CD-A16							42.500	1.152E-01						
													006-CD-A17							42.500	1.561E-01						
													006-CD-A18							42.500	1.215E-01						
													006-CD-A19		533	14.9	23.7	50.4	42.8	42.500	1.724E-01						
													006-CD-A20		424	17.9	26.0	56.1	40.1	42.500	1.177E-01						
														006-CD-B1										45.000	9.155E-02	45.000	1.149E-01
														006-CD-B2	380	62.5		58.8	35.9					45.000	8.650E-02	45.000	1.128E-01
														006-CD-B3	371	67.8		56.7	41.6					45.000	9.423E-02	45.000	1.112E-01
														006-CD-B4	501	26.4	29.8	52.0	42.2					45.000	1.361E-01	45.000	1.753E-01
									Normal TRISO, thin buffer					006-CD-B5	434	55.1		56.8	38.4					45.000	1.012E-01	45.000	1.348E-01
														006-CD-B6	392	68.3		59.1	41.4					45.000	9.988E-02	45.000	1.162E-01
														006-CD-B7										45.000	8.690E-02	45.000	1.111E-01
														006-CD-B8										45.000	8.967E-02	45.000	1.158E-01
														006-CD-B9	520	23.4	26.4	51.8	42.6					45.000	1.348E-01	45.000	1.783E-01
														006-CD-B10										45.000	8.794E-02	45.000	1.114E-01
														006-CD-B11	552	26.9	24.6	49.1	40.8					45.000	1.555E-01	45.000	2.153E-01
														006-CD-B12										45.000	9.429E-02	45.000	1.153E-01
														006-CD-B13	499	48.7		48.6	35.5					45.000	1.369E-01	45.000	1.836E-01
														006-CD-B14	403	65.1		57.1	40.5					45.000	1.062E-01	45.000	1.301E-01
														006-CD-B15										45.000	9.844E-02	45.000	1.233E-01
														006-CD-B16										45.000	8.929E-02	45.000	1.128E-01
														006-CD-B17										45.000	1.328E-01	45.000	1.683E-01
														006-CD-B18										45.000	9.963E-02	45.000	1.196E-01
														006-CD-B19	379	51.6		61.3	37.5					45.000	8.432E-02	45.000	1.071E-01
														006-CD-B20	368	65.1		58.5	42.5					45.000	9.275E-02	45.000	1.102E-01
														006-CD-B21	443	24.1	31.7	54.8	42.0					45.000	1.126E-01	45.000	1.386E-01
														006-CD-B22										45.000	9.124E-02	45.000	1.149E-01
														006-CD-B23	400	54.4		59.1	42.6					45.000	9.245E-02	45.000	1.098E-01
														006-CD-B24	403	70.3		55.5	37.8					45.000	1.094E-01	45.000	1.391E-01
														006-CD-B25										45.000	9.040E-02	45.000	1.236E-01
														006-CD-B26										45.000	8.862E-02	45.000	1.173E-01
														006-CD-B27										45.000	9.424E-02	45.000	1.145E-01
														006-CD-B28										45.000	9.786E-02	45.000	1.185E-01
														006-CD-B29	396	20.6	32.4	57.8	41.0					45.000	8.653E-02	45.000	1.153E-01
														006-CD-B30										45.000	9.071E-02	45.000	1.156E-01

Figure 4.29. Sample from the Particle Library

Task 10. EVALUATE ELECTRICAL PROPERTY EQUIVALENCE BETWEEN DUO_2 AND ZrO_2

Four batches of uranium-bearing AGR particles were shipped to ISU in early FY2005. These were analyzed at ISU from March 1-4, 2005. The impedance analyzer devoted to this task at PNNL was shipped to ISU to conduct the electrical impedance measurements side by side with the radiographic measurements. The four sample sets evaluated included:

1. 500-µm DUO_2 kernels

2. 350-µm DUO_2 kernels

3. 350-µm NUCO kernels

4. TRISO coated 500-µm DUO_2 kernels

The inductive and capacitive impedance sensors shipped to ISU were designed to investigate particles having a total diameter between 400 µm and 900 µm. The fully coated 500-µm DUO_2 particles were found to be too large to fit inside either sensor and could not be evaluated with the in-line electrical methods.

All three sets of bare kernels were found to have no effect on the inductive impedance sensor, as expected, since no electrically conductive coatings are present. Therefore, most of the electrical measurements were obtained with the capacitive sensor on the 350-µm and 500-µm kernels.

A comparison between the capacitive impedance and the radiographically determined diameter of the nominal 500-µm DUO_2 kernels is shown in Figure 4.30. The capacitive impedance sensor used for this measurement could have been made more sensitive to changes in kernel diameter and stoichiometry by reducing its size from 900 µm to 600 µm.
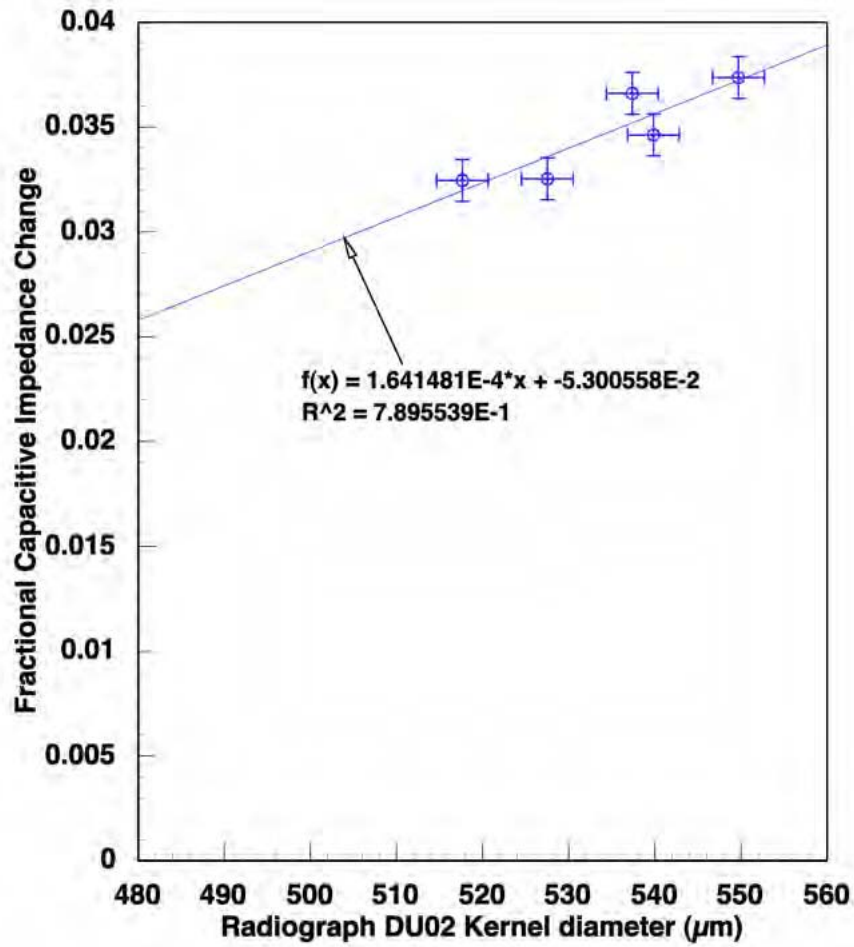
Figure 4.30. Fractional Capacitive Impedance Plotted Against Kernel Diameter Measured By Micro-Focus Radiography

The measurement sensitivity was reduced even further for the smaller 350-μm kernels due to a reduced sensor fill-factor. It fact, "rattle-room" was observed to surround most of the particles of less than 400-μm diameter. As shown in Figure 4.31, quantitative information was obtained, but at a larger uncertainty.
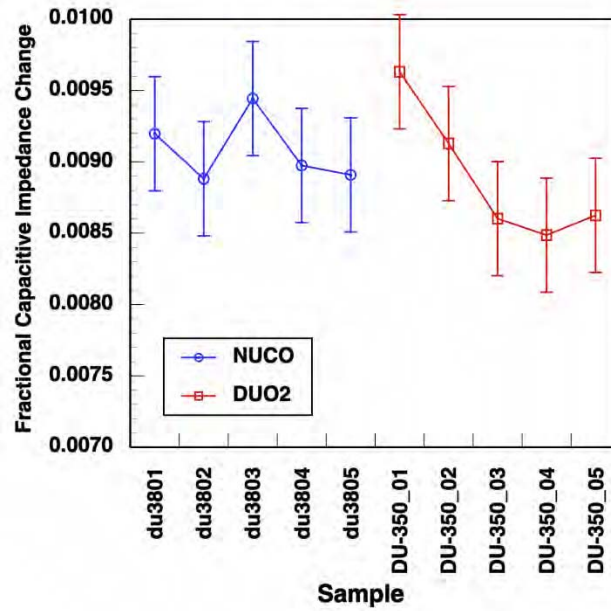
Figure 4.31. Fractional Capacitive Impedance as Measured for Five DUO$_2$ and Five NUCO Kernel Samples of 350-µm Diameter

An estimate was made for the dielectric constant of DUO$_2$ by comparing the capacitive impedance with that of ZrO$_2$ beads of similar diameter. The results for these measurements are shown in Figure 4.32. Results from a more thorough evaluation of the capacitive impedance of beads made from different materials are shown in Figure 4.33. Figure 4.34 shows only the average capacitive impedance values. These measurement results suggest that DUO$_2$ has a dielectric constant slightly greater than that of ZrO$_2$, and that ZrO$_2$ has a significantly greater dielectric constant than glass.
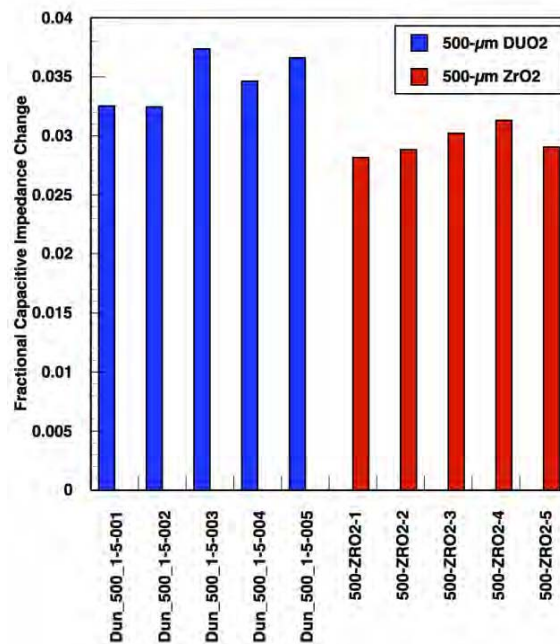
Figure 4.32. Capacitive Impedance of Similarly Sized ZrO$_2$ and DUO$_2$ Kernels
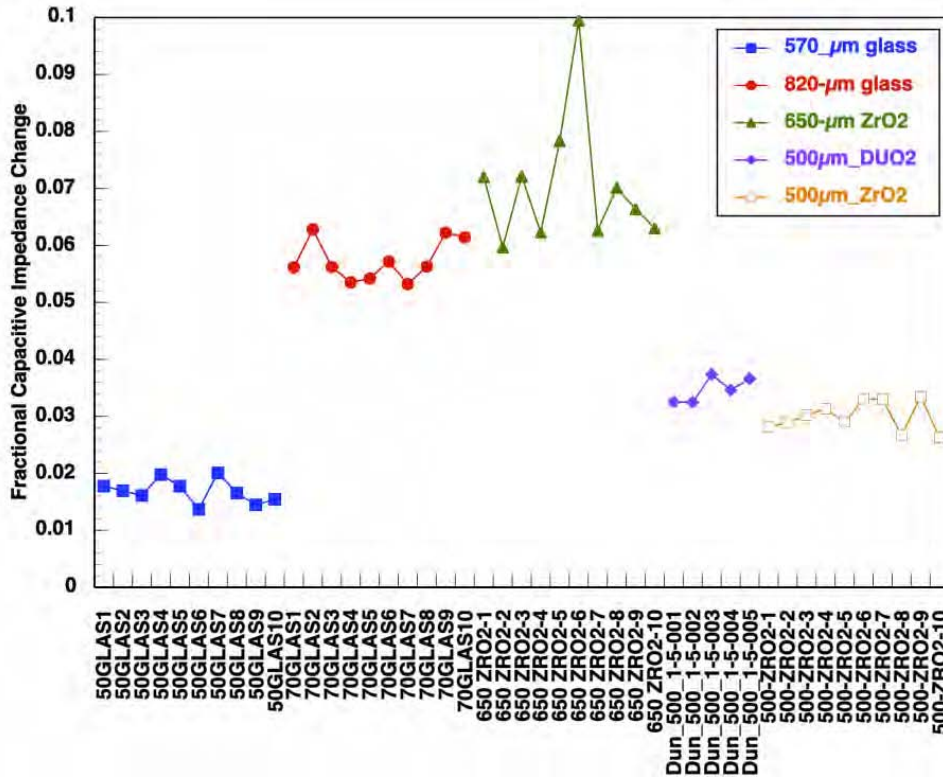
Figure 4.33. Capacitive Impedance Measured for Two Sizes of Glass Spheres and ZrO_2 Kernels, and 500-µm DUO_2 Kernels
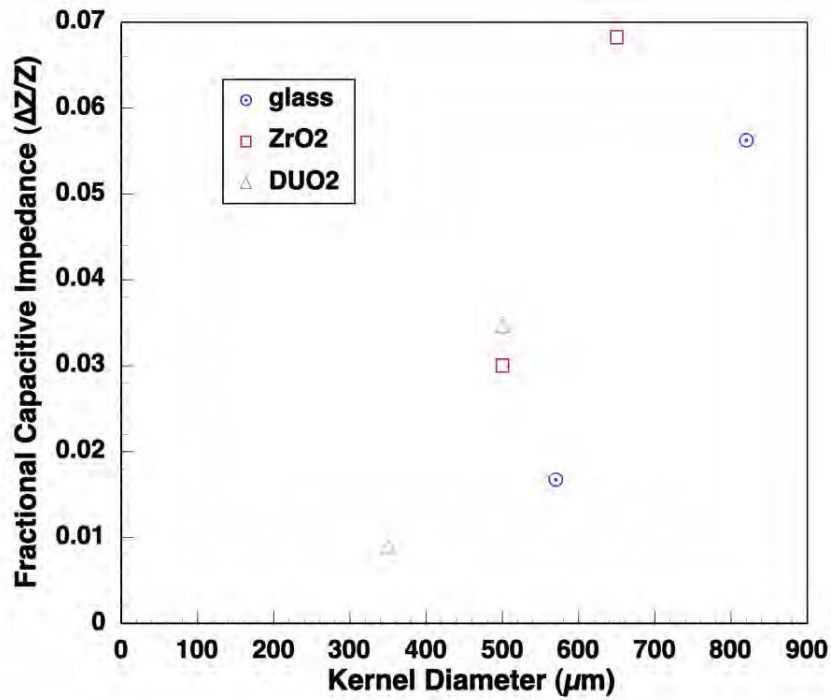
Figure 4.34. The Average Capacitive Impedance Values Shown in Figure 4.33

Task 11. DESIGN AND DEVELOP CAPILLARY PARTICLE FLOW TUBE SYSTEM

Progress this year included further evaluation of the in-line electromagnetic measurements relative to particle and layer dimensions derived from radiography. A modified inductive (coil) sensor was evaluated for on-line implementation. This sensor measured the apparent change in coil impedance as the particles passed between two coaxial coils (in the stationary measurements, the particles were placed inside a single coil). This concept was found to greatly simplify particle flow in the particle inspection process. However, the new split-coil sensor was found to be about one-tenth as sensitive to particle properties as the original single-coil sensor that required the particle to be in the center of the coil. Therefore, the original single-coil design was chosen for implementation.

  Dynamic measurements have been shown to be as reliable as the static measurements. The only remaining issue is production-rate measurements. In the final implementation of this technique, which is beyond the scope of this project, modified sensors would be fabricated to operate at about 100 µs per measurement, allowing about 10 measurements to be recorded as a particle passes through each EM sensor. Similar sensors have been implemented for other applications. A conceptual prototype inspection system that incorporates a capacitive sensor as well as an inductive sensor is illustrated in Figure 4.35.

Task 12-17. COMBINED TASKS –DEMONSTRATION OF TECHNICAL FEASIBILITY USING ELECTRICAL (INDUCTIVE AND CAPACITIVE IMPEDANCE) SENSOR MEASUREMENTS FOR HIGH-SPEED DEFECT DETECTION AND SORTING

Funding constraints this project year limited the scope of this task. Because of the funding shortfall for FY2005 of $97K, the project was re-scoped (reference the appendix to this Task 12-17, PNNL NERI 005-001, October 13, 2004). This change to the project scope condensed each of the original tasks 12-17 into a single task, similar to the original Task 16–Final Laboratory Scale Demonstration of Each NDE Method Found to Meet the Project Objectives. For the remainder of this project, the primary objective was to demonstrate technical feasibility for using electrical (inductive and capacitive impedance) sensor measurements for high-speed defect detection and sorting. The activities that were completed on this task included: 1) the design of a particle feeder system to demonstrate the ability to examine particles at a rapid inspection rate, and 2) the creation of a final demonstration video that provides an overview of the proposed inspection technique.

Particle Feeder Concept

The design of the particle feeder took into account the need to rapidly inspect the individual TRISO particles. This requirement coupled with the requirement to limit the amount of "fill factor" (distance between the induction coil and particle, and the capacitance sensor and particle) inspired the development of a pneumatic system to transfer the particles through the coil for the measurement. Figure 4.35 illustrates the particle feeder concept. Pressurized air is blown through the bottom of the particle feeder to provide suspension of the particles. The air pressure is regulated to form a cloud of particles. As particles pass by the entrance to the induction coil they are captured by a vacuum pickup. This provides a relatively constant particle velocity through the sensor assembly. The TRISO particles tend to have a carbide dust associated with them, which can plug the vacuum pickup. This is mostly eliminated by an open hopper with a screen, which allows the dust debris to be blown out of the top of the particle feeder assembly.
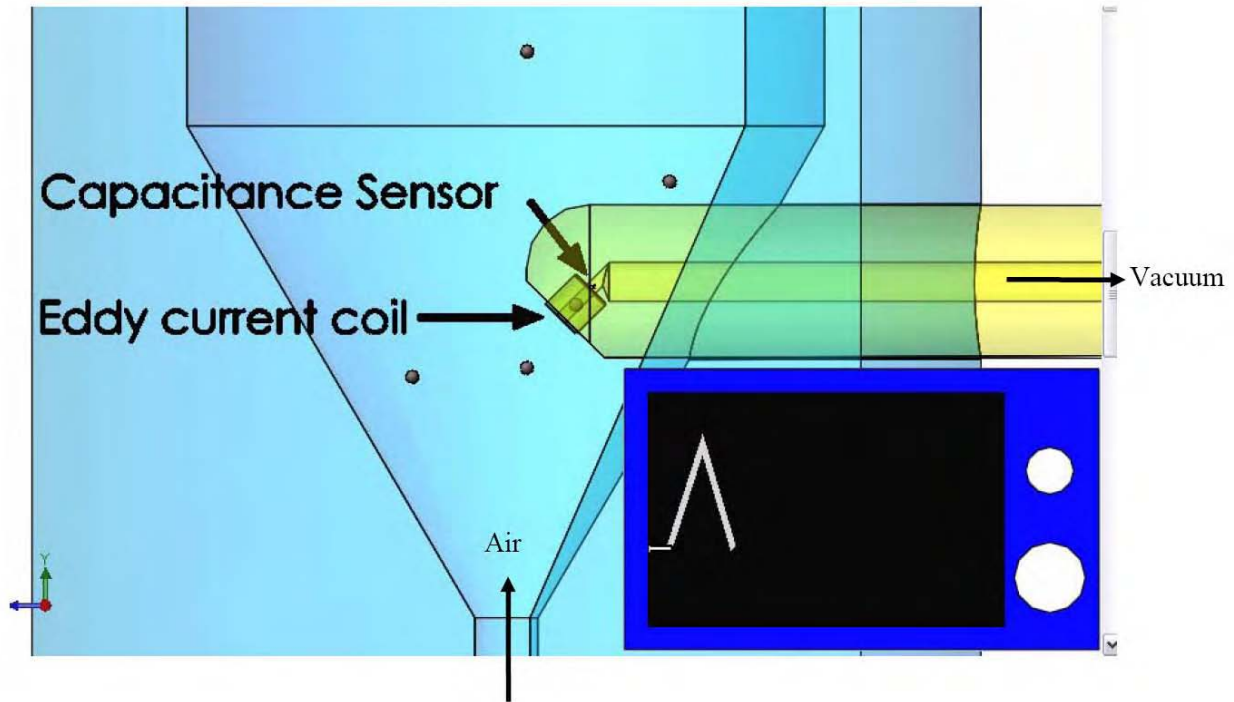
Figure 4.35. Particle Feeder Concept

Consideration was given to the plugging (Figure 4.36) of the pick-up tube by more than one particle trying to enter the sensor. It was found that the turbulent condition in the hopper caused by the suspension of the particles reduces the chances of plugging. Numerous particles pass directly over the entrance portal, continuously colliding with any particles that might begin plugging the entrance. These collisions free up the portal for the next particle to enter. Experimentation has showed that the orientation of the pick-up tube is critical in keeping the flow of particles into the sensor relatively constant. The face of the sensor is, therefore, angled such that particles with the greatest potential to collide with particles that may be plugging the sensor can occur.
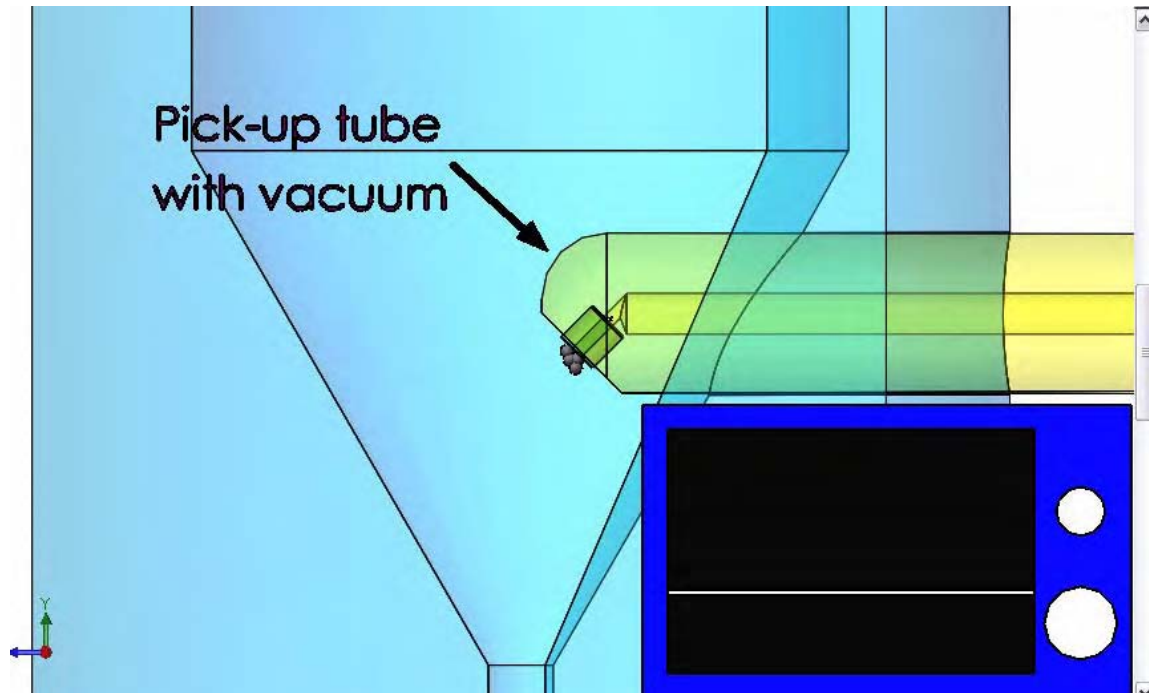
Figure 4.36. Plugging of Particles at Sensor Entrance

Particle Feeder Design

The particle hopper is constructed out of clear acrylic material so that the particle cloud can be observed as it swirls around the pick-up tube. The vacuum pick-up tube containing the inductive and capacitive sensors was also fabricated out of clear acrylic material to observe the particles entering the sensors and moving along the tube. The vacuum pressure is regulated to provide constant particle flow. The air input used to create the particle suspension is also regulated so that a relatively uniform cloud of particles is maintained. Figures 4.37 and 4.38 provide the fabrication drawings of the particle hopper and pick-up tube assemblies.
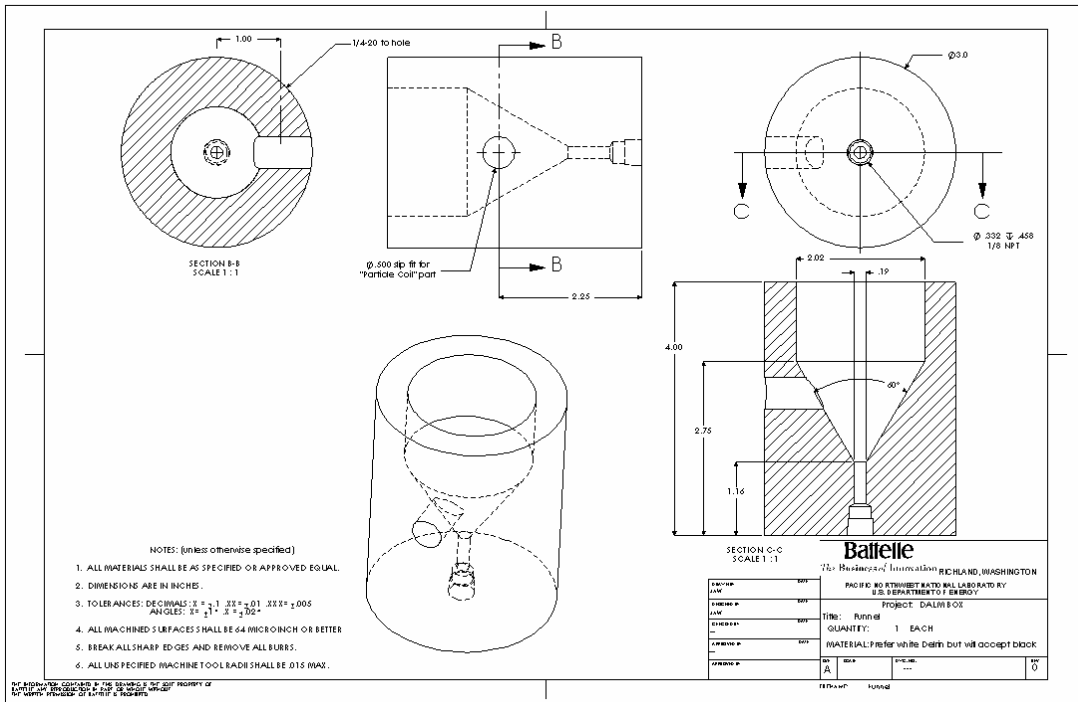
Figure 4.37. Particle Feeder Hopper Assembly
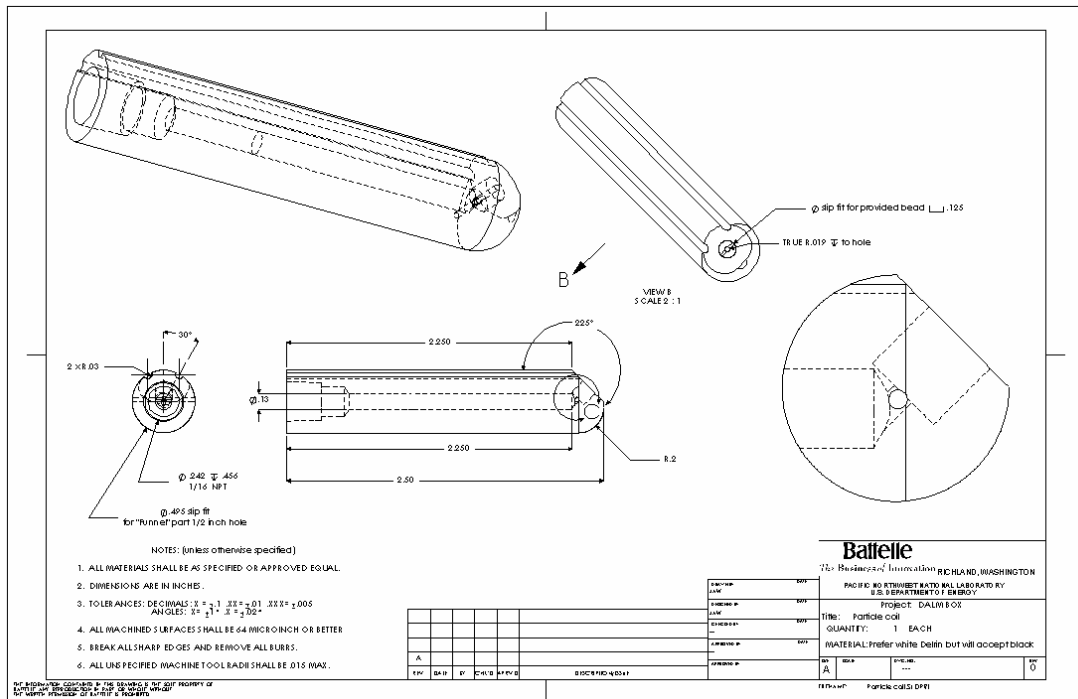
Figure 4.38. Particle Feeder Pick-up Tube Assembly

4.42

TRISO Inspection System Testing

The particle feeder hopper and pick-up tube assemblies were fabricated and readied for bench-top testing. The diameter of the portal through the sensors was fabricated to meet the largest anticipated full TRISO particle that would satisfy the dimensional acceptance criteria described in the particle fabrication specification. The idea is to minimize the distance between the coil and particle or to simply provide the maximum "fill factor" for reliable impedance measurements.

Figure 4.39 shows the components that comprise the prototype system used to perform proof-of-principal testing of the TRISO inspection system. Figure 4.40 shows particles suspended in the hopper.
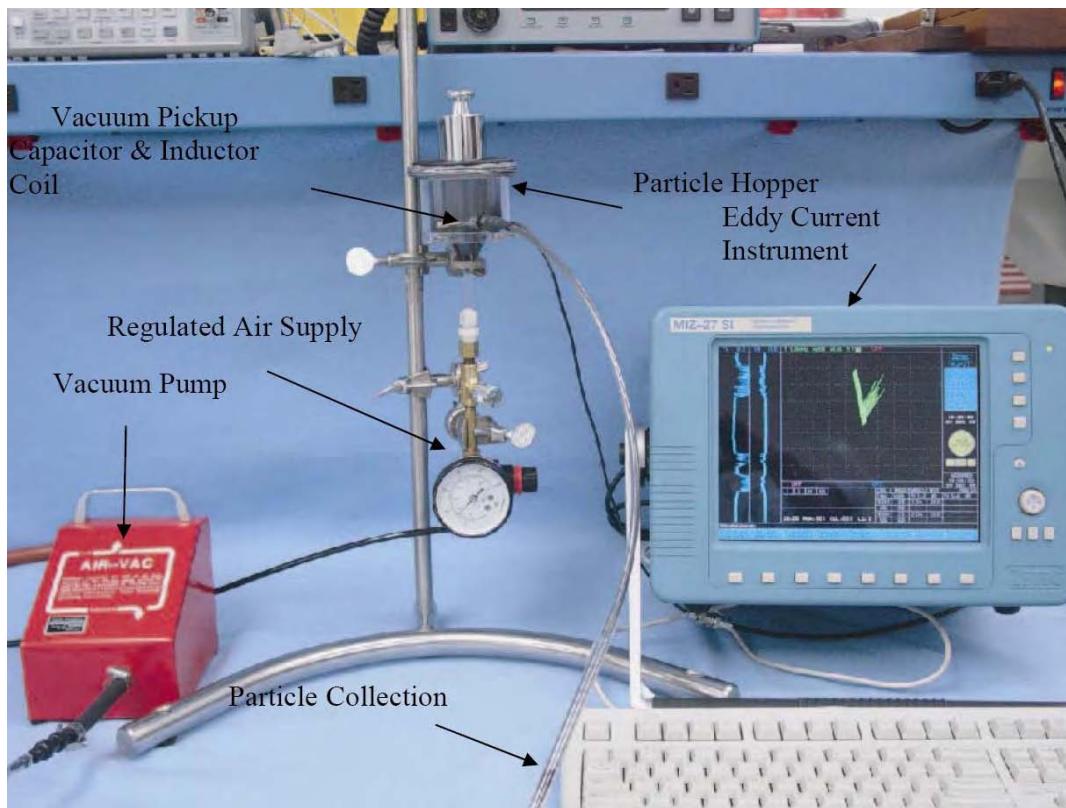
Figure 4.39. Overall Test System

Figure 4.40. Suspension of Particles in Hopper

The flow rate of particles through the inductive and capacitive sensors can be adjusted by regulating the number of particles in the hopper, the air pressure in the hopper, and the vacuum pressure pulling particles from the hopper. Initial tests indicated that flow rates from 300 to 1000 particles/min could be easily achieved. Ensuring that measurements are made when particles are optimally positioned in the sensors can be achieved by optical sensing and triggering or by simply utilizing a sufficiently high sample rate. Once a particle is measured and evaluated, it can be directed to a collection bin using pulsed air. This is a timing operation frequently used in current process lines within industry. Figure 4.41 shows the collection of particles that have passed through the inductive and capacitive sensors in the prototype TRISO inspection system.

Thousands of Individual Particles Collected in Bin
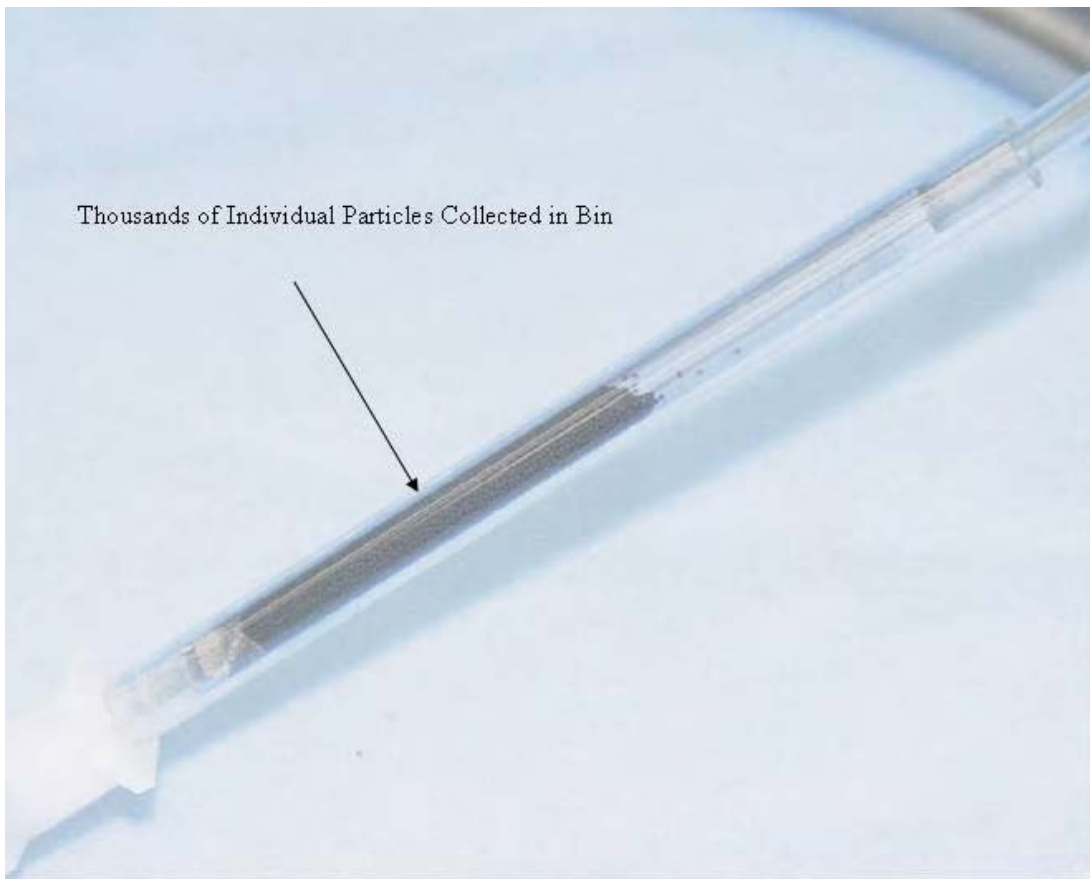
Figure 4.41. Examined Particles Collected in Bin

4.3 FY2005 Presentations and Publications

A project overview entitled "Nondestructive Characterization of TRISO Coated Particle Fuel" was presented at The University of Michigan Nuclear Engineering Department Fall Colloquia on October 29, 2004.

4.4 FY2005 Financial Summary

Cumulative Cost Performance
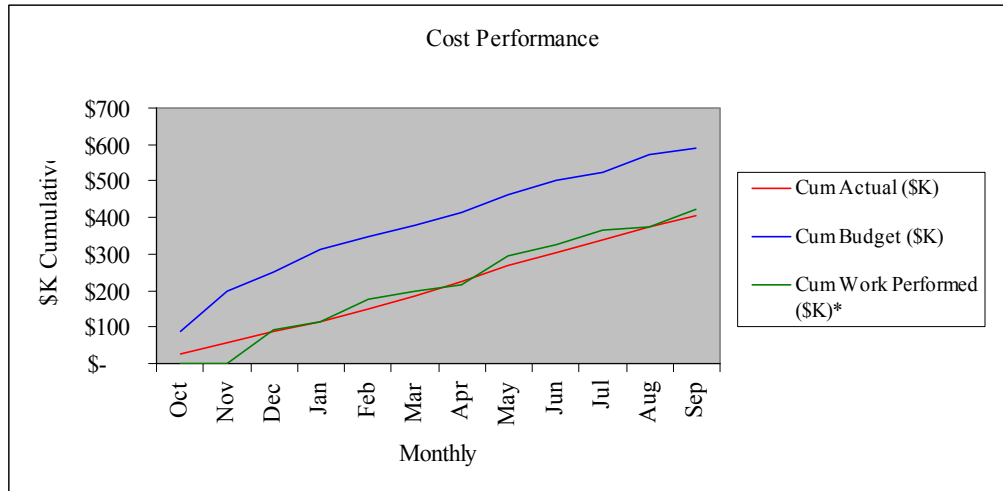
	Oct	Nov	Dec	Jan	Feb	Mar	Apr	May	Jun	Jul	Aug	Sep
Cum Budget ($K)	$ 87	$ 198	$ 252	$ 315	$ 348	$ 378	$ 412	$ 462	$ 500	$ 525	$ 570	$ 592
Cum Work Performed ($K)*	$ -	$ -	$ 91	$ 113	$ 174	$ 200	$ 216	$ 295	$ 327	$ 365	$ 375	$ 423
Cum Actual ($K)	$ 25	$ 56	$ 89	$ 117	$ 152	$ 187	$ 225	$ 267	$ 302	$ 340	$ 376	$ 407
	Note: Percent complete first taken in December for FY05; therefore, zero values for October and November.											

Annual Cost Performance

At the end of the fourth quarter, a positive cumulative cost variance of 4% ($17K) and a small negative schedule variance of –3% (-$11K) occurred. Baseline change request 05-002 to incorporate agreed-upon changes and request a no-cost time extension through January, 2006 was approved and implemented in the month of August, removing schedule and cost variances during that month.

PNNL's fourth quarter positive cumulative cost variance is seen predominantly within the Project Integration and Reporting Task and is attributed to efficiencies for final reporting work completed during the final quarter. While GA has a small positive cost variance while awaiting data analysis, it is offset by a small negative variance from ISU.

A negative cumulative schedule variance is attributed to a delay in receipt at PNNL of quarterly and annual reports from ARA. Improvement on the schedule will occur from the timely submittal of the final report by the end of January, 2006.

4.5 FY2005 Project Milestones

Milestone & Deliverables	Planned Completion	Revised Completion	Actual Completion	Percent Complete
FY2004 Annual Report Complete	Oct—04	Jul-05	Nov-05	100
Final Report Complete	Dec-05	Jan-06	Jan-06	100

4.6 FY2005 Appendices

FY2005 Funding Reduction Impact on NERI Project No. 02-103

November 23, 2004

In Summary

NERI project No. 02-103, for developing advanced NDE approaches to automating NGNP particle fuel QA/QC, has made major progress in its first two years, but received a significant funding shortfall in its final year, FY2005. This budgetary action is having a significant impact on the planned project outcomes. The most significant impacts are highlighted below each of the following task descriptions.

Tasks

Develop Particle Defect Library

Description

X-ray characterization of surrogate and DUO_2 particles coated at ORNL to have specific properties. Radiographic techniques are being used to sort standard particles from those purposely coated to have defective coating parameters and irregular sized kernels. Iowa State University is leading this task, initially designed with an emphasis on graduate student support for developing and implementing a methodology to analyze a broad sampling of particles representing the typical defects encountered in the CVD coating process.

Impact

Reduction in graduate student involvement—eliminate 300 hours of graduate student support for radiographic particle analysis and eliminate another student working to develop automatic image analysis routines. This will reduce the number and types of defective particles for demonstrating and calibrating the high-speed NDE particle measurement methods. Must eliminate X-ray characterization of particles that have laser or focused ion beam induced cracks or "holes".

This will reduce the number and range of characterized particles in library for use in other tasks.

High-Speed Defect Detection Demonstration

Description

Design, develop and demonstrate a laboratory-scale particle inspection system to measure the electrical properties of particles flowing past sensors. The sensors are magnetically and electrically coupled to the particles and are capable of identifying detects (particle properties outside specifications) in real time.

This task also includes selecting defective particles from a radiographically characterized library of particles and finding the relationship between defective conditions and EM sensor response.

Impact

The demonstration would be reduced from fully-automated to semi-automated (each group of particles reloaded for multiple passes) and inspection speeds reduced by at least 500%, to particle flow rates ranging between zero and five particles-per-second—well below the speed threshold for defect detection and expected reactor refueling requirements. Defect types will be limited to missing and thin coating layers. Defects such as cracks, thin spots, and coating structure must be eliminated.

Kernel chemistry effect

Description

In this task, measurable effects kernel chemistry may have on the coating layers will be evaluated. Remote sensor measurements on surrogate-coated kernels will be compared with unirradiated depleted uranium oxide (DUO_2) and natural uranium oxycarbide (NUCO) fuel kernels having the same AGR coatings applied. The results will be used as a reference in interpreting all prior and future electrical property measurements derived from surrogate-coated kernels. These measurements are also intended to evaluate the possibility of providing additional quantitative relationships between electrical properties and kernel chemistry.

Impact

Reduce the amount of surrogate material that can be analyzed (and coated) in attempts to find surrogate coated kernels with equivalent coating thicknesses to DUO_2 coated particles. This necessitates extrapolations among wider differences in coating layer thicknesses, creating greater uncertainty in the validation between coated surrogate and fueled kernels. Similar limitations must be placed on the amount of DUO_2 coated kernels that can be characterized using X-ray methods. Initially, at least 25 particles for each of eight different uranium based particles were to be characterized. That number has now been reduced to less than six particles from each particle type.

Ultrasonic Development Tasks

Description

Two ultrasonic methods continue to show potential benefits for automatic particle defect detection and process control. They include: 1) a Resonant Ultrasound (RUS) method for statistical batch sampling of individual particles, and 2) a gas-coupled, through-transmission method for on-process batch characterization in a model coater. Both methods require additional testing using particles and apparatus obtained only recently.

Additional testing of the on-process batch characterization method includes measurements to verify the accuracy and resolution of particle diameter measurements. Prior work was limited to uncharacterized particle batches, where particle diameters specifications were uncertain by greater than ±15%. We now have the capability to sort particles with sufficient accuracy to produce batches meeting diameter

variation specifications within ±5%. Also, prior measurements had considerable variations in the gas flow rates and temperature, thought to be partially responsible for the variability seen in the acoustic attenuation signals measured as a function of particle diameter. Additional testing with these sources of error reduced will determine the potential benefit of this method to existing and future fuel development programs.

The existing RUS instrumentation was shown to be restricted to particle diameters much larger than 1 mm—well above the AGR specification for TRISO particles. The relatively large mass of the measurement transducer imposes this constraint on particle size. A recently identified transducer was demonstrated to overcome this limitation and obtain expected results using TRISO coated surrogate particles. This fixture costs about $1500 and could be installed to existing apparatus in about one-day. Evaluation studies will require testing several particles recently added to the defect library of surrogate-coated particles.

Impact

- The ultrasonic method for on-process coating monitoring will be scaled back, from evaluating variations among coating parameters to evaluating only total particle diameter.

- After upgrading the RUS instrumentation to include the lower-mass transducer, only a very limited set (about 10% of the originally planned range of samples) of X-ray characterized particles could be evaluated, leaving the uncertainty for this capability relatively undefined.

Defect introduction

Description

The initial project plan included *implanting* defects into the standard particles using such methods as pulsed laser drilling or focused ion beams to produce micron-scale defect conditions observed to occasionally appear in some CVD coatings, particularly in the SiC layer. Both 2-D and 3-D X-ray imaging methods developed at Iowa State University would be used to image the density variations created by the artificial defects. The higher speed NDE inspection methods being developed at PNNL would then be used to evaluate the possibility of detecting such defects in a real-time fabrication situation.

Impact

Task elimination; due primarily to a funding shortfall in support of the X-ray characterization work at Iowa State University and the defect implantation process into particles with the standard coatings.

GA Involvement

Description

GA is providing technical support for developing and testing a laboratory scale automatic particle inspection demonstration system. GA's input will help define an appropriate test matrix of defective surrogate particles to include defects that cannot be detected at production speeds using existing technology. GA will also review demonstration measurement results for their ability to potentially satisfy

future acceptance/rejection criteria expected to be placed on coated-particles for advanced gas cooled reactors.

GA will provide guidance and assist PNNL in selecting and obtaining additional particles from ORNL. This includes at least two shipments of depleted and natural uranium coated particles to be shipped to ISU for radiographic and electrical testing, as well as additional surrogate particles found necessary to complete the particle inspection demonstration system. GA will continue to coordinate technical activities between this project and the AGR Fuel Development and Qualification Program at ORNL. GA will help PNNL define acceptance and rejection parameters related to the NDE measurements that will be used in formulating an NDE Quality Index.

Impact

GA cannot attend two project team coordination meetings and the high-speed defect detection demonstration. The project team meetings, therefore, will be reduced to one. GA will also scale back their involvement with each of the above tasks where ISU and PNNL have reduced scope.

Project coordination

Description

PNNL is coordinating the NERI particle fuel QA/QC Project No. 02-103, as well as developing the required NDE automation technology. Technical activities and research related to NGNP particle fuel characterization being conducted at ISU, ORNL and GA are being assimilated into quarterly and annual reports.

Impact

Retaining maximum focus on their primary role, ISU will suspend the writing of one-page monthly status reports and provide only brief quarterly and final technical reports—expanding PNNL's project integration task, and further impacting the technical tasks.

5.0   Project Results and Conclusions

The purpose of this NERI project was to evaluate, develop and demonstrate NDE technologies that have the potential to be automated to meet production throughput requirements for TRISO particles. The research included in-line measurements, on-process measurements, and advanced off-line NDE measurements. The techniques evaluated to accomplish this included electrical measurements (inductive and capacitive), acoustic microscopy, resonant ultrasound spectroscopy, high-resolution radiography and computed tomography, transmission and diffuse field ultrasound, and optical measurements.

5.1 Electrical Measurement Techniques

The techniques investigated in this NERI project included electrical measurements of inductive impedance and capacitive impedance.

The inductive measurement technique is based on the principles of electromagnetic induction. A test coil of wire is excited by an alternating current (AC), which in turn produces a varying electromagnetic field around the coil. When this test coil is placed in proximity to a conductive test sample, an electrical current (eddy currents) will be induced in this sample.   Eddy currents induced in a sample then generate a secondary electromagnetic field in the inducing coil and the combined magnetic field (apparent in the test coil) determines the AC coil impedance for the coil-sample system. It is this quantity that provides an integrated measure of particle properties. The secondary electromagnetic field sensed by the test coil depends on the electrical conductivity, magnetic permeability, and geometry (with respect to the coil's electromagnetic field) of the sample. Therefore, by measuring the real and imaginary components of the coil impedance, it is possible to obtain both electromagnetic properties and geometric structural information about a sample.

In the capacitance method, a potential difference is applied between two parallel metal plates to establish an electric field. By measuring the voltage across the plates and the current flow, it is possible to determine the change in capacitance caused by the material, such as a TRISO particle, inserted between the plates.

Numerical Modeling

The inductive and capacitive measurements were numerically modeled in a preliminary manner in 2003 to derive a basic understanding of the measurement processes and to ensure that the measurements conformed to the predictions of theory. Some additional modeling was done in 2005 to more fully examine the contributions of the particle layers to the measurements made using induction and capacitance sensors. This modest effort also provided estimates of the performance of the specific sensors that were constructed and utilized in 2005. As in the initial modeling effort, the commercial software packages Oersted® and Electro® (from Integrated Engineering Software, Inc.) were used to compute sensor responses to particles representing a wide range of variations from the specified nominal particle structure. For the most part, this exercise addressed the effects of variations in the thicknesses or diameters of the various layers of the TRISO particles. The effect of layers that are anomalously thin at the poles or at the equator of a given particle was briefly evaluated. The effects of flaws that could not be modeled as rotationally symmetrical features were not considered. Nevertheless, the results were helpful in determining the capabilities and limitations of the induction and capacitance sensors.

Induction Sensor

The geometry of the induction-sensor model is shown in Figure 5.1. This Oersted® screen image shows partial cross sections of an 82-turn coil and an ideal TRISO particle. Rotational symmetry about the X = 0 axis is assumed. The calculated quantity is the complex impedance of the coil at a specified frequency (in this case, 45 MHz, the frequency used for most of the EM measurements made in 2005). The real part of the impedance corresponds to the apparent resistance of the coil; the imaginary term corresponds to the apparent impedance associated with the inductance of the coil.
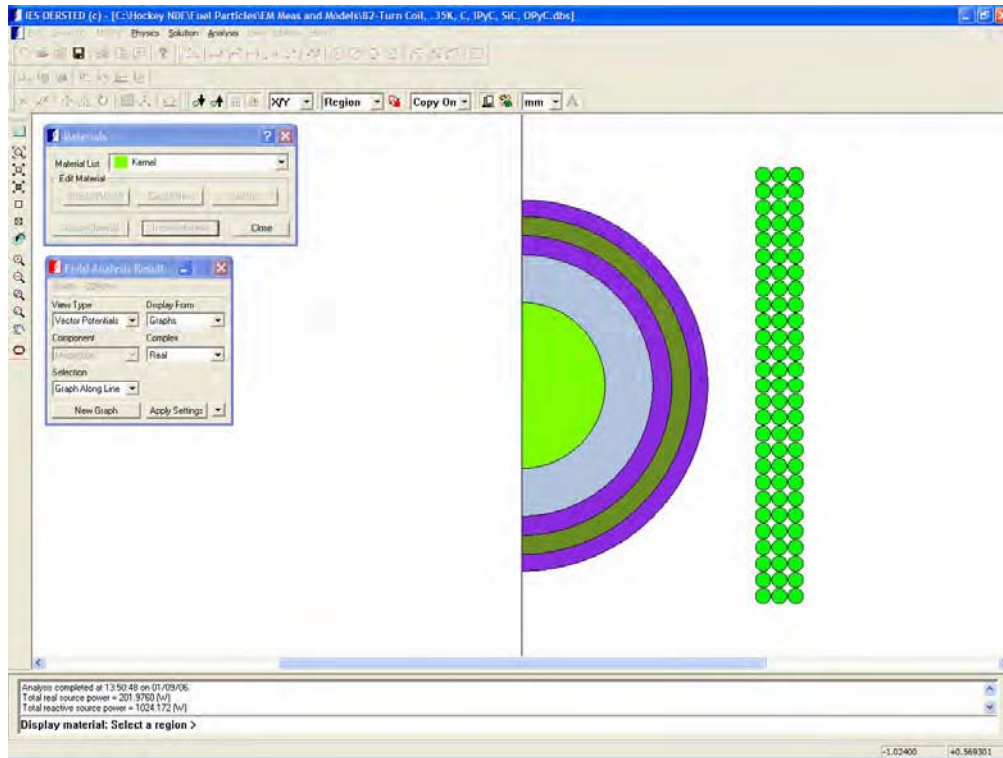
Figure 5.1. Oersted® screen image showing the EM coil model with a TRISO particle

The complex impedance of a coil enclosing a layered, partially conductive, TRISO particle is a function of the electrical properties (primarily the conductivity and, to a lesser degree, the dielectric constant) of the layered components. Because there were no data available on the electrical properties of those specific materials, it was necessary to use values derived from the literature and from manufacturers' Internet sites. The values derived from those sources were found to range over several orders of magnitude, depending on how the materials were produced, their crystal structure, and their form (powder, solid, thin film, etc.). Thus, the values used in the models were, at best, reasonable guesses. Some of those values may be substantially different from the actual values, but the general results of the modeling appear to be consistent with the measurements that have been made. The values of electrical conductivity and dielectric constant used in the models are listed in Table 5.1.

Table 5.1. Electrical Conductivities and Dielectric Constants used in Numerical Modeling

Component	Conductivity (S/m)	Dielectric Constant
Kernel	0	4
Buffer	10^5	3
IPyC	10^6	5
SiC	10^2	7
OPyC	10^6	5

As previously discussed in Section 2.2, Task 2, the calculated values of complex impedance did not agree with the measured values due to the effects of distributed capacitance present in the wire leads and structure of the coil, but not included in the model. The combination of inductance and capacitance produces a resonance in the sensor coil that cannot be directly modeled with the Oersted® software. The approach used in 2003 was to combine the numerical inductance model with an analytical equivalent circuit (Figure 5.2) that includes a capacitance.

The numerical model was used to compute the frequency-dependent resistance and inductance of the coil and the coil-particle combination. Those values were then used, together with a best-fit estimate of the coil and lead capacitance, to compute the true complex impedance at the frequency of the measurement. Because it has already been demonstrated that this procedure establishes the desired correspondence between the calculated values and the measured values, it was not considered necessary to apply it to the 2005 modeling results. Thus, the calculated impedance values presented below represent only the contributions of the resistive and inductive components of the modeled coil and particles.
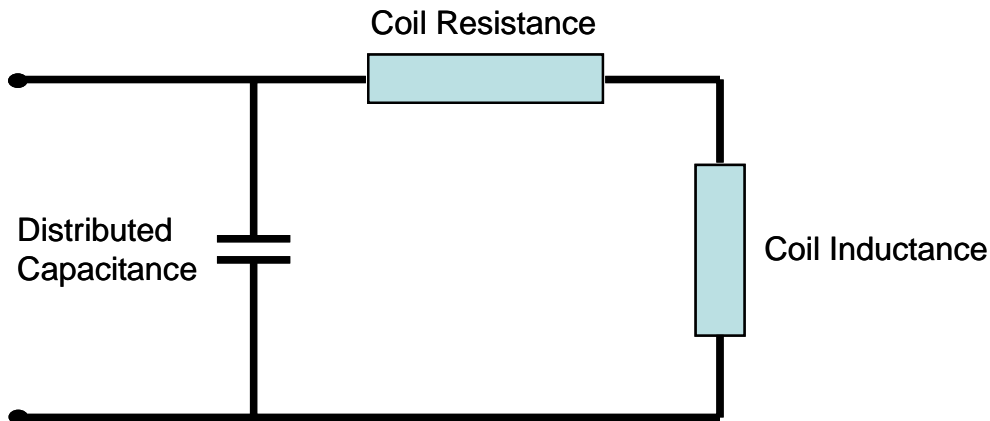
Figure 5.2. Equivalent circuit

The complex impedance of the coil was calculated for a set of synthetic particles in which the dimensions of the kernel and each of its overlying layers varied over a wide range, as shown in Table 5.2. The results, which describe the response of the induction sensor to particles containing layers both within and outside specified limits, are plotted in Figure 5.3. The fractional impedance components of each particle were plotted as functions of the total carbon volume (the sum of the buffer and PyC volumes) because they correlate more closely with the total particle volume than with any other simple particle parameter.

Table 5.2. Range of Layer Dimensions used in Numerical Modeling

Component	Dimensions, mm		
	Min	**Max**	**Nominal**
Kernel Diameter	0.250	0.418	0.350
Buffer Thickness	0.000	0.150	0.100
IPyC Thickness	0.000	0.050	0.040
SiC Thickness	0.000	0.060	0.040
OPyC Thickness	0.000	0.060	0.035
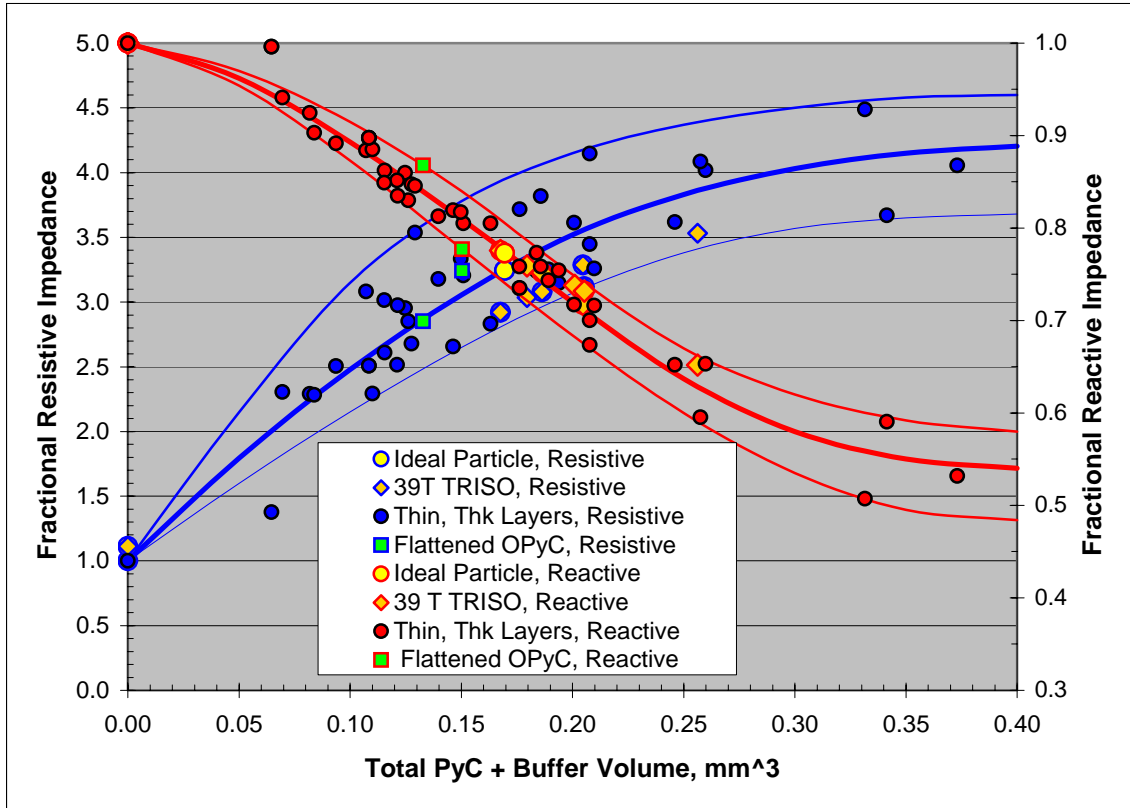
Figure 5.3. Calculated Fractional Impedance Components as Functions of the Total Carbon Volume

This graph is a reasonable summary of the results derived from modeling the response of the induction sensor. The blue and red lines have no fundamental significance, but were included to clarify the general trends of the data and to show the approximate bounds on the impedance values associated with the parameter variations shown in Table 5.1. The heavy blue and red lines show the general functional relationships of the fractional impedance components to the total carbon volume. The scatter around those lines represents a complex weaker dependence on the detailed permutations of the variable layer dimensions in the synthetic particles. Values for ideal particles (i.e., particles that conform exactly to the specified kernel diameter and layer thickness) lie near the center of the plot, where the distributions of resistive and reactive data intersect. The scatter in the plotted data can be reduced somewhat by plotting the resistive and reactive components as functions of weighted combinations of the carbon-layer volumes; however, it is not clear how helpful that more-complex process would be.

Only two points (one blue and one red) lie outside the boundary lines. These correspond to particles consisting only of a kernel and a buffer (both of nominal dimensions). The impedance values for particles that contained at least one PyC layer, in addition to a kernel and a buffer, lie close to the trend lines. Particles containing only a kernel and a SiC layer are virtually non-conductive and cannot support significant eddy currents; therefore, their fractional impedance components have values very close to 1.0.

Seven particles from batch NUCO350-39T were modeled using layer dimensions derived from radiographic measurements. The calculated impedance components for six of those particles are close to the values for a nominal particle. Although their OPyC layers are relatively thick (avg. 0.053 mm), their total carbon volumes are close to the nominal value of 0.17 mm^3. The seventh particle would probably be considered out of spec because of a large (0.416-mm) kernel, a thick (0.056 mm) OPyC layer, and a total carbon volume of 0.256 mm^3.

The components of the complex coil impedance are determined by the dimensions, physical properties, and electrical properties of the particle layers. The extraction of explicit information about those parameters is limited by having too many unknowns and too few independent data. Nevertheless, the results discussed above suggest that inductance measurements using an enclosing coil can provide a good estimate of total carbon volume, and that it is possible to define a range of impedance values that corresponds to acceptable particles. Combining the inductance measurements with a capacitive measurement of the total volume of the particle, as discussed below, should provide a good means of separating good particles from bad. Nevertheless, it is necessary to address the issue of non-uniqueness; i.e., the possibility that different combinations of parameters can yield the same impedance values, and that an unfortunate combination of parameters could occasionally lead to an erroneous acceptance of a particle. An example is provided in Table 5.3, where the fractional impedance components of an ideal particle and an out of-spec particle are compared. In the latter particle, a very thin buffer is balanced by an enlarged kernel and thick PyC layers. The carbon volumes and the total volumes of the particles are identical. As expected, the reactive impedance components have nearly the same value for both particles, while a small difference in the values of the resistive components reflects the different layering of the particles. In a real-world measurement, it is unlikely, that the bad particle would be recognized as such on the basis of that small difference in impedance.

Table 5.3. Range of Layer Dimensions used in Numerical Modeling

Component	Dimensions, mm	
	Ideal	**Bad**
Kernel Diameter	0.350	0.396
Buffer Thickness	0.100	0.007
IPyC Thickness	0.040	0.070
SiC Thickness	0.040	0.042
OPyC Thickness	0.035	0.073
Carbon Volume (mm^3)	0.170	0.170
Total Volume (mm^3)	0.248	0.248
Resistive Impedance	3.24	2.84
Reactive Impedance	0.773	0.760

For the most part, the detection and characterization of flaws, other than anomalous layer thicknesses, have not been addressed by numerical modeling in this project. However, calculations were made to

explore the effects of a thin OPyC layer at the poles and at the equator of an otherwise ideal particle (the poles are at the top and bottom of the particle, as shown in Figure 5.1). In each case, the anomalously thin area was smoothly tapered from the nominal thickness of 0.035 mm to 0.005 mm. The results of these calculations are shown as blue and green squares in Figure 5.3. As expected, the changes in the impedance components as a result of OPyC thinning are greater when the thinning is on the equator than when it is on the poles. This is primarily OPyC thinning near the equator reduces the total carbon volume more than thinning near the poles. Another factor is that eddy currents are not distributed uniformly through the outer layers of the particle. As illustrated in Figure 5.4, the eddy currents spread radially until they are bounded by the surface of the particle or constrained by the magnetic field. As a result, the eddy current density is greatest in a broad zone near the equator of a particle.

In Figure 5.5, the eddy current density at the particle's equator is displayed as a function of radial distance from the center of the particle at frequencies of 20, 45, 90, and 135 MHz. It is evident that, at the highest frequency, most of the eddy current power is confined to the OPyC layer. At lower frequencies, a larger fraction of the eddy current power penetrates into the deeper layers.
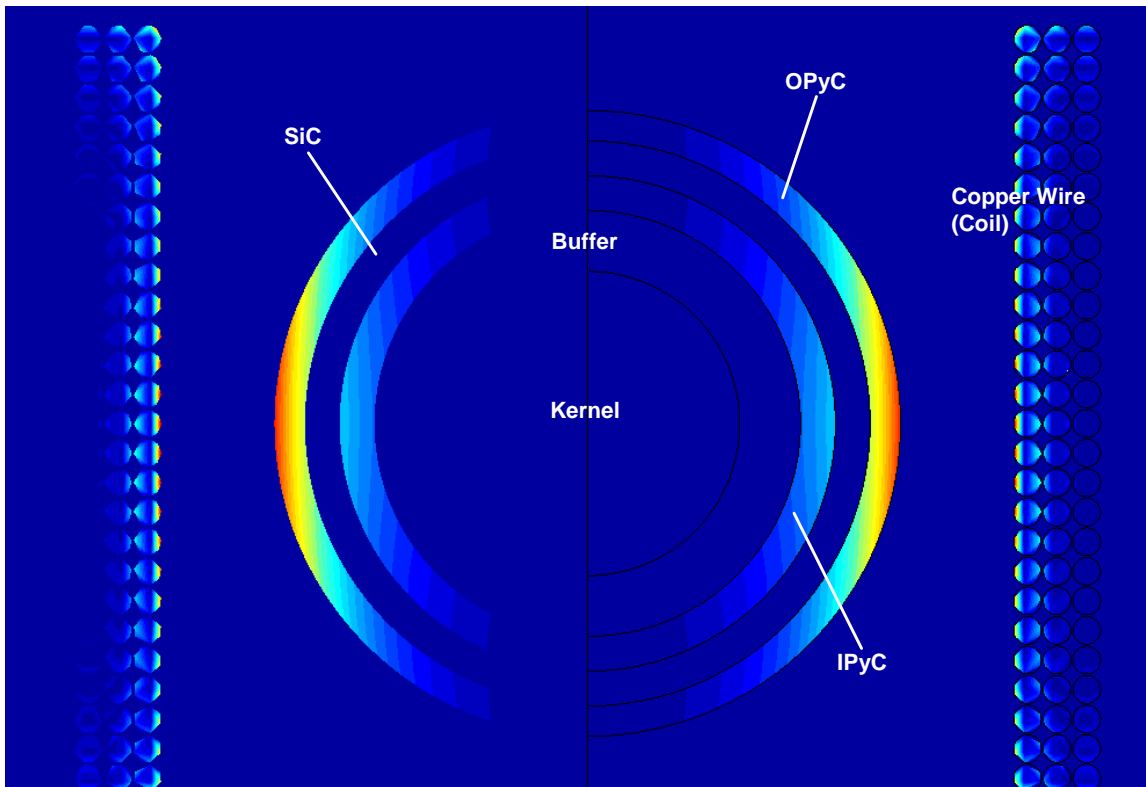
Figure 5.4. Distribution of Eddy Currents in a TRISO Particle at 45 MHz
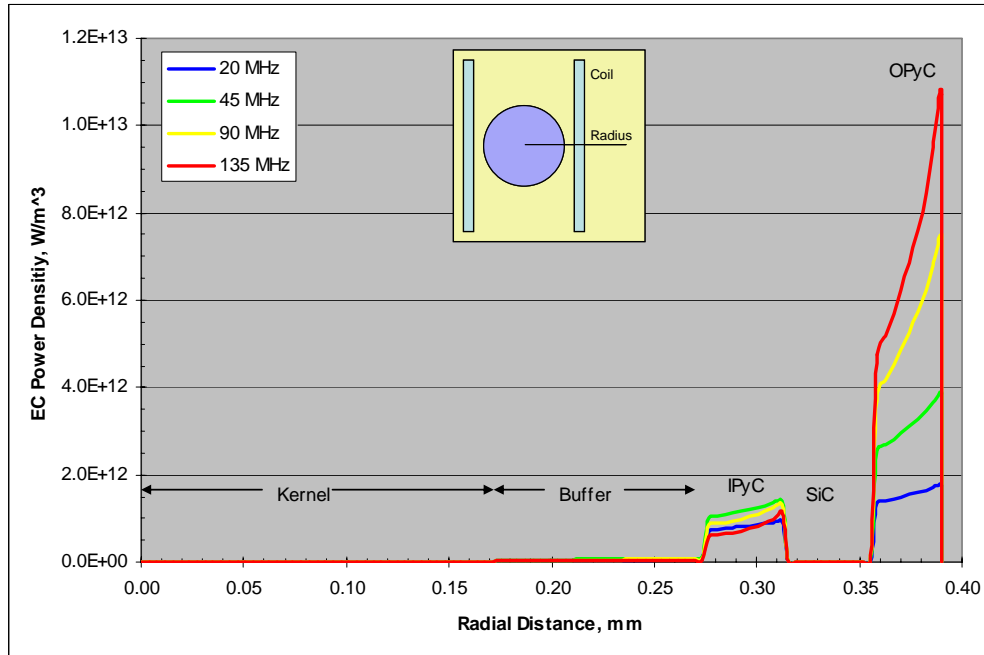
Figure 5.5. Eddy Current Power Density Profiles Along an Equatorial Radius

Capacitive Sensor

The geometry of the capacitance-sensor model is shown in Figure 5.6. This Electro® screen image shows partial cross sections of the wire-end capacitor and an ideal TRISO particle. Rotational
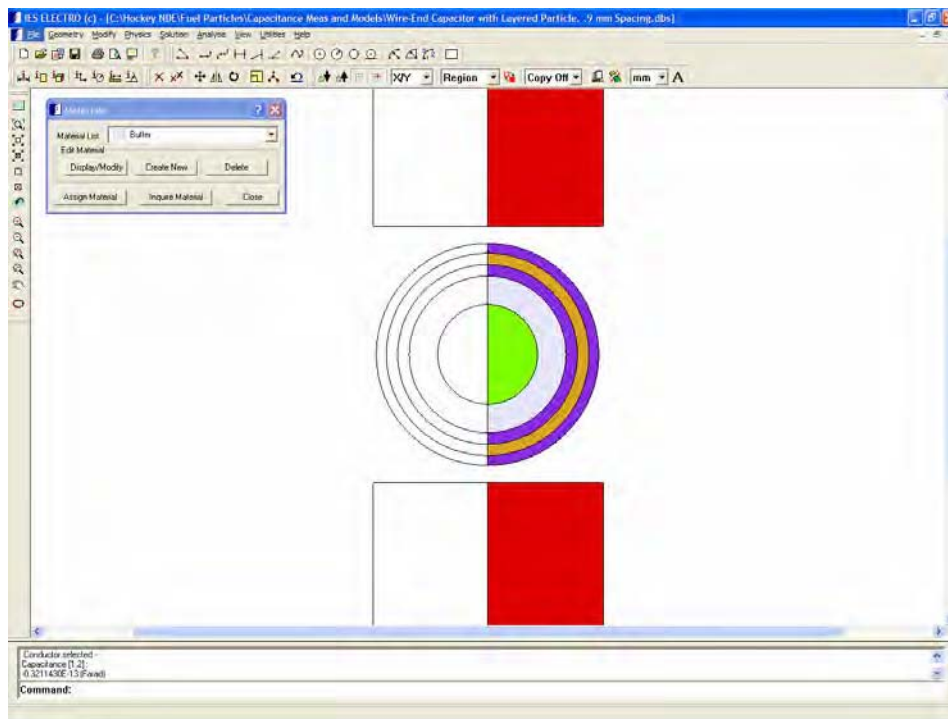
Figure 5.6. Electro® Screen Image Showing the Capacitance Sensor Model with a TRISO Particle

symmetry about the X = 0 axis is assumed. The calculated quantity is the capacitance of the structure consisting of the wire ends, the air gap, and the particle centered in the gap. That capacitance, in general, is a function of the dimensions and electrical properties of the layers that form the particle. In this case, given the estimated electrical properties shown in Table 5.1, the dominant factors are the volume and electrical conductivity of the outer (OPyC) layer. The results of the numerical modeling are graphically summarized in Figure 5.7. The computed values are presented as the fractional change in capacitance, C_f, when a particle is inserted into the space between the electrodes; i.e., $C_f = (C - C_0)/C_0$, where C and C_0 are, respectively, the capacitance with and without the particle present.

The curve shown in Figure 5.7 essentially represents a fill-factor function that describes the increase in capacitance as the air gap is filled by a conductor of increasing volume. If the outer layer of a particle is even slightly conductive (even the assumed conductivity of SiC, 100 S/m, is sufficient), charges distribute themselves on its surface to form an equipotential surface, as shown in Figure 5.8. Additional charges are required on the electrode surfaces to support the increased voltage gradient in the spaces between the particle and the electrodes. This increases the capacitance by virtue of the relation C = Q/V, where Q is the charge and V is the fixed voltage between the electrodes. If the top and bottom of the particle are not too close to the electrodes (i.e., if the particle is not too large), the increase in capacitance is the same as it would be if the electrodes of an empty capacitor were moved closer together by a distance that would reduce the volume between the electrodes by an amount equal to the volume of the particle. This alternate perspective is consistent with the expression for the capacitance of two parallel plates: C = $\varepsilon_0 A/d$, where ε_0 is the permittivity of free space, A is the surface area of each electrode, and d is the distance between the electrodes.
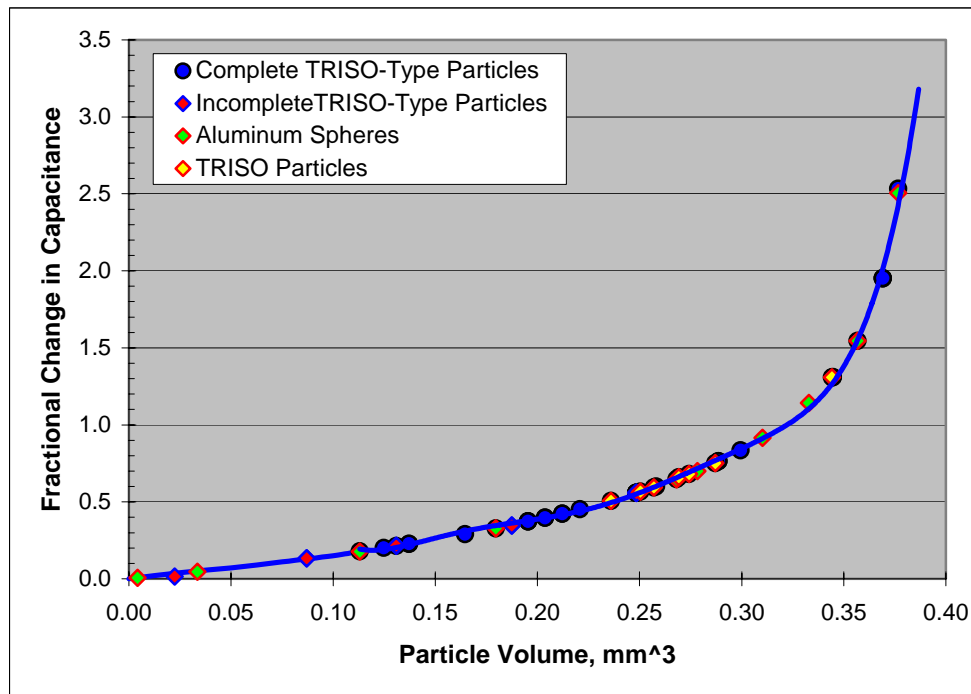
Figure 5.7. Fractional Change in Capacitance as a Function of Particle Volume for TRISO Particles and Aluminum Spheres

5.8
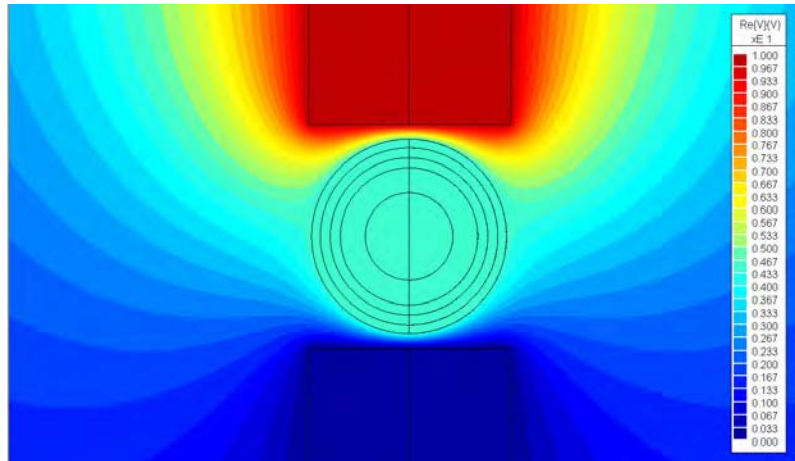
Figure 5.8. Equipotential Lines in the Capacitor with a TRISO Particle Present

The net effect is that the capacitance measured at the electrodes is a good measure of the total volume of a particle and is independent of the properties of its inner layers. This is further demonstrated in Figure 5.7 by the fact that the values of capacitive change produced by aluminum spheres (green diamonds) lie on the same curve as the values produced by complete and incomplete TRISO particles.

Measured capacitive and dimensional data (for the same particles), were plotted to confirm that the measurements yield values that are functions of particle volume as predicted by the modeling. The results are shown in Figure 5.9. The measured quantity was capacitive impedance rather than the capacitance itself; however, when expressed as fractional change, the quantities are the same. As expected, the plotted impedance data from seven different coating batches, encompassing a range of complete and partially coated particles, are distributed about a curve (black line) that, except for a scale factor, is nearly identical to the one based on calculated capacitance (blue line, from Figure 5.7). A measured datum from a stainless steel ball bearing also falls directly on the two curves.
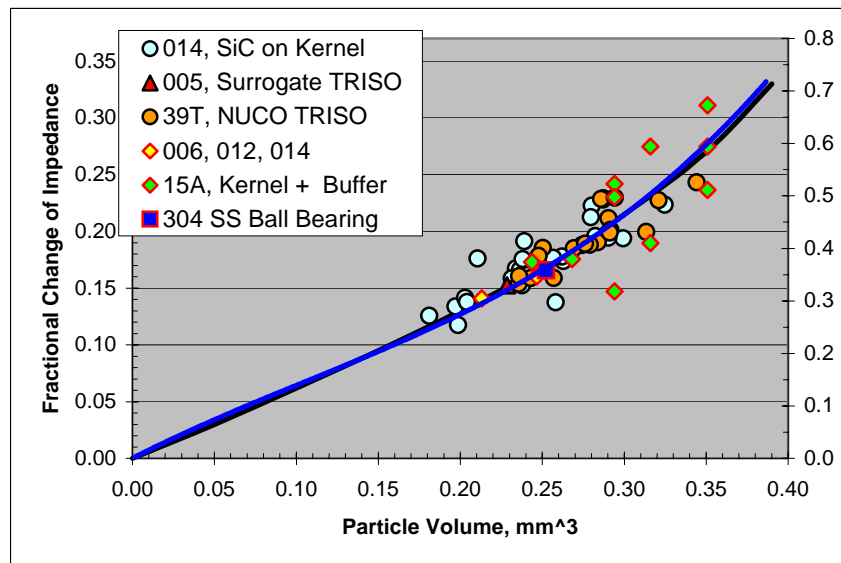
Figure 5.9. Measured Fractional Impedance Change as a Function of Particle Volume

The scaling factor needed to match the measured data to the calculated data is primarily the result of a difference between the measured capacitance of the empty physical sensor and the calculated capacitance of the empty modeled sensor. That difference, in turn, is caused by the presence of stray capacitance in the physical sensor. The scatter shown in the plot of the measured data may be attributed to factors such as:

- The use of different sensors with different electrode spacings. A 0.90-mm spacing was used in the calculations; several different spacings were used in the measurements.

- Variable stray capacitance.

- Errors in the capacitive measurements -- sensitivity to temperature variations, small setup differences, proximity of hands during data acquisition, etc.

- Errors in the dimensional measurements. Some uncertainty is associated with the radiographic measurements -- particles were not perfectly round and measurements were made in one plane. The diameters of the 15A particles were measured with a micrometer. It was difficult to obtain accurate and repeatable measurements because of the softness of the carbon buffers.

Statistical Modeling

The statistical analyses fit predictive models for inductive and capacitive impedance as a function of dimensional characteristics of particles as determined by radiography. Ideally, such analyses would use a "rich" data set of "acceptable" and "unacceptable" particles with respect to the dimensional features considered to show that the impedance measurements indeed differ for the two groups. This would be a fairly complex activity "unacceptable" particles could occur in many forms. Potentially, manufacturing parameter values and non-dimensional properties such as coating density could be included along with dimensional characteristics in such modeling as well. Ideally, in such modeling, the predictive models will indicate ranges for the impedance measurements for acceptable particles, and unacceptable particles will fall outside of these ranges. Given a "rich" data set as mentioned before, reasonable confidence could be established that the impedance measurements can indeed be used to sort the acceptable and unacceptable particles.

Data acquired during this project are, however, somewhat limited. The first data set considered includes surrogate particles, some of which are anomalous to the extent that certain coating layers are missing. A rich data set would have even more sets of conditions of unacceptable particles. The second data set is from particle batch NUCO350-39T, which is more representative of a typical batch of coated particles, and which was more extensively analyzed. Due to the rather extreme difference in the nature of the two data sets, separate models were fit to each data set.

The details of the analyses of the surrogate data and of batch 39T are shown in Appendix C. A stepwise approach was used to determine those dimensional features (among kernel volume, buffer volume, IPyC volume, SIC volume, and OPyC volume, as well as total carbon volume and particle volume) that could best explain the observed variability in the inductive and capacitive impedance measurements. Cross-products (also called interaction terms) of these volume quantities and their squared terms were also considered as candidate explanatory variables.

Made-up groupings including a "nominal" particle, "borderline" particles, "more extreme" particles, and "most extreme" particles were used in conjunction with the two resulting models to predict their inductive

and capacitive impedance results. In the tables presented in Appendix C, green-shaded particles are deemed acceptable based on the predicted impedance responses while yellow-shaded particles are deemed unacceptable.

For batch 39T particles, the model (capacitive impedance only) is fit to particles that are within specification and dimensionally closer to the nominal particle than are the particles in the borderline, more extreme, and most extreme groupings. Because the resultant model is "extrapolating" outside the range of dimensional features within which the model was fit in predicting the fractional impedance change values for the extreme particles the impedance predictions for these particles become pretty extreme. For this reason, a considerable number of the particles in these groupings are deemed unacceptable. Conversely, the models (inductive impedance and capacitive impedance) for the surrogate particle data set are fit to particles that are more dimensionally diverse relative to a nominal particle; consequently, these models tend to accept more of the extreme particles.

In an effort to generate inductive and capacitive impedance models based on a richer data set, the data set in Table 5.4 was also fit using the stepwise regression methodology. This data set uses the average dimensional features and impedance responses for most of the surrogate and NUCO particle batches for which such data was acquired in the course of the project. These data provide a more extensive set of anomalous conditions of particles (missing layers) to provide input to the models.

The same 97 particles (nominal, borderline, more extreme, and most extreme) were then used to generate predicted responses and to determine the "acceptability" of such particles. Note that "acceptable" in the previous analyses was taken to be the response range of 0.14 to 0.24 for the inductive and capacitive impedances. For the new models, based on Figures 5.10 and 5.11, the ranges were taken to be 0.10 to 0.24 for inductive impedance and 0.11 to 0.24 for capacitive impedance. These ranges were used to determine the green and yellow shading of acceptable and unacceptable particles as shown in Tables C.13 through C.20 in Appendix C.

Four additional particles were added to the end of the 97 particles. These additional particles were defined to have nominal dimensional features, but with a particular layer missing in each case. The particles having a missing buffer layer or a missing OPyC layer were predicted to have inductive impedance values outside the acceptable range and the particles having a missing IPyC or SiC layer were predicted to have inductive impedance values within the acceptable range.. But for capacitive impedance, all of the hypothetical defective particles were predicted to have impedance values outside the acceptable range except for the particle having a missing SiC layer, which was predicted to have a capacitive impedance marginally above the lower acceptable limit.

As with the surrogate model, the batch average models are fit to a data set that includes some rather extreme particles; consequently, most of the 97 additional particles are predicted to be acceptable because they are not particularly extreme compared to the particles used to fit the models. The capacitive impedance model rejects considerably more of the "most extreme" particles than does the inductive impedance model.

Note that this work is not intended to rigorously defend the use of the electronic measurement method as an inspection tool, but rather to present a methodology on how subsequent studies might be applied to make such a defense.
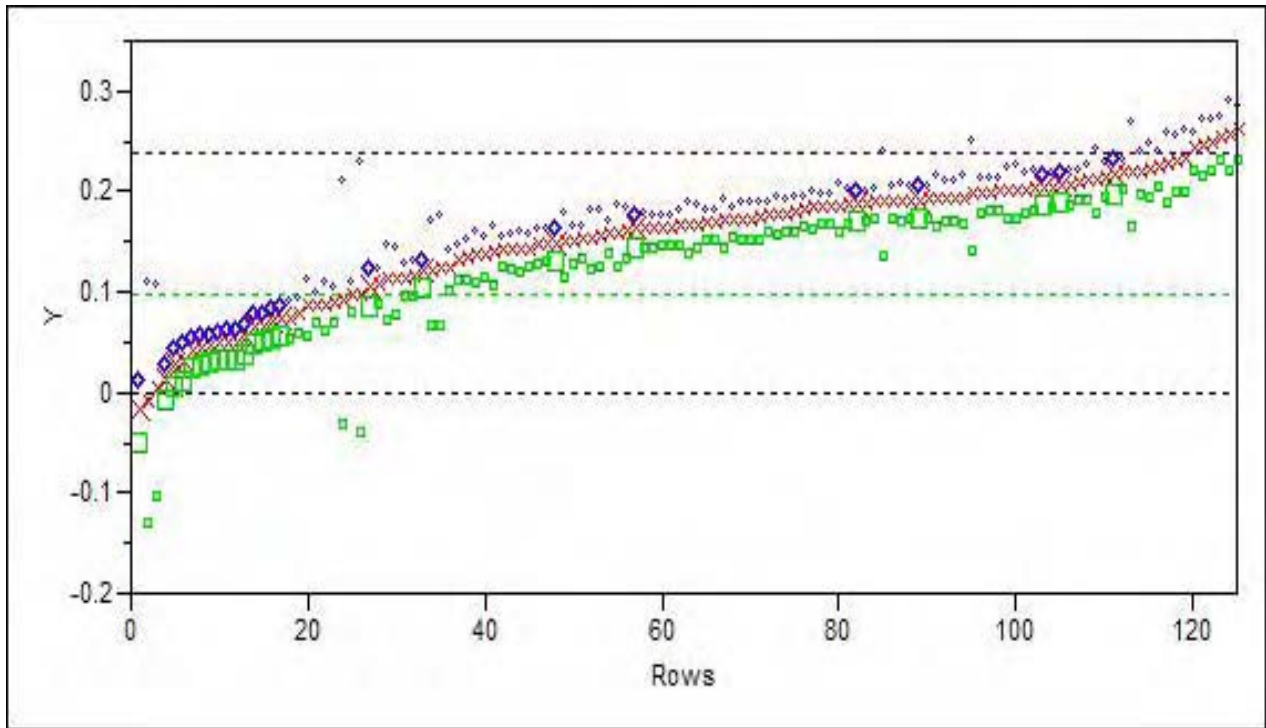
Figure 5.10. Inductive Impedance Batch Average Prediction Values and Prediction Limits
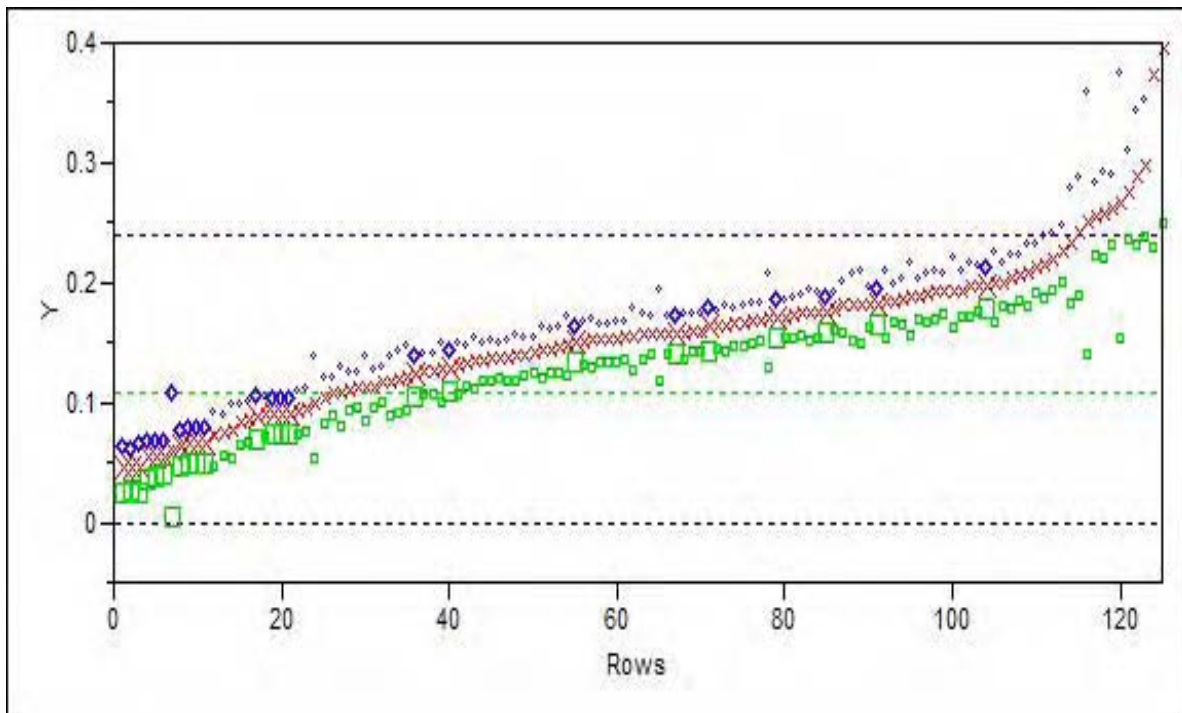
Figure 5.11. Capacitive Impedance Batch Average Prediction Values and Prediction Limits

5.12

Analysis and Conclusions for NERI QA/QC Project Electromagnetic Measurements

As discussed in Sections 3.2 Task 6 and 4.2 Task 6, inductive and capacitive impedance measurements were performed on various batches of surrogate coated particles during FY2004 and the first half of FY2005. The results of those measurements suggest that a measurement approach employing both types of impedance measurements in tandem might be capable of identifying particles with out-of-specification coating thicknesses. In the last quarter of FY2005 and the first quarter of FY2006, inductive and capacitive impedance measurements were performed on samples from a number of NUCO particle batches that had been fabricated by ORNL for the Advanced Gas Reactor Fuel Development and Qualification Program. Additionally, an extensive effort to populate the particle library (see Appendix B) with all of the data generated during the course of the program was completed. These two developments made it possible to perform a more global and quantitative evaluation of the impedance measurement data, the results of which are summarized below.

In defining the desired properties of the surrogate particle batches to be fabricated specifically by ORNL for use as particle standards in this project, it was decided to use two populations of different-size kernels for several of the batches. This was done so that each batch could potentially be the source of particle standards covering a broad size range. This approach was based on the anticipation that relatively large numbers of particles from each batch would be dimensionally characterized by ISU and that particles having the desired coating thicknesses and particle diameters would then be selected for EM measurements. However, the time required to generate the X-radiographic dimensional data turned out to be far greater than anticipated and, as a result, the amount of dimensional data generated for use by the program was limited. Furthermore, coordination of the impedance measurements at PNNL with the X-radiographic measurements at ISU proved difficult, which further limited the number of particles for which both EM measurement data and X-radiographic data were acquired. In the absence of an adequate database, the large range in particle size within a batch of particles often made interpretation of the EM measurement results difficult. Consequently, the approach taken in the current evaluation is to perform a more global evaluation of the data and to derive conclusions about the relationship between the EM measurements and the dimensional properties of coated particles using the population of batch-average data for all of the surrogate particle and NUCO particle batches.

Figure 5.12 plots the batch average fractional inductive impedance change versus batch average particle volume and carbon volume (i.e., combined volume of the buffer layer, IPyC layer, and OPyC layer). The plotted data are tabulated in Table 5.4. Figure 5.12 indicates that the fractional inductive impedance values measured for coated particles having a wide variety of properties are primarily influenced by the volume of carbon in the particles, which is consistent with the prediction of the inductive impedance mathematical model (see Numerical Modeling earlier in this section). The correlation coefficient R^2) for carbon volume versus fractional inductive impedance change is 0.908. The fractional inductive impedance also correlates reasonably well with particle volume ($R^2 = 0.626$), but this is because carbon volume and particle volume are, with one exception, well correlated for the coated particles that were measured. The exception is batch 14-B. The particles in this batch have only a SiC layer deposited directly onto a ZrO_2 kernel. The extremely low fractional inductive impedance change values measured for particles from this batch make it clear that it is carbon volume, not particle volume that has the primary influence on the inductive impedance measurements.
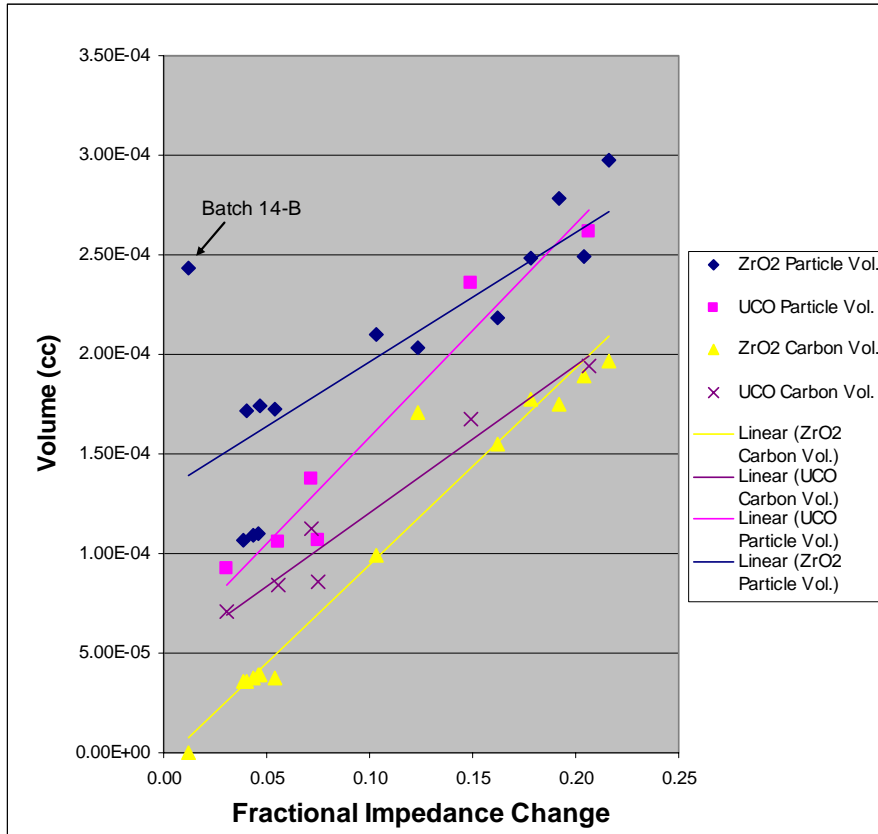
Figure 5.12. Carbon and Particle Volume versus Inductive Impedance

Although not shown in Figure 5.12, the relationship between OPyC density and inductive impedance was also evaluated. The correlation coefficient (R^2) for OPyC density versus fractional inductive impedance change as determined for all of the full TRISO batches in Table 5.4 is 0.707. So, OPyC volume does not correlate as well with fractional inductive impedance change as does the combined volume of all of the pyrocarbon coatings (i.e., carbon volume in Figure 5.12), which indicates that the induction impedance sensor is "seeing" more of the particle than just the OPyC layer.

Table 5.4. Summary of Particle Batch Dimensional and EM Measurement Data

Batch	Particle Type	Kernel Dia.	Buffer	IPyC	SiC	OPyC	Carbon Vol.	Particle Vol.	Ind. Imp.	Cap. Imp.	Ind. - Cap.
Surrogate Particles											
7-A	Kernel + IPyC layer	515	0	40	0	0	3.877E-05	1.103E-04	0.0461	0.0685	-0.0224
8-A	Kernel + IPyC layer	515	0	37	0	0	3.547E-05	1.070E-04	0.0389	0.0656	-0.0267
9-A	Kernel + IPyC layer	515	0	39	0	0	3.767E-05	1.092E-04	0.0437	0.0666	-0.0229
14-B	Kernel + SiC layer	693	0	0	41	0	0.000E+00	2.437E-04	0.0117	0.1622	-0.1505
5-B	Full TRISO	372	100	33	51	35	1.751E-04	2.783E-04	0.1920	0.1609	0.0311
12-B	Full TRISO, but no SiC	350	100	40	0	40	1.650E-04	1.874E-04	0.1231	0.0866	0.0365
13-A	Full TRISO with thin SiC	363	96	32	29	35	1.549E-04	2.183E-04	0.1619	0.1216	0.0403
6-CD	Full TRISO with thin buffer	451	19	28	55	41	9.920E-05	2.096E-04	0.1033	0.1292	-0.0259
11-E	Full TRISO	350	120	40	35	40	2.116E-04	2.887E-04	0.1784	N.M	N.A
5-D	Full TRISO	392	77	41	48	52	1.967E-04	2.972E-04	0.2162	0.1976	0.0186
13-C	Full TRISO with thin SiC	379	81	40	24	56	1.895E-04	2.494E-04	0.2044	0.1631	0.0413
7-AA	Kernel + IPyC + SiC	515	0	40	49	0	3.877E-05	1.743E-04	0.0468	0.0907	-0.0439
8-AA	Kernel + IPyC + SiC	515	0	37	50	0	3.547E-05	1.713E-04	0.0400	0.0825	-0.0425
9-AA	Kernel + IPyC + SiC	515	0	39	49	0	3.767E-05	1.728E-04	0.0544	0.0893	-0.0349
UCO Particles											
39T	Full TRISO	365	97	40	30	48	1.939E-04	2.615E-04	0.2068	0.1915	0.0153
41T	Full TRISO	365	99	40	30	32	1.674E-04	2.355E-04	0.1492	0.1450	0.0042
58B	Kernel + Buffer	345	108	0	0	0	7.094E-05	9.245E-05	0.0308	0.0423	-0.0115
66BI	Kernel + Buffer + IPyC	361	105	35	0	0	1.126E-04	1.373E-04	0.0715	0.0665	0.0050
IPyC-5	Kernel + Buffer + IPyC	345	90	31	0	0	8.440E-05	1.059E-04	0.0560	0.0551	0.0009
IPyC-6	Kernel + Buffer + IPyC	345	93	29	0	0	8.549E-05	1.070E-04	0.0754	0.0560	0.0194

The inductive impedance measurements performed on particles having only a buffer layer or a buffer and IPyC layer indicate that the density of the pyrocarbon layers also influences the inductive impedance. In Figure 5.13 and Figure 5.14, fractional inductive impedance change is plotted against carbon volume and carbon mass, respectively. The correlation coefficient for pyrocarbon volume versus fractional inductive impedance is 0.908, and the correlation coefficient for pyrocarbon mass versus fractional inductive impedance is 0.964. Included in the data points plotted in Figures 5.13 and 5.14 are NUCO particle batches IPyC-5 and IPyC-6. These batches were specifically selected for EM measurements because they have IPyC layers of significantly different densities (1.75 g/cc and 1.96 g/cc, as measured at ORNL, for batches IPyC-5 and IPyC-6, respectively). As shown in Table 5.4, the average fractional inductive impedance change measured for particles from batch IPyC-6 is significantly higher than that measured for particles from IPyC-5 even though the average volumes of the pyrocarbon layers in the particles from the two batches are almost the same. On the other hand, the average mass of the pyrocarbon layers is about 5.5% higher in batch IPyC-6 than in batch IPyC-5, which is more consistent with the higher average fractional inductive impedance change measured for the particles from batch IPyC-6. However, even though pyrocarbon density has some influence on the inductive impedance measurements, this will be a second order effect because of the relatively small ranges in density that would be expected for the

pyrocarbon layers in the TRISO coating system. Consequently, it is considered unlikely that such measurements (at least at the frequency at which they were performed in this study) would be useful in distinguishing the small differences in IPyC and OPyC density that are important to the irradiation performance of the TRISO particles.
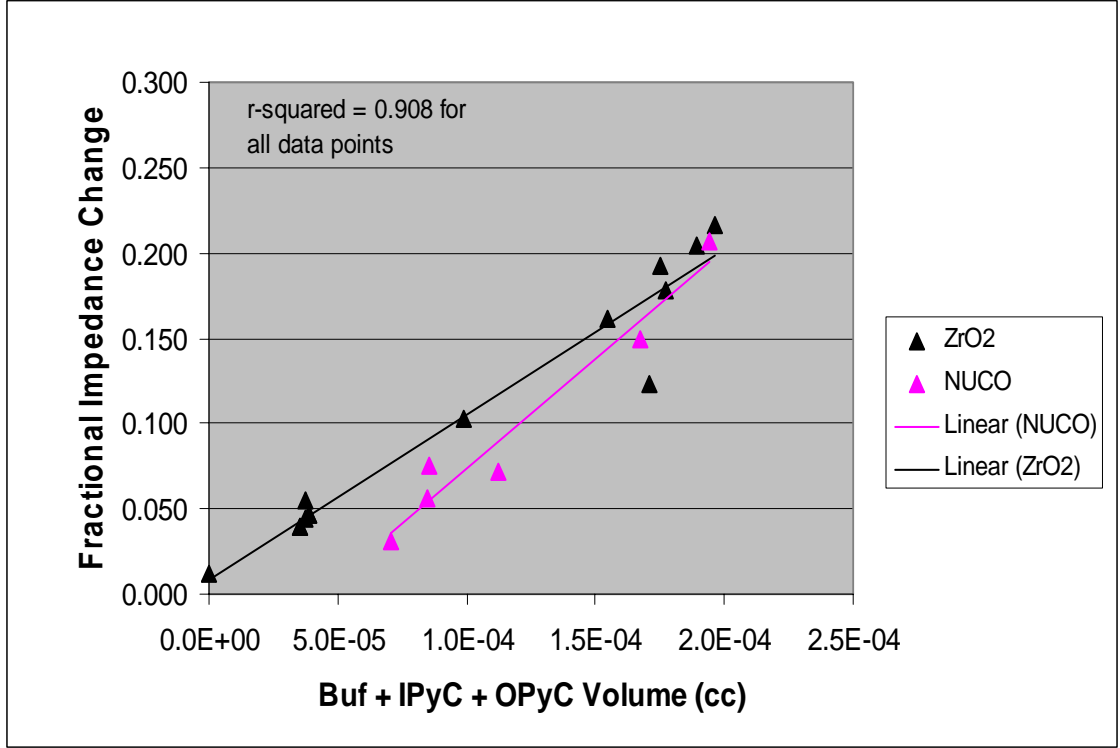
Figure 5.13. Fractional Inductive Impedance Change versus PyC Coating Volume

Figure 5.15 plots the batch average fractional capacitive impedance change versus batch average particle volume and SiC volume. The plotted data are tabulated in Table 5.4. Figure 5.15 indicates that the fractional capacitive impedance values measured for coated particles having a wide variety of properties are primarily influenced by the volume of the particles, which is consistent with the prediction of the capacitive impedance mathematical model (see Numerical Modeling earlier in this section). The correlation coefficient (R^2) for particle volume versus fractional capacitive impedance change is 0.916. However, as is evident from Figure 5.15, SiC volume and fractional capacitive impedance change are not well correlated.
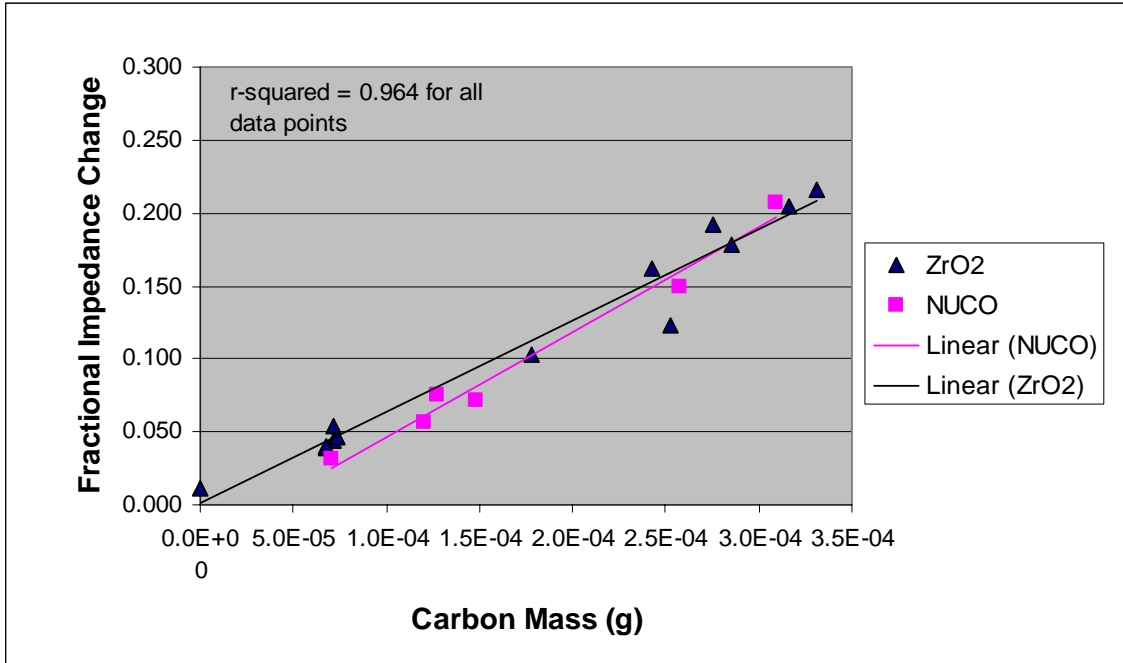
Figure 5.14. Fractional Inductive Impedance Change versus Carbon Mass
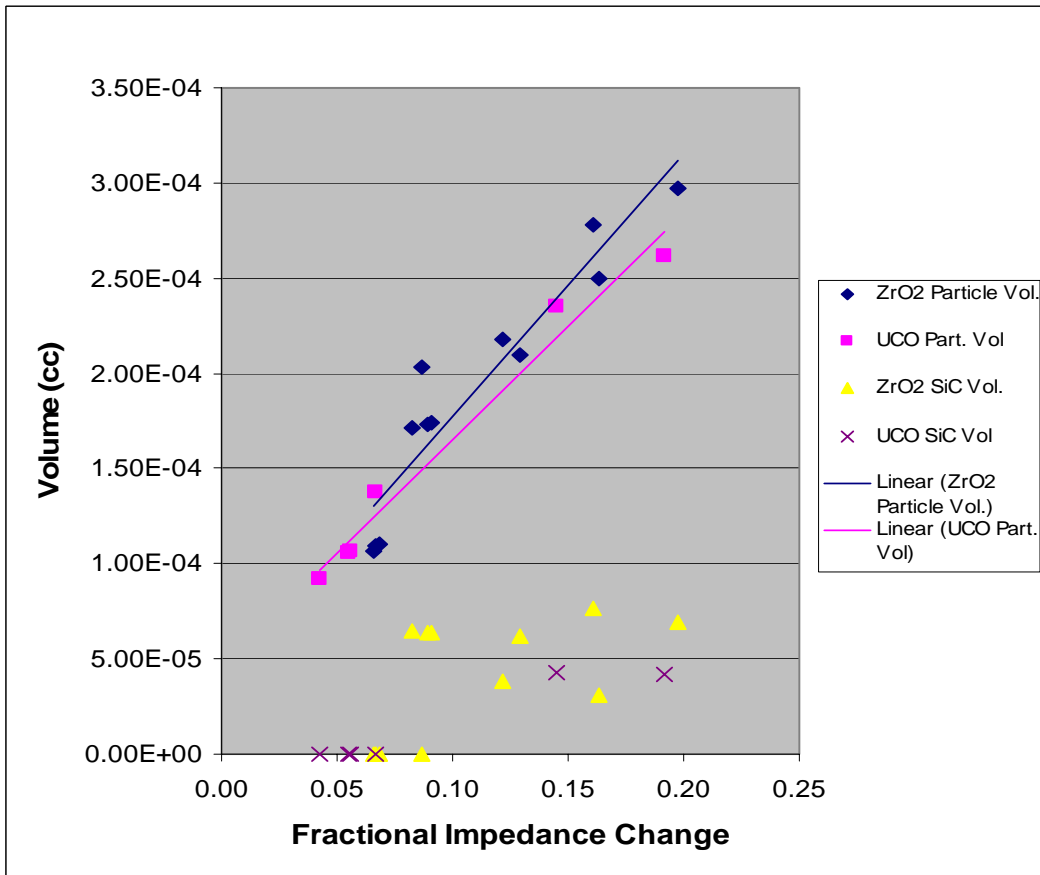
Figure 5.15. SiC Volume and Particle Volume versus Capacitive Impedance

Figure 5.16 plots the difference between the fractional inductive impedance change and the fractional capacitive impedance change versus the ratio of particle volume to carbon mass. As anticipated based on the good correlation between inductive impedance and carbon mass and between capacitive impedance and particle volume, the impedance difference and the particle volume/carbon volume ratio are shown in Figure 5.16 to be reasonably well correlated.
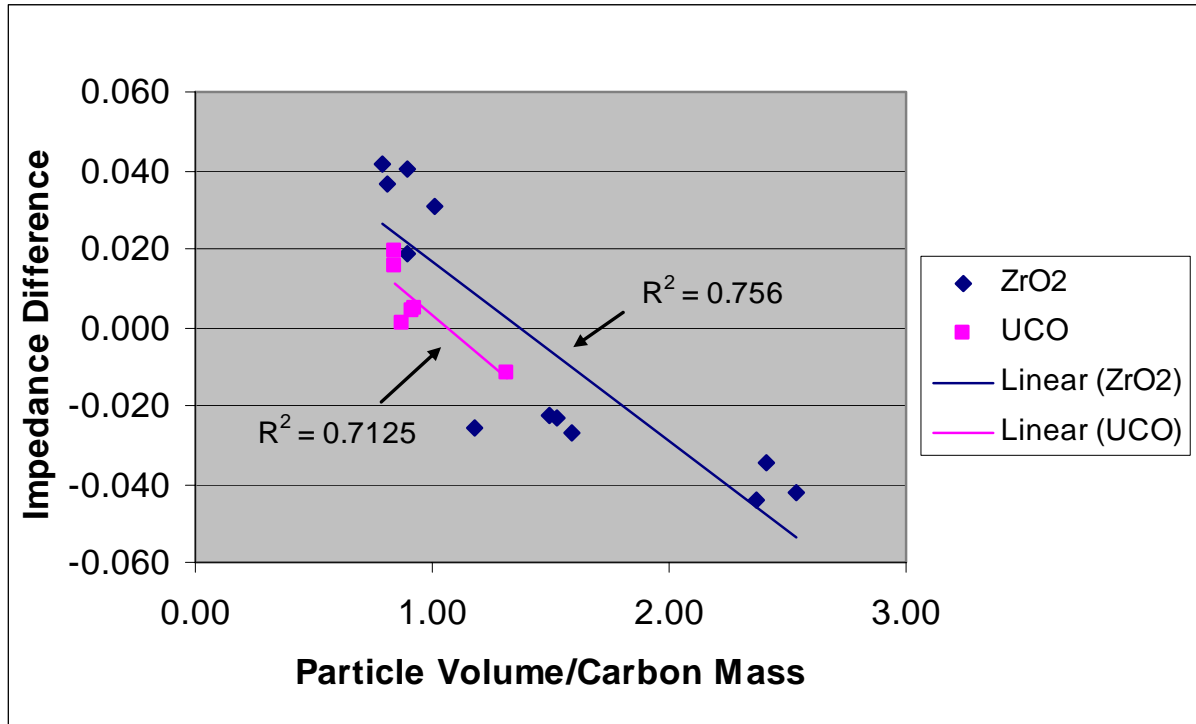
Figure 5.16. Particle Volume/Carbon Mass versus Inductive - Capacitive Impedance Change

As noted above, this project was able to obtain samples in the last quarter of FY2005 from some of the NUCO coated particles batches fabricated by ORNL for the AGR Fuel Development and Qualification Program. This was an important development in that it allowed EM measurements to be performed on NUCO coated particles and to be compared with the EM measurements on surrogate particles. As can be seen in Figures 5.12 through 5.15, the NUCO and surrogate EM measurements comprise consistent sets of data that correlate about the same with carbon volume, carbon mass, and particle diameter, consistent with the predictions of the inductive impedance and capacitive impedance mathematical models (see Numerical Modeling earlier in this section). This evidence that the surrogate particle data and NUCO particle data comprise consistent data sets confirms the applicability of the surrogate particle data to fuel particles having uranium kernels.

Obtaining fully coated NUCO particles from ORNL was also an important development from the standpoint that the NUCO coated-particle batches are far more representative (than the surrogate particle batches) of production material with respect to particle-to-particle variability. Thus, access to this material gave the project a better opportunity to explore the sensitivity of the EM measurements to identify atypical particles within a representative TRISO coated particle batch. This was accomplished by measuring the fractional impedance change in both an induction sensor and a capacitance sensor for 100 particles from batch NUCO350-39T. The mean fractional inductive impedance change, mean fractional

capacitive impedance change, and mean difference between the inductive and capacitive impedance changes, and the standard deviations for each were calculated for the first 91 particles (the last 9 particles were excluded because the capacitive impedance measurements appear to be indicative of a measurement problem). Table 5.5 reports the means and standard deviations for these measurements.

Table 5.5. EM Measurement Mean Values and Standard Deviations for Batch NUCO350-39T

Parameter	Mean Value	Standard Deviation
Fractional inductive impedance change	0.2067	0.0187
Fractional capacitive impedance change	0.1915	0.0178
Fractional impedance change difference (I-C)	0.0152	0.0113

The normal deviate (Z) for each EM parameter was calculated for each of the 91 particles, then ordered from the smallest to the largest value. Particles having the largest and smallest Z values for each EM parameter were selected for X-radiographic determination of the kernel diameter and coating thicknesses. A number of particles having Z values near zero for all EM parameters were also selected for X-radiographic examination. The purpose of the X-radiographic examinations was to determine if the EM measurements are distinguishing between typical and atypical particles.

The results of this evaluation are summarized in Table 5.6. In general, the results in Table 5.6 show that the EM measurements have good sensitivity to detect both atypical and typical particles. Each of the four particles selected for examination on the basis of giving near-zero Z values for all of the measured EM parameters have kernel diameters and coating thicknesses that are approximately the same. Additionally, the majority of the particles selected on the basis of giving high or low Z values for fractional inductive impedance change and/or fractional capacitive impedance change have large or small kernel diameters and/or coating thicknesses that are consistent with the high or low measured fractional impedance changes, as indicated in the comments column of Table 5.6. The only EM parameter that is not generally consistent with the kernel diameter and coating thickness measurement data for batch NUCO350-39T is the impedance change difference. It is concluded that this parameter, which is subject to larger measurement uncertainty because it is affected by measurement error in both the inductive and capacitive impedance measurements, is not sufficiently sensitive to be useful in discerning between relatively small differences in kernel diameter and coating thickness such as are present in the measured particles from batch NUCO350-39T.

It should be noted, however, that none of the NUCO350-39T particles giving high positive or negative Z values for fractional inductive impedance change or fractional capacitive impedance change would be considered to be defective particles based on the AGR fuel specifications. This suggests that a Z-based particle rejection criterion that might be established for each of the three EM parameters in a tandem inductance-capacitance inspection/sorting operation should be set at values of Z somewhat less than -2 and greater than +2.

To determine the sensitivity of the EM measurements to detect defective particles and to estimate what the rejection criterion (based on Z) might be for the various EM parameters, the EM measurement results for various surrogate particle batches that were fabricated to be representative of defective particles were compared with results for the "nominal" particle for batch NUCO350-39T. Specifically, Z values were calculated for each EM parameter for each of the defective surrogate particle batches based on the measured EM parameter for the surrogate batches and the corresponding mean value and standard

5.19

deviation for batch NUCO350-39T. Table 5.7 summarizes the results of this analysis. The results suggest that the approach of using inductive impedance and capacitive impedance measurements in tandem should provide the capability to detect particles having a missing buffer layer (defined as a buffer coating having a thickness of less than 20 μm) even in a particle having a kernel far larger than is likely to be present in a production fuel particle batch. The results also suggest that this tandem approach could detect particles having a missing SiC layer and perhaps even a thin SiC layer (defined as having a thickness of less than 20 μm), and a missing OPyC layer.

In conclusion, the evaluation of the results of the EM methods presented above indicates that inductive and capacitance impedance measurements could provide a means of sorting TRISO fuel particles with respect to particle volume and pyrocarbon mass (or volume), respectively, and that these techniques, when used together, should provide an effective means of sorting out particles that are dimensionally atypical, including particles with missing or excessively thin coating layers. Furthermore, as described in Section 4.2, Task 12-17, PNNL has designed and built a prototype automated EM method inspection system and demonstrated the system (in a video provided to DOE) at an inspection rate of approximately 500 to 1000 particles/min. Substantially higher inspection rates would be possible using more sophisticated equipment. These results are considered to be important because it appears that the EM methods can provide an enhanced inspection capability relative to currently available methods (e.g., screening, roller micrometer, etc., particle size analyzer, etc.) that are capable of sorting particles only on size (particle diameter).

There is also some indication that the inductive impedance method could be used to characterize the IPyC layer (in buffer and IPyC-coated particles) and the OPyC layer with respect to density, but it is doubtful that the inductive impedance measurement would detect small density differences in the presence of the expected particle-to-particle variations in PyC layer thickness. However, if the measurement is used as an in-line go/no-go check of the acceptability of batch average PyC density, the capability to detect small differences in density should not be necessary.

Although theory indicates that the inductive impedance measurements might be influenced by differences in PyC microstructure, the project did not develop any empirical evidence supporting this, and it is again doubtful that differences in microstructure could be detected in the presence of the expected variations in PyC layer volume. It is probably correct to conclude that the EM methods, at least as they were performed in this study, do not have the capability to detect structural defects in the PyC or the SiC coating layers. However, it should be emphasized that the scope of the EM methods task did not include optimization of the frequency, and that based on the results of the modeling work performed in this project, it is likely that different frequencies would give better results for different properties.

Although no particles having a missing or thin ($\leq$ 20-μm) IPyC layer were available for this study, the results shown on Figure 5.12 and in Table 5.7 suggest that such a particle would have a sufficiently low fractional inductance impedance change to be flagged as a defective particle. The results in Table 5.6 and Table 5.7 also suggest that the rejection criterion for fuel particles from typical production coating batches should be set at about $Z < -3$ and $Z > 3$ for all of the EM parameters (e.g., fractional inductive impedance change, fractional capacitive impedance change, and mean fractional impedance difference).

In a further effort to determine the feasibility of using the EM parameters to detect defective particles in production batches of AGR fuel particles, the EM parameters for a nominal AGR particle (i.e., having the nominal kernel diameter and coating thicknesses specified in the AGR Fuel Product Specification) and for

various defective particles (having missing or thin coating layers) were calculated using the statistical models developed from stepwise regression analysis of the batch average EM measurement data presented in Table 5.4 (see Statistical Modeling earlier in this section). Table 5.8 summarizes the results of this analysis, which, for the most part, confirm the conclusions reached from the evaluation of the defective surrogate particles summarized in Table 5.7. Specifically, the data in Table 5.8 suggest that one or more of the EM parameters has the capability, with fairly wide margin, to detect otherwise nominal particles having a missing or thin buffer layer, a missing IPyC layer, or a missing OPyC layer. Furthermore, the wide margin in the capability to detect these defects in otherwise nominal particles suggests that it should be possible to detect these same defects in particles having off-nominal kernel diameters or coating thicknesses consistent with the expected distribution of these properties in production coating batches. However, the predicted EM parameters calculated in Table 5.8 for a nominal AGR particle having a missing SiC layer do not confirm the conclusion from the defective surrogate particle evaluation that a particle having a missing SiC layer would be detected. Specifically, such a particle would not be rejected based on a rejection criterion of $Z < -3$ or $Z > 3$, but, the low Z values for both inductive impedance (-1.93) and capacitive impedance (-1.91) would suggest that the particle is atypical. Clearly, the rejection criterion (if based on Z) would need to be optimized to obtain an acceptable quality-versus-yield tradeoff in a particle sorting operation utilizing the EM parameters as the basis for accepting or rejecting coated particles.

Table 5.6. Summary of EM Measurement Data for NUCO Coated Particle Batch NUCO350-39T

Particle ID	Fractional Ind. Imp. Change (I)	Z	Fractional Cap. Imp. Change (C)	Z	I-C	Z	Summary of EM Response	Kernel Dia. (µm)	Buffer (µm)	IPyC (µm)	SiC (µm)	OPyC (µm)	Part. Dia. (µm)	Carbon Vol. Ratio (CVR)	Particle Vol. Ratio (PVR)	Pvol/Cvol	Comments
Nominal	0.2070	0.00	0.1920	0.00	0.0150	0.00	N/A	360	99	40	33	52	808	1.00	1.00	1.35	Hypothetical particle having the average kernal diameter and coating layer thicklnesses of particles 39T-21, 39T-35, 39T-63, and 39T-77
39T-A21	0.2063	-0.02	0.1881	-0.19	0.0182	0.27	Typical	351	97	42	34	56	806	1.00	0.99	1.34	Carbon vol. and particle vol. are about the same as for nominal particle
39T-A35	0.2047	-0.11	0.1904	-0.06	0.0143	-0.08	Typical	352	104	40	35	53	816	1.03	1.03	1.34	"
39T-A63	0.2043	-0.13	0.1882	-0.19	0.0161	0.09	Typical	370	94	41	35	50	811	0.98	1.01	1.38	"
39T-A77	0.2046	-0.11	0.1891	-0.13	0.0155	0.02	Typical	364	100	38	32	51	808	1.00	1.00	1.35	"
39T-A17	0.1725	-1.83	0.1855	-0.34	-0.0130	-2.49	low I, low I-C	356	86	38	37	52	782	0.88	0.91	1.39	Low I consistent with low CVR (due to thin buffer); C is high for low PVR, which explains low I-C
39T-A37	0.1747	-1.71	0.1590	-1.83	0.0157	0.05	low I, low C	348	93	39	37	52	789	0.91	0.93	1.38	Low I and low C consistent with low CVR and low PVR (due to small kernel and thin buffer)
39T-A57	0.1759	-1.64	0.1539	-2.11	0.0220	0.61	low I, low C	360	76	41	34	52	767	0.82	0.85	1.40	Low I and low C consistent with low CVR and low PVR (due to thin buffer)
39T-A75	0.1860	-1.11	0.1590	-1.83	0.0270	1.04	low I, low C	352	89	37	34	52	774	0.86	0.88	1.37	Low I and low C consistent with low CVR and low PVR
39T-A82	0.1737	-1.76	0.1607	-1.73	0.0130	-0.19	low I, low C	356	73	43	37	53	767	0.82	0.85	1.41	Low I and low C (due to thin buffer) consistent with low CVR and low PVR
39T-A4	0.2464	2.12	0.2279	2.04	0.0185	0.29	high I, high C	404	90	34	33	51	819	1.00	1.04	1.40	High I and high C are not consistent with particle properties
39T-A20	0.2610	2.90	0.2433	2.90	0.0177	0.23	high I, high C	416	100	41	30	56	870	1.25	1.25	1.34	High I and high C consistent with high CVR and high PVR (due to large kernel)
39T-A26	0.2537	2.51	0.2116	1.13	0.0421	2.37	high I, high I-C	379	103	35	33	51	822	1.04	1.05	1.36	High I (which explains high I-C) is not consistent with CVR
39T-A32	0.2165	0.52	0.2284	2.07	-0.0119	-2.38	high C, low I-C	362	115	32	32	49	817	1.04	1.03	1.34	High C (which explains low I-C) is not consistent with PVR
39T-A33	0.2254	1.00	0.2297	2.14	-0.0043	-1.72	high C, low I-C	376	100	41	33	50	825	1.06	1.07	1.36	High C (which explains low I-C) is not consistent with PVR
39T-A56	0.2499	2.30	0.2273	2.01	0.0226	0.65	high I, high I-C	385	112	37	29	55	850	1.20	1.16	1.31	High I and high C consistent with high CVR and high PVR (due to large kernel)
39T-A68	0.1964	-0.55	0.2012	0.54	-0.0048	-1.76	low I-C	408	93	35	31	49	823	1.02	1.06	1.39	Low C is not consistent with high CVR, which explains low I-C
39T-A22	0.2344	1.48	0.1996	0.46	0.0348	1.73	high I-C	380	103	37	35	57	843	1.13	1.13	1.35	C is low for high PVR, which explains high I-C
39T-A29	0.2311	1.30	0.1851	-0.36	0.0460	2.71	high I-C	351	102	39	33	52	801	0.98	0.97	1.34	High I (which explains high I-C) is not consistent with CVR
39T-A67	0.2356	1.54	0.1783	-0.74	0.0573	3.71	high I-C	370	90	37	32	46	779	0.87	0.90	1.39	High I (which explains high I-C) is not consistent with CVR

Table 5.7. Summary of Evaluation of EM Parameters for Defective Surrogate Fuel Particle Batches

Particle ID	Type of Defect	Fractional Ind. Imp. Change Value (I)	Z	Fractional Cap. Imp. Change Value (C)	Z	I - C Value	Z	Kernel Dia. (µm)	Buffer (µm)	IPyC (µm)	SiC (µm)	OPyC (µm)	Part. Dia. (µm)	Carbon Vol. Ratio (CVR)	Particle Vol. Ratio (PVR)	Pvol/Cvol	Comments
39T nominal	Reference Particle	0.2070	0.00	0.1920	0.00	0.0150	0.00	360	99	40	33	52	808	1.00	1.00	1.35	
12-B nominal	Missing SiC	0.1231	-4.49	0.0866	-5.92	0.0365	1.90	396	111	28	0	28	730	0.83	0.74	1.19	Particle would be rejected on low I and low C; high I-C is indicative of low Pvol/Cvol, which suggests low SiC volume (i.e., a thin or missing SiC layer)
6-CD nominal	Thin buffer, large kernel	0.1033	-5.55	0.1292	-3.53	-0.0259	-3.62	451	19	28	54	41	735	0.48	0.75	2.10	Particle would be rejected on low I and low C; low I-C is indicative of high Pvol/Cvol, which suggests low carbon volume (i.e., a thin or missing PyC layer)
6-CD-B11	Thin buffer, very large kernel	0.1555	-2.75	0.2153	1.31	-0.0598	-6.62	552	27	25	49	41	836	0.69	1.11	2.17	The very large kernel increases I and C (relative to 6-CD nominal) into acceptable ranges. However, the particle would be rejected on low I-C
6-CD-B29	Missing buffer	0.0865	-6.44	0.1530	-2.19	-0.0665	-7.21	396	21	32	58	41	700	0.44	0.65	2.00	Particle would be rejected on low I and low C; low I-C is indicative of high Pvol/Cvol, which suggests low carbon volume (i.e., a thin or missing PyC layer)
13-C-A7	Thin SiC	0.2168	0.52	0.1658	-1.47	0.0510	3.19	386	90	39	22	56	798	1.01	0.96	1.29	Particle would be accepted on I and C; but would be rejected on high I-C, which is indicative of low Pvol/Cvol suggesting low SiC volume
8AA-A10	Missing buffer & OPyC, large kernel	0.0350	-9.20	0.0844	-6.04	-0.0494	-5.70	520	0	38	51	0	699	0.18	0.65	4.80	Particle would be rejected on low I and low C; low I-C is indicative of high Pvol/Cvol, which suggests low carbon volume (i.e., a thin or missing PyC layer)
66-BI	Missing SiC & OPyC	0.0715	-7.25	0.0665	-7.05	0.0050	-0.88	361	105	35	0	0	641	0.55	0.50	1.22	Particle would be rejected on low I and low C

Table 5.8. Summary of Evaluation of Predicted EM Parameters for Defective AGR Fuel Particles

Particle ID	Type of Defect	Fractional Ind. Imp. Change Value (I)	Z	Fractional Cap. Imp. Change Value (C)	Z	I - C Value	Z	Kernel Dia. (μm)	Buffer (μm)	IPyC (μm)	SiC (μm)	OPyC (μm)	Part. Dia. (μm)	Carbon Vol. Ratio (CVR)	Particle Vol. Ratio (PVR)	Pvol/Cvol	Comments
AGR nominal particle	Reference Particle	0.1870	0.00	0.1700	0.00	0.0170	0.00	350	100	40	35	40	780	1.00	1.00	1.40	
AGR defective particle	Missing Buffer	0.0890	-5.24	0.0880	-4.61	0.0010	-1.42	350	0	40	35	40	580	0.32	0.41	1.83	Particle would be rejected on low I and low C; low I-C indicates high Pvol/Cvol, which suggests low carbon volume (i.e., a thin or missing buffer or PyC layer)
AGR defective particle	Very Thin Buffer	0.1110	-4.06	0.0920	-4.38	0.0190	0.18	350	20	40	35	40	620	0.42	0.50	1.68	Particle would be rejected on low I and low C; I-C is higher than expected based on Pvol/Cvol
AGR defective particle	Missing IPyC	0.1720	-0.80	0.0860	-4.72	0.0860	6.11	350	100	0	35	40	700	0.67	0.72	1.50	Particle would be rejected on low C; I is higher than expected based on Cvol and I-C is much higher than expected based on Pvol/Cvol
AGR defective particle	Missing SiC	0.1510	-1.93	0.1360	-1.91	0.0150	-0.18	350	100	40	0	40	710	0.93	0.75	1.14	Particle would not be rejected based on Z values if rejection criterion is IZI > 2; however, the low Z values for both I and C suggest that the particle is atypical
AGR defective particle	Thin SiC	0.1640	-1.23	0.1500	-1.12	0.0140	-0.27	350	100	40	15	40	740	0.96	0.85	1.25	Particle would not be rejected
AGR defective particle	Missing OPyC	0.0730	-6.10	0.0880	-4.61	-0.0150	-2.83	350	100	40	35	0	700	0.61	0.72	1.66	Particle would be rejected on low I and low C; low I-C indicates high Pvol/Cvol, which suggests low carbon volume (i.e., a thin or missing buffer or PyC layer)

5.2 Acoustic Microscopy

The acoustic microscopy approach to characterizing coated surrogate fuel particles was evaluated during the early phase of this NERI project. The concept was to determine the degree of penetration and the feasibility of acquiring measurements such as layer thickness, material properties, and detecting localized changes in microstructure. Initially a modeling approach was taken to ascertain whether defect signatures could be characterized. This approach was taken because the TRISO particle layers are relatively thin and discrimination of echoes from the different layers would be extremely difficult. It was determined that the reflection coefficient was sensitive to layer thickness. Prior to the availability of coated particles, glass spheres were examined using the acoustic microscopy system at PNNL. Working at 50 MHz, it was possible to see gross feature differences between damaged and undamaged glass spheres. However; as work progressed, it was evident that to image and resolve micron-size defects in coated TRISO particles, it would be necessary to work at the extreme high end of the frequency range for ultrasonics, above 250 MHz and perhaps as high as 1 GHz. This would require a substantial amount of funding and was determined to be beyond the scope of this project. Consideration was given to the ability of the system to detect only conditions indicative of a materials property deviation from those of a standard.

5.3 Resonant Ultrasound Spectroscopy

These data indicate the resonance modes of TRISO particles are extremely sensitive to internal defects including thin layers, missing layers and to the size and shape of the particles. Even though there is variability in the location, number and shape of the resonant peaks for nominally identical particles, the defective particles are clearly distinguishable from normal TRISO particles. With the current laboratory system, these measurements can be performed at approximately 1 measurement per second by narrowing in on the region near 3 MHz, where the dominant resonant peaks in normal TRISO particles occur. The speed of measurement can be increased to several per second and automated and coupled with the particle handling system.

Further work is needed to evaluate the capability of RUS to perform inspection of TRISO particles and to identify a method to rapidly inspect particles using RUS. The current method used to acquire the data at PNNL is accurate but slow.

5.4 High-resolution Radiography and Computed Tomography

In the early phases of this NERI project, it became apparent that using computed tomography for characterizing particle density distribution was not efficient. After processing large volumes of high-resolution data (~ 1-GB) for each particle and considering that it takes about 90 minutes to produce a single image, it quickly became apparent that a faster and more efficient method was necessary. Digital radiography was found to be a faster and more efficient method for assessing batches of particles and selecting those with the most representative features thought to degrade the particle performance. Using the micro-focus digital radiography system at ISU's Center for Nondestructive Evaluation, images with a 3-µm pixel size were readily attained. This system can produce high-resolution images suitable for characterization of layers in fuel particles

Using this radiographic method at ISU, particles were characterized and important dimensional data was input into the particle library. This data provided physical evidence of kernel size, coating layer

thickness, and particle ovality. This formed the basis for the correlation of electrical measurements to known particle parameters.

Though a very effective method to determine dimensional geometries (and density) of the TRISO particles, the radiographic method is not well suited for a high-speed in-line process stream and should be considered as an off-line tool for batch sampling with statistical analysis.

5.5 Transmission and Diffuse Field Ultrasound

In this NERI project, work was performed to determine how effective transmission ultrasound could be utilized to provide bulk measurement capabilities of TRISO particles. To evaluate the potential for in-situ measurements of particle properties, air-coupled ultrasonic measurements were utilized. Ultrasonic characterization and examination of materials requires a correlation of measurable ultrasonic parameters such as acoustic speed of sound (time-of-flight), attenuation (amplitude), and frequency response information, to the conditions, geometry and physical properties of interest in the material under test. For this evaluation, glass beads of three average particle sizes were used as surrogates to the nuclear fuel particles. An air-coupled ultrasonic pulse-compression technique was used to insonify the glass spheres with sufficient energy to obtain measurements of speed of sound and attenuation. The speed and relative attenuation of the propagating sound wave were measured using the results from the broadband pulse compression technique. Relative attenuation measurements were made by comparing the frequency-dependent signal amplitude through two different wave propagation paths, thus minimizing the effects of acoustic impedance and various other factors affecting ultrasonic wave propagation. Using the data from multiple measurements, analysis of variance was performed on the data and 95% confidence limits were calculated for amplitude at each frequency. The differences in attenuation spectra from each glass sphere size distribution are small when compared to the actual particle size distributions. Based on the results from this testing, the air-coupled ultrasonic technique does not appear to have the required sensitivity to changes in coating thickness for the frequency range and particle sizes of interest. If the nuclear fuel particles were to be transferred through a liquid medium, where a higher frequency ultrasonic setup could be used, determination of average particle size would be much more feasible using both velocity and attenuation parameters.

Diffuse field ultrasound was considered as a possible method for bulk measurement of TRISO particles. As part of this NERI only a minimal literature survey was performed. The bulk of the ultrasound work was directed towards the transmission technique.

5.6 Optical Measurements

The optical work investigated as part of this NERI project included the development of instrumentation, algorithms and procedures for characterization/inspection of fuel particles using optical imaging methods. Originally two parallel paths of investigation were proposed within the scope of "optical inspection" 1) profilometry and 2) image analysis. Because ORNL was developing a capability in optical profilometry, the work at PNNL concentrated on image analysis. The image analysis approach considered both an off-line (static) laboratory scale characterization, and an in-line inspection capability.

Methods for static image digitization of particles were developed to support the evaluation of requirements for automated systems, including resolution issues and hardware issues driven by

production requirements. The result was a practical approach to digitizing images of individual particles using an available optical microscope with images recorded using a "prosumer" digital camera, and image processing with a commercial image processing and analysis software package. Detection of surface anomalies on the order of 1- to 2 μm was achieved and measurement capabilities were on the order of 5 μm.

The methods used for the initial results were refined and following a decision to emphasize off-line automated characterization, hardware was identified and algorithm developed for an off-line automated digital camera/microscope system for image digitization and automated characterization of particle surface features. A high-speed in-line inspection capability was investigated in parallel with the off-line system. Detectors were researched and identified for use in a multi-camera, multi-line-of-sight concept for providing high-resolution images of particles on the fly, at speeds sufficient for parallel lines to achieve a throughput in the order of 200 particles/sec. Tradeoffs in an optical characterization system include spatial resolution, throughput and cost. Beginning with a standard video-based machine vision inspection system, methods for increasing spatial resolution normally result in lower throughput and/or higher cost. Conversely, the methods of increasing throughput normally result in lower resolution and/or higher cost. For diameter measurements and roundness derived from diameter, profilometry systems can be the least costly and can provide the highest throughput. Image-based systems will be slower and more costly, so would not be the choice if only diameter (and derived parameters) is required. For detecting 1-μm pits expected under certain fabrication conditions, only the highest resolution is likely to provide adequate detection capability, calling for the Canon camera/Leica microscope combination at 10X, with single particle throughput. For in-line inspection, it appears that the ability to digitize individual particles at resolutions approaching the Canon camera/Leica microscope combination at 5X might be achievable, at rates of around 100 particles/sec. This would entail a camera having 100 frames/sec. or greater speed and 1- mega-pixel or greater resolution. At current prices, cameras of this type cost upwards of $5000. In addition, it is likely that processing will need to be implemented in hardware – for example Field-Programmable Gate Arrays[a] (FPGAs), a type of logic chip that can be programmed.

––––––––––––––––––––

(a) FPGAs support thousands of electronic gates. They are especially popular for prototyping integrated circuit designs. Once the design is set, hardwired chips are produced for faster performance.

6.0   Project Recommendations

The following table summarizes the scope, conclusions, and recommendations (for further work) from the NERI QA/QC.

Table 6.1. Summary of Inspection Methods and Results

Scope, Conclusions, and Recommendations for Further Work		
Method Evaluated	**Conclusions**	**Recommendations**
Electromagnetic methods (inductive and capacitive impedance measurements)	Good potential demonstrated for real-time in-line screening of coated fuel particles having atypical size and coating layer thickness. Potentially useful for detecting particles having other types of coating defects, but this capability not demonstrated during the project.	Optimize sensor frequency for specific coated particle properties. Refine sensor designs as a means of detecting cracks and other non-geometric coating flaws. Optimize sensor design to reduce measurement uncertainty. Determine feasibility of using capacitive impedance measurements to detect NUCO kernels having poor stoichiometry.
Resonance ultrasound spectroscopy (RUS)	Good potential for application to off-line, and possibly in-line, inspection of coated particles for geometric (e.g., coating layer thickness) and non-geometric flaws. However, mechanical coupling of a transducer to the small coated particles is problematic for high-speed inspection.	Evaluate laser ultrasonic resonance methods and develop a non contact inspection technique.
Optical surface inspection	Good potential for off-line and, possibly, in-line inspection of coated particles having visual coating defects.	Develop specifications for, build, and demonstrate a prototypic high-speed inspection system.
Acoustic microscopy	No potential for application to coated-particle QC at ultrasonic frequencies below 250 MHz. Must have 1-5 micron resolution to be useful.	None

Scope, Conclusions, and Recommendations for Further Work		
Method Evaluated	**Conclusions**	**Recommendations**
Transmission and diffuse field ultrasound	Transmission ultrasound did not have the required sensitivity to changes in particle size in the ultrasound frequency range evaluated. Diffuse field ultrasound was not evaluated.	None
X-radiography and computed tomography	Both techniques have good potential for use in off-line inspection of coated particles. Computed tomography work was limited because it was too time consuming to be effective in supporting project objectives.	None

The recommendations for further work to advance the development of inspection capabilities for TRISO particles are discussed in greater detail below.

6.1 Electrical Measurement Techniques

As mentioned in Section 5, the eddy current density is a function of radial distance from the center of the particle. At the highest frequency, most of the eddy current power is confined to the OPyC layer. At lower frequencies, a larger fraction of the eddy current power penetrates into the deeper layers. This leads to the possibility that additional information about layer thicknesses could be obtained by (**Recommendation #1)** measuring the coil impedance at multiple frequencies. An aggressive implementation of this concept would be to use a short (wideband) pulse to excite the eddy currents. This would potentially provide a maximum amount of depth-dependent information at the cost of a larger volume of data and greater complexity in data processing (e.g., the use of a Fourier transform).

Because a coil of the type used in this project interrogates the entire particle and induces eddy currents throughout a substantial portion of the conductive outer layers of a particle, it is not sensitive to localized flaws such as cracks or gold spots. Improved spatial resolution could be achieved by using a (**Recommendation #2)** very small pancake-type coil that would cover only a small portion of the particle's surface and would induce eddy currents in a much smaller volume. This approach would require multiple coils or in-place rotation of each particle to inspect its entire surface area or volume.

The measurement uncertainties apparently associated with the existing capacitive sensors can be reduced by a second-generation design that reduces stray capacitance and the effects of external factors. This might involve (**Recommendation #3)** integration of the capacitor electrodes and the associated electronics in a compact MEMS-like device. Combining it with a similarly miniaturized and integrated induction sensor of the type discussed above would increase the accuracy and precision of these

complementary measurements. It would also facilitate the implementation of an automated high-speed inspection process to detect particles that are dimensionally flawed.   Additionally, investigations into the use of capacitive impedance (**Recommendation #4)** as a means of detecting individual NUCO kernels having unacceptable stoichiometry should be considered.

6.2 Acoustic Microscopy

No conclusive evidence was found to support any further development of an acoustic microscopy system at frequencies below 200 MHz. Therefore, there is no recommendation to pursue further acoustic microscopy studies at this time.

6.3 Resonant Ultrasound Spectroscopy

Development of an RUS inspection system using (**Recommendation #5**) advanced resonant techniques should be considered. A concept of this inspection system is shown in Figure 6.1. The premise is that individual particles are dropped through an inspection zone. The zone is created by laser ultrasonic techniques that couple to the particle and excites the resonant frequencies. An acoustic sensing unit acquires the resonant data and a go/no-go type analysis is performed in near real-time. Particles that fall outside of an established acceptance criterion are rejected and shot from the inspection stream using compressed air or other mechanical means. Further studies are necessary to ensure the accuracy and repeatability of the RUS system's inspection capability.
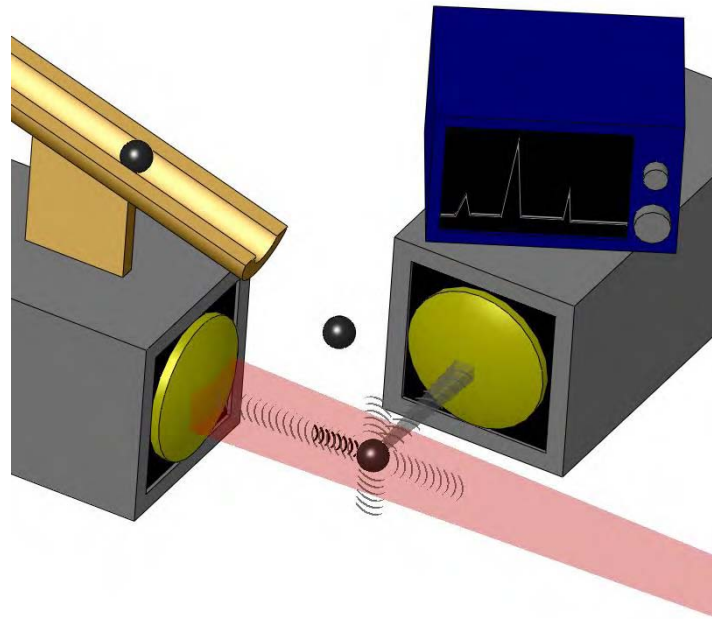
Figure 6.1. Conceptual RUS Inspection System

6.4 High-Resolution Radiography and Computed Tomography

No conclusive evidence was found to support any further development beyond what is already available for radiography and computed tomography. Therefore, there are no recommendations to pursue further studies at this time.

6.5 Transmission and Diffuse-Field Ultrasound

No conclusive evidence was found to support any further development of a transmission or diffuse field ultrasonic system. Therefore, there is no recommendation to pursue further studies at this time.

6.6 Optical Measurements

Based on the findings for optical digital image analysis, and the assumption that the objective is to look to technology that can be fielded in a 5-10 year timeframe, (**Recommendation #6)** define specifications for an optical inspection system, including parameters to be measured, and performance in terms of throughput and precision, and develop a prototypical optical inspection system capable of inspecting particles at a rate of 500- 1000 particles/min. This would include a handling system capable of presenting the particles to the imaging system with the required mechanical precision and speed.

7.0   NERI Project Final Financial Information

Cumulative Expenditure Summary
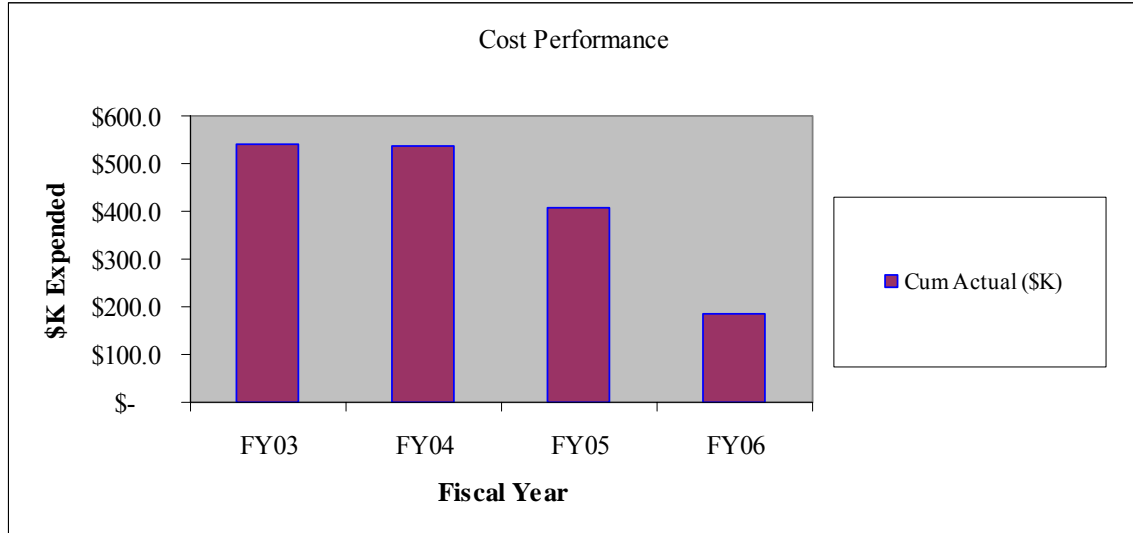
Cost Performance

	FY03	FY04	FY05	FY06	Total
Cum Actual ($K)	$ 540.1	$ 538.2	$ 405.8	$ 186.0	$ 1,670.1
	Note: FY06 reflects planned expenditure				

Cost Performance

Fiscal Year 2003

Expenditures in FY2003: $540.1K

Spending lagged in the first quarter of FY2003 while subcontracts and non-disclosure agreements with ISU and GA were negotiated. Over the last three quarters of the year spending accelerated, peaking in September. Funds were deobligated during the second quarter as a result of anticipated closure of the DOE Oakland Operations Office at the end of FY2003. DOE headquarters reinstated funding in the fourth quarter. FY2004 funding was received in August.

Fiscal Year 2004

Expenditures in FY2004: $538.2K

Spending was slow during the first quarter, with improvement occurring in the second, third and fourth quarters. A dip in spending during the final month of the fiscal year was the result of a pass back in funding received. While PNNL was on track with completing the year on budget, the final pass back changed that position. GA finished the year under budget with scope remaining and ISU completed the

year over budget for commensurate scope. FY2005 funding notification was received in August reflecting a $182K reduction in funding.

Testing of uranium-based materials was not completed in FY2004, aligning with the AGR program schedule. A request to complete associated activities was planned for the final year of the project. Remaining PNNL scope included final-quarter and FY2004 annual report preparation, on-process measurements testing, and NDE method verification of the depleted uranium samples. GA was unable to prepare documentation of the effects of QC methods on fuel due to insufficient data generated thus far. ISU scope remaining incomplete included radiographic work and characterization of depleted uranium particles. A change request was in preparation during the final quarter for completion of remaining activities, for PNNL and GA, with carryover funding available.

Fiscal Year 2005

Expenditures in FY2005: $405.8K

An FY2005 funding shortfall of $183.0K was received and partially reinstated with an unexpected FY2004 year-end pass back. Carryover funding was requested and approved via Baseline Change Request 05-001. Funding shortfall remaining at the end of FY2005 was $101.7K.

A lagging schedule for the High-Speed Defect Detection Demonstration Task and the UT On-Process Characterization Task into the third quarter culminated with a baseline change request that was prepared and approved in the fourth quarter to incorporate agreed-upon changes. This resulted in a rebaselining of remaining work and a no-cost time extension. The project was extended through January 31, 2006, to complete the final project report for this three-year project. A small positive cost variance was carried through all four quarters.

PNNL awaited receipt of radiographic data from ISU, putting the task behind schedule beginning the first quarter. The task continued to be behind schedule in the second quarter based on delay in a decision for the demonstration sample set. At an early summer project review, a new approach for a final demonstration was submitted and approved. The UT On-Process Characterization Task lagged initially because of transition of a key staff member to the newly formed Battelle Energy Alliance who were awarded the INL contract, and continued through the fourth quarter of the fiscal year. The Project Integration and Reporting Task was delayed awaiting receipt of the FY2004 annual report and FY2005 first and second quarterly reports from ARA Associates.

Fiscal Year 2006

Expenditures in FY2006: $186.0K

A four-month extension to the project was granted in FY2005, to complete the FY2004 annual report, the FY2005 quarterly reports, and the final project report.

Baseline Change Requests

Baseline change requests submitted and approved are outlined below.

BCR No	BCR Subject	Approval
BCR 03-001	FY2003 Scope time extension and Carryover	10-02-03
BCR 05-001	FY2004 Schedule Extension and Reinstatement of FY2005 Scope	10-27-04
BCR 05-002	No Cost Time Extension for Final Report Completion	8-08-05

Appendix A

Change Request Form

Change Request No.: PNNL NFRT 05-002	Date of Request: July 19, 2005
WBS ID: All WBS IDs Included	Title: No-Cost Time Extension to the Innovative Low-Cost Approaches to Automating QA/QC of Fuel Particle Production Using On-Line Nondestructive Methods for Higher Reliability Project
Name of Originator: Allan F. Pardini	Type of Change: Scope _____ Schedule _XX_ Cost ___
Schedule Change:	Budget Change: $0
Start: from 10-01-02 to 10-01-02 Finish: from 08-30-05 to 01-31-06	Original budget: $1,625,150 New budget: $1,625,150

Description of Change:

The Pacific Northwest National Laboratory (PNNL) is requesting a no cost time extension on the **Innovative Low-Cost Approaches to Automating QA/QC of Fuel Particle Production Using On-Line Nondestructive Methods for Higher Reliability Project.**

An extension from the current project completion date of August 30, 2005, to a completion date of January 31, 2006 is requested.

This extension shall enable completion of essential technical work and preparation of a three year culminating project report. Fiscal Year 2005 schedule changes for receipt of depleted uranium particles and analysis shifts completion of the final project report beyond the current project completion date. Reasons for schedule changes include the following:

- *Delay in receiving the first batch of depleted uranium particles at Iowa State University (ISU).*
The scheduled delivery date for transfer of the first batch of depleted uranium particles to ISU from Oak Ridge National Laboratory (ORNL) was October 2004. The delivery actually took place in March of 2005, 5 months behind schedule. This delay caused a schedule impact which could not be rectified.

- *Delay in receiving the second batch of depleted uranium particles at Iowa State University.*
The scheduled delivery date for transfer of the second batch of depleted uranium particles to ISU from ORNL was March 2005. The delivery is now set for somewhere between mid July and mid August, approximately 4 months behind schedule. This delay will cause a further delay in the project.

The changes identified therefore provide the basis for a no cost time extension to January 31, 2006.

Impact if not approved:

There are many tasks identified in the statement of work that will not be completed or will be truncated if the extension is not granted. Specifically:

Task 3 Define Quality Index
Task 4a NDE Characterization of Particles
Task 9 Test Particles in Standard Particle Library
Task 10 Coated UO_2
Task 14 Implement Quality Index
Task 17 NDE Design Parameters
Task 18 Project Management/reports

Approvals (as required):

Project Manager	Date	PMT Product Line	Date	Client	Date
Allan F. Pardini	7/19/05	Carazza	7/19/05	K. Osborn	8/8/05

A.1

Appendix B

This appendix provides the overall particle database that was compiled from research conducted on this NERI project. The coloring of rows was done based on the objective of the research, for example, to ascertain the responses from specific particle layers. If we look at particle batches 1-B and 2-B, the objective was to compare a full buffer to a thin buffer with all of the others absent. The zero values in the columns for IPyC, SiC, and OPyC indicate that these layers are missing. This concept was developed for the rest of the particle table.

Table header groups: Desired Particle Sizes - Based on Specification | Objective | Number of Samples Examined | Measurement Notes | Specific Particles Examined | Radiographic Data | Electromagnetic Data (Older data not used in analyses) | Electromagnetic Data (Optimum Frequency, used in analyses)

Run Number	Date Shipped	Kernel dia (µm)	Particle batch(s) to use	Kernal size spilt by SA	Buffer Thickness (µm)	IPYC Thickness (µm)	SiC Thickness (µm)	OPYC Thickness (µm)	Objective	Inductive Impedance Samples	Capacitive Impedance Samples	Radiography Samples	Measurement Notes	Set #1	Set #2	RT Kernel dia (µm)	RT Buffer Thickness (µm)	RT IPYC Thickness (µm)	RT SiC Thickness (µm)	RT OPYC Thickness (µm)	Inductive Excitation Frequency (MHz)	Inductive Impedance (Fractional)	Capacitive Excitation Frequency (MHz)	Capacitive Impedance (Fractional)	Inductive Excitation Frequency (MHz)	Inductive Impedance (Fractional)	Capacitive Excitation Frequency (MHz)	Capacitive Impedance (Fractional)
1-B	21-Jan-2004	250-450	300 and 400	50/50	100	0	0	0	Compare full buffer with thin Buffer with other layers absent	10	0	2		001-B1		541	35.6											
														001-B2														
														001-B3														
														001-B4														
														001-B5		403	96.8											
														001-B6														
														001-B7														
														001-B8														
														001-B9														
														001-B10														
														001-B11							40.980	4.253E-02						
														001-B12							40.980	8.697E-02						
														001-B13							40.980	8.892E-02						
														001-B14							40.980	4.566E-02						
														001-B15							40.980	4.790E-02						
														001-B16							40.980	4.241E-02						
														001-B17							40.980	4.454E-02						
														001-B18							40.980	3.706E-02						
														001-B19							40.980	6.782E-02						
														001-B20							40.980	3.927E-02						
2-B	23-Jan-2004	350-550	400 and 500	50/50	20	0	0	0		10	0	6		002-B1		533	23.3											
														002-B2							41.255	5.374E-03						
														002-B3							41.255	7.198E-03						
														002-B4														
														002-B5		523	24.5											
														002-B6							41.255	7.631E-03						
														002-B7							41.255	6.865E-03						
														002-B8							41.255	8.880E-03						
														002-B9							41.255	7.287E-03						
														002-B10		538	15.9											
														002-B11		528	21.9											
														002-B12							41.255	8.828E-03						
														002-B13														
														002-B14														
														002-B15							41.255	6.650E-03						
														002-B16							41.255	6.018E-03						
														002-B17							41.255	7.421E-03						
														002-B18														
														002-B19		545	18.4											
														002-B20		637	24.0											

Run Number	Date Shipped	Desired Particle Sizes - Based on Specification							Objective	Number of Samples Examined			Measurement Notes	Specific Particles Examined			Radiographic Data						Electromagnetic Data (Older data not used in analyses)				Electromagnetic Data (Optimum Frequency, used in analyses)			
		Kernel dia (µm)	Particle batch(s) to use	Kernal size spilt by SA	Buffer Thickness (µm)	IPYC Thickness (µm)	SiC Thickness (µm)	OPYC Thickness (µm)		Inductive Impedance Samples	Capacitive Impedance Samples	Radiography Samples		Set #1	Set #2		RT Kernel dia (µm)	RT Buffer Thickness (µm)	RT IPYC Thickness (µm)	RT SiC Thickness (µm)	RT OPYC Thickness (µm)		Inductive Excitation Frequency (MHz)	Inductive Impedance (Fractional)	Capacitive Excitation Frequency (MHz)	Capacitive Impedance (Fractional)	Inductive Excitation Frequency (MHz)	Inductive Impedance (Fractional)	Capacitive Excitation Frequency (MHz)	Capacitive Impedance (Fractional)
3-B	20-Jan-2004	250-450	300 and 400	50/50	100	40	0	0		20	0	12	Radiography & coil on same particles	003-B1			408	175.9	26.9											
														003-B2			359	102.2	30.7											
														003-B3																
														003-B4																
														003-B5																
														003-B6																
														003-B7			425	98.4	29.8											
														003-B8																
														003-B9																
														003-B10																
														003-B11			396	100.0	28.0					1.468E-01						
														003-B12			310	111.3	28.0					8.951E-02						
														003-B13			397	102.0	25.8					1.342E-01						
														003-B14																
														003-B15			439	104.6	23.1					1.671E-01						
														003-B16			334	112.0	27.2					1.112E-01						
														003-B17			401	106.0	29.2					1.439E-01						
														003-B18			378	105.7	27.2					1.336E-01						
														003-B19			315	112.4	55.0					1.518E-01						
														003-B20			407	108.0	27.8					1.499E-01						
4-A	23-Jan-2004	350-550	400 and 500	50/50	20	40	0	0	Compare full buffer with thin Buffer beneath normal IPyC	20 from 004-A 20 from 004-B	0	4	Only 10 measurements are with small coil	004-A-A1													40.980	1.056E-01		
														004-A-A2													40.980	9.184E-02		
														004-A-A3													40.980	9.022E-02		
														004-A-A4													40.980	1.035E-01		
														004-A-A5													40.980	8.096E-02		
														004-A-A6			410	22.7	37.8											
														004-A-A7			529	23.4	29.7											
														004-A-A8													40.980	4.736E-02		
														004-A-A9			368	21.3	37.8											
														004-A-A10																
														004-A-A11																
														004-A-A12													40.980	5.215E-02		
														004-A-A13													40.980	8.342E-02		
														004-A-A14													40.980	5.432E-02		
														004-A-A15			512	23.3	30.1											
														004-A-A16													40.980	8.944E-02		
														004-A-A17																
														004-A-A18																
														004-A-A19																
														004-A-A20																
															004-B-A1															
															004-B-A2															
															004-B-A3															
															004-B-A4															
															004-B-A5															
															004-B-A6															
															004-B-A7															
															004-B-A8															
															004-B-A9															
															004-B-A10															
															004-B-A11															
															004-B-A12															
															004-B-A13															
															004-B-A14															
															004-B-A15															
															004-B-A16															
															004-B-A17															
															004-B-A18															
															004-B-A19															
															004-B-A20															

Run Number	Date Shipped	Kernel dia (µm)	Particle batch(s) to use	Kernal size split by SA	Buffer Thickness (µm)	IPYC Thickness (µm)	SiC Thickness (µm)	OPYC Thickness (µm)	Objective	Inductive Impedance Samples	Capacitive Impedance Samples	Radiography Samples	Measurement Notes	Set #1	Set #2	RT Kernel dia (µm)	RT Buffer Thickness (µm)	RT IPYC Thickness (µm)	RT SiC Thickness (µm)	RT OPYC Thickness (µm)	Old Inductive Excitation Frequency (MHz)	Old Inductive Impedance (Fractional)	Old Capacitive Excitation Frequency (MHz)	Old Capacitive Impedance (Fractional)	Opt Inductive Excitation Frequency (MHz)	Opt Inductive Impedance (Fractional)	Opt Capacitive Excitation Frequency (MHz)	Opt Capacitive Impedance (Fractional)
7-A	23-Jan-2004	480-520	500	100	0	40	0	0		10	10	14	Radiography was not from the same particles as impedance	007-A-A1		567		37.1										
														007-A-A2							41.163	6.015E-02			45.000	3.706E-02	45.000	6.126E-02
														007-A-A3											45.000	5.013E-02	45.000	7.097E-02
														007-A-A4		521		38.8										
														007-A-A5							41.163	6.461E-02			45.000	4.136E-02	45.000	6.801E-02
														007-A-A6														
														007-A-A7											45.000	3.907E-02	45.000	6.712E-02
														007-A-A8							41.163	6.274E-02			45.000	4.794E-02	45.000	7.403E-02
														007-A-A9							41.163	6.693E-02			45.000	4.019E-02	45.000	6.774E-02
														007-A-A10							41.163	7.162E-02			45.000	5.444E-02	45.000	7.210E-02
														007-A-A11		524		39.5										
														007-A-A12							41.163	7.848E-02			45.000	6.139E-02	45.000	7.330E-02
														007-A-A13											45.000	3.189E-02	45.000	6.324E-02
														007-A-A14		522		39.3										
														007-A-A15		517		37.4			41.163	7.535E-02			45.000	5.704E-02	45.000	6.746E-02
														007-A-A16		517		37.4										
														007-A-A17							41.163	6.417E-02						
														007-A-A18							41.163	5.940E-02						
														007-A-A19														
														007-A-A20														
8-A	23-Jan-2004	480-520	500	100	0	40	0	0	IPyC coating variants on Kernel	10	10	19		008-A-A1		507		33.8										
														008-A-A2														
														008-A-A3							41.163	5.688E-02			45.000	4.081E-02	45.000	6.387E-02
														008-A-A4											45.000	3.084E-02	45.000	6.733E-02
														008-A-A5							41.163	5.089E-02			45.000	3.808E-02	45.000	6.336E-02
														008-A-A6							41.163	6.844E-02			45.000	4.748E-02	45.000	7.456E-02
														008-A-A7							41.163	4.511E-02			45.000	3.521E-02	45.000	6.777E-02
														008-A-A8							41.163	6.425E-02			45.000	4.468E-02	45.000	6.893E-02
														008-A-A9							41.163	5.703E-02			45.000	3.727E-02	45.000	6.599E-02
														008-A-A10		516		36.0										
														008-A-A11							41.163	4.873E-02			45.000	3.803E-02	45.000	6.611E-02
														008-A-A12							41.163	4.353E-02			45.000	3.416E-02	45.000	5.937E-02
														008-A-A13							41.163	5.145E-02			45.000	4.276E-02	45.000	5.913E-02
														008-A-A14							41.163	6.406E-02						
														008-A-A15		509		34.2										
														008-A-A16		506		35.5										
														008-A-A17														
														008-A-A18														
														008-A-A19		531		34.7										
														008-A-A20														
9-A	23-Jan-2004	480-520	500	100	0	40	0	0		10	10	6		009-A-A1											45.000	4.718E-02	45.000	6.651E-02
														009-A-A2											45.000	5.070E-02	45.000	7.624E-02
														009-A-A3							41.163	9.316E-02			45.000	3.634E-02	45.000	6.350E-02
														009-A-A4		522		30.3										
														009-A-A5							41.163	9.331E-02			45.000	4.537E-02	45.000	6.631E-02
														009-A-A6		521		35.8										
														009-A-A7							41.163	9.805E-02			45.000	5.110E-02	45.000	6.943E-02
														009-A-A8							41.163	9.446E-02			45.000	4.656E-02	45.000	6.663E-02
														009-A-A9							41.163	9.071E-02			45.000	2.942E-02	45.000	6.196E-02
														009-A-A10		522		35.4										
														009-A-A11							41.163	5.033E-02			45.000	3.880E-02	45.000	6.123E-02
														009-A-A12		506		36.9										
														009-A-A13							41.163	6.016E-02			45.000	4.421E-02	45.000	6.602E-02
														009-A-A14							41.163	6.929E-02			45.000	4.708E-02	45.000	6.779E-02
														009-A-A15							41.163	5.757E-02						
														009-A-A16							41.163	5.040E-02						
														009-A-A17		507		39.4										
														009-A-A18		516		38.1										
														009-A-A19														
														009-A-A20														

Run Number	Date Shipped	Desired Particle Sizes - Based on Specification							Objective	Number of Samples Examined			Measurement Notes	Specific Particles Examined		Radiographic Data					Electromagnetic Data (Older data not used in analyses)				Electromagnetic Data (Optimum Frequency, used in analyses)			
		Kernel dia (µm)	Particle batch(s) to use	Kernal size spilt by SA	Buffer Thickness (µm)	IPYC Thickness (µm)	SiC Thickness (µm)	OPYC Thickness (µm)		Inductive Impedance Samples	Capacitive Impedance Samples	Radiography Samples		Set #1	Set #2	RT Kernel dia (µm)	RT Buffer Thickness (µm)	RT IPYC Thickness (µm)	RT SiC Thickness (µm)	RT OPYC Thickness (µm)	Inductive Excitation Frequency (MHz)	Inductive Impedance (Fractional)	Capacitive Excitation Frequency (MHz)	Capacitive Impedance (Fractional)	Inductive Excitation Frequency (MHz)	Inductive Impedance (Fractional)	Capacitive Excitation Frequency (MHz)	Capacitive Impedance (Fractional)
10-B	10-Feb-2004	480-520	500	100	0	20	0	0	Thin IPyC on kernel	20	0	0		010-B-B1							Inductive Data Available at PNNL but not listed in this table.							
14-B	9-Feb-2004	620	650				35		SiC on Kernel	0	10	35		014-B-1		683			47.0									
														014-B-2		718			47.8									
														014-B-3		636			40.8									
														014-B-4		651			39.8									
														014-B-5		669			40.2									
														014-B-6		695			49.9						45.000	2.491E-03	45.000	1.739E-01
														014-B-7		708			50.4									
														014-B-8		732			49.0						45.000	5.236E-04	45.000	1.940E-01
														014-B-9		654			34.0						45.000	1.934E-03	45.000	1.339E-01
														014-B-10		638			32.0						45.000	-7.835E-04	45.000	1.257E-01
														014-B-11		693			40.4						45.000	2.663E-03	45.000	1.710E-01
														014-B-12		731			45.3						45.000	2.731E-03	45.000	1.945E-01
														014-B-13		764			44.4						45.000	3.414E-03	45.000	2.234E-01
														014-B-14		719			46.4						45.000	2.942E-03	45.000	2.225E-01
														014-B-15		693			37.8						45.000	1.332E-03	45.000	1.525E-01
														014-B-16		726			29.5						45.000	2.257E-03	45.000	1.742E-01
														014-B-17		682			41.3						45.000	2.637E-03	45.000	1.673E-01
														014-B-18		704			43.0						45.000	3.720E-03	45.000	1.375E-01
														014-B-19		668			35.0						45.000	2.406E-03	45.000	1.762E-01
														014-B-20		724			45.0						45.000	1.155E-03	45.000	1.958E-01
														014-B-21		699			40.2						45.000	1.395E-03	45.000	1.718E-01
														014-B-22		692			39.0						45.000	1.075E-02	45.000	1.914E-01
														014-B-23		730			44.3						45.000	1.012E-02	45.000	2.291E-01
														014-B-24		688			39.6						45.000	1.034E-02	45.000	1.661E-01
														014-B-25		693			38.0						45.000	1.066E-02	45.000	1.596E-01
														014-B-26		693			42.6									
														014-B-27		690			41.0						45.000	9.989E-03	45.000	1.613E-01
														014-B-28		704			45.0						45.000	1.105E-02	45.000	1.779E-01
														014-B-29		654			35.0						45.000	9.787E-03	45.000	1.176E-01
														014-B-30		660			34.6						45.000	1.128E-02	45.000	1.415E-01
														014-B-31		683			39.4						45.000	1.311E-02	45.000	1.586E-01
														014-B-32		720			45.7						45.000	1.228E-02	45.000	2.126E-01
														014-B-33		660			35.3						45.000	1.250E-02	45.000	1.378E-01
														014-B-34		685			42.0						45.000	1.280E-02	45.000	1.757E-01
														014-B-35		700			44.2						45.000	1.296E-02	45.000	1.766E-01

Run Number	Date Shipped	Kernel dia (µm)	Particle batch(s) to use	Kernal size spilt by SA	Buffer Thickness (µm)	IPYC Thickness (µm)	SiC Thickness (µm)	OPYC Thickness (µm)	Objective	Inductive Impedance Samples	Capacitive Impedance Samples	Radiography Samples	Measurement Notes	Set #1	Set #2	RT Kernel dia (µm)	RT Buffer Thickness (µm)	RT IPYC Thickness (µm)	RT SiC Thickness (µm)	RT OPYC Thickness (µm)	Ind Exc Freq (MHz) (older)	Ind Imp (Fractional) (older)	Cap Exc Freq (MHz) (older)	Cap Imp (Fractional) (older)	Ind Exc Freq (MHz) (opt)	Ind Imp (Fractional) (opt)	Cap Exc Freq (MHz) (opt)	Cap Imp (Fractional) (opt)
5-B	17-Feb-2004	250-450	300 and 400	50/50	100	40	35	40	Normal TRISO	20	10	6		005-B1							43.469	1.770E-01	43.469	1.442E-01	45.000	1.737E-01		
														005-B2		402	101.2	32.8	47.8	36.4	43.469	2.174E-01			45.000	2.271E-01		
														005-B3							43.469	1.816E-01	43.469	1.470E-01	45.000	1.885E-01		
														005-B4							43.469	2.155E-01	43.469	1.807E-01	45.000	1.864E-01		
														005-B5		394	73.4	26.4	47.5	35.0	43.469	2.005E-01			45.000	1.978E-01		
														005-B6							43.469	1.759E-01	43.469	1.525E-01	45.000	2.154E-01		
														005-B7							43.469	1.843E-01	43.469	1.624E-01	45.000	1.739E-01		
														005-B8							43.469	1.743E-01	43.469	1.632E-01	45.000	1.861E-01		
														005-B9							43.469	2.117E-01	43.469	1.812E-01	45.000	1.964E-01		
														005-B10		388	112.8	29.9	48.4	27.7	43.469	2.300E-01			45.000	1.749E-01		
														005-B11		335	111.6	36.2	54.9	37.0	43.469	1.861E-01						
														005-B12							43.469	2.086E-01	43.469	1.730E-01				
														005-B13							43.469	2.148E-01	43.469	1.742E-01				
														005-B14							43.469	1.769E-01	43.469	1.590E-01				
														005-B15							43.469	1.864E-01	43.469	1.521E-01				
														005-B16							43.469	1.810E-01	43.469	1.560E-01				
														005-B17							43.469	1.786E-01	43.469	1.562E-01				
														005-B18		386	103.7	34.4	52.4	38.8	43.469	2.039E-01						
														005-B19							43.469	1.828E-01	43.469	1.513E-01				
														005-B20		327	98.2	37.8	56.2	37.0	43.469	1.735E-01						
12-B	20-Jan-2004	300-400	300 and 400	50/50	100	40	0	40	Normal TRISO, missing SiC 20 from 012 20 from 012-B	20	10	25		012-BC1											45.000	1.109E-01	45.000	7.853E-02
														012-BC2											45.000	1.125E-01	45.000	7.795E-02
														012-BC3											45.000	1.177E-01	45.000	7.965E-02
														012-BC4							45.000	1.066E-01			45.000	1.032E-01		6.919E-02
														012-BC5							45.000	1.441E-01			45.000	1.032E-01		
														012-BC6											45.000	1.143E-01	45.000	1.128E-01
														012-BC7											45.000	1.582E-01	45.000	8.336E-02
														012-BC8											45.000	1.446E-01	45.000	1.006E-01
														012-BC9											45.000	1.180E-01	45.000	8.652E-02
														012-BC10											45.000	1.042E-01	45.000	7.385E-02
															012-B1-B1	322.5	124.0	32.4	0	32.4	42.357	1.247E-01						
															012-B1-B2						42.357	1.683E-01						
															012-B1-B3	451.5	120.0	28.4	0	28.4	42.357	2.433E-01	42.357	1.359E-01				
															012-B1-B4	400	105.8	29.3	0	29.3	42.357	1.745E-01						
															012-B1-B5	334.8	116.6	28.95	0	28.95	42.357	1.290E-01	42.357	8.280E-02				
															012-B1-B6						42.357	1.733E-01	42.357	1.077E-01				
															012-B1-B7						42.357	1.317E-01						
															012-B1-B8	345.4	122.6	34.15	0	34.15	42.357	1.558E-01	42.357	8.803E-02				
															012-B1-B9						42.357	1.916E-01	42.357	9.714E-02				
															012-B1-B10						42.357	1.267E-01	42.357	8.671E-02				
															012-B1-B11						42.357	1.364E-01	42.357	1.285E-01				
															012-B1-B12						42.357	1.643E-01	42.357	8.440E-02				
															012-B1-B13						42.357	1.871E-01	42.357	1.121E-01				
															012-B1-B14						42.357	1.654E-01	42.357	8.809E-02				
															012-B1-B15	287.9	117.0	28.35	0	28.35	42.357	1.936E-01	42.357	1.136E-01				
															012-B1-B16						42.357	1.695E-01	42.357	8.832E-02				
															012-B1-B17	340.3	107.0	29.5	0	29.5	42.357	1.372E-01	42.357	8.475E-02				
															012-B1-B18						42.357	1.703E-01	42.357	9.155E-02				
															012-B1-B19	447	111.0	29.5	0	29.5	42.357	2.043E-01	42.357	1.039E-01				
															012-B1-B20						42.357	1.326E-01						
12-B 5 Additional Particles Examined														12B_1		449	106.2		54.7									
														12B_2		378	119.9		60.0									
														12B_3		310	125.8		58.8									
														12B_4		365	116.6		56.5									
														12B_5		398	108.8		54.3									

Desired Particle Sizes - Based on Specification; Number of Samples Examined; Specific Particles Examined; Radiographic Data; Electromagnetic Data (Older data not used in analyses); Electromagnetic Data (Optimum Frequency, used in analyses)

Run Number	Date Shipped	Kernel dia (µm)	Particle batch(s) to use	Kernel size split by SA	Buffer Thickness (µm)	IPYC Thickness (µm)	SiC Thickness (µm)	OPYC Thickness (µm)	Objective	Inductive Impedance Samples	Capacitive Impedance Samples	Radiography Samples	Measurement Notes	Set #1	Set #2	RT Kernel dia (µm)	RT Buffer Thickness (µm)	RT IPYC Thickness (µm)	RT SiC Thickness (µm)	RT OPYC Thickness (µm)	Old Inductive Excitation Frequency (MHz)	Old Inductive Impedance (Fractional)	Old Capacitive Excitation Frequency (MHz)	Old Capacitive Impedance (Fractional)	Opt Inductive Excitation Frequency (MHz)	Opt Inductive Impedance (Fractional)	Opt Capacitive Excitation Frequency (MHz)	Opt Capacitive Impedance (Fractional)
13-A	17-Feb-2004		300 and 400	50/50	100	40	20	40	Normal TRISO, thin SiC	20	10	42		013-A1		422.9	85.4	30.2	30.5	30.3	43.469	1.983E-01			45.000	1.780E-01	45.000	1.289E-01
														013-A2		427.1	137.2	45.4	44	45.1	43.469	1.444E-01			45.000	1.512E-01	45.000	1.079E-01
														013-A3							43.469	1.491E-01			45.000	1.515E-01	45.000	1.191E-01
														013-A4							43.469	1.465E-01			45.000	1.668E-01	45.000	1.177E-01
														013-A5							43.469	1.568E-01			45.000	1.487E-01	45.000	1.272E-01
														013-A6							43.469	1.489E-01			45.000	1.723E-01	45.000	1.247E-01
														013-A7							43.469	1.479E-01			45.000	1.745E-01	45.000	1.272E-01
														013-A8							43.469	1.622E-01			45.000	1.601E-01	45.000	1.260E-01
														013-A9							43.469	1.643E-01			45.000	1.447E-01	45.000	1.049E-01
														013-A10							43.469	1.700E-01			45.000	1.713E-01	45.000	1.325E-01
														013-A11							43.469	1.554E-01						
														013-A12							43.469	1.627E-01						
														013-A13							43.469	1.786E-01						
														013-A14							43.469	1.650E-01						
														013-A15							43.469	1.662E-01						
														013-A16							43.469	1.462E-01						
														013-A17		340.6	116.4	31.8	28.4	33.3	43.469	1.811E-01						
														013-A18		337.9	101.5	29.6	31.9	37.4	43.469	1.645E-01						
														013-A19							43.469	1.606E-01						
														013-A20							43.469	1.748E-01						
13-A 5 Additional Particles Examined															13_A1	392	87.0	34.2	28.4	34.4								
															13_A2	318	98.1	30.8	31.4	34.0								
															13_A3	381	98.8	30.3	28.3	36.3								
															13_A4	382	86.0	31.6	29.6	34.0								
															13_A5	344	109.4	34.6	28.6	35.3								
6-CD	23-Feb-2004	350-550	400 and 500	50/50	20	40	35	40	Normal TRISO, thin buffer	20	0	7		006-CD-A1							42.500	1.657E-01			45.000	1.297E-01		
														006-CD-A2		419	18.5	31.2	59.0	40.0	42.500	1.066E-01			45.000	9.944E-02		
														006-CD-A3		543	15.3	26.1	49.4	39.9	42.500	1.637E-01			45.000	9.229E-02		
														006-CD-A4							42.500	1.252E-01			45.000	1.296E-01		
														006-CD-A5		508	18.1	27.2	53.9	43.5	42.500	1.498E-01			45.000	1.370E-01		
														006-CD-A6							42.500	1.106E-01			45.000	9.731E-02		
														006-CD-A7							42.500	1.161E-01			45.000	9.656E-02		
														006-CD-A8							42.500	1.600E-01			45.000	9.253E-02		
														006-CD-A9		400	26.6	34.1	56.3	41.5	42.500	1.230E-01			45.000	1.049E-01		
														006-CD-A10		489	18.8	24.2	50.1	40.0	42.500	1.450E-01			45.000	9.936E-02		
														006-CD-A11							42.500	1.584E-01						
														006-CD-A12							42.500	1.262E-01						
														006-CD-A13							42.500	1.653E-01						
														006-CD-A14							42.500	1.272E-01						
														006-CD-A15							42.500	1.159E-01						
														006-CD-A16							42.500	1.152E-01						
														006-CD-A17							42.500	1.561E-01						
														006-CD-A18							42.500	1.215E-01						
														006-CD-A19		533	14.9	23.7	50.4	42.8	42.500	1.724E-01						
														006-CD-A20		424	17.9	26.0	56.1	40.1	42.500	1.177E-01						
															006-CD-B1										45.000	9.155E-02	45.000	1.149E-01
															006-CD-B2	380	62.5		58.8	35.9					45.000	8.650E-02	45.000	1.128E-01
															006-CD-B3	371	67.8		56.7	41.6					45.000	9.423E-02	45.000	1.112E-01
															006-CD-B4	501	26.4	29.8	52.0	42.2					45.000	1.361E-01	45.000	1.753E-01
															006-CD-B5	434	55.1		56.8	38.4					45.000	1.012E-01	45.000	1.348E-01
															006-CD-B6	392	68.3		59.1	41.4					45.000	9.988E-02	45.000	1.162E-01
															006-CD-B7										45.000	8.690E-02	45.000	1.111E-01
															006-CD-B8										45.000	8.967E-02	45.000	1.158E-01
															006-CD-B9	520	23.4	26.4	51.8	42.6					45.000	1.348E-01	45.000	1.783E-01
															006-CD-B10										45.000	8.794E-02	45.000	1.114E-01
															006-CD-B11	552	26.9	24.6	49.1	40.8					45.000	1.555E-01	45.000	2.153E-01
															006-CD-B12										45.000	9.429E-02	45.000	1.153E-01
															006-CD-B13	499	48.7		48.6	35.5					45.000	1.369E-01	45.000	1.836E-01
															006-CD-B14	403	65.1		57.1	40.5					45.000	1.062E-01	45.000	1.301E-01
															006-CD-B15										45.000	9.844E-02	45.000	1.233E-01
															006-CD-B16										45.000	8.929E-02	45.000	1.128E-01
															006-CD-B17										45.000	1.328E-01	45.000	1.683E-01
															006-CD-B18										45.000	9.963E-02	45.000	1.196E-01
															006-CD-B19	379	51.6		61.3	37.5					45.000	8.432E-02	45.000	1.071E-01
															006-CD-B20	368	65.1		58.5	42.5					45.000	9.275E-02	45.000	1.102E-01
															006-CD-B21	443	24.1	31.7	54.8	42.0					45.000	1.126E-01	45.000	1.386E-01
															006-CD-B22										45.000	9.124E-02	45.000	1.149E-01
															006-CD-B23	400	54.4		59.1	42.6					45.000	9.245E-02	45.000	1.098E-01
															006-CD-B24	403	70.3		55.5	37.8					45.000	1.094E-01	45.000	1.391E-01
															006-CD-B25										45.000	9.040E-02	45.000	1.236E-01
															006-CD-B26										45.000	8.862E-02	45.000	1.173E-01
															006-CD-B27										45.000	9.424E-02	45.000	1.145E-01
															006-CD-B28										45.000	9.786E-02	45.000	1.185E-01
															006-CD-B29	396	20.6	32.4	57.8	41.0					45.000	8.653E-02	45.000	1.153E-01
															006-CD-B30										45.000	9.071E-02	45.000	1.156E-01

Run Number	Date Shipped	Kernel dia (μm)	Particle batch(s) to use	Kernal size spilt by SA	Buffer Thickness (μm)	IPYC Thickness (μm)	SiC Thickness (μm)	OPYC Thickness (μm)	Objective	Inductive Impedance Samples	Capacitive Impedance Samples	Radiography Samples	Measurement Notes	Set #1	Set #2	RT Kernel dia (μm)	RT Buffer Thickness (μm)	RT IPYC Thickness (μm)	RT SiC Thickness (μm)	RT OPYC Thickness (μm)	Inductive Excitation Frequency (MHz) [Older]	Inductive Impedance (Fractional) [Older]	Capacitive Excitation Frequency (MHz) [Older]	Capacitive Impedance (Fractional) [Older]	Inductive Excitation Frequency (MHz) [Optimum]	Inductive Impedance (Fractional) [Optimum]	Capacitive Excitation Frequency (MHz) [Optimum]	Capacitive Impedance (Fractional) [Optimum]
5-D	23-Oct-2004	400	400	100	100	40	40	40	Normal TRISO redo to correct SiC thickness	10	10	5		005-D-A1											45.000	2.282E-01	45.000	2.281E-01
														005-D-A2		431	62.8	39.5	46.3	52.3					45.000	2.164E-01	45.000	1.738E-01
														005-D-A3		368	79.9	40.4	45.6	54.9					45.000	2.097E-01	45.000	1.795E-01
														005-D-A4		381	82.8	40.8	51.9	50.1					45.000	2.066E-01	45.000	1.959E-01
														005-D-A5		385	76.6	41.7	49.5	51.6					45.000	2.338E-01	45.000	2.242E-01
														005-D-A6											45.000	2.072E-01	45.000	1.976E-01
														005-D-A7											45.000	2.037E-01	45.000	1.733E-01
														005-D-A8		393	80.3	42.2	45.7	50.6					45.000	2.379E-01	45.000	2.373E-01
														005-D-A9											45.000	2.117E-01	45.000	1.906E-01
														005-D-A10											45.000	2.066E-01	45.000	1.756E-01
13-C	23-Oct-2004	400	400	100	100	40	20	40	Normal TRISO, thin SiC; redo to correct SiC thickness	10	10	5		013-C-A1		386	83.5	34.6	23.8	53.9					45.000	1.950E-01	45.000	1.537E-01
														013-C-A2		375	80.3	49.9	23.2	58.2					45.000	2.067E-01	45.000	1.710E-01
														013-C-A3											45.000	2.034E-01	45.000	1.555E-01
														013-C-A4											45.000	2.080E-01	45.000	1.657E-01
														013-C-A5		375	67.1	36.7	24.1	53.8					45.000	1.954E-01	45.000	1.526E-01
														013-C-A6		372	86.4	42.0	25.4	57.3					45.000	1.954E-01	45.000	1.731E-01
														013-C-A7		386	89.8	38.8	21.5	56.1					45.000	2.168E-01	45.000	1.658E-01
														013-C-A8											45.000	2.035E-01	45.000	1.644E-01
														013-C-A9											45.000	2.044E-01	45.000	1.641E-01
														013-C-A10											45.000	2.150E-01	45.000	1.653E-01
11-E	11-Mar-2004	350	300-400	50/50	100	40	35	40	Metal Inclusions (Not Verified)	20	0	0	See no difference from 5-B	011-E-A1							43.383	1.968E-01						
														011-E-A2							43.383	1.495E-01						
														011-E-A3							43.383	1.570E-01						
														011-E-A4							43.383	2.012E-01						
														011-E-A5							43.383	1.762E-01						
														011-E-A6							43.383	1.724E-01						
														011-E-A7							43.383	1.691E-01						
														011-E-A8							43.383	2.032E-01						
														011-E-A9							43.383	1.621E-01						
														011-E-A10							43.383	1.724E-01						
														011-E-A11							43.383	1.639E-01						
														011-E-A12							43.383	1.916E-01						
														011-E-A13							43.383	1.763E-01						
														011-E-A14							43.383	1.700E-01						
														011-E-A15							43.383	1.865E-01						
														011-E-A16							43.383	1.546E-01						
														011-E-A17							43.383	2.106E-01						
														011-E-A18							43.383	1.692E-01						
														011-E-A19							43.383	1.966E-01						
														011-E-A20							43.383	1.884E-01						

Run Number	Date Shipped	Desired Particle Sizes - Kernel dia (µm)	Particle batch(s) to use	Kernal size spilt by SA	Buffer Thickness (µm)	IPYC Thickness (µm)	SiC Thickness (µm)	OPYC Thickness (µm)	Objective	Inductive Impedance Samples	Capacitive Impedance Samples	Radiography Samples	Measurement Notes	Specific Particles Examined Set #1	Set #2	RT Kernel dia (µm)	RT Buffer Thickness (µm)	RT IPYC Thickness (µm)	RT SiC Thickness (µm)	RT OPYC Thickness (µm)	EM(old) Inductive Excitation Frequency (MHz)	EM(old) Inductive Impedance (Fractional)	EM(old) Capacitive Excitation Frequency (MHz)	EM(old) Capacitive Impedance (Fractional)	EM(opt) Inductive Excitation Frequency (MHz)	EM(opt) Inductive Impedance (Fractional)	EM(opt) Capacitive Excitation Frequency (MHz)	EM(opt) Capacitive Impedance (Fractional)
15-A	7-Jun-2004	200	200	100	390	0	0	0	Undersized kernel with extra thick buffer	0	0	0	Didn't send to ISU															
16-A	8-Jun-2004	200	200	100	375	0	0	0	Undersized kernel with extra thick buffer	0	0	0	Didn't send to ISU															
AGR DUO$_2$	12-Dec-2004	500	500	100	0	0	0	0	AGR material shipped to ISU to test for equavalence to surrogate material	0	5	5																
AGR DUO$_2$ (DUN350)	12-Dec-2004	350	350	100	0	0	0	0		0	5	5		DUN350-A1													45.000	1.356E-02
														DUN350-A2													45.000	1.579E-02
														DUN350-A3													45.000	1.361E-02
														DUN350-A4													45.000	1.387E-02
														DUN350-A5													45.000	1.353E-02
AGR coated DUO$_2$	12-Dec-2004	500	500	100	100	40	35	40		0 coil too small	0	5																
AGR NUCO 69300	12-Dec-2004	350	350	100	0	0	0	0		0	5	5		69300-A1													45.000	1.083E-02
														69300-A2													45.000	1.349E-02
														69300-A3													45.000	9.281E-03
														69300-A4													45.000	1.145E-02
														69300-A5													45.000	1.421E-02
007-AA	22-Oct-2004	500	500	100	0	45	35	0	Run 7, 8, & 9-A with SiC layer added	10	10	0		007AA-A1											45.000	4.991E-02	45.000	8.820E-02
														007AA-A2		497		40.9	47.2						45.000	4.343E-02	45.000	8.731E-02
														007AA-A3											45.000	5.097E-02	45.000	9.289E-02
														007AA-A4		551		42.0	49.3						45.000	5.590E-02	45.000	1.143E-01
														007AA-A5											45.000	4.434E-02	45.000	8.926E-02
														007AA-A6		501		46.1	49.8						45.000	4.383E-02	45.000	8.147E-02
														007AA-A7											45.000	4.561E-02	45.000	8.558E-02
														007AA-A8		522		42.4	50.5						45.000	5.009E-02	45.000	9.517E-02
														007AA-A9											45.000	4.118E-02	45.000	8.759E-02
														007AA-A10		502		41.3	48.8						45.000	4.252E-02	45.000	8.483E-02
008-AA	22-Oct-2004	500	500	100	0	40	35	0		10	10	0		008AA-A1											45.000	4.205E-02	45.000	8.638E-02
														008AA-A2											45.000	3.819E-02	45.000	8.001E-02
														008AA-A3		509		40.6	50.0						45.000	4.340E-02	45.000	7.602E-02
														008AA-A4											45.000	4.237E-02	45.000	8.240E-02
														008AA-A5		516		39.5	48.9						45.000	3.828E-02	45.000	8.758E-02
														008AA-A6											45.000	4.393E-02	45.000	8.535E-02
														008AA-A7											45.000	4.345E-02	45.000	8.686E-02
														008AA-A8		502		37.6	50.2						45.000	3.371E-02	45.000	7.555E-02
														008AA-A9											45.000	3.934E-02	45.000	7.999E-02
														008AA-A10		520		38.0	51.3						45.000	3.498E-02	45.000	8.440E-02
009-AA	22-Oct-2004	500	500	100	0	40	35	0		10	10	0		009AA-A1		492		40.4	50.0						45.000	4.489E-02	45.000	8.130E-02
														009AA-A2											45.000	5.445E-02	45.000	9.195E-02
														009AA-A3											45.000	4.916E-02	45.000	8.239E-02
														009AA-A4		528		40.3	48.5						45.000	6.225E-02	45.000	9.971E-02
														009AA-A5											45.000	5.734E-02	45.000	9.123E-02
														009AA-A6		519		43.0	49.5						45.000	5.336E-02	45.000	8.554E-02
														009AA-A7											45.000	6.306E-02	45.000	9.644E-02
														009AA-A8											45.000	5.439E-02	45.000	9.448E-02
														009AA-A9		543		40.2	48.9						45.000	5.818E-02	45.000	9.713E-02
														009AA-A10		493		44.9	48.0						45.000	4.721E-02	45.000	7.286E-02

Run Number	Date Shipped	Desired Particle Sizes - Based on Specification							Objective	Number of Samples Examined			Measurement Notes	Specific Particles Examined			Radiographic Data						Electromagnetic Data (Older data not used in analyses)				Electromagnetic Data (Optimum Frequency, used in analyses)			
		Kernel dia (µm)	Particle batch(s) to use	Kernal size spilt by SA	Buffer Thickness (µm)	IPYC Thickness (µm)	SiC Thickness (µm)	OPYC Thickness (µm)		Inductive Impedance Samples	Capacitive Impedance Samples	Radiography Samples		Set #1	Set #2		RT Kernel dia (µm)	RT Buffer Thickness (µm)	RT IPYC Thickness (µm)	RT SiC Thickness (µm)	RT OPYC Thickness (µm)		Inductive Excitation Frequency (MHz)	Inductive Impedance (Fractional)	Capacitive Excitation Frequency (MHz)	Capacitive Impedance (Fractional)	Inductive Excitation Frequency (MHz)	Inductive Impedance (Fractional)	Capacitive Excitation Frequency (MHz)	Capacitive Impedance (Fractional)
17E	22-Oct-2004	500	500	100	100	40	0	0		20	20	0																		
17BB	22-Oct-2004	500	500	100	100	40	0	0		20	20	0																		
17B	22-Oct-2004	500	500	100	100	40	35	0		20	20	0																		
18C	22-Oct-2004	500	500	100	100	40	0	0		20	20	0																		
18CC	22-Oct-2004	500	500	100	100	40	35	0		20	10	0																		
18F	22-Oct-2004	500	500	100	100	40	0	0	Buffer and IPyC coated Particles, with and without SiC	20	20	0											Inductive and Capacitive data is available at PNNL but not listed in this table.							
18FF	22-Oct-2004	500	500	100	100	40	35	0		0	0	0																		
19A	22-Oct-2004	500	500	100	100	50	0	0		0	0	0																		
19AA	22-Oct-2004	500	500	100	100	40	35	0		0	0	0																		
19C	22-Oct-2004	500	500	100	100	40	0	0		0	0	0																		
19CC	22-Oct-2004	500	500	100	100	40	35	0		0	0	0																		
20A	22-Oct-2004	500	500	100	100	40	0	0		20	20	0																		
20AA	22-Oct-2004	500	500	100	100	40	35	0		20	20	0																		
21A	22-Oct-2004	500	500	100	100	40	0	0		20	20	0																		
21AA	22-Oct-2004	500	500	100	100	40	35	0		20	20	0																		
22B	22-Oct-2004	500	500	100	100	40	0	0		20	20	0																		
22BB	22-Oct-2004	500	500	100	100	40	35	0		20	20	0																		

Run Number	Date Shipped	Kernel dia (µm)	Particle batch(s) to use	Kernal size spilt by SA	Buffer Thickness (µm)	IPYC Thickness (µm)	SiC Thickness (µm)	OPYC Thickness (µm)	Objective	Inductive Impedance Samples	Capacitive Impedance Samples	Radiography Samples	Measurement Notes	Set #1	Set #2	RT Kernel dia (µm)	RT Buffer Thickness (µm)	RT IPYC Thickness (µm)	RT SiC Thickness (µm)	RT OPYC Thickness (µm)	Inductive Excitation Frequency (MHz)	Inductive Impedance (Fractional)	Capacitive Excitation Frequency (MHz)	Capacitive Impedance (Fractional)	Inductive Excitation Frequency (MHz)	Inductive Impedance (Fractional)	Capacitive Excitation Frequency (MHz)	Capacitive Impedance (Fractional)
NUCO350-39T-A	14-Aug-2005								Triso coated NUCO					39T-A1											45.000	1.988E-01	45.000	1.798E-01
														39T-A2											45.000	2.123E-01	45.000	2.075E-01
														39T-A3											45.000	1.865E-01	45.000	1.774E-01
														39T-A4		403.9	90.0	34	32.5	50.8					45.000	2.464E-01	45.000	2.279E-01
														39T-A5											45.000	1.900E-01	45.000	1.727E-01
														39T-A6											45.000	2.073E-01	45.000	1.749E-01
														39T-A7											45.000	1.881E-01	45.000	1.687E-01
														39T-A8											45.000	1.958E-01	45.000	1.875E-01
														39T-A9											45.000	1.988E-01	45.000	1.886E-01
														39T-A10											45.000	1.968E-01	45.000	1.841E-01
														39T-A11											45.000	1.910E-01	45.000	1.895E-01
														39T-A12											45.000	1.894E-01	45.000	1.654E-01
														39T-A13											45.000	1.791E-01	45.000	1.646E-01
														39T-A14											45.000	1.996E-01	45.000	1.888E-01
														39T-A15											45.000	1.879E-01	45.000	1.829E-01
														39T-A16											45.000	1.912E-01	45.000	1.941E-01
														39T-A17		356	86.4	37.9	36.5	52.2					45.000	1.725E-01	45.000	1.855E-01
														39T-A18											45.000	2.048E-01	45.000	1.989E-01
														39T-A19											45.000	2.011E-01	45.000	1.808E-01
														39T-A20		415.7	100.3	40.7	30.2	55.7					45.000	2.610E-01	45.000	2.433E-01
														39T-A21		350.5	96.7	41.7	33.8	55.6					45.000	2.063E-01	45.000	1.881E-01
														39T-A22		380.1	102.6	36.8	35.2	56.7					45.000	2.344E-01	45.000	1.996E-01
														39T-A23											45.000	2.059E-01	45.000	1.789E-01
														39T-A24											45.000	2.147E-01	45.000	1.857E-01
														39T-A25											45.000	2.374E-01	45.000	2.042E-01
														39T-A26		378.6	102.8	34.9	33.1	50.7					45.000	2.537E-01	45.000	2.116E-01
														39T-A27											45.000	2.393E-01	45.000	2.109E-01
														39T-A28											45.000	2.279E-01	45.000	1.949E-01
														39T-A29		350.8	101.9	38.9	32.8	51.6					45.000	2.311E-01	45.000	1.851E-01
														39T-A30											45.000	2.207E-01	45.000	1.862E-01
														39T-A31											45.000	1.944E-01	45.000	1.722E-01
														39T-A32		362.3	114.5	32.2	32	48.8					45.000	2.165E-01	45.000	2.284E-01
														39T-A33		376.1	100.1	40.8	33.3	50.4					45.000	2.254E-01	45.000	2.297E-01
														39T-A34											45.000	1.791E-01	45.000	1.673E-01
														39T-A35		352.1	104.2	40	34.6	52.9					45.000	2.047E-01	45.000	1.904E-01
														39T-A36											45.000	1.995E-01	45.000	1.823E-01
														39T-A37		347.5	92.8	38.7	37	52.2					45.000	1.747E-01	45.000	1.590E-01
														39T-A38											45.000	1.939E-01	45.000	1.866E-01
														39T-A39											45.000	1.933E-01	45.000	1.769E-01
														39T-A40											45.000	2.039E-01	45.000	1.948E-01
														39T-A41											45.000	1.995E-01	45.000	1.912E-01
														39T-A42											45.000	2.186E-01	45.000	2.028E-01
														39T-A43											45.000	1.984E-01	45.000	1.853E-01
														39T-A44											45.000	2.280E-01	45.000	2.045E-01
														39T-A45											45.000	2.223E-01	45.000	2.237E-01
														39T-A46											45.000	2.111E-01	45.000	1.962E-01
														39T-A47											45.000	1.945E-01	45.000	1.915E-01
														39T-A48											45.000	1.816E-01	45.000	1.799E-01
														39T-A49											45.000	2.255E-01	45.000	2.149E-01
														39T-A50											45.000	1.931E-01	45.000	1.701E-01

Run Number	Date Shipped	Kernel dia (µm)	Particle batch(s) to use	Kernal size spilt by SA	Buffer Thickness (µm)	IPYC Thickness (µm)	SiC Thickness (µm)	OPYC Thickness (µm)	Objective	Inductive Impedance Samples	Capacitive Impedance Samples	Radiography Samples	Measurement Notes	Set #1	Set #2	RT Kernel dia (µm)	RT Buffer Thickness (µm)	RT IPYC Thickness (µm)	RT SiC Thickness (µm)	RT OPYC Thickness (µm)	Inductive Excitation Frequency (MHz)	Inductive Impedance (Fractional)	Capacitive Excitation Frequency (MHz)	Capacitive Impedance (Fractional)	Inductive Excitation Frequency (MHz)	Inductive Impedance (Fractional)	Capacitive Excitation Frequency (MHz)	Capacitive Impedance (Fractional)
39T-A51																									45.000	2.010E-01	45.000	1.854E-01
39T-A52																									45.000	2.137E-01	45.000	1.989E-01
39T-A53																									45.000	2.078E-01	45.000	1.949E-01
39T-A54																									45.000	2.394E-01	45.000	2.185E-01
39T-A55																									45.000	2.054E-01	45.000	1.876E-01
39T-A56																384.7	112.2	36.6	28.9	54.7					45.000	2.499E-01	45.000	2.273E-01
39T-A57																359.7	76.3	41.3	34.1	51.7					45.000	1.759E-01	45.000	1.539E-01
39T-A58			2.055E-01																						45.000	2.055E-01	45.000	1.979E-01
39T-A59			2.136E-01																						45.000	2.136E-01	45.000	2.014E-01
39T-A60			2.276E-01																						45.000	2.276E-01	45.000	2.163E-01
39T-A61			1.831E-01																						45.000	1.831E-01	45.000	1.688E-01
39T-A62			1.864E-01																						45.000	1.864E-01	45.000	1.696E-01
39T-A63																369.7	94.3	41.1	35.4	49.7					45.000	2.043E-01	45.000	1.882E-01
39T-A64																									45.000	1.927E-01	45.000	1.862E-01
39T-A65																									45.000	2.036E-01	45.000	1.787E-01
39T-A66																									45.000	1.976E-01	45.000	1.901E-01
39T-A67																370.2	90.1	36.8	32.1	45.6					45.000	2.356E-01	45.000	1.783E-01
39T-A68																407.9	93.2	34.9	30.7	48.6					45.000	1.964E-01	45.000	2.012E-01
39T-A69																									45.000	1.950E-01	45.000	1.849E-01
39T-A70																									45.000	2.054E-01	45.000	1.940E-01
39T-A71																									45.000	2.208E-01	45.000	2.052E-01
39T-A72																									45.000	2.103E-01	45.000	1.896E-01
39T-A73																									45.000	2.010E-01	45.000	1.916E-01
39T-A74																									45.000	2.072E-01	45.000	1.854E-01
39T-A75			1.860E-01													351.7	88.6	36.8	34.1	51.7					45.000	1.860E-01	45.000	1.590E-01
39T-A76			1.837E-01																						45.000	1.837E-01	45.000	1.731E-01
39T-A77			2.046E-01													363.9	100.4	38.2	32.4	51					45.000	2.046E-01	45.000	1.891E-01
39T-A78			2.185E-01																						45.000	2.241E-01	45.000	2.168E-01
39T-A79																									45.000	2.185E-01	45.000	2.116E-01
39T-A80																									45.000	2.418E-01	45.000	2.211E-01
39T-A81			2.113E-01																						45.000	2.113E-01	45.000	2.056E-01
39T-A82																355.7	73.4	43	36.5	52.6					45.000	1.737E-01	45.000	1.607E-01
39T-A83																									45.000	2.166E-01	45.000	2.172E-01
39T-A84																									45.000	1.980E-01	45.000	1.765E-01
39T-A85																									45.000	1.997E-01	45.000	1.801E-01
39T-A86																									45.000	2.044E-01	45.000	1.866E-01
39T-A87																									45.000	2.071E-01	45.000	2.014E-01
39T-A88																									45.000	2.137E-01	45.000	1.995E-01
39T-A89			1.990E-01																						45.000	1.990E-01	45.000	1.776E-01
39T-A90			2.083E-01																						45.000	2.083E-01	45.000	2.006E-01
39T-A91																									45.000	2.130E-01	45.000	2.014E-01
39T-A92			1.053E-01													367.3	105.9	38.7	31	51.9					45.000	1.053E-01	45.000	1.989E-01
39T-A93																									45.000	2.117E-01	45.000	1.731E-01
39T-A94			2.019E-01																						45.000	2.019E-01	45.000	1.212E-01
39T-A95																									45.000	2.117E-01	45.000	1.408E-01
39T-A96																									45.000	2.125E-01	45.000	1.520E-01
39T-A97																									45.000	1.942E-01	45.000	1.486E-01
39T-A98																									45.000	2.104E-01	45.000	1.681E-01
39T-A99																									45.000	2.174E-01	45.000	1.631E-01
39T-A100																									45.000	2.008E-01	45.000	1.694E-01

Run Number	Date Shipped	Desired Particle Sizes - Based on Specification							Objective	Number of Samples Examined			Measurement Notes	Specific Particles Examined		Radiographic Data					Electromagnetic Data (Older data not used in analyses)				Electromagnetic Data (Optimum Frequency, used in analyses)			
		Kernel dia (μm)	Particle batch(s) to use	Kernal size spilt by SA	Buffer Thickness (μm)	IPYC Thickness (μm)	SiC Thickness (μm)	OPYC Thickness (μm)		Inductive Impedance Samples	Capacitive Impedance Samples	Radiography Samples		Set #1	Set #2	RT Kernel dia (μm)	RT Buffer Thickness (μm)	RT IPYC Thickness (μm)	RT SiC Thickness (μm)	RT OPYC Thickness (μm)	Inductive Excitation Frequency (MHz)	Inductive Impedance (Fractional)	Capacitive Excitation Frequency (MHz)	Capacitive Impedance (Fractional)	Inductive Excitation Frequency (MHz)	Inductive Impedance (Fractional)	Capacitive Excitation Frequency (MHz)	Capacitive Impedance (Fractional)
NUCO350-41T-A	14-Aug-2005													41T-A1											45.000	1.364E-01	45.000	1.415E-01
			45.000											41T-A2											45.000	1.411E-01	45.000	1.342E-01
		1.616E-01												41T-A3											45.000	1.616E-01	45.000	1.676E-01
		1.583E-01												41T-A4											45.000	1.583E-01	45.000	1.522E-01
														41T-A5											45.000	1.607E-01	45.000	1.482E-01
														41T-A6											45.000	1.643E-01	45.000	1.498E-01
														41T-A7											45.000	1.616E-01	45.000	1.570E-01
														41T-A8											45.000	1.464E-01	45.000	1.331E-01
														41T-A9											45.000	1.574E-01	45.000	1.515E-01
														41T-A10											45.000	1.479E-01	45.000	1.401E-01
														41T-A11											45.000	1.421E-01	45.000	1.379E-01
														41T-A12											45.000	1.434E-01	45.000	1.346E-01
														41T-A13											45.000	1.441E-01	45.000	1.391E-01
														41T-A14											45.000	1.505E-01	45.000	1.589E-01
														41T-A15											45.000	1.502E-01	45.000	1.422E-01
														41T-A16											45.000	1.316E-01	45.000	1.296E-01
														41T-A17											45.000	1.622E-01	45.000	1.532E-01
														41T-A18											45.000	1.370E-01	45.000	1.432E-01
														41T-A19											45.000	1.492E-01	45.000	1.501E-01
														41T-A20											45.000	1.385E-01	45.000	1.353E-01
NUCO350-58B-A	14-Aug-2005								Buffer coated NUCO					58B-A1											45.000	2.197E-02	45.000	4.442E-02
														58B-A2											45.000	3.045E-02	45.000	4.090E-02
														58B-A3											45.000	2.664E-02	45.000	4.244E-02
														58B-A4											45.000	3.620E-02	45.000	4.092E-02
														58B-A5											45.000	3.056E-02	45.000	4.144E-02
														58B-A6											45.000	3.158E-02	45.000	4.123E-02
														58B-A7											45.000	3.230E-02	45.000	4.173E-02
														58B-A8											45.000	3.410E-02	45.000	4.328E-02
														58B-A9											45.000	3.230E-02	45.000	4.783E-02
														58B-A10											45.000	3.339E-02	45.000	4.315E-02
														58B-A11											45.000	2.681E-02	45.000	3.544E-02
														58B-A12											45.000	3.327E-02	45.000	4.432E-02
														58B-A13											45.000	2.969E-02	45.000	4.199E-02
														58B-A14											45.000	3.194E-02	45.000	4.712E-02
														58B-A15											45.000	2.944E-02	45.000	3.946E-02
														58B-A16											45.000	2.309E-02	45.000	3.487E-02
														58B-A17											45.000	3.389E-02	45.000	4.069E-02
														58B-A18											45.000	2.939E-02	45.000	4.713E-02
														58B-A19											45.000	3.663E-02	45.000	4.609E-02
														58B-A20											45.000	3.252E-02	45.000	4.191E-02

Table columns (most cells empty): Run Number | Date Shipped | **Desired Particle Sizes - Based on Specification** [Kernel dia (µm), Particle batch(s) to use, Kernal size spilt by SA, Buffer Thickness (µm), IPYC Thickness (µm), SiC Thickness (µm), OPYC Thickness (µm)] | Objective | **Number of Samples Examined** [Inductive Impedance Samples, Capacitive Impedance Samples, Radiography Samples] | Measurement Notes | **Specific Particles Examined** [Set #1, Set #2] | **Radiographic Data** [RT Kernel dia (µm), RT Buffer Thickness (µm), RT IPYC Thickness (µm), RT SiC Thickness (µm), RT OPYC Thickness (µm)] | **Electromagnetic Data (Older data not used in analyses)** | **Electromagnetic Data (Optimum Frequency, used in analyses)**

Only the Run Number, Date Shipped, Objective, Set #1, and the Optimum-Frequency Electromagnetic Data columns contain values:

Run Number	Date Shipped	Objective	Set #1	Inductive Excitation Frequency (MHz)	Inductive Impedance (Fractional)	Capacitive Excitation Frequency (MHz)	Capacitive Impedance (Fractional)
NUCO350-66BI-A	14-Aug-2005		66BI-A1	45.000	8.668E-02	45.000	7.303E-02
			66BI-A2	45.000	7.611E-02	45.000	6.214E-02
			66BI-A3	45.000	9.156E-02	45.000	3.493E-02
			66BI-A4	45.000	6.821E-02	45.000	1.332E-02
			66BI-A5	45.000	6.830E-02	45.000	1.364E-02
			66BI-A6	45.000	7.223E-02	45.000	1.621E-02
			66BI-A7	45.000	7.798E-02	45.000	2.096E-02
			66BI-A8	45.000	5.602E-03	45.000	1.401E-02
			66BI-A9	45.000	8.349E-02	45.000	2.416E-02
			66BI-A10	45.000	8.095E-02	45.000	2.075E-02
			66BI-A11	45.000	7.563E-02	45.000	6.716E-02
			66BI-A12	45.000	7.115E-02	45.000	6.531E-02
			66BI-A13	45.000	7.150E-02	45.000	6.613E-02
			66BI-A14	45.000	7.185E-02	45.000	6.532E-02
			66BI-A15	45.000	6.926E-02	45.000	6.192E-02
			66BI-A16	45.000	7.024E-02	45.000	6.658E-02
			66BI-A17	45.000	6.095E-02	45.000	5.677E-02
			66BI-A18	45.000	7.647E-02	45.000	6.832E-02
			66BI-A19	45.000	7.511E-02	45.000	7.069E-02
			66BI-A20	45.000	7.712E-02	45.000	6.873E-02
NUCO350-IPyC-5	14-Aug-2005	BIP coated NUCO	IPyC-5-A1	45.000	5.096E-02	45.000	5.293E-02
			IPyC-5-A2	45.000	5.009E-02	45.000	5.436E-02
			IPyC-5-A3	45.000	5.595E-02	45.000	5.141E-02
			IPyC-5-A4	45.000	5.959E-02	45.000	5.593E-02
			IPyC-5-A5	45.000	6.941E-02	45.000	6.481E-02
			IPyC-5-A6	45.000	5.000E-02	45.000	5.339E-02
			IPyC-5-A7	45.000	5.594E-02	45.000	5.657E-02
			IPyC-5-A8	45.000	5.431E-02	45.000	5.515E-02
			IPyC-5-A9	45.000	6.978E-02	45.000	6.354E-02
			IPyC-5-A10	45.000	5.071E-02	45.000	5.102E-02
			IPyC-5-A11	45.000	5.111E-02	45.000	5.079E-02
			IPyC-5-A12	45.000	5.482E-02	45.000	5.449E-02
			IPyC-5-A13	45.000	5.780E-02	45.000	5.118E-02
			IPyC-5-A14	45.000	5.032E-02	45.000	5.441E-02
			IPyC-5-A15	45.000	6.238E-02	45.000	5.514E-02
			IPyC-5-A16	45.000	5.228E-02	45.000	5.578E-02
			IPyC-5-A17	45.000	4.432E-02	45.000	5.015E-02
			IPyC-5-A18	45.000	5.943E-02	45.000	5.582E-02
			IPyC-5-A19	45.000	5.805E-02	45.000	5.870E-02
			IPyC-5-A20	45.000	6.192E-02	45.000	5.586E-02
NUCO350-IPyC-6	14-Aug-2005		IPyC-6-A1	45.000	7.435E-02	45.000	5.689E-02
			IPyC-6-A2	45.000	7.123E-02	45.000	4.783E-02
			IPyC-6-A3	45.000	6.734E-02	45.000	5.191E-02
			IPyC-6-A4	45.000	7.848E-02	45.000	6.004E-02
			IPyC-6-A5	45.000	6.175E-02	45.000	5.154E-02
			IPyC-6-A6	45.000	6.449E-02	45.000	5.703E-02
			IPyC-6-A7	45.000	6.622E-02	45.000	6.049E-02
			IPyC-6-A8	45.000	7.080E-02	45.000	5.661E-02
			IPyC-6-A9	45.000	6.460E-02	45.000	4.994E-02
			IPyC-6-A10	45.000	5.319E-02	45.000	5.526E-02
			IPyC-6-A11	45.000	7.338E-02	45.000	5.149E-02
			IPyC-6-A12	45.000	6.914E-02	45.000	5.214E-02
			IPyC-6-A13	45.000	8.468E-02	45.000	5.933E-02
			IPyC-6-A14	45.000	9.524E-02	45.000	6.008E-02
			IPyC-6-A15	45.000	7.978E-02	45.000	6.058E-02
			IPyC-6-A16	45.000	9.317E-02	45.000	6.070E-02
			IPyC-6-A17	45.000	8.729E-02	45.000	No Data
			IPyC-6-A18	45.000	8.453E-02	45.000	5.097E-02
			IPyC-6-A19	45.000	8.141E-02	45.000	6.214E-02
			IPyC-6-A20	45.000	8.680E-02	45.000	5.934E-02

B.14

Appendix C

Appendix C provides the statistical analysis of the NERI project data.

Inductive impedance is considered first (see page C.7). A stepwise approach was used that brings in, in sequence, the statistically most significant terms for explaining the inductive impedance response. The first table, called "current estimates", lists all the candidate variables being considered. The second table shows the sequence of modeling steps made by the software.

At the first step, carbon volume is entered into the model giving an R^2 value of 0.9721. That is, 97% of the variability in inductive impedance can be explained by the carbon volume alone for the surrogate particles in the data set. The square root of this quantity, 0.986, is the commonly used correlation coefficient. Note that the value of "P" in the final column for this first step is 2 which indicate two terms are now in the predictive model, the intercept term, which is always generically included, and now the carbon volume as well.

With carbon volume in the model, only 3% of the inductive impedance variability remains unexplained, but none-the-less, to explain part of this 3%, the buffer volume by IPyC Volume interaction is brought into the model in Step 2. This actually brings in three terms since the two main effects will also be brought in with this interaction effect. Thus the new model will be increased to having five terms, and R^2 increases to 0.9804. While this increase in R^2 is "statistically significant" one would wonder about its practical importance. And this applies even more-so to the remaining entries into the model in subsequent steps. Incrementally, R^2 continues to increase in statistically significant steps, but in terms of prediction capability, there is likely little difference between the models at the various steps.

Note that an interaction term being significant means that the influence of one of the main effects on the response depends on the value of the other main effects. The impact on the response of an increased value of one of the main effects would depend on whether relatively small or large values of the other main effect are used. Without significant interaction, the impact of main effect changes on the response does not depend at all on other main effects. Thus models are much simpler without interaction terms, but if such interaction terms are statistically significant, models that do not include them cannot be as successful at explaining the response variability.

Note at the final step, a term is actually removed from the model. This could occur at any point in the process since adding successive terms can make previous terms less important and no longer needed.

The final, statistically optimal model, with $R^2 = 0.9919$, then has 10 terms in it, one being the intercept. They are marked by X's in the Current Estimates table.

The second page of the inductive impedance analysis (see page C.8) applies this specific model and gives more information than the stepwise approach did. Of particular interest is the "Parameter Estimates" table. This gives the predictive equation for this model. Given the dimensions of a candidate particle, the associated volumes could be computed and plugged into the equation to obtain a predicted inductive impedance value (with associated confidence limits as well).

As an example of applying these parameter estimates, the intercept value 0.11117914 would have 3285.94017 times a new buffer volume added to it, and so on for each main effect. Note for example the negative relationship of impedance with carbon value. In the prediction equation, one would subtract -99.248711 times the carbon volume.

For an interaction term, like buffer volume by particle volume, the product of those two new volumes would be multiplied by 80034190.8 and added. For a squared term, like SIC-squared, the square of the new SIC volume would be multiplied by 4.74058e7 and subtracted due to the minus sign. In this manner predictive values can be obtained.

More simply the statistical software will provide these predicted values after the models are fit as well as 95% confidence prediction limits. For a particular set of dimensional features, 95% of particles with those features would be expected to have inductive impedance values within such prediction limits. The prediction value itself can be thought of as an average response for such particles. In this manner Table C-1 was generated for the 35 surrogate particles used in the modeling.

In addition, the dimensional features of other particular particles of interest can be added to the data set to obtain their predicted values as well; however these new particles are not included in the original model fitting (they could not be since no impedance responses are available for them). In this manner the "nominal" and "borderline" particles in Table C-2 are generated. "Nominal" here refers to the nominal manufacturing specifications shown as 350, 100, 40, 35, and 40 for the respective layers.

"Borderline" particles go to all combinations of the manufacturing limits 350 + 10, 100 + 10, 40 + 4, 35 + 3, and 40 + 4. Thus the first of these 32 particles is the high, high, high, high, high combination of 360, 110, 44, 38, and 44. This is quite a large particle, but still within the proposed specifications. The 32nd of these particles is the opposite combination of all the low values, 340, 90, 36, 32, and 36, a very small particle, but again within specifications.

Table C-3, called "more extreme", uses more extreme particles by doubling the + limits from the borderline case, that is, 350 + 20, 100 + 20, 40 + 8, 35 + 6, and 40 + 8. Table C-4 is even more extreme in that its particles go to even more extreme limits that are listed as what "1% of a manufacturing batch" may or may not exceed (or be less than). Thus in each case another 32 particles are included through the various combinations of high/low conditions.

Combining Tables C-1 through C-4 gives 132 particles with predicted inductive impedance values, the original 35 particles used in the modeling and 97 more from the nominal particles and the three sets of 32 high/low combinations. The predicted values associated with these 132 particles are ordered and plotted in Figure C.1.

Lastly the analysis for the batch average data begins on page C-26 and with the same approach as considered earlier.
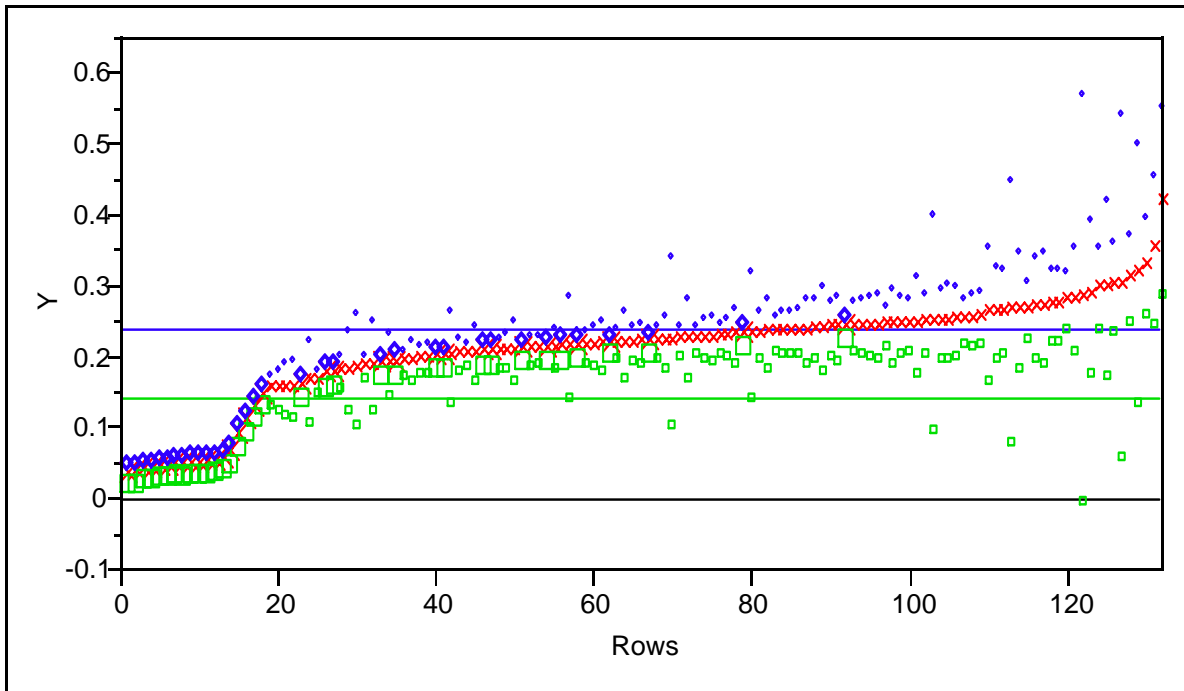
Figure C.1. Inductive Impedance Surrogate Prediction Values and Prediction Limits

Red x's are the predicted values, blue diamonds the upper prediction limits, and green squares the lower prediction limits. The actual surrogate particles are represented by the larger symbols among these. Note that the first 14 of these surrogate particles were actually missing the buffer and OPyC layers and lead to the extremely low inductive impedance values.

From Figure C.1, one might suggest that inductive impedance values for acceptable particles tend to lie in the range from approximately 0.11 to 0.24. These are respectively the green and blue dotted horizontal lines on the figure. If one used these values as "acceptance limits" for inductive impedance values for particle predicted values, then on Tables C-1 through C-4, particles shaded green would have been deemed acceptable and particles shaded yellow would have been deemed unacceptable.

With the ideally richer data set that would include broader types of unacceptable particles, one could have repeated this process with the goal that the unacceptable particles all ultimately get shaded yellow after the modeling and prediction, and other candidate acceptable particles get shaded green. We are restricted for the moment to observe the patterns shown by the current shading that is based solely on the rather limited surrogate data set. The reader is invited to draw conclusions regarding the shading patterns with respect to the impact of the various dimensional features on particle acceptability based on this modeling of inductive impedance responses.

Following the inductive impedance analysis, the very same sequence of analysis steps is given for the capacitive impedance responses (page C-13) for the surrogate particles. Note that a more compact model is obtained that uses only the kernel, buffer and SIC volumes and their squares. IPyC and OPyC volumes were not brought into the model as being useful additions to those factors. This is unfortunate since now the predicted values for other candidate particles will not depend on their IPyC or OPyC dimensions at

all. Apparently a feature of this particular set of surrogate particles is that the IPyC and OPyC values simply didn't add any information useful for explaining the capacitive impedance value variability, at least not in addition to what the kernel buffer, and SIC volumes already accomplish.

Additionally, in the first step under step history that a group of three terms were brought into the model as providing the most statistically significant contribution. They are the buffer volume by particle volume interaction term and those two main effects as well. But then note in the final step that both the particle volume term and the particle volume by buffer volume interaction term were then removed from the model to leave only kernel, buffer, and SIC terms.

Note also that the same acceptable range of capacitive impedance responses (0.14 to 0.24) was selected in Figure C.2 as was the case in Figure C.1 for inductive impedance and was used for the yellow/green shading on candidate particles in Tables C-5 through C-8. The results here are more "forgiving" in that many more of the candidate particles are considered acceptable (shaded green).
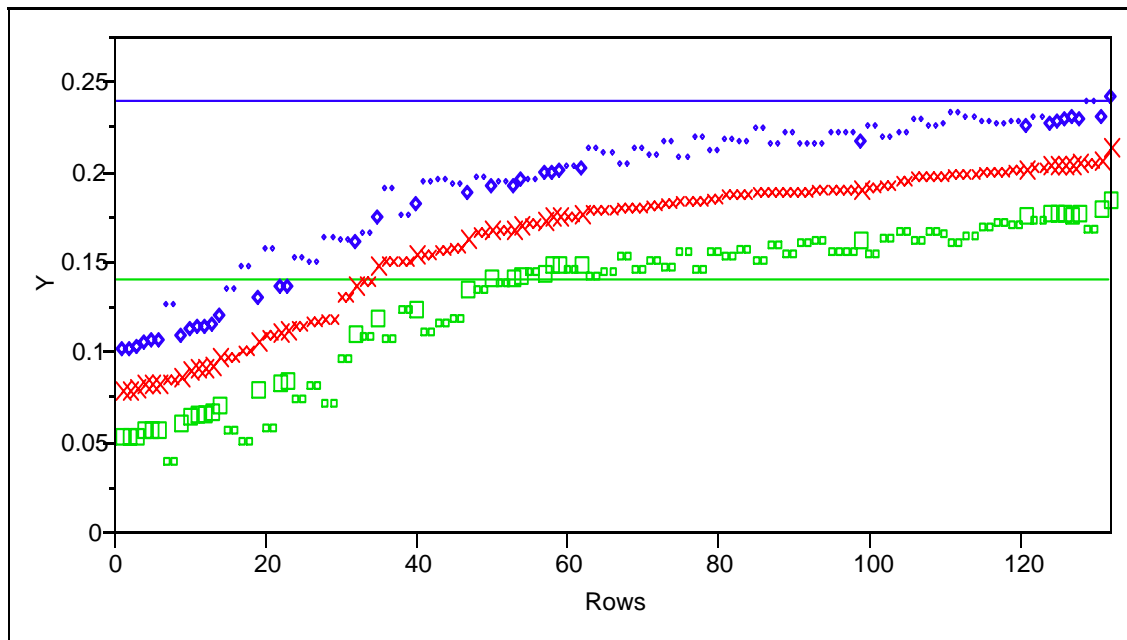
Figure C.2. Capacitive Impedance Surrogate Prediction Values and Prediction Limits

The remaining pages in this appendix present the same analyses based on the batch 39T particles. Note that these particles were more consistent with respect to dimensional features than were the surrogate particles. No useful inductive impedance model resulted from the stepwise analysis, so no analyses was given beyond that point.

Finally, two figures are given of the capacitive impedance model predictions. The second (Figure C.4) is simply the first (Figure C.3) truncated at zero. And again the response range from 0.14 to 0.24 is not unreasonable and was used for the yellow/green shading on candidate particles in Table C-9 to C-12.

Note that the Batch 39T results are the "least forgiving" in that fewer of the candidate particles are considered acceptable (shaded green) than was the case in the surrogate cases. This is because the 39T

particles are more consistent dimensionally, and the candidate particles than lie more readily outside that values for which the 39T model was established.
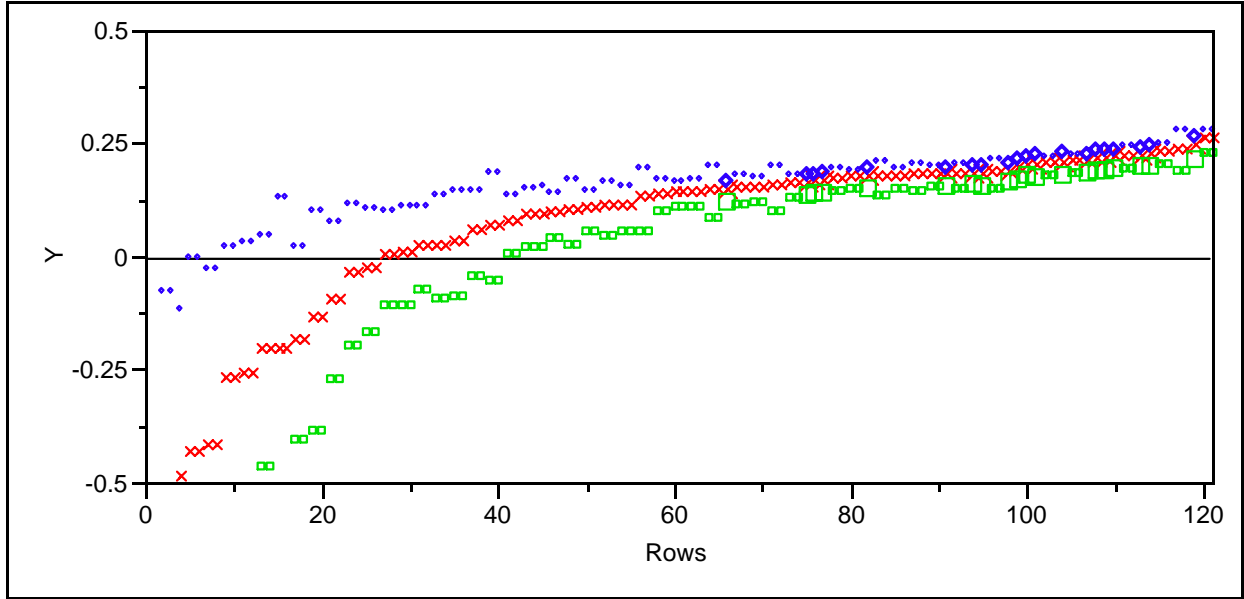
Figure C.3. Capacitive Impedance 39T Prediction Values and Prediction Limits
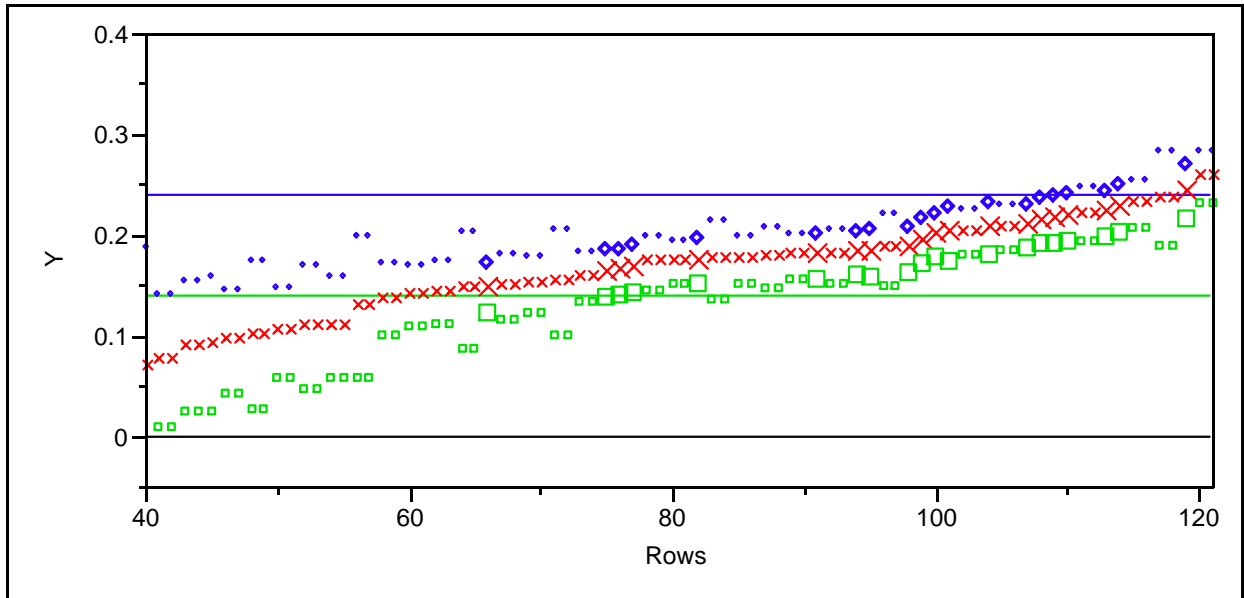
Figure C.4. Capacitive Impedance 39T Prediction Values and Prediction Limits (truncated)

Stepwise Fit

Response:
Inductive Imp

Current Estimates

	SSE	DFE	MSE	RSquare				
	0.001626	25	0.000065	0.9919				
Lock	Entered	Parameter		Estimate	nDF	SS	F Ratio	Prob>F
X	X	Intercept		0.11117914	1	0	0.000	1.0000
		Kernel Volume		0	0	0	.	.
	X	Buffer Volume		3285.94017	3	0.002544	13.037	0.0000
	X	IPyC Volume		-6695.244	3	0.002255	11.556	0.0001
	X	SIC Volume		-968.17511	3	0.002246	11.513	0.0001
		OPyC Volume		0	0	0	.	.
	X	Carbon Volume		-99.248711	2	0.002282	17.540	0.0000
	X	Particle Volume		930.998263	1	0.001222	18.790	0.0002
		Kernel Volume*Buffer Volume		0	0	0	.	.
		Kernel Volume*IPyC Volume		0	0	0	.	.
		Kernel Volume*SIC Volume		0	0	0	.	.
		Kernel Volume*OPyC Volume		0	0	0	.	.
		Kernel Volume*Carbon Volume		0	0	0	.	.
		Kernel Volume*Particle Volume		0	0	0	.	.
	X	Buffer Volume*IPyC Volume		80034190.8	1	0.000439	6.745	0.0155
		Buffer Volume*SIC Volume		0	1	0.000075	1.161	0.2920
		Buffer Volume*OPyC Volume		0	0	0	.	.
	X	Buffer Volume*Carbon Volume		-2.71365e7	1	0.001193	18.343	0.0002
		Buffer Volume*Particle Volume		0	1	0.000057	0.873	0.3594
	X	IPyC Volume*SIC Volume		117526606	1	0.001552	23.864	0.0001
		IPyC Volume*OPyC Volume		0	0	0	.	.
		IPyC Volume*Carbon Volume		0	1	0.000009	0.135	0.7164
		IPyC Volume*Particle Volume		0	1	0.000005	0.068	0.7969
		SIC Volume*OPyC Volume		0	0	0	.	.
		SIC Volume*Carbon Volume		0	1	0.000065	1.005	0.3260
		SIC Volume*Particle Volume		0	1	0.000069	1.067	0.3120
		OPyC Volume*Carbon Volume		0	0	0	.	.
		OPyC Volume*Particle Volume		0	0	0	.	.
		Carbon Volume*Particle Volume		0	1	0.000024	0.360	0.5541
		Kernel Volume*Kernel Volume		0	0	0	.	.
		Buffer Volume*Buffer Volume		0	1	0.000045	0.684	0.4162
		IPyC Volume*IPyC Volume		0	1	0.000002	0.034	0.8556
	X	SIC Volume*SIC Volume		-4.74058e7	1	0.001382	21.242	0.0001
		OPyC Volume*OPyC Volume		0	0	0	.	.
		Carbon Volume*Carbon Volume		0	1	0.000003	0.037	0.8484
		Particle Volume*Particle Volume		0	1	0.000023	0.344	0.5629

Step History

Step	Parameter	Action	"Sig Prob"	Seq SS	RSquare	Cp	p
1	Carbon Volume	Entered	0.0000	0.194229	0.9721	38.453	2
2	Buffer Volume*IPyC Volume	Entered	0.0134	0.001651	0.9804	23.868	5
3	IPyC Volume*Particle Volume	Entered	0.0723	0.000671	0.9837	19.506	7
4	SIC Volume*Carbon Volume	Entered	0.0674	0.000609	0.9868	15.918	9
5	Buffer Volume*Carbon Volume	Entered	0.0770	0.000316	0.9884	13.974	10
6	SIC Volume*SIC Volume	Entered	0.0557	0.000335	0.9900	11.795	11
7	IPyC Volume*SIC Volume	Entered	0.0194	0.000429	0.9922	8.4484	12
8	IPyC Volume*Particle Volume	Removed	0.9192	7.128e-7	0.9922	6.4573	11
9	SIC Volume*Carbon Volume	Removed	0.3260	0.000065	0.9919	5.2724	10

Response Inductive Imp   Actual by Predicted Plot
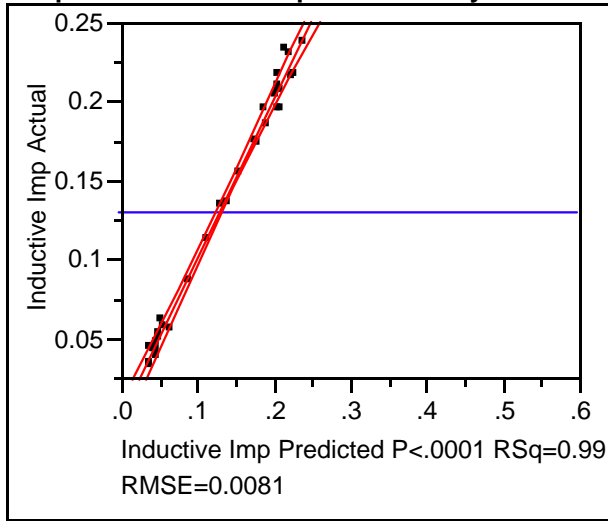
Summary of Fit

RSquare	0.991862
RSquare Adj	0.988932
Root Mean Square Error	0.008065
Mean of Response	0.130803
Observations (or Sum Wgts)	35

Analysis of Variance

Source	DF	Sum of Squares	Mean Square	F Ratio
Model	9	0.19817329	0.022019	338.5570
Error	25	0.00162596	0.000065	Prob > F
C. Total	34	0.19979925		<.0001

Parameter Estimates

Term	Estimate	Std Error	t Ratio	Prob>|t|
Intercept	0.1111791	0.064511	1.72	0.0972
Buffer Volume	3285.9402	585.5546	5.61	<.0001
IPyC Volume	-6695.244	1726.659	-3.88	0.0007
SIC Volume	-968.1751	1287.988	-0.75	0.4593
Carbon Volume	-99.24871	267.4485	-0.37	0.7137
Particle Volume	930.99826	214.7752	4.33	0.0002
Buffer Volume*IPyC Volume	80034191	30816300	2.60	0.0155
Buffer Volume*Carbon Volume	-27136518	6336068	-4.28	0.0002
IPyC Volume*SIC Volume	117526606	24058372	4.89	<.0001
SIC Volume*SIC Volume	-47405773	10285667	-4.61	0.0001

Prediction Profiler

C.8
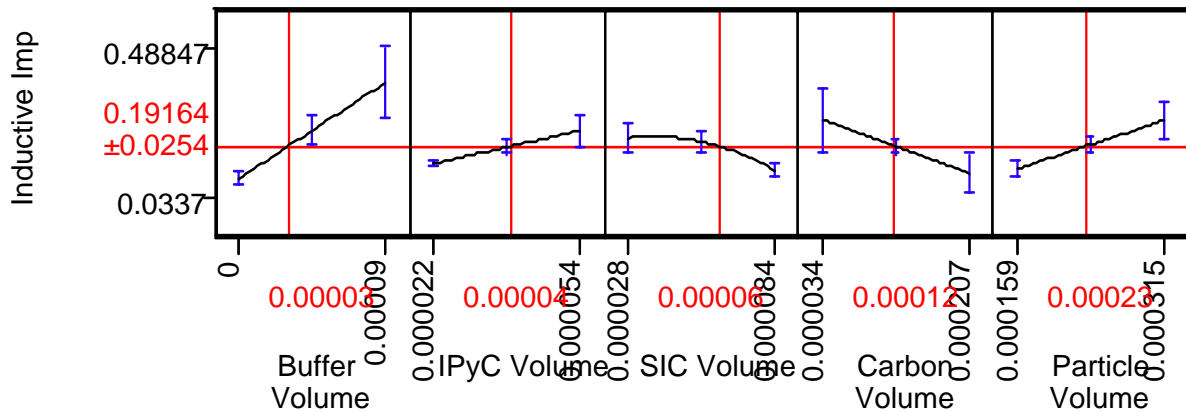
Table C-1. Inductive Impedance Surrogate Prediction Values for "Surrogate" Particles

Particle ID	Kernel	Buffer	IPyC	SIC	OPyC		Predicted Inductive Imp	Lower 95% Indiv Inductive Imp	Upper 95% Indiv Inductive Imp
007AA-A2	497	0	40.9	47.2	0		0.045	0.027	0.062
007AA-A4	551	0	42	49.3	0		0.064	0.045	0.083
007AA-A6	501	0	46.1	49.8	0		0.047	0.029	0.065
007AA-A8	522	0	42.4	50.5	0		0.048	0.031	0.066
007AA-A10	502	0	41.3	48.8	0		0.043	0.026	0.061
008AA-A3	509	0	40.6	50	0		0.042	0.025	0.059
008AA-A5	516	0	39.5	48.9	0		0.045	0.028	0.063
008AA-A8	502	0	37.6	50.2	0		0.037	0.019	0.055
008AA-A10	520	0	38	51.3	0		0.038	0.021	0.055
009AA-A1	492	0	40.4	50	0		0.038	0.020	0.055
009AA-A4	528	0	40.3	48.5	0		0.052	0.034	0.069
009AA-A6	519	0	43	49.5	0		0.050	0.033	0.068
009AA-A9	543	0	40.2	48.9	0		0.057	0.039	0.074
009AA-A10	493	0	44.9	48	0		0.045	0.028	0.063
005-B2	402	101.2	32.8	47.8	36.4		0.225	0.206	0.245
005-B6	394	73.4	26.4	47.5	35		0.175	0.154	0.196
005-B10	388	112.8	29.9	48.4	27.7		0.220	0.200	0.240
005-B11	335	111.6	36.2	54.9	37		0.192	0.173	0.211
005-B18	386	103.7	34.4	52.4	38.8		0.202	0.182	0.222
005-B20	327	98.2	37.8	56.2	37		0.179	0.159	0.199
005-D-A2	431	62.8	39.5	46.3	52.3		0.223	0.205	0.242
005-D-A3	368	79.9	40.4	45.6	54.9		0.206	0.186	0.225
005-D-A4	381	82.8	40.8	51.9	50.1		0.209	0.191	0.228
005-D-A5	385	76.6	41.7	49.5	51.6		0.214	0.196	0.232
005-D-A8	393	80.3	42.2	45.7	50.6		0.240	0.219	0.260
013-C-A1	386	83.5	34.6	23.8	53.9		0.206	0.187	0.226
013-C-A2	375	80.3	49.9	23.2	58.2		0.205	0.183	0.227
013-C-A5	375	67.1	36.7	24.1	53.8		0.186	0.164	0.208
013-C-A6	372	86.4	42	25.4	57.3		0.210	0.192	0.228
013-C-A7	386	89.8	38.8	21.5	56.1		0.206	0.187	0.226
006-CD-B4	501	26.4	29.8	52	42.2		0.141	0.123	0.159
006-CD-B9	520	23.4	26.4	51.8	42.6		0.131	0.112	0.150
006-CD-B11	552	26.9	24.6	49.1	40.8		0.155	0.134	0.175
006-CD-B21	443	24.1	31.7	54.8	42		0.112	0.093	0.130
006-CD-B29	396	20.6	32.4	57.8	41		0.089	0.069	0.110

Table C-2. Inductive Impedance Surrogate Prediction Values for "Nominal"/"Borderline" Particles

Particle ID	Kernel	Buffer	IPyC	SIC	OPyC		Predicted Inductive Imp	Lower 95% Indiv Inductive Imp	Upper 95% Indiv Inductive Imp
Nominal	350	100	40	35	40		0.251	0.221	0.280
Borderline	360	110	44	35	40		0.293	0.253	0.333
	360	110	44	38	44		0.315	0.259	0.370
	360	110	44	38	36		0.284	0.245	0.324
	360	110	44	32	44		0.306	0.251	0.360
	360	110	36	32	36		0.241	0.219	0.263
	360	110	36	38	44		0.262	0.233	0.291
	360	110	36	38	36		0.244	0.221	0.266
	360	110	36	32	44		0.264	0.233	0.295
	360	90	44	32	36		0.251	0.222	0.280
	360	90	44	38	44		0.263	0.222	0.303
	360	90	44	38	36		0.244	0.215	0.274
	360	90	44	32	44		0.256	0.215	0.296
	360	90	36	32	36		0.222	0.201	0.242
	360	90	36	38	44		0.233	0.205	0.261
	360	90	36	38	36		0.223	0.202	0.245
	360	90	36	32	44		0.234	0.204	0.264
	340	110	44	32	36		0.272	0.239	0.305
	340	110	44	38	44		0.290	0.243	0.337
	340	110	44	38	36		0.265	0.232	0.298
	340	110	44	32	44		0.282	0.236	0.329
	340	110	36	32	36		0.231	0.210	0.251
	340	110	36	38	44		0.248	0.221	0.275
	340	110	36	38	36		0.233	0.212	0.254
	340	110	36	32	44		0.250	0.221	0.279
	340	90	44	32	36		0.232	0.206	0.258
	340	90	44	38	44		0.241	0.205	0.276
	340	90	44	38	36		0.226	0.199	0.252
	340	90	44	32	44		0.235	0.199	0.270
	340	90	36	32	36		0.209	0.189	0.230
	340	90	36	38	44		0.218	0.191	0.245
	340	90	36	38	36		0.211	0.189	0.233
	340	90	36	32	44		0.219	0.190	0.248

Table C-3. Inductive Impedance Surrogate Prediction Values for "More Extreme" Particles

Particle ID	Kernel	Buffer	IPyC	SIC	OPyC		Predicted Inductive Imp	Lower 95% Indiv Inductive Imp	Upper 95% Indiv Inductive Imp
More Extreme	370	120	48	41	48		0.349	0.279	0.419
	370	120	48	41	32		0.412	0.303	0.522
	370	120	48	29	48		0.316	0.253	0.378
	370	120	48	29	32		0.376	0.276	0.475
	370	120	32	41	48		0.194	0.148	0.239
	370	120	32	41	32		0.252	0.227	0.277
	370	120	32	29	48		0.212	0.173	0.251
	370	120	32	29	32		0.268	0.237	0.298
	370	80	48	41	48		0.251	0.223	0.279
	370	80	48	41	32		0.268	0.219	0.317
	370	80	48	29	48		0.230	0.202	0.257
	370	80	48	29	32		0.246	0.199	0.293
	370	80	32	41	48		0.195	0.175	0.216
	370	80	32	41	32		0.212	0.184	0.239
	370	80	32	29	48		0.206	0.185	0.227
	370	80	32	29	32		0.221	0.188	0.254
	330	120	48	41	48		0.299	0.257	0.342
	330	120	48	41	32		0.344	0.269	0.419
	330	120	48	29	48		0.274	0.235	0.314
	330	120	48	29	32		0.316	0.246	0.386
	330	120	32	41	48		0.194	0.159	0.229
	330	120	32	41	32		0.235	0.211	0.259
	330	120	32	29	48		0.209	0.182	0.237
	330	120	32	29	32		0.248	0.220	0.276
	330	80	48	41	48		0.209	0.187	0.232
	330	80	48	41	32		0.218	0.182	0.255
	330	80	48	29	48		0.194	0.170	0.217
	330	80	48	29	32		0.202	0.166	0.239
	330	80	32	41	48		0.180	0.160	0.200
	330	80	32	41	32		0.188	0.161	0.216

C.11

Table C-4. Inductive Impedance Surrogate Prediction Values for "Most Extreme" Particles

Particle ID	Kernel	Buffer	IPyC	SIC	OPyC		Predicted Inductive Imp	Lower 95% Indiv Inductive Imp	Upper 95% Indiv Inductive Imp
Most Extreme	400	120	56	41	48		0.512	0.344	0.680
	400	120	56	41	32		0.595	0.378	0.812
	400	120	56	29	48		0.435	0.293	0.576
	400	120	56	29	32		0.513	0.325	0.702
	400	120	30	41	48		0.167	0.100	0.234
	400	120	30	41	32		0.241	0.214	0.269
	400	120	30	29	48		0.195	0.137	0.253
	400	120	30	29	32		0.265	0.233	0.297
	400	55	56	41	48		0.241	0.211	0.271
	400	55	56	41	32		0.246	0.201	0.290
	400	55	56	29	48		0.204	0.177	0.232
	400	55	56	29	32		0.209	0.168	0.249
	400	55	30	41	48		0.180	0.160	0.200
	400	55	30	41	32		0.184	0.156	0.211
	400	55	30	29	48		0.190	0.164	0.216
	400	55	30	29	32		0.194	0.158	0.229
	300	120	56	41	48		0.316	0.262	0.369
	300	120	56	41	32		0.350	0.266	0.433
	300	120	56	29	48		0.274	0.227	0.321
	300	120	56	29	32		0.307	0.232	0.381
	300	120	30	41	48		0.184	0.151	0.216
	300	120	30	41	32		0.213	0.189	0.237
	300	120	30	29	48		0.200	0.174	0.226
	300	120	30	29	32		0.228	0.201	0.255
	300	55	56	41	48		0.140	0.119	0.161
	300	55	56	41	32		0.134	0.110	0.159
	300	55	56	29	48		0.123	0.098	0.147
	300	55	56	29	32		0.118	0.090	0.145
	300	55	30	41	48		0.146	0.113	0.179
	300	55	30	41	32		0.141	0.103	0.179
	300	55	30	29	48		0.151	0.106	0.197
	300	55	30	29	32		0.147	0.097	0.196

Stepwise Fit
Response:
Capacitive Imp

Current Estimates

	SSE	DFE	MSE	RSquare	RSquare Adj		Cp		
	0.003866	28	0.0001381	0.9554	0.9458		56.930426		
Lock	Entered	Parameter		Estimate	nDF		SS	F Ratio	Prob>F
X	X	Intercept		-0.0683169	1		0	0.000	1.0000
	X	Kernel Volume		-1001.1051	2		0.002213	8.014	0.0018
	X	Buffer Volume		4910.78375	2		0.033355	120.790	0.0000
		IPyC Volume		0	1		3.324e-7	0.002	0.9619
	X	SIC Volume		4578.87964	2		0.004474	16.202	0.0000
		OPyC Volume		0	1		0.000042	0.297	0.5901
		Carbon Volume		0	1		0.000032	0.225	0.6392
		Particle Volume		0	1		0.000032	0.228	0.6371
		Kernel Volume*Buffer Volume		0	1		0.000054	0.385	0.5400
		Kernel Volume*IPyC Volume		0	2		0.000092	0.315	0.7323
		Kernel Volume*SIC Volume		0	1		0.000053	0.375	0.5454
		Kernel Volume*OPyC Volume		0	2		0.000091	0.315	0.7327
		Kernel Volume*Carbon Volume		0	2		0.0001	0.345	0.7113
		Kernel Volume*Particle Volume		0	2		0.000103	0.356	0.7037
		Buffer Volume*IPyC Volume		0	2		0.000175	0.617	0.5472
		Buffer Volume*SIC Volume		0	1		0.000011	0.078	0.7821
		Buffer Volume*OPyC Volume		0	2		0.000105	0.361	0.7001
		Buffer Volume*Carbon Volume		0	2		0.000109	0.378	0.6888
		Buffer Volume*Particle Volume		0	2		0.000061	0.207	0.8146
		IPyC Volume*SIC Volume		0	2		0.000021	0.070	0.9321
		IPyC Volume*OPyC Volume		0	3		0.000073	0.159	0.9226
		IPyC Volume*Carbon Volume		0	3		0.00016	0.360	0.7823
		IPyC Volume*Particle Volume		0	3		0.00011	0.243	0.8653
		SIC Volume*OPyC Volume		0	2		0.000076	0.261	0.7723
		SIC Volume*Carbon Volume		0	2		0.000055	0.189	0.8290
		SIC Volume*Particle Volume		0	2		0.00007	0.239	0.7893
		OPyC Volume*Carbon Volume		0	3		0.000295	0.689	0.5675
		OPyC Volume*Particle Volume		0	3		0.0001	0.222	0.8802
		Carbon Volume*Particle Volume		0	3		0.000411	0.992	0.4125
	X	Kernel Volume*Kernel Volume		15906951.6	1		0.000577	4.178	0.0505
	X	Buffer Volume*Buffer Volume		-4.22269e7	1		0.019804	143.433	0.0000
		IPyC Volume*IPyC Volume		0	2		0.000271	0.981	0.3882
	X	SIC Volume*SIC Volume		-3.57699e7	1		0.000725	5.252	0.0296
		OPyC Volume*OPyC Volume		0	2		0.000121	0.419	0.6620
		Carbon Volume*Carbon Volume		0	2		0.000106	0.367	0.6967
		Particle Volume*Particle Volume		0	2		0.000033	0.111	0.8954

Step History

Step	Parameter	Action	"Sig Prob"	Seq SS	RSquare	Cp	p
1	Buffer Volume*Particle Volume	Entered	0.0000	0.078419	0.9053	138.27	4
2	SIC Volume*SIC Volume	Entered	0.0052	0.002497	0.9342	91.938	6
3	Buffer Volume*Buffer Volume	Entered	0.0146	0.001111	0.9470	71.538	7
4	Kernel Volume*Kernel Volume	Entered	0.0873	0.000785	0.9561	59.711	9
5	Particle Volume	Removed	0.8146	0.000061	0.9554	56.93	7

Response Capacitive Imp   Actual by Predicted Plot

Capacitive Imp Predicted P<.0001
RSq=0.96 RMSE=0.0118
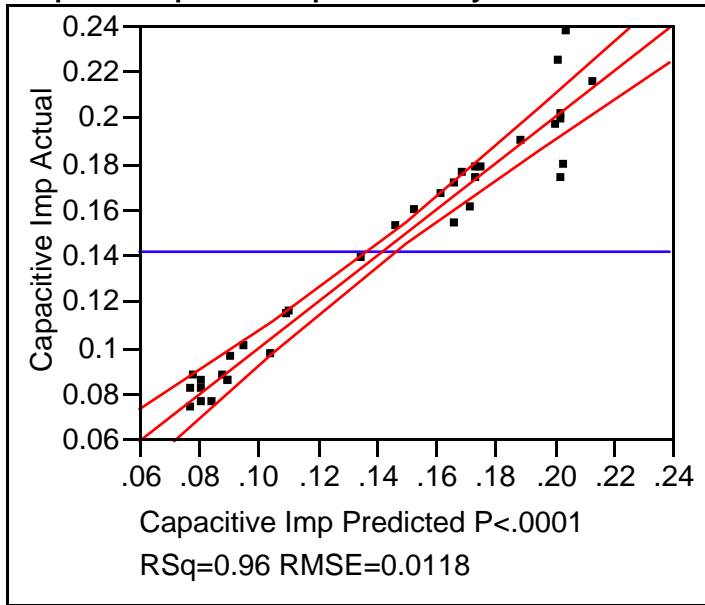
Summary of Fit

RSquare	0.955367
RSquare Adj	0.945803
Root Mean Square Error	0.01175
Mean of Response	0.141714
Observations (or Sum Wgts)	35

Analysis of Variance

Source	DF	Sum of Squares	Mean Square	F Ratio
Model	6	0.08275158	0.013792	99.8903
Error	28	0.00386598	0.000138	Prob > F
C. Total	34	0.08661756		<.0001

Parameter Estimates

Term	Estimate	Std Error	t Ratio	Prob>|t|
Intercept	-0.068317	0.045433	-1.50	0.1439
Kernel Volume	-1001.105	863.2625	-1.16	0.2560
Buffer Volume	4910.7838	316.2109	15.53	<.0001
SIC Volume	4578.8796	1647.778	2.78	0.0096
Kernel Volume*Kernel Volume	15906952	7782186	2.04	0.0505
Buffer Volume*Buffer Volume	-42226947	3525861	-11.98	<.0001
SIC Volume*SIC Volume	-35769929	15607623	-2.29	0.0296

Prediction Profiler

C.14
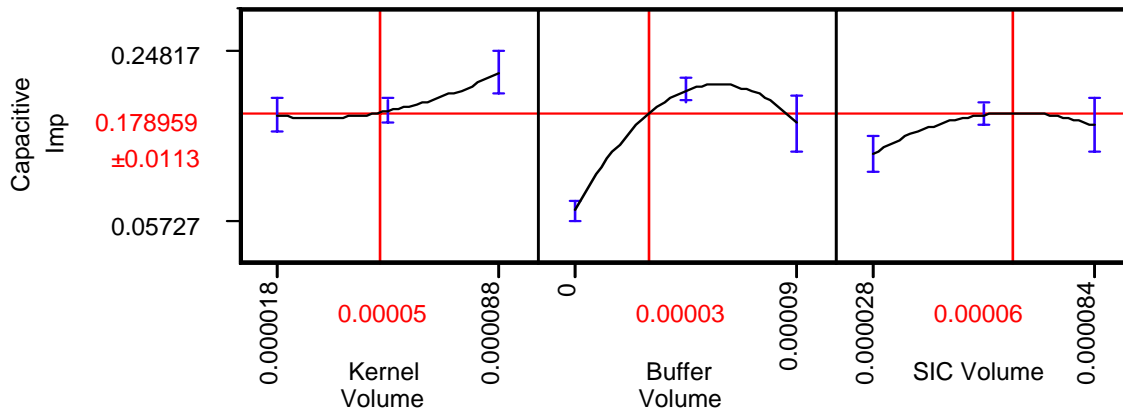
Table C-5. Capacitive Impedance Surrogate Prediction Values for Surrogate Particles

Particle ID	Kernel	Buffer	IPyC	SIC	OPyC		Predicted Inductive Imp	Lower 95% Indiv Inductive Imp	Upper 95% Indiv Inductive Imp
007AA-A2	497	0	40.9	47.2	0		0.078	0.053	0.104
007AA-A4	551	0	42	49.3	0		0.110	0.083	0.137
007AA-A6	501	0	46.1	49.8	0		0.081	0.056	0.106
007AA-A8	522	0	42.4	50.5	0		0.091	0.066	0.116
007AA-A10	502	0	41.3	48.8	0		0.081	0.056	0.107
008AA-A3	509	0	40.6	50	0		0.085	0.060	0.110
008AA-A5	516	0	39.5	48.9	0		0.089	0.064	0.113
008AA-A8	502	0	37.6	50.2	0		0.082	0.057	0.107
008AA-A10	520	0	38	51.3	0		0.090	0.065	0.115
009AA-A1	492	0	40.4	50	0		0.077	0.052	0.103
009AA-A4	528	0	40.3	48.5	0		0.095	0.070	0.121
009AA-A6	519	0	43	49.5	0		0.090	0.065	0.115
009AA-A9	543	0	40.2	48.9	0		0.105	0.079	0.131
009AA-A10	493	0	44.9	48	0		0.077	0.052	0.103
005-B2	402	101.2	32.8	47.8	36.4		0.176	0.149	0.203
005-B6	394	73.4	26.4	47.5	35		0.203	0.176	0.229
005-B10	388	112.8	29.9	48.4	27.7		0.153	0.124	0.182
005-B11	335	111.6	36.2	54.9	37		0.189	0.162	0.217
005-B18	386	103.7	34.4	52.4	38.8		0.172	0.143	0.200
005-B20	327	98.2	37.8	56.2	37		0.203	0.175	0.231
005-D-A2	431	62.8	39.5	46.3	52.3		0.202	0.176	0.229
005-D-A3	368	79.9	40.4	45.6	54.9		0.203	0.176	0.230
005-D-A4	381	82.8	40.8	51.9	50.1		0.200	0.175	0.226
005-D-A5	385	76.6	41.7	49.5	51.6		0.202	0.177	0.228
005-D-A8	393	80.3	42.2	45.7	50.6		0.205	0.179	0.231
013-C-A1	386	83.5	34.6	23.8	53.9		0.167	0.140	0.193
013-C-A2	375	80.3	49.9	23.2	58.2		0.167	0.141	0.193
013-C-A5	375	67.1	36.7	24.1	53.8		0.147	0.119	0.176
013-C-A6	372	86.4	42	25.4	57.3		0.174	0.147	0.200
013-C-A7	386	89.8	38.8	21.5	56.1		0.162	0.135	0.189
006-CD-B4	501	26.4	29.8	52	42.2		0.170	0.142	0.197
006-CD-B9	520	23.4	26.4	51.8	42.6		0.174	0.148	0.201
006-CD-B11	552	26.9	24.6	49.1	40.8		0.213	0.184	0.242
006-CD-B21	443	24.1	31.7	54.8	42		0.135	0.109	0.161
006-CD-B29	396	20.6	32.4	57.8	41		0.111	0.084	0.137

Table C-6. Capacitive Impedance Surrogate Prediction Values for "Nominal"/"Borderline" Particles

Particle ID	Kernel	Buffer	IPyC	SIC	OPyC		Predicted Inductive Imp	Lower 95% Indiv Inductive Imp	Upper 95% Indiv Inductive Imp
Nominal	350	100	40	35	40		0.196	0.165	0.227
Borderline	360	110	44	38	44		0.189	0.156	0.223
	360	110	44	38	36		0.182	0.147	0.217
	360	110	44	32	44		0.189	0.156	0.223
	360	110	44	32	36		0.182	0.147	0.217
	360	110	36	38	44		0.188	0.154	0.222
	360	110	36	38	36		0.180	0.145	0.214
	360	110	36	32	44		0.188	0.154	0.222
	360	110	36	32	36		0.180	0.145	0.214
	360	90	44	38	44		0.202	0.172	0.231
	360	90	44	38	36		0.191	0.163	0.220
	360	90	44	32	44		0.202	0.172	0.231
	360	90	44	32	36		0.191	0.163	0.220
	360	90	36	38	44		0.200	0.170	0.229
	360	90	36	38	36		0.188	0.160	0.216
	360	90	36	32	44		0.200	0.170	0.229
	360	90	36	32	36		0.188	0.160	0.216
	340	110	44	38	44		0.198	0.164	0.231
	340	110	44	38	36		0.189	0.155	0.222
	340	110	44	32	44		0.198	0.164	0.231
	340	110	44	32	36		0.189	0.155	0.222
	340	110	36	38	44		0.196	0.162	0.230
	340	110	36	38	36		0.186	0.153	0.219
	340	110	36	32	44		0.196	0.162	0.230
	340	110	36	32	36		0.186	0.153	0.219
	340	90	44	38	44		0.199	0.169	0.229
	340	90	44	38	36		0.187	0.159	0.216
	340	90	44	32	44		0.199	0.169	0.229
	340	90	44	32	36		0.187	0.159	0.216
	340	90	36	38	44		0.196	0.166	0.226
	340	90	36	38	36		0.184	0.156	0.212
	340	90	36	32	44		0.196	0.166	0.226
	340	90	36	32	36		0.184	0.156	0.212

TableC-7. Capacitive Impedance Surrogate Prediction Values for "More Extreme" Particles

Particle ID	Kernel	Buffer	IPyC	SIC	OPyC	Predicted Inductive Imp	Lower 95% Indiv Inductive Imp	Upper 95% Indiv Inductive Imp
More Extreme	370	120	48	38	48	0.154	0.120	0.188
	370	120	48	32	48	0.154	0.120	0.188
	370	120	48	38	32	0.148	0.106	0.191
	370	120	48	32	32	0.148	0.106	0.191
	370	120	32	38	48	0.156	0.119	0.194
	370	120	32	32	48	0.156	0.119	0.194
	370	120	32	38	32	0.143	0.102	0.185
	370	120	32	32	32	0.143	0.102	0.185
	370	80	48	38	48	0.202	0.174	0.230
	370	80	48	32	48	0.202	0.174	0.230
	370	80	48	38	32	0.182	0.155	0.208
	370	80	48	32	32	0.182	0.155	0.208
	370	80	32	38	48	0.199	0.171	0.227
	370	80	32	32	48	0.199	0.171	0.227
	370	80	32	38	32	0.174	0.148	0.201
	370	80	32	32	32	0.174	0.148	0.201
	330	120	48	38	48	0.191	0.157	0.225
	330	120	48	32	48	0.191	0.157	0.225
	330	120	48	38	32	0.177	0.141	0.213
	330	120	48	32	32	0.177	0.141	0.213
	330	120	32	38	48	0.190	0.154	0.226
	330	120	32	32	48	0.190	0.154	0.226
	330	120	32	38	32	0.170	0.136	0.205
	330	120	32	32	32	0.170	0.136	0.205
	330	80	48	38	48	0.191	0.161	0.222
	330	80	48	32	48	0.191	0.161	0.222
	330	80	48	38	32	0.167	0.138	0.195
	330	80	48	32	32	0.167	0.138	0.195
	330	80	32	38	48	0.186	0.156	0.216
	330	80	32	32	48	0.186	0.156	0.216
	330	80	32	38	32	0.159	0.130	0.188
	330	80	32	32	32	0.159	0.130	0.188

Table C-8. Capacitive Impedance Surrogate Prediction Values for "Most Extreme" Particles

Particle ID	Kernel	Buffer	IPyC	SIC	OPyC		Predicted Inductive Imp	Lower 95% Indiv Inductive Imp	Upper 95% Indiv Inductive Imp
Most Extreme	400	120	56	41	48		0.107	0.071	0.144
	400	120	56	41	32		0.107	0.071	0.144
	400	120	56	29	48		0.115	0.066	0.165
	400	120	56	29	32		0.115	0.066	0.165
	400	120	30	41	48		0.116	0.074	0.158
	400	120	30	41	32		0.116	0.074	0.158
	400	120	30	29	48		0.109	0.059	0.159
	400	120	30	29	32		0.109	0.059	0.159
	400	55	56	41	48		0.183	0.157	0.209
	400	55	56	41	32		0.183	0.157	0.209
	400	55	56	29	48		0.161	0.136	0.187
	400	55	56	29	32		0.161	0.136	0.187
	400	55	30	41	48		0.176	0.149	0.202
	400	55	30	41	32		0.176	0.149	0.202
	400	55	30	29	48		0.149	0.123	0.176
	400	55	30	29	32		0.149	0.123	0.176
	300	120	56	41	48		0.206	0.171	0.240
	300	120	56	41	32		0.206	0.171	0.240
	300	120	56	29	48		0.189	0.154	0.224
	300	120	56	29	32		0.189	0.154	0.224
	300	120	30	41	48		0.201	0.165	0.238
	300	120	30	41	32		0.201	0.165	0.238
	300	120	30	29	48		0.178	0.145	0.211
	300	120	30	29	32		0.178	0.145	0.211
	300	55	56	41	48		0.136	0.102	0.170
	300	55	56	41	32		0.136	0.102	0.170
	300	55	56	29	48		0.108	0.071	0.144
	300	55	56	29	32		0.108	0.071	0.144
	300	55	30	41	48		0.122	0.088	0.156
	300	55	30	41	32		0.122	0.088	0.156
	300	55	30	29	48		0.094	0.054	0.134
	300	55	30	29	32		0.094	0.054	0.134

Stepwise Fit

Response:
Inductive Imp

Current Estimates

	SSE	DFE	MSE	RSquare	RSquare Adj		AIC		
	0.0195145	18	0.0010841	0.2573	0.2161		-134.647		
Lock	Entered	Parameter		Estimate	nDF	SS	F Ratio	Prob>F	
X	X	Intercept		0.0233715	1	0	0.000	1.0000	
		Kernel Volume		0	1	0.000972	0.892	0.3583	
		Buffer Volume		0	1	0.000079	0.069	0.7958	
		IPyC Volume		0	1	0.000744	0.674	0.4231	
		SIC Volume		0	1	0.00001	0.008	0.9278	
		OPyC Volume		0	1	0.000511	0.457	0.5082	
		Carbon Volume		0	1	0.000989	0.907	0.3542	
	X	Particle Volume		662.476885	1	0.006761	6.237	0.0224	
		Kernel Volume*Buffer Volume		0	3	0.001205	0.329	0.8045	
		Kernel Volume*IPyC Volume		0	3	0.001603	0.448	0.7226	
		Kernel Volume*SIC Volume		0	3	0.001432	0.396	0.7578	
		Kernel Volume*OPyC Volume		0	3	0.001368	0.377	0.7710	
		Kernel Volume*Carbon Volume		0	3	0.001091	0.296	0.8276	
		Kernel Volume*Particle Volume		0	2	0.000972	0.420	0.6644	
		Buffer Volume*IPyC Volume		0	3	0.000805	0.215	0.8843	
		Buffer Volume*SIC Volume		0	3	0.001355	0.373	0.7736	
		Buffer Volume*OPyC Volume		0	3	0.001206	0.329	0.8042	
		Buffer Volume*Carbon Volume		0	3	0.00171	0.480	0.7008	
		Buffer Volume*Particle Volume		0	2	0.000169	0.070	0.9327	
		IPyC Volume*SIC Volume		0	3	0.002586	0.764	0.5317	
		IPyC Volume*OPyC Volume		0	3	0.002128	0.612	0.6176	
		IPyC Volume*Carbon Volume		0	3	0.001732	0.487	0.6964	
		IPyC Volume*Particle Volume		0	2	0.001138	0.496	0.6183	
		SIC Volume*OPyC Volume		0	3	0.001944	0.553	0.6538	
		SIC Volume*Carbon Volume		0	3	0.001514	0.420	0.7410	
		SIC Volume*Particle Volume		0	2	0.000853	0.365	0.6995	
		OPyC Volume*Carbon Volume		0	3	0.002151	0.619	0.6133	
		OPyC Volume*Particle Volume		0	2	0.001818	0.822	0.4573	
		Carbon Volume*Particle Volume		0	2	0.001129	0.491	0.6208	
		Kernel Volume*Kernel Volume		0	2	0.001094	0.475	0.6302	
		Buffer Volume*Buffer Volume		0	2	0.000083	0.034	0.9666	
		IPyC Volume*IPyC Volume		0	2	0.0011	0.478	0.6287	
		SIC Volume*SIC Volume		0	2	0.000403	0.168	0.8464	
		OPyC Volume*OPyC Volume		0	2	0.002462	1.155	0.3399	
		Carbon Volume*Carbon Volume		0	2	0.00112	0.487	0.6232	
		Particle Volume*Particle Volume		0	1	0.000238	0.210	0.6524	

Step History

Step	Parameter	Action	"Sig Prob"	Seq SS	RSquare	p
1	Particle Volume	Entered	0.0224	0.006761	0.2573	2

No model worth analyzing further.

Stepwise Fit

Response:
Capacitive Imp

Current Estimates

	SSE	DFE	MSE	RSquare
	0.0010779	12	0.0000898	0.9184

Lock	Entered	Parameter	Estimate	nDF	SS	F Ratio	Prob>F
X	X	Intercept	-2.3044415	1	0	0.000	1.0000
	X	Kernel Volume	-5223.9649	3	0.000904	3.356	0.0553
	X	Buffer Volume	-8560.9444	2	0.001438	8.006	0.0062
		IPyC Volume	0	1	1.864e-7	0.002	0.9660
	X	SIC Volume	115381.274	4	0.001356	3.773	0.0328
		OPyC Volume	0	1	0.000002	0.015	0.9032
		Carbon Volume	0	1	4.523e-7	0.005	0.9470
		Particle Volume	0	1	4.523e-7	0.005	0.9470
		Kernel Volume*Buffer Volume	0	1	0.000063	0.680	0.4270
		Kernel Volume*IPyC Volume	0	2	0.000022	0.103	0.9033
	X	Kernel Volume*SIC Volume	561572259	1	0.000158	1.759	0.2094
		Kernel Volume*OPyC Volume	0	2	0.000008	0.038	0.9632
		Kernel Volume*Carbon Volume	0	2	0.000032	0.151	0.8619
		Kernel Volume*Particle Volume	0	2	0.000032	0.151	0.8619
		Buffer Volume*IPyC Volume	0	2	0.000005	0.023	0.9770
	X	Buffer Volume*SIC Volume	206576828	1	0.000145	1.612	0.2283
		Buffer Volume*OPyC Volume	0	2	0.000002	0.010	0.9897
		Buffer Volume*Carbon Volume	0	2	0.000002	0.009	0.9906
		Buffer Volume*Particle Volume	0	2	0.000004	0.021	0.9797
		IPyC Volume*SIC Volume	0	2	0.000075	0.375	0.6965
		IPyC Volume*OPyC Volume	0	3	0.00001	0.027	0.9936
		IPyC Volume*Carbon Volume	0	3	0.000005	0.015	0.9973
		IPyC Volume*Particle Volume	0	3	0.000004	0.011	0.9984
		SIC Volume*OPyC Volume	0	2	0.000003	0.014	0.9858
		SIC Volume*Carbon Volume	0	2	0.000027	0.130	0.8799
		SIC Volume*Particle Volume	0	2	0.000027	0.130	0.8799
		OPyC Volume*Carbon Volume	0	3	0.000005	0.015	0.9974
		OPyC Volume*Particle Volume	0	3	0.000004	0.011	0.9983
		Carbon Volume*Particle Volume	0	0	0	.	.
	X	Kernel Volume*Kernel Volume	-342307415	1	0.00052	5.786	0.0332
		Buffer Volume*Buffer Volume	0	1	0.000001	0.015	0.9063
		IPyC Volume*IPyC Volume	0	2	0.000046	0.221	0.8057
	X	SIC Volume*SIC Volume	-1.49881e9	1	0.00112	12.469	0.0041
		OPyC Volume*OPyC Volume	0	2	0.000015	0.069	0.9339
		Carbon Volume*Carbon Volume	0	2	5.398e-7	0.003	0.9975
		Particle Volume*Particle Volume	0	2	9.713e-7	0.005	0.9955

Step History

Step	Parameter	Action	"Sig Prob"	Seq SS	RSquare	p
1	Buffer Volume	Entered	0.0000	0.01002	0.7590	2
2	Kernel Volume	Entered	0.0370	0.000737	0.8148	3
3	SIC Volume*SIC Volume	Entered	0.2057	0.000465	0.8500	5
4	Buffer Volume*SIC Volume	Entered	0.0939	0.000371	0.8781	6
5	Kernel Volume*Kernel Volume	Entered	0.0691	0.000373	0.9064	7
6	Kernel Volume*SIC Volume	Entered	0.2094	0.000158	0.9184	8

Response Capacitive Imp   Actual by Predicted Plot
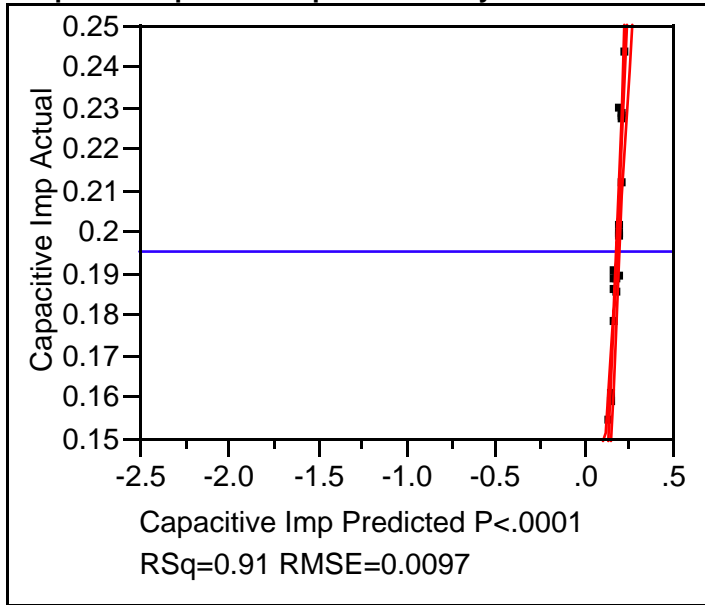
Summary of Fit

RSquare	0.907388
RSquare Adj	0.864644
Root Mean Square Error	0.009698
Mean of Response	0.19526
Observations (or Sum Wgts)	20

Analysis of Variance

Source	DF	Sum of Squares	Mean Square	F Ratio
Model	6	0.01197927	0.001997	21.2284
Error	13	0.00122266	0.000094	Prob > F
C. Total	19	0.01320193		<.0001

Parameter Estimates

Term	Estimate	Std Error	t Ratio	Prob>|t|
Intercept	-1.78013	0.670251	-2.66	0.0198
Kernel Volume	-20638.36	14059.27	-1.47	0.1659
Buffer Volume	1030.144	277.7709	3.71	0.0026
SIC Volume	88851.879	28247.25	3.15	0.0077
Kernel Volume*SIC Volume	889767603	3.4307e8	2.59	0.0223
Kernel Volume*Kernel Volume	-3.4179e8	1.4561e8	-2.35	0.0354
SIC Volume*SIC Volume	-1.1685e9	3.4315e8	-3.41	0.0047

Prediction Profiler

C.21
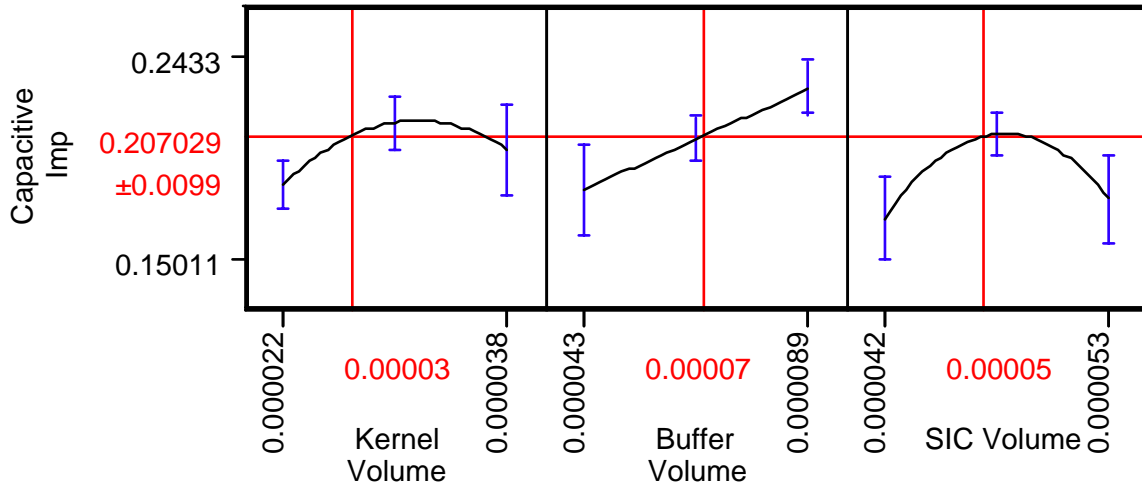
Table C-9. Capacitive Impedance 39T Prediction Values for Batch 39T Particles

Particle ID	Kernel	Buffer	IPyC	SIC	OPyC		Predicted Inductive Imp	Lower 95% Indiv Inductive Imp	Upper 95% Indiv Inductive Imp
39T-A4	403.9	90	34	32.5	50.8		0.218	0.194	0.242
39T-A17	356	86.4	37.9	36.5	52.2		0.180	0.157	0.203
39T-A20	415.7	100.3	40.7	30.2	55.7		0.244	0.215	0.272
39T-A21	350.5	96.7	41.7	33.8	55.6		0.182	0.160	0.205
39T-A22	380.1	102.6	36.8	35.2	56.7		0.202	0.174	0.230
39T-A26	378.6	102.8	34.9	33.1	50.7		0.223	0.199	0.246
39T-A29	350.8	101.9	38.9	32.8	51.6		0.187	0.163	0.210
39T-A32	362.3	114.5	32.2	32	48.8		0.216	0.193	0.240
39T-A33	376.1	100.1	40.8	33.3	50.4		0.215	0.192	0.238
39T-A35	352.1	104.2	40	34.6	52.9		0.182	0.158	0.207
39T-A37	347.5	92.8	38.7	37	52.2		0.168	0.143	0.193
39T-A56	384.7	112.2	36.6	28.9	54.7		0.226	0.202	0.251
39T-A57	359.7	76.3	41.3	34.1	51.7		0.148	0.122	0.173
39T-A63	369.7	94.3	41.1	35.4	49.7		0.195	0.172	0.218
39T-A67	370.2	90.1	36.8	32.1	45.6		0.175	0.151	0.198
39T-A68	407.9	93.2	34.9	30.7	48.6		0.208	0.181	0.235
39T-A75	351.7	88.6	36.8	34.1	51.7		0.164	0.140	0.188
39T-A77	363.9	100.4	38.2	32.4	51		0.201	0.179	0.223
39T-A82	355.7	73.4	43	36.5	52.6		0.163	0.138	0.187
39T-A92	367.3	105.9	38.7	31	51.9		0.209	0.187	0.232

Table C-10. Capacitive Impedance 39T Prediction Values for "Nominal"/"Borderline" Particles

Particle ID	Kernel	Buffer	IPyC	SIC	OPyC		Predicted Inductive Imp	Lower 95% Indiv Inductive Imp	Upper 95% Indiv Inductive Imp
Nominal	350	100	40	35	40		0.180	0.156	0.203
Borderline	360	110	44	38	44		0.033	-0.085	0.152
	360	110	44	38	36		0.033	-0.085	0.152
	360	110	44	32	44		0.204	0.181	0.227
	360	110	44	32	36		0.204	0.181	0.227
	360	110	36	38	44		0.101	0.026	0.177
	360	110	36	38	36		0.101	0.026	0.177
	360	110	36	32	44		0.208	0.185	0.231
	360	110	36	32	36		0.208	0.185	0.231
	360	90	44	38	44		0.150	0.117	0.184
	360	90	44	38	36		0.150	0.117	0.184
	360	90	44	32	44		0.174	0.151	0.196
	360	90	44	32	36		0.174	0.151	0.196
	360	90	36	38	44		0.176	0.152	0.201
	360	90	36	38	36		0.176	0.152	0.201
	360	90	36	32	44		0.152	0.123	0.180
	360	90	36	32	36		0.152	0.123	0.180
	340	110	44	38	44		0.055	-0.040	0.150
	340	110	44	38	36		0.055	-0.040	0.150
	340	110	44	32	44		0.180	0.152	0.208
	340	110	44	32	36		0.180	0.152	0.208
	340	110	36	38	44		0.110	0.048	0.172
	340	110	36	38	36		0.110	0.048	0.172
	340	110	36	32	44		0.178	0.148	0.208
	340	110	36	32	36		0.178	0.148	0.208
	340	90	44	38	44		0.143	0.111	0.175
	340	90	44	38	36		0.143	0.111	0.175
	340	90	44	32	44		0.137	0.100	0.173
	340	90	44	32	36		0.137	0.100	0.173
	340	90	36	38	44		0.159	0.133	0.185
	340	90	36	38	36		0.159	0.133	0.185
	340	90	36	32	44		0.110	0.059	0.161
	340	90	36	32	36		0.110	0.059	0.161

Table C-11. Capacitive Impedance 39T Prediction Values for "More Extreme" Particles

Particle ID	Kernel	Buffer	IPyC	SIC	OPyC		Predicted Inductive Imp	Lower 95% Indiv Inductive Imp	Upper 95% Indiv Inductive Imp
More Extreme	370	120	48	41	48		-0.431	-0.866	0.004
	370	120	48	41	32		-0.431	-0.866	0.004
	370	120	48	29	48		0.231	0.206	0.256
	370	120	48	29	32		0.231	0.206	0.256
	370	120	32	41	48		-0.138	-0.384	0.109
	370	120	32	41	32		-0.138	-0.384	0.109
	370	120	32	29	48		0.222	0.195	0.249
	370	120	32	29	32		0.222	0.195	0.249
	370	80	48	41	48		0.090	0.024	0.157
	370	80	48	41	32		0.090	0.024	0.157
	370	80	48	29	48		0.096	0.043	0.148
	370	80	48	29	32		0.096	0.043	0.148
	370	80	32	41	48		0.173	0.146	0.200
	370	80	32	41	32		0.173	0.146	0.200
	370	80	32	29	48		0.001	-0.106	0.109
	370	80	32	29	32		0.001	-0.106	0.109
	330	120	48	41	48		-0.257	-0.552	0.038
	330	120	48	41	32		-0.257	-0.552	0.038
	330	120	48	29	48		0.175	0.135	0.215
	330	120	48	29	32		0.175	0.135	0.215
	330	120	32	41	48		-0.039	-0.197	0.120
	330	120	32	41	32		-0.039	-0.197	0.120
	330	120	32	29	48		0.146	0.087	0.205
	330	120	32	29	32		0.146	0.087	0.205
	330	80	48	41	48		0.105	0.059	0.150
	330	80	48	41	32		0.105	0.059	0.150
	330	80	48	29	48		0.006	-0.106	0.118
	330	80	48	29	32		0.006	-0.106	0.118
	330	80	32	41	48		0.140	0.109	0.171
	330	80	32	41	32		0.140	0.109	0.171
	330	80	32	29	48		-0.095	-0.272	0.081
	330	80	32	29	32		-0.095	-0.272	0.081

Table C-12. Capacitive Impedance 39T Prediction Values for "Most Extreme" Particles

Particle ID	Kernel	Buffer	IPyC	SIC	OPyC		Predicted Inductive Imp	Lower 95% Indiv Inductive Imp	Upper 95% Indiv Inductive Imp
Most Extreme	400	120	56	41	48		-0.808	-1.543	-0.073
	400	120	56	41	32		-0.808	-1.543	-0.073
	400	120	56	29	48		0.237	0.190	0.284
	400	120	56	29	32		0.237	0.190	0.284
	400	120	30	41	48		-0.204	-0.543	0.135
	400	120	30	41	32		-0.204	-0.543	0.135
	400	120	30	29	48		0.258	0.231	0.284
	400	120	30	29	32		0.258	0.231	0.284
	400	55	56	41	48		0.154	0.101	0.206
	400	55	56	41	32		0.154	0.101	0.206
	400	55	56	29	48		0.022	-0.071	0.116
	400	55	56	29	32		0.022	-0.071	0.116
	400	55	30	41	48		0.186	0.150	0.222
	400	55	30	41	32		0.186	0.150	0.222
	400	55	30	29	48		-0.187	-0.403	0.029
	400	55	30	29	32		-0.187	-0.403	0.029
	300	120	56	41	48		-0.270	-0.565	0.026
	300	120	56	41	32		-0.270	-0.565	0.026
	300	120	56	29	48		0.130	0.058	0.201
	300	120	56	29	32		0.130	0.058	0.201
	300	120	30	41	48		0.024	-0.093	0.140
	300	120	30	41	32		0.024	-0.093	0.140
	300	120	30	29	48		0.069	-0.052	0.189
	300	120	30	29	32		0.069	-0.052	0.189
	300	55	56	41	48		0.076	0.009	0.143
	300	55	56	41	32		0.076	0.009	0.143
	300	55	56	29	48		-0.205	-0.460	0.051
	300	55	56	29	32		-0.205	-0.460	0.051
	300	55	30	41	48		-0.026	-0.164	0.112
	300	55	30	41	32		-0.026	-0.164	0.112
	300	55	30	29	48		-0.417	-0.810	-0.023
	300	55	30	29	32		-0.417	-0.810	-0.023

Stepwise Fit

Response:
Inductive Imp

Current Estimates

	SSE	DFE	MSE	RSquare	RSquare Adj				
	0.0004309	11	0.0000392	0.9953	0.9919				

Lock	Entered	Parameter	Estimate	nDF	SS	F Ratio	Prob>F
X	X	Intercept	-0.0219782	1	0	0.000	1.0000
	X	Kernel Volume	-902.64936	3	0.003705	31.525	0.0000
		Buffer Volume	0	1	0.000043	1.100	0.3189
	X	IPyC Volume	2613.53411	3	0.001144	9.730	0.0020
		SIC Volume	0	1	0.000043	1.099	0.3191
	X	OPyC Volume	1323.43021	3	0.004977	42.347	0.0000
		Carbon Volume	0	1	0.000043	1.096	0.3198
	X	Particle Volume	782.490115	3	0.000872	7.416	0.0055
		Kernel Volume*Buffer Volume	0	2	0.000045	0.525	0.6089
	X	Kernel Volume*IPyC Volume	8696271.84	1	0.000099	2.528	0.1401
		Kernel Volume*SIC Volume	0	2	0.000047	0.551	0.5948
	X	Kernel Volume*OPyC Volume	-4.07136e7	1	0.001236	31.546	0.0002
		Kernel Volume*Carbon Volume	0	2	0.000045	0.521	0.6106
		Kernel Volume*Particle Volume	0	1	0.000002	0.044	0.8388
		Buffer Volume*IPyC Volume	0	2	0.000047	0.552	0.5940
		Buffer Volume*SIC Volume	0	3	0.000047	0.327	0.8062
		Buffer Volume*OPyC Volume	0	2	0.000048	0.570	0.5846
		Buffer Volume*Carbon Volume	0	3	0.000073	0.541	0.6677
		Buffer Volume*Particle Volume	0	2	0.000043	0.501	0.6219
		IPyC Volume*SIC Volume	0	2	0.000046	0.539	0.6008
		IPyC Volume*OPyC Volume	0	1	0.000021	0.503	0.4944
		IPyC Volume*Carbon Volume	0	2	0.000046	0.539	0.6012
	X	IPyC Volume*Particle Volume	-1.88735e7	1	0.000536	13.687	0.0035
		SIC Volume*OPyC Volume	0	2	0.000049	0.573	0.5832
		SIC Volume*Carbon Volume	0	3	0.000064	0.467	0.7136
		SIC Volume*Particle Volume	0	2	0.000044	0.513	0.6151
		OPyC Volume*Carbon Volume	0	2	0.000048	0.571	0.5844
	X	OPyC Volume*Particle Volume	5185247.94	1	0.000551	14.055	0.0032
		Carbon Volume*Particle Volume	0	2	0.000043	0.499	0.6229
		Kernel Volume*Kernel Volume	0	1	0.000046	1.201	0.2989
		Buffer Volume*Buffer Volume	0	2	0.000071	0.895	0.4422
		IPyC Volume*IPyC Volume	0	1	9.587e-8	0.002	0.9633
		SIC Volume*SIC Volume	0	2	0.000057	0.688	0.5271
		OPyC Volume*OPyC Volume	0	1	5.399e-7	0.013	0.9130
		Carbon Volume*Carbon Volume	0	2	0.000044	0.514	0.6147
		Particle Volume*Particle Volume	0	1	0.000003	0.067	0.8009

Step History

Step	Parameter	Action	"Sig Prob"	Seq SS	RSquare	p
1	Kernel Volume*OPyC Volume	Entered	0.0000	0.089211	0.9766	4
2	IPyC Volume*Particle Volume	Entered	0.0152	0.001152	0.9893	7
3	OPyC Volume*Particle Volume	Entered	0.0077	0.000452	0.9942	8
4	Kernel Volume*IPyC Volume	Entered	0.1401	0.000099	0.9953	9

Response Inductive Imp   Actual by Predicted Plot
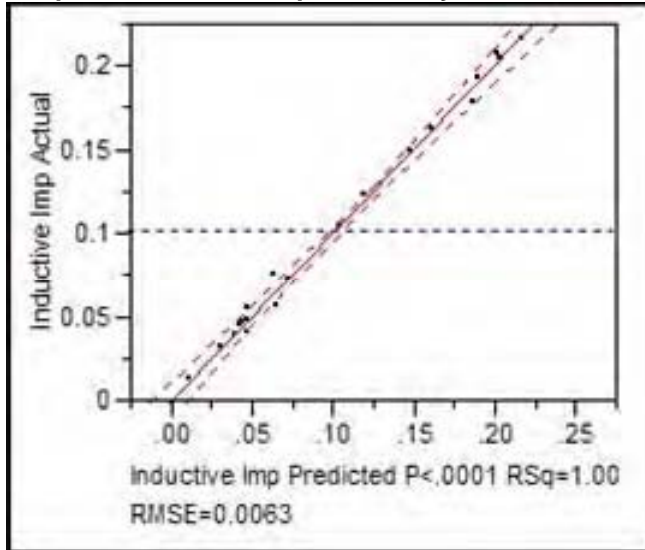
Summary of Fit

RSquare	0.995283
RSquare Adj	0.991852
Root Mean Square Error	0.006259
Mean of Response	0.10253
Observations (or Sum Wgts)	20

Analysis of Variance

Source	DF	Sum of Squares	Mean Square	F Ratio
Model	8	0.09091310	0.011364	290.1167
Error	11	0.00043088	0.000039	Prob > F
C. Total	19	0.09134398		<.0001

Parameter Estimates

Term	Estimate	Std Error	t Ratio	Prob>|t|
Intercept	-0.022013	0.016599	-1.33	0.2117
Kernel Volume	-903.762	185.8216	-4.86	0.0005
IPyC Volume	2614.1016	523.817	4.99	0.0004
OPyC Volume	1323.9498	383.0022	3.46	0.0054
Particle Volume	783.20357	188.4426	4.16	0.0016
Kernel Volume*IPyC Volume	8725480.2	5472848	1.59	0.1392
Kernel Volume*OPyC Volume	-40736738	7248788	-5.62	0.0002
IPyC Volume*Particle Volume	-18889378	5102511	-3.70	0.0035
OPyC Volume*Particle Volume	5185558.3	1383019	3.75	0.0032

Prediction Profiler

C.27
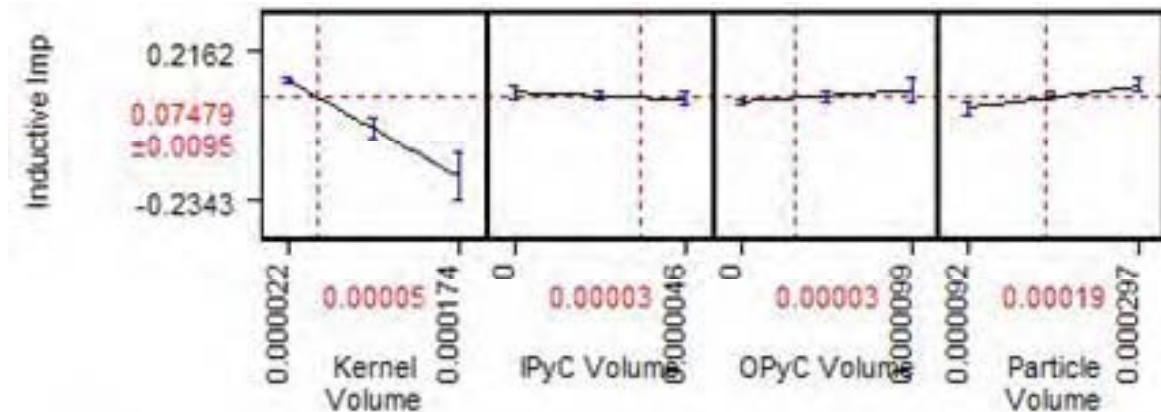
Table C-13. Inductive Impedance Batch Average Prediction Values

Batch ID	Kernel	Buffer	IPyC	SIC	OPyC		Predicted Inductive Imp	Lower 95% Indiv Inductive Imp	Upper 95% Indiv Inductive Imp
1-B	350	100	0	0	0		0.026	0.006	0.046
2-B	450	20	0	0	0		-0.017	-0.049	0.015
3-B	375	107	30	0	0		0.071	0.055	0.086
4-B	450	20	40	0	0		0.053	0.038	0.069
7-A	515	0	40	0	0		0.045	0.029	0.060
8-A	515	0	37	0	0		0.040	0.025	0.056
9-A	515	0	39	0	0		0.043	0.028	0.059
14-B	693	0	0	41	0		0.011	-0.008	0.031
5-B	372	100	33	51	35		0.190	0.173	0.208
12-B	396	111	28	0	28		0.119	0.104	0.134
13-A	363	96	32	29	35		0.162	0.145	0.178
6-CD	451	19	28	55	41		0.105	0.086	0.124
11-E	350	100	40	35	40		0.187	0.171	0.202
5-D	392	77	41	48	52		0.217	0.198	0.235
13-C	379	81	40	24	56		0.204	0.188	0.220
7-AA	515	0	40	49	0		0.048	0.032	0.063
8-AA	515	0	37	50	0		0.048	0.032	0.063
9-AA	515	0	39	49	0		0.048	0.032	0.063
39T	365	97	40	30	48		0.203	0.187	0.218
41T	365	99	40	30	32		0.148	0.131	0.165
58B	345	108	0	0	0		0.031	0.012	0.050
66BI	361	105	35	0	0		0.073	0.056	0.089
IPyC-5	345	90	31	0	0		0.066	0.050	0.081
IPyC-6	345	93	29	0	0		0.065	0.049	0.080

TableC-14. Inductive Impedance Batch Average Prediction Values for "Nominal"/"Borderline" Particles

Batch ID	Kernel	Buffer	IPyC	SIC	OPyC		Predicted Inductive Imp	Lower 95% Indiv Inductive Imp	Upper 95% Indiv Inductive Imp
Nominal	350	100	40	35	40		0.187	0.171	0.202
Borderline	360	110	44	38	44		0.200	0.175	0.226
	360	110	44	38	36		0.166	0.139	0.193
	360	110	44	32	44		0.193	0.168	0.217
	360	110	44	32	36		0.160	0.134	0.187
	360	110	36	38	44		0.218	0.202	0.234
	360	110	36	38	36		0.183	0.168	0.199
	360	110	36	32	44		0.209	0.193	0.224
	360	110	36	32	36		0.176	0.161	0.191
	360	90	44	38	44		0.191	0.175	0.207
	360	90	44	38	36		0.162	0.144	0.179
	360	90	44	32	44		0.184	0.167	0.200
	360	90	44	32	36		0.156	0.139	0.174
	360	90	36	38	44		0.199	0.181	0.216
	360	90	36	38	36		0.169	0.153	0.185
	360	90	36	32	44		0.190	0.173	0.207
	360	90	36	32	36		0.162	0.146	0.178
	340	110	44	38	44		0.211	0.192	0.230
	340	110	44	38	36		0.177	0.157	0.197
	340	110	44	32	44		0.203	0.184	0.222
	340	110	44	32	36		0.171	0.151	0.191
	340	110	36	38	44		0.223	0.204	0.242
	340	110	36	38	36		0.189	0.172	0.205
	340	110	36	32	44		0.214	0.195	0.232
	340	110	36	32	36		0.181	0.165	0.198
	340	90	44	38	44		0.198	0.181	0.215
	340	90	44	38	36		0.169	0.152	0.185
	340	90	44	32	44		0.190	0.173	0.207
	340	90	44	32	36		0.163	0.146	0.180
	340	90	36	38	44		0.201	0.180	0.222
	340	90	36	38	36		0.172	0.153	0.191
	340	90	36	32	44		0.192	0.171	0.213
	340	90	36	32	36		0.165	0.146	0.183

Table C-15. Inductive Impedance Batch Average Prediction Values for "More Extreme" Particles

Batch ID	Kernel	Buffer	IPyC	SIC	OPyC		Predicted Inductive Imp	Lower 95% Indiv Inductive Imp	Upper 95% Indiv Inductive Imp
More Extreme	370	120	48	41	48		0.200	0.143	0.258
	370	120	48	41	32		0.124	0.066	0.182
	370	120	48	29	48		0.186	0.133	0.238
	370	120	48	29	32		0.119	0.067	0.172
	370	120	32	41	48		0.260	0.235	0.284
	370	120	32	41	32		0.181	0.164	0.197
	370	120	32	29	48		0.236	0.217	0.255
	370	120	32	29	32		0.167	0.151	0.182
	370	80	48	41	48		0.194	0.174	0.214
	370	80	48	41	32		0.139	0.117	0.161
	370	80	48	29	48		0.179	0.159	0.199
	370	80	48	29	32		0.131	0.110	0.153
	370	80	32	41	48		0.207	0.185	0.229
	370	80	32	41	32		0.151	0.134	0.168
	370	80	32	29	48		0.187	0.167	0.207
	370	80	32	29	32		0.138	0.121	0.155
	330	120	48	41	48		0.234	0.205	0.264
	330	120	48	41	32		0.158	0.126	0.191
	330	120	48	29	48		0.218	0.190	0.245
	330	120	48	29	32		0.151	0.121	0.181
	330	120	32	41	48		0.266	0.237	0.295
	330	120	32	41	32		0.190	0.170	0.209
	330	120	32	29	48		0.242	0.217	0.268
	330	120	32	29	32		0.175	0.157	0.193
	330	80	48	41	48		0.209	0.191	0.228
	330	80	48	41	32		0.154	0.137	0.171
	330	80	48	29	48		0.193	0.174	0.213
	330	80	48	29	32		0.144	0.127	0.162
	330	80	32	41	48		0.206	0.178	0.235
	330	80	32	41	32		0.152	0.130	0.173
	330	80	32	29	48		0.187	0.160	0.213
	330	80	32	29	32		0.138	0.118	0.159

Table C-16. Inductive Impedance Batch Average Prediction Values for "Most Extreme" Particles

Batch ID	Kernel	Buffer	IPyC	SIC	OPyC		Predicted Inductive Imp	Lower 95% Indiv Inductive Imp	Upper 95% Indiv Inductive Imp
Most Extreme	400	120	56	41	48		0.098	-0.039	0.235
	400	120	56	41	32		0.026	-0.104	0.157
	400	120	56	29	48		0.092	-0.033	0.218
	400	120	56	29	32		0.032	-0.086	0.150
	400	120	30	41	48		0.252	0.221	0.283
	400	120	30	41	32		0.172	0.151	0.193
	400	120	30	29	48		0.227	0.204	0.251
	400	120	30	29	32		0.158	0.140	0.176
	400	55	56	41	48		0.151	0.118	0.184
	400	55	56	41	32		0.109	0.078	0.141
	400	55	56	29	48		0.141	0.109	0.172
	400	55	56	29	32		0.106	0.076	0.135
	400	55	30	41	48		0.166	0.147	0.186
	400	55	30	41	32		0.123	0.107	0.140
	400	55	30	29	48		0.148	0.130	0.167
	400	55	30	29	32		0.111	0.095	0.128
	300	120	56	41	48		0.229	0.194	0.265
	300	120	56	41	32		0.156	0.117	0.194
	300	120	56	29	48		0.215	0.181	0.249
	300	120	56	29	32		0.151	0.115	0.186
	300	120	30	41	48		0.263	0.226	0.299
	300	120	30	41	32		0.190	0.164	0.215
	300	120	30	29	48		0.239	0.206	0.272
	300	120	30	29	32		0.174	0.151	0.197
	300	55	56	41	48		0.189	0.164	0.213
	300	55	56	41	32		0.143	0.123	0.162
	300	55	56	29	48		0.174	0.149	0.199
	300	55	56	29	32		0.134	0.114	0.154
	300	55	30	41	48		0.159	0.129	0.188
	300	55	30	41	32		0.116	0.094	0.139
	300	55	30	29	48		0.142	0.113	0.170
	300	55	30	29	32		0.104	0.083	0.126
Missing Layers	350	0	40	35	40		0.089	0.067	0.112
	350	100	0	35	40		0.172	0.131	0.213
	350	100	40	0	40		0.151	0.132	0.169
	350	100	40	35	0		0.073	0.053	0.092

Stepwise Fit

Response:
Capacitive Imp.

Current Estimates

	SSE	DFE	MSE	RSquare	RSquare Adj		Cp	AIC
	0.0004363	11	0.0000397	0.9901	0.9838		.	-186.949

Lock	Entered	Parameter	Estimate	nDF	SS	F Ratio	Prob>F
X	X	Intercept	0.05021488	1	0	0.000	1.0000
	X	Kernel Volume	103.92496	2	0.000494	6.221	0.0156
	X	Buffer Volume	51.4504335	2	0.00216	27.227	0.0001
	X	IPyC Volume	-1603.3416	2	0.000584	7.360	0.0094
		SIC Volume	0	0	0	.	.
		OPyC Volume	0	0	0	.	.
	X	Carbon Volume	115.309957	2	0.002338	29.470	0.0000
	X	Particle Volume	383.348	1	0.001246	31.421	0.0002
	X	Kernel Volume*Buffer Volume	-3.62357e7	1	0.000277	6.980	0.0229
		Kernel Volume*IPyC Volume	0	1	0.000011	0.250	0.6276
		Kernel Volume*SIC Volume	0	0	0	.	.
		Kernel Volume*OPyC Volume	0	0	0	.	.
		Kernel Volume*Carbon Volume	0	1	0.000013	0.301	0.5955
		Kernel Volume*Particle Volume	0	1	6.751e-7	0.015	0.9034
		Buffer Volume*IPyC Volume	0	1	0.00003	0.736	0.4109
		Buffer Volume*SIC Volume	0	0	0	.	.
		Buffer Volume*OPyC Volume	0	0	0	.	.
		Buffer Volume*Carbon Volume	0	1	8.792e-7	0.020	0.8898
		Buffer Volume*Particle Volume	0	1	0.000012	0.274	0.6120
		IPyC Volume*SIC Volume	0	0	0	.	.
		IPyC Volume*OPyC Volume	0	0	0	.	.
	X	IPyC Volume*Carbon Volume	15564102	1	0.00023	5.790	0.0348
		IPyC Volume*Particle Volume	0	1	0.000014	0.323	0.5824
		SIC Volume*OPyC Volume	0	0	0	.	.
		SIC Volume*Carbon Volume	0	0	0	.	.
		SIC Volume*Particle Volume	0	0	0	.	.
		OPyC Volume*Carbon Volume	0	0	0	.	.
		OPyC Volume*Particle Volume	0	0	0	.	.
		Carbon Volume*Particle Volume	0	1	0.000012	0.282	0.6067
		Kernel Volume*Kernel Volume	0	1	0.000003	0.080	0.7835
		Buffer Volume*Buffer Volume	0	1	5.823e-7	0.013	0.9103
		IPyC Volume*IPyC Volume	0	1	0.000007	0.156	0.7014
		SIC Volume*SIC Volume	0	0	0	.	.
		OPyC Volume*OPyC Volume	0	0	0	.	.
		Carbon Volume*Carbon Volume	0	1	0.000011	0.253	0.6259
		Particle Volume*Particle Volume	0	1	0.000046	1.178	0.3032

Step History

Step	Parameter	Action	"Sig Prob"	Seq SS	RSquare	Cp	p
1	Particle Volume	Entered	0.0000	0.040429	0.9159	.	2
2	Buffer Volume*Buffer Volume	Entered	0.0249	0.001443	0.9486	.	4
3	IPyC Volume*Carbon Volume	Entered	0.0016	0.001602	0.9849	.	7
4	Kernel Volume*Buffer Volume	Entered	0.1201	0.00023	0.9901	.	9
5	Buffer Volume*Buffer Volume	Removed	0.9103	5.823e-7	0.9901	.	8

Response Capacitive Imp.   Actual by Predicted Plot
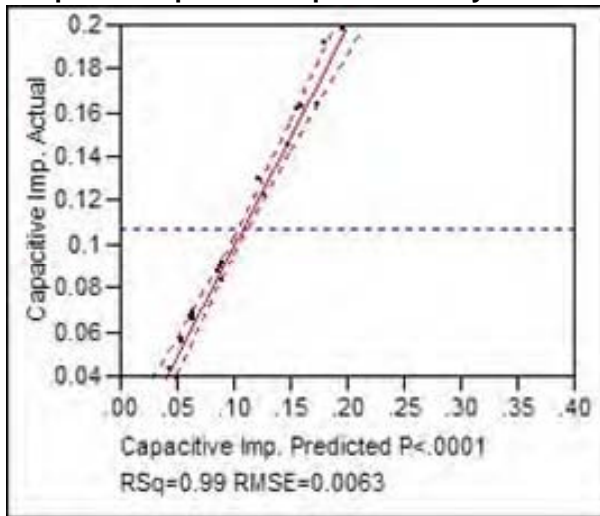
Summary of Fit

RSquare	0.990115
RSquare Adj	0.983824
Root Mean Square Error	0.006298
Mean of Response	0.107411
Observations (or Sum Wgts)	19

Analysis of Variance

Source	DF	Sum of Squares	Mean Square	F Ratio
Model	7	0.04370324	0.006243	157.3924
Error	11	0.00043634	0.000040	Prob > F
C. Total	18	0.04413958		<.0001

Parameter Estimates

Term	Estimate	Std Error	t Ratio	Prob>|t|
Intercept	0.0502149	0.034049	1.47	0.1683
Kernel Volume	103.92496	235.6673	0.44	0.6678
Buffer Volume	51.450434	375.3136	0.14	0.8934
IPyC Volume	-1603.342	477.5603	-3.36	0.0064
Carbon Volume	115.30996	356.5359	0.32	0.7524
Particle Volume	383.348	68.3887	5.61	0.0002
Kernel Volume*Buffer Volume	-36235696	13715534	-2.64	0.0229
IPyC Volume*Carbon Volume	15564102	6468195	2.41	0.0348

Prediction Profiler

C.33
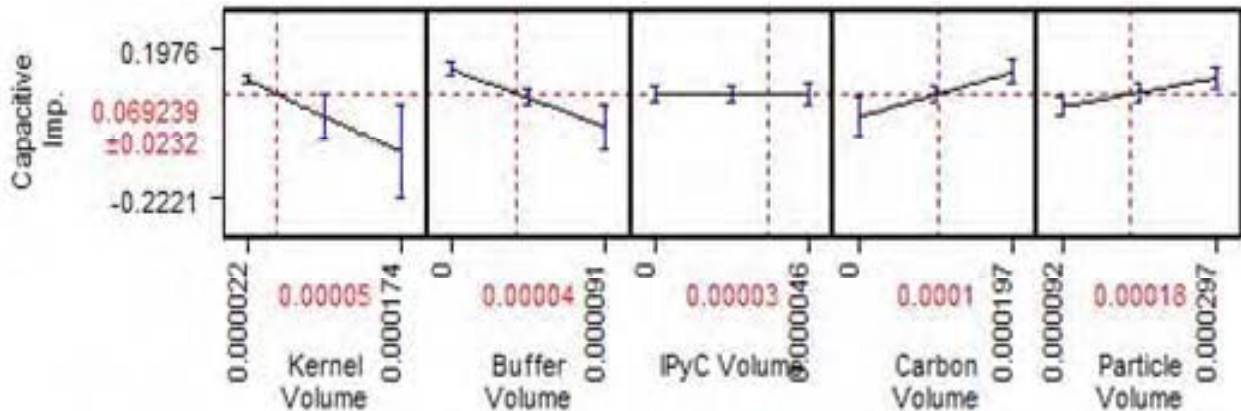
Table C-17. Capacitive Impedance Batch Average Prediction Values

Batch ID	Kernel	Buffer	IPyC	SIC	OPyC		Predicted Inductive Imp	Lower 95% Indiv Inductive Imp	Upper 95% Indiv Inductive Imp
1-B	350	100	0	0	0		0.044	0.024	0.064
2-B	450	20	0	0	0		0.057	0.004	0.110
3-B	375	107	30	0	0		0.053	0.036	0.070
4-B	450	20	40	0	0		0.045	0.024	0.067
7-A	515	0	40	0	0		0.066	0.050	0.081
8-A	515	0	37	0	0		0.065	0.050	0.081
9-A	515	0	39	0	0		0.066	0.050	0.081
14-B	693	0	0	41	0		0.162	0.142	0.181
5-B	372	100	33	51	35		0.157	0.140	0.173
12-B	396	111	28	0	28		0.088	0.069	0.107
13-A	363	96	32	29	35		0.127	0.110	0.144
6-CD	451	19	28	55	41		0.123	0.106	0.141
11-E	350	100	40	35	40		0.170	0.153	0.186
5-D	392	77	41	48	52		0.196	0.179	0.213
13-C	379	81	40	24	56		0.174	0.158	0.191
7-AA	515	0	40	49	0		0.090	0.074	0.106
8-AA	515	0	37	50	0		0.090	0.074	0.106
9-AA	515	0	39	49	0		0.090	0.074	0.106
39T	365	97	40	30	48		0.181	0.165	0.197
41T	365	99	40	30	32		0.149	0.134	0.165
58B	345	108	0	0	0		0.044	0.026	0.063
66BI	361	105	35	0	0		0.063	0.047	0.079
IPyC-5	345	90	31	0	0		0.055	0.039	0.070
IPyC-6	345	93	29	0	0		0.054	0.039	0.069

Table C-18. Capacitive Impedance Batch Average Prediction Values for "Nominal"/"Borderline" Particles

Batch ID	Kernel	Buffer	IPyC	SIC	OPyC		Predicted Inductive Imp	Lower 95% Indiv Inductive Imp	Upper 95% Indiv Inductive Imp
Nominal	350	100	40	35	40		0.170	0.153	0.186
Borderline	360	110	44	38	44		0.225	0.200	0.250
	360	110	44	38	36		0.202	0.178	0.226
	360	110	44	32	44		0.217	0.193	0.242
	360	110	44	32	36		0.195	0.172	0.219
	360	110	36	38	44		0.187	0.170	0.205
	360	110	36	38	36		0.168	0.152	0.185
	360	110	36	32	44		0.181	0.164	0.198
	360	110	36	32	36		0.162	0.146	0.178
	360	90	44	38	44		0.184	0.167	0.201
	360	90	44	38	36		0.165	0.148	0.181
	360	90	44	32	44		0.177	0.160	0.194
	360	90	44	32	36		0.159	0.142	0.175
	360	90	36	38	44		0.157	0.140	0.174
	360	90	36	38	36		0.141	0.125	0.157
	360	90	36	32	44		0.151	0.134	0.168
	360	90	36	32	36		0.135	0.120	0.151
	340	110	44	38	44		0.213	0.192	0.233
	340	110	44	38	36		0.192	0.172	0.212
	340	110	44	32	44		0.206	0.185	0.226
	340	110	44	32	36		0.186	0.166	0.205
	340	110	36	38	44		0.180	0.158	0.202
	340	110	36	38	36		0.163	0.142	0.183
	340	110	36	32	44		0.174	0.152	0.196
	340	110	36	32	36		0.157	0.137	0.177
	340	90	44	38	44		0.174	0.157	0.191
	340	90	44	38	36		0.156	0.140	0.173
	340	90	44	32	44		0.168	0.150	0.185
	340	90	44	32	36		0.151	0.134	0.167
	340	90	36	38	44		0.151	0.130	0.171
	340	90	36	38	36		0.136	0.118	0.154
	340	90	36	32	44		0.145	0.125	0.165
	340	90	36	32	36		0.131	0.113	0.149

Table C-19. Capacitive Impedance Batch Average Prediction Values for "More Extreme" Particles

Batch ID	Kernel	Buffer	IPyC	SIC	OPyC		Predicted Inductive Imp	Lower 95% Indiv Inductive Imp	Upper 95% Indiv Inductive Imp
More Extreme	370	120	48	41	48		0.301	0.243	0.359
	370	120	48	41	32		0.244	0.193	0.294
	370	120	48	29	48		0.283	0.227	0.340
	370	120	48	29	32		0.229	0.180	0.278
	370	120	32	41	48		0.203	0.184	0.221
	370	120	32	41	32		0.162	0.145	0.180
	370	120	32	29	48		0.188	0.170	0.207
	370	120	32	29	32		0.150	0.134	0.167
	370	80	48	41	48		0.199	0.178	0.220
	370	80	48	41	32		0.159	0.139	0.179
	370	80	48	29	48		0.185	0.165	0.206
	370	80	48	29	32		0.148	0.128	0.167
	370	80	32	41	48		0.147	0.127	0.166
	370	80	32	41	32		0.118	0.102	0.134
	370	80	32	29	48		0.135	0.116	0.154
	370	80	32	29	32		0.108	0.093	0.124
	330	120	48	41	48		0.266	0.235	0.297
	330	120	48	41	32		0.218	0.190	0.245
	330	120	48	29	48		0.250	0.220	0.280
	330	120	48	29	32		0.205	0.178	0.231
	330	120	32	41	48		0.190	0.158	0.223
	330	120	32	41	32		0.156	0.130	0.183
	330	120	32	29	48		0.177	0.146	0.209
	330	120	32	29	32		0.145	0.119	0.172
	330	80	48	41	48		0.175	0.157	0.193
	330	80	48	41	32		0.142	0.125	0.159
	330	80	48	29	48		0.163	0.145	0.181
	330	80	48	29	32		0.132	0.115	0.148
	330	80	32	41	48		0.136	0.113	0.160
	330	80	32	41	32		0.112	0.095	0.130
	330	80	32	29	48		0.126	0.104	0.149
	330	80	32	29	32		0.104	0.087	0.121

Table C-20. Capacitive Impedance Batch Average Prediction Values for "Most Extreme" Particles

Batch ID	Kernel	Buffer	IPyC	SIC	OPyC		Predicted Inductive Imp	Lower 95% Indiv Inductive Imp	Upper 95% Indiv Inductive Imp
Most Extreme	400	120	56	41	48		0.400	0.253	0.547
	400	120	56	41	32		0.324	0.197	0.450
	400	120	56	29	48		0.379	0.236	0.522
	400	120	56	29	32		0.306	0.183	0.430
	400	120	30	41	48		0.195	0.174	0.215
	400	120	30	41	32		0.151	0.128	0.175
	400	120	30	29	48		0.179	0.159	0.200
	400	120	30	29	32		0.138	0.115	0.161
	400	55	56	41	48		0.201	0.171	0.231
	400	55	56	41	32		0.158	0.131	0.186
	400	55	56	29	48		0.187	0.157	0.216
	400	55	56	29	32		0.147	0.120	0.174
	400	55	30	41	48		0.127	0.109	0.144
	400	55	30	41	32		0.102	0.085	0.118
	400	55	30	29	48		0.116	0.098	0.134
	400	55	30	29	32		0.093	0.076	0.109
	300	120	56	41	48		0.278	0.239	0.317
	300	120	56	41	32		0.229	0.196	0.262
	300	120	56	29	48		0.262	0.225	0.300
	300	120	56	29	32		0.216	0.184	0.248
	300	120	30	41	48		0.172	0.132	0.212
	300	120	30	41	32		0.143	0.110	0.176
	300	120	30	29	48		0.160	0.121	0.200
	300	120	30	29	32		0.134	0.101	0.166
	300	55	56	41	48		0.138	0.120	0.156
	300	55	56	41	32		0.112	0.094	0.130
	300	55	56	29	48		0.128	0.109	0.146
	300	55	56	29	32		0.104	0.086	0.121
	300	55	30	41	48		0.105	0.085	0.124
	300	55	30	41	32		0.089	0.069	0.109
	300	55	30	29	48		0.097	0.078	0.116
	300	55	30	29	32		0.083	0.062	0.103
Missing Layer	350	0	40	35	40		0.084	0.056	0.112
	350	100	0	35	40		0.086	0.051	0.121
	350	100	40	0	40		0.136	0.119	0.154
	350	100	40	35	0		0.088	0.070	0.106

Appendix D

Intellectual Property Inventory

An invention report (Battelle IPID 14936-E, "High Speed Fuel Particle Inspection System," brief description provided below) associated with the NERI project was submitted by project staff to Battelle's Intellectual Property Legal Services and has been subsequently disclosed to the U.S. Department of Energy in accordance with prime contract requirements. A decision was made by Battelle to file a U.S. Patent Application on the invention; preparation of the Application is in progress.

A sub-millimeter size induction coil and capacitance sensor has been developed for in-process testing of TRISO coated fuel particles. The invention that follows uses these technologies in a novel way so that they are able to inspect TRISO particle spheres at speeds of over 300 particles/min. The invention consists of an induction sensor, capacitance sensor, one funnel shaped enclosure, one compressed air inlet at the bottom of the funnel, one regulator/valve to control the compressed air flow, one pickup tube penetrating the side and into the center of the funnel region, one vacuum pump evacuating air from the tube, one screen with a mesh size smaller than the particles but larger than the dust (created by the particles).

Appendix E

Program Publications

1. 40th WANTO Meeting (Weapons Agencies Nondestructive Testing Organization) held at PNNL and titled "Micro-NDE", presented by Dr. Leonard Bond on April 22-24, 2003.

2. R. Hockey, L. Bond , M. Good and J. Gray, 2003. "QA/QC for Advanced Fuel Particle Production", Transactions Of The American Nuclear Society, Advances in Nuclear Fuel, Vol. 88, TANSAO 88 1–938 (2003), ISSN: 0003-018X. Presented at the 2003 ANS Annual Meeting, June 1–5, 2003; San Diego, California, pp. 412—413.

3. S. Ahmed and P. D. Panetta 2003. "Effects of Layer Properties on the Ultrasonic Resonance of Composite Spheres", Review of Progress in Quantitative NDE, KI Convention Center – Green Bay, Wisconsin; July 27 – August 1, 2003.

4. S. Ahmed and R. L. Hockey 2003, "Effects of Shape and Layer Defects on Resonance Frequencies of Spheres", presented in the NDE 2003 Conference, December 11-13, 2003, India.

5. R. Hockey, L.J. Bond, C. Batishko, J.N. Gray, J. Saurwein, and R. Lowden, "Advances in Automated QA/QC for TRISO Fuel Particle Production," Proceedings of ICAPP '04, Pittsburgh, PA USA, June 13-17, 2004; Paper 4213

6. R. Hockey, R. Mathews, L. Bond, and J. Gray, "Combining X-Ray, Eddy Current & Electric Field Measurement Techniques for Automating Particle Fuel Characterization", Review of Progress in Quantitative Nondestructive Evaluation, Edited by D.O. Thompson and D. E. Chimenti, Plenum Press, New York, July, 2004.

7. R. Hockey, presentation at The University of Michigan titled "Nondestructive Characterization of TRISO Coated Particle Fuel". October 2004.

Appendix F

Acronyms

AGR	Advanced Gas-Cooled Reactor
ANS	American Nuclear Society
AVR	Arbeitsgemeinshaft Versuchsreaktor
CARS	Coherent Anti-Stoke Raman Spectroscopy
DOE	Department of Energy
DOE-NE	DOE Office of Nuclear Energy
EM	Electromagnetic
EMATs	Electromagnetic acoustic transducers
GA	General Atomics
GT-MHR	Gas Turbine-Modular Helium Reactor
HTGR	High-Temperature Gas Reactor
HTTR	High-Temperature Test Reactor
INL	Idaho National Laboratory
ISU	Iowa State University
NERI	Nuclear Energy Research Initiative
NDE	Nondestructive Evaluation
NRC	Nuclear Regulatory Commission
ORNL	Oak Ridge National Laboratory
PBMR	Pebble Bed Modular Reactor
PNNL	Pacific Northwest National Laboratory
QA /QC	Quality Assurance/Quality Control
QAP	Quality Assurance Program
R&D	Research and Development
RUS	Resonant Ultrasound Spectroscopy
SEM	Scanning Electron Microscope
TEM	Transmission Electron Microscope
TOF	Time-of-Flight
TRISO	Tri-isotropic (fuel)
UT	Ultrasonic Testing
VHTR	Very High Temperature Reactor

Glossary

Chemical Vapor Deposition (CVD)
The high temperature process used in applying the materials to produce the TRISO fuel particles.

Eddy Current
The electrical currents induced into a material when an alternating magnetic field in present. Sometimes eddy current is referred to as the inductive impedance method used to measure the electrically conductive properties of a material.

PyC
The pyrolitic carbon layers present on the TRISO particle. There is an inner pyrolytic carbon layer designated as **IPyC** and outer pyrolytic carbon layer designated as **OPyC**.

SiC
The silicon carbide layer present on the TRISO particle.

TRISO
Standard abbreviation used to describe the fully coated fuel particle having three isotropic layers—pyrolytic carbon, SiC, and pyrolytic carbon—over the buffer coated fuel kernel.

Distribution

No. of
Copies

OFFSITE

1   KK Osborne
U. S. Department of Energy
1955 Fremont Ave. MS 1235
Idaho Falls, ID 83401

3   U.S. Department of Energy
Office of Advanced Nuclear Research
NE-20 /Germantown Building
19901 Germantown Road
Germantown, MD 20874
Attn: MA Feltus
        FJ Goldner
        SM Schuppner

1   RL Hockey
Applied Research Associates, Inc.
4300 San Mateo Blvd. NE
Suite 220
Albuquerque, NM 87110

1   JN Gray
CNDE, Iowa State University
Iowa State University
215A ASC II
1915 Scholl Road
Ames, IA 50011-3042

1   JJ Saurwein
General Atomics
3550 General Atomics Court
San Diego, CA 92121

1   LJ Bond
Idaho National Laboratory
P.O. Box 1625/MS 3898
Idaho Falls, ID 83415-3898

1   DA Petti
Idaho National Laboratory
P.O. Box 1625/MS 3860
Idaho Falls, ID 83415-3898

2   Oak Ridge National Laboratory
P.O. Box 2008
Oak Ridge, TN 37831
Attn: JH Miller
        RA Lowden

No. of
Copies

ONSITE

16   Pacific Northwest National Laboratory

S Ahmed	K5-26
JL Buelt	P7-27
CR Batishko	K5-26
M Flake	K5-26
MS Good	K5-26
DL Greenslade	K9-78
R Mathews	K5-26
M Morra	K5-26
PD Panetta	K5-26
AF Pardini	K5-26
GA Sandness	K5-26
BJ Tucker	K5-26
ML Watkins	K5-26
DR Weier	K6-08
WC Weimer	K9-09
Project File (1)	